SIGNIFICANCE OF FLUID INCLUSIONS IN THE C—O—H FLUID SYSTEM OF THE UPPER ZONE, BUSHVELD IGNEOUS COMPLEX, SOUTH AFRICA

By:

MUSAWENKOSI BUTHELEZI

(698422)

School of Geosciences, University of the Witwatersrand,

Private Bag 3, WITS, 2050,

RSA.

A DISSERTATION SUBMITTED TO THE FACULTY OF SCIENCE, UNIVERSITY OF THE WITWATERSRAND, JOHANNESBURG FOR THE DEGREE OF MASTER OF SCIENCE

UNIVERSITY OF THE
WITWATERSRAND,
JOHANNESBURG

Declaration

I Musawenkosi Buthelezi declare that this dissertation is my own work. It is being submitted for degree of Master of Science in the University of the Witwatersrand, Johannesburg. It has not been submitted before for any degree or examination in any other University.

_____ Date: _____

Musawenkosi Buthelezi

School of Geosciences University of the Witwatersrand Johannesburg

Abstract

Fluid inclusions in the Upper Zone quartz of the Bellevue drillcore and quartz of the monzonite/two-feldspar granite from the Stoffberg area are studied by a suite of advanced high-precision methods. The accessory magmatic quartz of the Bellevue drillcore samples hosts a complex suite of H_2O-CO_2-CH_4 fluid inclusions which have thus far received very little attention. For the abundant quartz in the Stoffberg samples (quartz monzonite/two-feldspar granite) hosts a simple suite of H_2O-NaCl, H_2O-$CaCl_2$ and H_2O-$MgCl_2$ fluid inclusions, which is yet to be described. CH_4-rich fluid inclusions of the Bellevue drillcore (e.g. olivine ferrodiorite, quartz anorthosite, anorthosite and leucogabbronorite) can be shown based on fluid inclusion petrography to be mainly part of the primary fluid inclusion assemblage. Based on conducted study four types of fluids were identified in Bellevue drillcore, all of them separated during the crystallization of volatile-rich residual melt of original mafic magma, whilst in the Stoffberg samples only three types of fluids were identified and are likely to be derivatives of the later felsic melts, probably of crustal melts. The melting temperatures of the carbonic ($CO_2 \pm CH_4$) of olivine ferrodiorites and leucogabbronorites, ranges from -59.7 to -56.8 ºC (mean = 58 ± 0.9 ºC; n=50), fluid inclusions, with their homogenization temperatures (TCO_2) ranging from 18.8 to 30 ºC (28 ± 3.6 ºC). The number of carbonic (CO_2 and CH_4) fluid inclusions in the Bellevue drillcore suggests that the carbonic (CO_2 and CH_4) fluids played a significant role, by acting as a geochemical barrier in shallow magmatic systems, which is contrary to the generally accepted idea that carbonic fluids are generally not a major component in such magmatic systems as these fluids tend to escape from magma at relatively deep environments. For the Stoffberg samples there is no evidence for carbonic (CO_2 and CH_4) fluid inclusions, which may imply that (CO_2 and CH_4) fluids played no part during the crystallization and cooling of the Stoffberg rocks. The Ti-in-quartz geothermometry suggests that the maximum temperature of entrapment from about 677 ± 29 to 767 ± 18ºC and 738 ± 35 and 799

± 22°C, at 3 kbar pressure, for the Bellevue core and Stoffberg samples, respectively. Based on the microthermometric, geochemical (Ti-in-quartz geothermometry) and petrographic evidence, the CH_4 observed in the samples of the Bellevue drillcore was produced by respeciation of the C-O-H fluids via in situ phase separation (immiscibility of the fluids in the H_2O-CO_2-CH_4 system) and probably the interaction of fluids with rocks during the late-stages of crystallization in the Bushveld Igneous Complex (BIC). This is further supported by the presence of graphite in H_2O-CO_2 bearing inclusions, in quartz anorthosite and leucogabbronorite. The lower melting temperature of aqueous-rich fluid inclusions, in olivine ferrodiorites and quartz anorthosites, suggest a later entrapment along cracks in quartz. This study further emphasizes the idea that the oxidation of reduced heterophase fluids could be the most important geochemical barrier caused the crystallization of solid mineral phases from heterophase fluids. The evidence presented in this study suggest that the Stoffberg material is unlikely to represent the most evolved part of the Rustenburg Layered Suite as previously suggested, but represents relic products of the Lebowa Granite Suite or crustal melts into which the Bushveld Igneous Complex intruded into.

Acknowledgements

I would like to thank my supervisors Prof. Lewis D. Ashwal and Prof. Paul Nex for their invaluable support and insight during the completion of this dissertation. Special thanks to Dr Rudolph Erasmus from the Physics Department for his assistance with use of the Horiba Jobin-Yvon LabRAM HR Raman spectrometer at university of the Witwatersrand, Microscopy and Micro-analysis unit. Dr Marta Sonika is also thanked for her support with microthermometric work and technical studies. I would also like to thank to Dr Peter Horvath for his help in the electron microprobe (EPMA) work. Mr Caiaphas Majola and Mr Sam Tshabalala also deserve a nod for their assistance in preparing the thin and thick sections. I would also like to extend my gratitude to National Research Fund, for their financial support in this project.

I would also like to thank my fellow student peers, Vuyolwethu Mahlalela, Bavisha Koorvaje, Siyanda Mgandi, Khuliso Masindi for their support and encouragement. Finally, I would like to extend my gratitude to Mathapelo Nhatchale (Fiancée) and family for their undying support during the completion of this dissertation.

TABLE OF CONTENTS

CHAPTER 2 METHODOLOGY

CHAPTER 3

List of Figures

Figure 4.1.1: Microphotographs of thin section from the Bellevue drillcore. a. Photomicrographs of olivine ferrodiorite from a depth of 105.23 m under cross-polarized light. Relatively fresh euhedral plagioclase laths are surrounded by anhedral clinopyroxenes. b. Photomicrograph of quartz anorthosite (sample BV-352.60) under cross-polarized light, showing highly altered plagioclase, associated with interstitial quartz. C. Triangular, patchy interstitial quartz surrounded by euhedral plagioclase laths from sample BV-1413.80. D. Rutile with small inclusions of quartz under plane polarized light from sample BV-83.69.

Figure 4.1.2: Microphotographs of thin section from the Bellevue drillcore. (a) Photomicrograph of an olivine ferrodiorite from a depth of 106.20 m under cross-polarized light, showing poikilitic biotite enclosing euhedral plagioclase laths. (B) Poikilitic amphibole enclosing plagioclase laths, apatite and quartz grains from sample BV-83.81. (C). Photomicrograph of olivine ferrodiorite from a depth of 106.20 m under cross-polarized light showing a poikilitic clinopyroxenes enclosing plagioclase laths. (D) Interstitial clinopyroxene between euhedral plagioclase laths from sample BV-893.90.

Figure 4.1.3: Microphotographs of thin section from the Stoffberg area. (a) Photomicrograph of granodiorite shows relatively fresh euhedral plagioclase lath with interstitial quartz (RGC-22). (B) Microphotograph of monzonite showing fresh euhedral plagioclase showing zoning patterns, with interstitial quartz and amphibole (RGC-12). (c) Photomicrograph of quartz monzonite showing highly altered plagioclase, with interstitial quartz (RGC-19). Photomicrograph of quartz monzonite showing plagioclase overgrown by alkali feldspars, surrounded by interstitial quartz (RGC-20). (E) Microphograph of pigeonite surrounded by euhedral plagioclase laths and interstitial quartz (RGC-12). (f) Abundant apatite in amphibole and oxide, with cumulate plagioclase at the edges (RGC-12). Amph-amphibole, plag-plagioclase, qrtz-quartz.

Figure 4.2.1: Microphotographs of various types of fluid inclusions from the Bellevue core samples at room temperature. Microphotograph of BV-417.90, P2 showing three fluid inclusion assemblages and these include primary (P), psuedosecondary (PS) and secondary fluid inclusion assemblages (S). P= primary, S= secondary and PS= psuedosecondary.

Figure 4.2.2: Microphotographs of various types of fluid inclusions from Bellevue core samples at room temperature.

Figure 4.2.2 (a): Photomicrograph of two-phase ─L and V─ fluid inclusions from sample BV-1454.35, P2.

Figure 4.2.2 (b): Dark one phase fluid inclusion from sample BV-417.90, in P1, comprise vapour only.

Figure 4.2.2 (c): Photomicrograph showing three phase fluid inclusion comprising two liquid (L_1 and L_2) phases and one vapour phase, from sample BV-417.90, P1.

Figure 4.2.2 (d): Microphotograph showing a three-component ─L, V and S phase─ fluid inclusion from sample BV-417.90, P.

Figure 4.2.3: Photomicrograph from sample BV-1454.35, P2, comprising a large solid crystal and comparatively minor proportions of liquid phase. 4

Figure 4.2.4: Photomicrograph showing cubic to spherical two-phase fluid inclusion comprising L and V phases, with varying proportions of liquid and vapour, from sample BV-417.90, P2, whereas photomicrograph

Figure 4.2.5: Microphotograph of secondary two-phase fluid inclusions exhibit relatively irregular forms from BV-417.90, P2 sample at room temperature.

Figure 4.3.1 (a) Microphotograph of RGC-19, P4 showing two fluid inclusion assemblages (FIA's) and these include primary (P) and secondary fluid inclusion assemblages (S), from interstitial quartz.

Figure 4.3.1 (b) Microphotograph shows similar types of FIA's, however, in a sample where there is an intergrowth of quartz and alkaline feldspars such as sample RGC-12, P6.

Figure 4.3.1 (c) Microphotograph of RGC-16, P7 shows two fluid inclusion assemblages (FIA's) and these include psuedosecondary (Ps) and secondary fluid inclusion assemblages (S), from interstitial quartz.

Figure 4.3.1 (d) Microphotograph shows similar types of FIA's, however, in a sample where there is an intergrowth of quartz and alkaline feldspars such as sample RGC-19, P2.

Figure 4.3.2: Microphotographs of various types of fluid inclusions from Bellevue core samples at room temperature. (a) Photomicrograph of two-phase ─liquid and vapour─ fluid inclusions from sample RGC-22, P3. (b) Dark one phase fluid inclusion from sample RGC-16, P3, comprising vapour-rich phase only. (c) Photomicrograph showing three phase fluid inclusion comprising two liquid phases and one vapour phase, from sample RGC-24, P1. (d) Photomicrograph from sample RGC-16, P1, comprising a large solid crystal and comparatively minor proportions of liquid phase.

Figure 4.3.3: (a) Microphotograph of cubic to spherical, two-phase inclusions LV-type of the primary FIA, from sample RGC-24, P1 in interstitial quartz.

Figure 4.3.4: Microphotograph of secondary two-phase fluid inclusions exhibit relatively immature forms from RGC-19, P3 sample at room temperature.

Figure 4.4 (a) Microphotograph of type 1 fluid inclusions from sample BV-910.10 (2)

Figure 4.4 (b) Microphotograph of type 2A fluid inclusions from sample BV-1413.80 (2)

Figure 4.4 (c) Microphotograph of type 2B fluid inclusions from sample BV-893.90 (2)

Figure 6.5: Histogram showing the melting temperatures for inclusions from anorthosite from the BV-01. These temperatures include: Tm ice (temperature of first melting (eutectic temperature)), Tm (H2O Final temperature of melting), and TmCLATH (Clathrate melting temperatures).

Figure 6.6: Histogram showing the temperature of homogenization for inclusions from anorthosite from the BV-01.

Figure 6.7: Histogram showing the melting temperatures for inclusions from anorthosite from the BV-01. These temperatures include: Tm ice (temperature of first melting (eutectic temperature)) and Tm (H2O Final temperature of melting).

Figure 6.8: Histogram showing temperature of homogenization for inclusions from Leucogabbronorite from the BV-01.

Figure 6.9: Diagram showing isochores of primary fluid inclusions from the Bellevue drillcore. Red lines represent isochores of carbonic fluid inclusion of the primary fluid assemblage and blue lines represents the isochores of the aqueous fluid inclusions of the primary fluid inclusion assemblage.

Figure 6.10: Diagram showing isochores of secondary fluid inclusions from the Bellevue drillcore. Red lines represent isochores of carbonic fluid inclusion of the secondary fluid assemblage and blue lines represents the isochores of the aqueous fluid inclusions of the secondary fluid inclusion assemblage.

Figure 6.11: Histogram showing melting temperatures for inclusions from quartz monzodiorite from the Stoffberg area. These temperatures include: Tm ice (temperature of first melting (eutectic temperature)) and Tm (H2O Final temperature of melting).

Figure 6.12: Histogram showing homogenization temperatures for inclusions from quartz monzodiorite from the Stoffberg area.

Figure 6.13: Histogram showing melting temperatures for inclusions from granodiorite from the Stoffberg area. These temperatures include: Tm ice (temperature of first melting (eutectic temperature)) and Tm (H2O Final temperature of melting).

Figure 6.14: Histogram showing homogenization temperatures inclusions from granodiorite from the Stoffberg area.

Figure 6.15: Histogram showing melting temperatures for inclusions from granodiorite from the Stoffberg area. These temperatures include: Tm ice (temperature of first melting (eutectic temperature)) and Tm (H2O Final temperature of melting).

Figure 6.16: Histogram showing homogenization temperatures for inclusions from monzodiorite from the Stoffberg area.

Figure 6.17: Plot showing isochores of aqueous fluid inclusions in quartz, from the Stoffberg area. Red lines represent isochores of aqueous fluid inclusion of the primary

fluid assemblage and blue lines represents the isochores of the aqueous fluid inclusions of the secondary fluid inclusion assemblage.

Figure 6.18. Average within-sample temperatures calculated from Ti-in-quartz concentration measurements of interstitial quartz grains in Bushveld samples, using three different TitaniQ calibrations. We consider the results from the 3 kbar calibration of Huang and Audétat (2012) (blue symbols) to be most appropriate for the Bushveld Complex samples. From samples RGC-12, -16, -19, -20, -22, and 24.

Figure 6.19. Temperature determinations for the Northern and South-Eastern limbs, of the Bushveld Igneous Complex, including solidus temperatures from the Ti-in-quartz of Buthelezi et al., (2017) (blue symbols) and from the Stoffberg area (red symbols, this study), and liquidus temperatures from the thermal modelling of Cawthorn and Walraven (1998) (green symbols). Results from Ti concentrations below the detection limit yield spuriously low temperatures, and are not plotted here. Thermal modelling by Cawthorn and Walraven (1998) for ~ 7.5 km of Bushveld mafic cumulate rocks (Lower to Upper Zones) yielded liquidus temperatures that decrease stratigraphically upward from the Lower Zone to the Upper Zone, whereas solidus temperatures reported in this study and that of Buthelezi et al. (2017) appear to be nearly constant with depth.

List of Tables

Table 6.3 Average within-sample Ti concentrations and corresponding temperatures calculated for Stoffberg samples, using the Ti-in-quartz calibrations of Huang and Audétat (2012) and Wark and Watson (2006).

Appendices 1-5

Appendix 1.1: Samples from Bellevue drillcore polished thick section description
Appendix 1.2: Samples from Stoffberg area polished thick section description
Appendix 2.1: Gas Ratios calculations in fluid inclusions, Bellevue drillcore
Appendix 2.2 Gas Ratios calculations in fluid inclusions, Stoffberg samples
Appendix 3.1.1: H2O-NaCl spreadsheet for calculations (for the BV-1 Samples)
Appendix 3.1.2: H2O-NaCl spreadsheet for calculations (for the Stoffberg Samples)
Appendix 3.2.1: Microthermometric Data for BV-1 samples (supplementary data)
Appendix 3.2.2: Isochore calculation in carbonic-rich complex fluid systems for BV-1 samples
Appendix 3.3.1: Isochore calculation in Aqueous-rich complex fluid systems for BV-1 samples
Appendix 3.3.2: Microthermometric Data for Stoffberg samples
Appendix 4.2.1: A: Ti concentrations and corresponding temperatures for individual spot analyses in sample RGC 24. Calculated temperatures are tabulated for several calibrations of the Ti-in-quartz thermometer, as discussed in the text
Appendix 4.2.2: Ti concentrations and corresponding temperatures for individual spot analyses in sample RGC 20. Calculated temperatures are tabulated for several calibrations of the Ti-in-quartz thermometer, as discussed in the text
Appendix 4.2.3: Ti concentrations and corresponding temperatures for individual spot analyses in sample RGC 22. Calculated temperatures are tabulated for several calibrations of the Ti-in-quartz thermometer, as discussed in the text
Appendix 4.2.4: Ti concentrations and corresponding temperatures for individual spot analyses in sample RGC 16. Calculated temperatures are tabulated for several calibrations of the Ti-in-quartz thermometer, as discussed in the text
Appendix 4.2.5: Ti concentrations and corresponding temperatures for individual spot analyses in sample RGC 12. Calculated temperatures are tabulated for several calibrations of the Ti-in-quartz thermometer, as discussed in the text
Appendix 4.2.6: Ti concentrations and corresponding temperatures for individual spot analyses in sample RGC 19. Calculated temperatures are tabulated for several calibrations of the Ti-in-quartz thermometer, as discussed in the text

CHAPTER 1

1.1 INTRODUCTION

Fluid inclusions hosted in felsic rocks have received far greater attention compared to those in ultramafic-mafic rocks. Hence, there are few insights about volatiles present in ultramafic-mafic magmatic systems. The principal aim of this research project is to investigate the significance of the fluid inclusions in ultramafic-mafic magmatic samples from the Bushveld Igneous Complex (BIC).

1.2 Geological Background on the nature and occurrence of Fluid Inclusions

Fluids are known to be a constituent part of many rock types, even though they occur in relatively low quantities. These fluids played an essential role in various geological processes (e.g. melting, (re)crystallization, mineral assemblages and secondary processes including alteration). The lattices of some rock-forming minerals host volatile constituents: amphiboles and micas host H_2O in the form of $(OH)^-$. Even quartz and many other minerals – olivine, which is an anhydrous mineral, can contain water at high temperatures (Spear and Selverstone, 1983; van den Kerkhof, 1988).

Gaseous species that are not bound to minerals occur as separate fluid phases, typically in the form of fluid inclusions. Methane is one of five “simple” species that appear to be most stable in fluid inclusions, whereas the “complex” species are restricted to extreme environments. Fluid inclusion gases other than CO_2 and H_2O, such as methane, occur as almost pure inclusions, but are more often present as components within inclusions e.g. carbon dioxide (mostly CO_2—CH_4) (van den Kerkhof, 1988).

Fluid inclusions represent trapped fluids that were at the pressures and temperatures of the rock formation when they were trapped. They can be trapped within crystals during localized recrystallization along fractures at some later time (secondary inclusions) or during initial growth from solution or during total recrystallization (primary inclusions). The trapped fluids

may consist of vapour, and/or liquid, and the composition of the fluids may include gas or gas-bearing liquids, pure water, brines of various salinity, and sulphide, silicate or carbonate daughter minerals, among others Bodnar (2003). Alternatively, solid components within the fluid inclusions may be crystals that were trapped during crystallization (Diamond, 2003). Therefore, these inclusions can provide information on fluid migration pathways and fossil hydrogeological systems.

Fluid inclusions are a useful tool for understanding various geological processes, particularly in materials from ore deposits, because they can provide important information on pressure and temperature conditions during ore formation (van den Kerkhof, 1988), and the nature of the ore-forming fluids (Roedder, 1979; Bodnar, 2003). The composition of fluid inclusions is indicative of the chemical environment at which the rock formed (reducing vs oxidizing, dry vs wet) (van den Kerkhof, 1988). They can be found in a variety of minerals, but are best preserved in the mineral quartz, because of its lack of cleavage, its easy healing and (re)crystallization properties, and its lack of reaction with the fluid inclusions (Roedder, 1984; van den Kerkhof, 1988).

The principal reason for investigating fluid inclusions is to constrain physio-chemical parameters such as temperature and pressure (P-T), as well as the chemistry of the fluid during trapping. Contents of fluid inclusions are rarely inert, and may have experienced post-trapping changes such as alteration (e.g. Goldstein, 2001). Hence, investigation of fluid inclusions requires detailed examination to ensure that there is no evidence for changes in volume or composition, or leakage at any stage in the evolution of the system. Thus, fluid inclusions ought to follow a path of constant density, which is commonly referred to as an isochore. This path is a univariant isochoric-isopleth in P-T space.

Fluid inclusions occur in a wide variety of environments. For example, they are found within rock-forming minerals in volcanic and plutonic rocks, within cementing minerals of sedimentary rocks, and metamorphic minerals in metamorphic rocks.

Sorby (1858) first described melt inclusions in volcanic rocks, and proved experimentally that most of the liquid phase in inclusions is represented by water. Although they are an unusual feature in igneous rocks, they have been documented in rock-forming minerals derived from a number of magmatic sequences, including both plutonic (e.g. Sobolev *et al*., 1974; Weisbrod, 1981; Roedder, 1984; Adersen, 1990; Larsen *et al*., 1992; Krot *et al*., 1994; Potter *et al*., 1998, 2004; Fall *et al*., 2007), and volcanic examples (e.g. Roedder, 1976; Gerlach, 1980; Gize and McDonald, 1993; Kelly, 1996; Frezzotti and Peccerillo, 2004; Klemd, 2004; Yong *et al*., 2007). There are still very limited data on fluid inclusions hosted in samples from layered mafic-ultramafic intrusions (LMI) (e.g., Ballhaus and Stumpfl, 1986; Frost and Touret, 1989; Schiffries, 1990; Larsen *et al*., 1992; Sonnethal, 1992; Glebvitsky *et al*., 2001; Ripley, 2005).

1.3 Fluid inclusions igneous rocks

Fluid inclusion studies in igneous rocks have documented a variety of fluids: H_2O, C_2O, N_2, CH_4 and saline (e.g. Ballhaus and Stumpfl, 1986; Schiffries, 1990; Pollard *et al*., 1991; Larsen *et al*., 1992; Robb *et al*., 1994; Freeman and Robb, 1995; Freeman *et al*., 1997; Glebovitsky *et al*., 2001; Ripley, 2005; Hanley *et al*., 2008; Zhitova *et al*. 2007, 2009, 2016). Saline solutions with variable amounts of chlorides (e.g. $CaCl_2$, KCl and NaCl) and other salts constitute most of the fluid inclusions. These fluids seldom occur as pure species, but rather mixtures due to the complexities inherited from natural processes. In addition to the salts, evidence from fluid inclusions from samples from the upper mantle show that fluid systems these are characterized by various combinations of carbon, oxygen, hydrogen and nitrogen (C-O-H-N) (Van den Kerkhof, 1988).

Fluid inclusion studies have raised key petrological questions, such as the involvement of significant amounts of CO_2 and H_2O in igneous rocks (Roedder, 1984), as well as the presence of CH_4 (e.g. Petersilie *et al*., 1961; Petersilie and Sørensen, 1970; Potter and Konnerup-Madsen, 2003). Some of these studies have also demonstrated that these fluids play important roles in igneous processes (i.e. fluid immiscibility, magma degassing). Fluid inclusion studies have led to the discovery of oil-gas fields in igneous basement rocks, such as the Ilímaussaq alkaline intrusion, Greenland in the 1950s, and the alkaline intrusions of Lovozero and Khibina of the Kola Peninsula, north west of Russia (e.g. Petersilie, 1962; Petersilie and Sørensen, 1970; Potter and Konnerup-Madsen, 2003).

Fluid inclusion studies have also produced invaluable information regarding the mineralization of PGEs and sulphides (e.g. Ballhaus and Stumpfl, 1986; Zhitova *et al*., 2007, 2009, 2016). Fluids in the form of magmatic volatiles in layered mafic intrusions are suggested to have played a significant role in the in processes of formation of PGE mineralization in differentiated mafic-ultramafic intrusive complexes (e.g. enrichment mechanisms and concentration of PGEs in the course of crystallization). This is supported by geochemical, textural and mineralogical evidence in LMI such as the Skaergaard intrusion, Greenland, Stillwater Complex, USA, and the Bushveld Complex South Africa (Schiffries, 1982; Volborth and Hanley, 1984; Ballhaus and Stumpfl, 1986; Boudreau, 1987; Sonneenthal, 1992; Meurer *et al.*, 1999; Willmore *et al*., 2000; McBinery, 2002; Hanley *et al*., 2008; Zhitova *et al.*, 2009, 2016; Kanitpanyacharoen and Boudreau, 2013).

1.4 Regional geology

The Bushveld Igneous Complex (BIC) crops out in the northern part of South Africa and it is the largest layered mafic intrusion on Earth (Figure 1), with a total areal extent greater than 100,000 km^2 (Cawthorn and Walraven, 1998; Wilson, 2015; Finn *et al*., 2015), with an average thickness of about 7.5 to 9.0 km for the layered ultramafic and mafic cumulate rocks, and a total volume > 1 million km^3 (e.g., Cawthorn and Walraven, 1998). The Bushveld Igneous Complex was emplaced at 2055 Ma into the Kaapvaal craton (Zeh *et al.*, 2015; Mungall *et al*., 2016), and contains the world's largest reserves of vanadium, chromium and platinum group elements (PGEs) (Lee, 1996).

The BIC is made up of three distinctive groups: The extrusive rocks of the Rooiberg group, which are the oldest of the three groups, followed by the intrusive mafic cumulate rocks of the Rustenburg Layered Suite (RLS), and then the intrusive felsic rocks of the Lebowa Granite Suite (Figure 1) (SACS, 1980; Scoon and Mitchell, 2012). The mafic cumulates of the Rustenburg Layered Suite are demonstrably older than the felsic rocks of the Lebowa Granite Suite (e.g. Wilson *et al.*, Van Tongeren, 2011). The voluminous magmatism of this intrusion occurred over a relatively short period, approximately 1 Ma, based on high precision U-Pb ages obtained by CA-ID-TIMS from zircons (Zeh *et al*., 2015; Mungall *et al*., 2016).

The BIC intruded into the supracrustal rocks of the Transvaal Supergroup and the rocks of the Rooiberg Group. These supracrustal rocks are mainly chemical and intracratonic clastic sedimentary rocks of Paleoproterozoic age (2551 to 2204 Ma) (Barton *et al*., 1994; Cawthorn and Walraven, 1998) and these include dolomite, sandstone and quartzite, with interlayered andesitic volcano-clastic sediments (Eriksson *et al.*, 1993; Barnes *et al*., 2009). The Transvaal Supergroup is presently exposed in 4 sedimentary basins that may have constituted a

continuous sedimentary basin that stretched across the entire Kaapvaal craton (Gleason *at al.*, 2011).

The BIC is subdivided into four limbs — the far Western limb, Northern, Western and Eastern limbs, at present levels of erosion, and with a fifth limb, the Southeastern limb (Bethal lobe), which is completely covered by sedimentary rocks of the Karoo Supergroup (Figure 1). These limbs have been widely interpreted to be magmatic bodies that are discrete (e.g. Cousins, 1959; Meyer and De Beer, 1987). However, more recent re-interpretations of the regional gravity signature, suggest that the Western and Eastern limbs represent a continuous body at depth (e.g. Cawthorn and Webb, 2001; Webb *et al*., 2004).

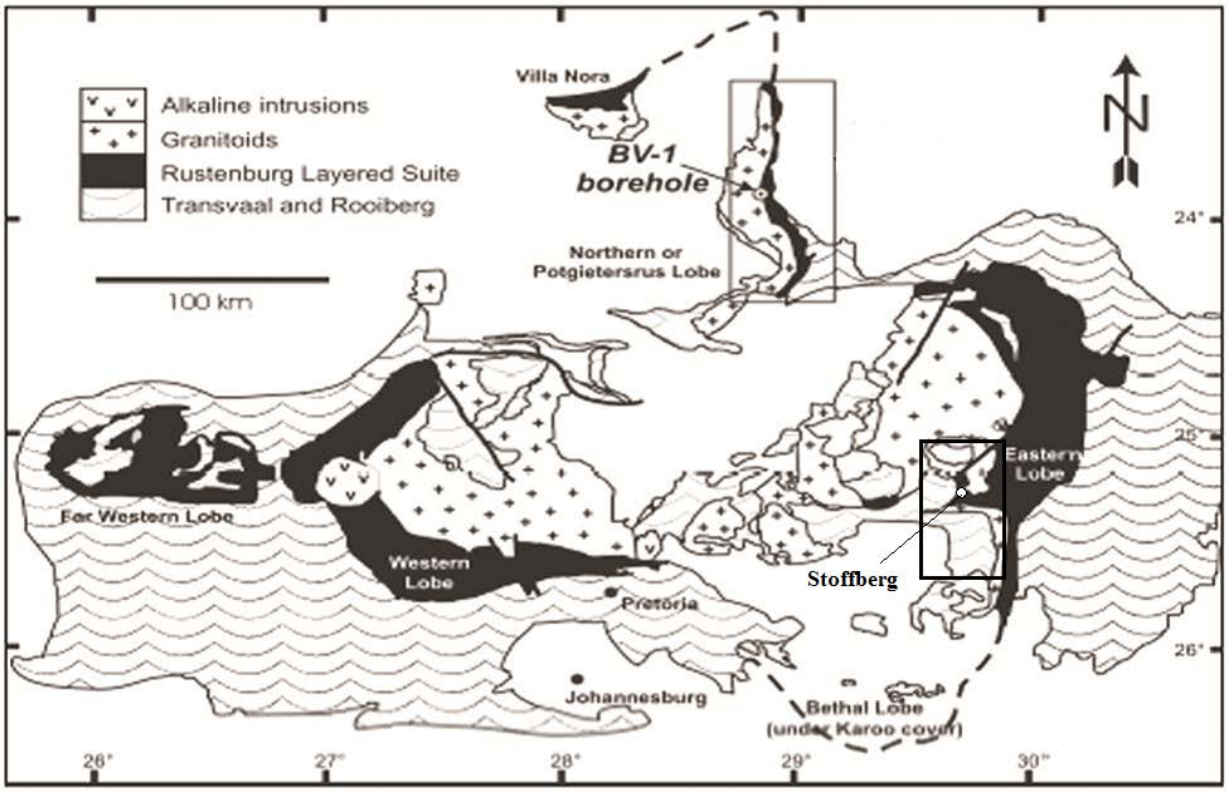

Figure 1: Generalized geological map of the Bushveld Igneous Complex showing the three distinctive groups of the BIC and the five limbs of the BIC (after Ashwal *et al*., 2005). The white open circle shows the location of Stoffberg area, whereas the white half open circle shows the location of the Bellevue drill core in the Northern limb, it is also marked by the rectangle area.

1.5 Rustenburg layered suite (RLS)

The RLS is subdivided into five stratigraphic units, primarily based on the dataset obtained from the Western and Eastern limbs, as these two limbs have more complete development of the stratigraphic coverage (e.g. SACS, 1980; Eales and Cawthorn, 1996; Ashwal *et al*., 2005). The subdivisions of the RLS from the base to the top are: the Marginal Zone, Lower, Critical, Main and Upper Zones (Barnes *et al*., 2009). Wilson (2015) recently discovered the Basal Ultramafic Sequence beneath the Marginal Zone in the Eastern Limb. The criteria for distinguishing the subdivisions of the RLS are not universally agreed upon (e.g. Kruger, 1990; Ashwal *et al*., 2005). However, these zones are generally distinguished based on the appearance or disappearance of key oxide and silicate minerals (Cawthorn *et al*., 2006; Cole *et al*., 2013).

1.6 The Geology of the Upper Zone

The Upper Zone of the BIC has a thickness of approximately 2000 m (Willemse, 1969); it is layered and represents the most laterally widespread zone of the RLS zones. This zone is interpreted as a highly differentiated, single cumulate pile that extends to the roof of the layered intrusion (Kruger *et al*., 1987; Kruger 2005), as it is characterized by highly differentiated progression of apatite-rich rocks, titaniferous magnetite, troctolite, anorthosite, ferrodiorite, ferrogabbronorite, gabbronorite and norite (Molyneux, 1974; Reynolds, 1985b; Kruger *et al*., 1987). The main cumulate phases of these lithological units are plagioclase (i.e. the dominant silicate mineral), iron-rich olivine, titanomagnetite, iron-rich pyroxenes and apatite (Wager and Brown; 1968; Lum, 2011), with some sporadic sulifides (von Gruenewaldt, 1976). Quartz, biotite, potassium feldspar and hornblende occur as intercumulus phases in these lithological units (Lum, 2011). Based on lithological correlations it is evident that rock successions and thickness of the UZ are different in different limbs of the BIC (von Gruenewaldt, 1973; Tegner

et al., 2006). The Upper Zone is present in 4 of the 5 limbs of the BIC and constitutes most of the rocks in the southern limb (Kruger, 2005).

The UZ it is characterized by the appearance of cumulus magnetite, that makes up ~5% of the gabbroic rocks throughout the sequence (Molyneaux, 1974). It also hosts numerous magnetite layers (more than twenty titanium-vanadium-magnetitite layers), where the magnetite layers generally occur in four groups containing up to seven layers each, (Molyneaux, 1974; Eales and Cawthorn, 1996), that contain only a minor amount of interstitial silicates (typically plagioclase). These layers of magnetite are frequently associated with an anorthosite footwall and host vanadium (Cawthorn *et al*., 2006; Cole *et al*., 2013), which makes up approximately 50% of the world's vanadium reserves (Kinnaird, 2005).

1.7 Eastern Limb

This limb of the BIC has received far greater attention as compared to the other limbs in terms of stratigraphic and regional mapping due to the great amount of exposure forming a rugged topography of arcuate and linear ridges representing various layered successions generated by the uplift of the region and subsequent erosion (Von Gruenewaldt, 1973; Sharpe, 1981; Molyneux, 2008; Scoon and Viljoen, 2016). However, the exposure of the uppermost cumulates is generally obscured by scree from the overlying material (Cawthorn, 2013).

The Eastern limb outcrops in such a way that it exhibits a complete sequence of the RLS from the harzburgitic rocks to fayalitic- and apatite-bearing diorites (Cameron, 1978; 1980; 1982) and dips gently to the southwest or west (Scoon and Viljoen, 2016). The Eastern limb in general has a maximum thickness of 8 ± 1 km, with some evidence for lateral thinning in some of the exposed sections in the southern part of the Eastern limb, near Dullstroom (Cawthorn and Walraven, 1998). According to Cawthorn and Walraven (1998) an estimated 30,000 km^2 total

area is occupied by the Eastern limb. This is based on gravity and magnetic data, metamorphic aureole, and minimum extent of outcrop.

The Eastern limb of the Bushveld Igneous Complex hosts a number of mineralized units─ and these include the (1) chromitite layers (LG1-7; MG1-5 and the UG1-3) of the Critical Zone; almost all of these chromitite layers host a significant amount of PGE's, but only the UG2 constitutes a primary ore reef or layer, (2) the Merensky reef, which is well renowned PGE rich reef, and (3) the magnetite-rich layers of the Upper Zone, which are the main source of vanadium, titanium and magnetite (Scoon and Viljoen, 2016).

1.8 Stoffberg Area

The Stoffberg area is located in the southern sector of the Eastern limb, of the Bushveld Igneous Complex (Figure 1). The geological succession of this area is largely dominated by rocks of the Upper Zone that occur beneath the extrusive rocks of the Rooiberg Group, the roof rocks to the intrusion. The thickness of these rocks ranges from 400 to 700 m in the Stoffberg area. It has been suggested that these rocks represent the most evolved magma of the Bushveld Igneous Complex (Cawthorn, 2013).

1.9 Northern Limb

The Northern limb of the Bushveld Igneous complex is exposed from about 30 kilometres SW of the town of Mokopane (formerly Potgietersrus), to about 25 kilometres north of Gilead, equalling a strike length of about 110 kilometres (Figure 1) (Ashwal *et al*., 2005). According to Van der Merwe (1978) an estimated 7275 km^2 total area of the Northern limb is covered by layered mafic cumulate rocks, but most workers of the BIC also include the layered mafic rocks north of Villa Nora as part of the Northern limb, which is an exposure that is approximately 320 km^2 in area (Figure 1) (Ashwal *et al*., 2005). A characteristic feature of the Northern limb

is the transgressive nature of the mafic cumulates with the country rocks of the Transvaal Supergroup and Archaean basement granitoids (Sharman *et al*., 2005). The total stratigraphies of the Eastern and Western limbs are relatively thicker than the Northern limb (Barnes and Maier, 2002) as the Lower Zone and the Critical Zone of the Northern limb are either absent or poorly developed (Schouwstra *et al*., 2000).

The Northern limb contains the Platreef, which is of major economic significance. The overall strike of the Platreef in the Northern limb is northwest or north (Kinnaird, 2005), with a strike length of about 30 kilometres Figure 1 (Lee, 1996; Ashwal *et al*., 2005). The Platreef comprises mainly pyroxenites and contains xenoliths of footwall rocks. It is irregularly mineralized with PGEs, copper and nickel.

1.10 The Bellevue (BV-1) Drillcore

The deep stratigraphic BV-1 borehole used in this study is approximately ~2950 m drilled on the farm Bellevue at an elevation ~980 m; and at latitude: 23°55’34.669” S, longitude: 28°45’20.327” E (Figure 1). This borehole is collared in the granites of the Lebowa Granite Suite (80 m in thickness), and drilled through the entire Upper Zone (1492 m vertical depth) to about halfway through the Main Zone (1374 m) and ends within a prominent troctolite layer (Ashwal *et al*., 2005).

1.11 Previous investigations relevant to the study

There are limited data on fluid inclusions hosted in mafic-ultramafic rocks compared to those in rocks of felsic composition (e.g. Ollila, 1981, 1984; Pollard *et al*., 1991; Robb *et al*., 1994; Freeman and Robb, 1995; Freeman *et al*.,1997 and Freeman, 1998). Hence, there is little insight about volatiles present in mafic-ultramafic magmatic systems from fluid inclusion studies such as the Bushveld Igneous Complex.

Fluid inclusions from the Bushveld Igneous Complex were first observed by Schiffries (1984), but data on these inclusions was first published by Ballhaus and Stumpfl (1986). Since, then a wide variety of fluid inclusions have been identified including– CH_4-rich, CO_2-rich and aqueous fluid inclusions (Schiffries, 1988, 1989, 1990, Zhitova *et al*., 2009, 2016). Most of these studies (see Table 1) were carried out from samples obtained from the Merensky Reef and the upper Critical Zone of the Bushveld Igneous Complex (Ballhaus and Stumpfl, 1986; Schiffries, 1990; Zhitova *et al*., 2007, 2009, 2016), with little focus on the other zones of the Complex.

Ballhaus and Stumpfl (1986) were the first to describe in detail the fluid inclusions and their relevance to platinum and sulphide mineralization in the BIC, using material collected from the mineralized pegmatitic pyroxenite orthocumulate, which forms at the base of the Merensky cyclic unit (Jackson, 14970; Ballhaus and Stumpfl, 1986). Most of the fluid inclusions they studied were secondary inclusions (Ballhaus and Stumpfl, 1986; Hanley *et al*., 2008). Their study showed that fluid inclusion data, complemented by the distribution pattern of PGEs and the composition of hydrous silicates emphasizes the significance of late-magmatic processes during platinum mineralization (Ballhaus and Stumpfl, 1986). Similar results were reported from the platiniferous J-M Reef of the Stillwater Complex (e.g. Boudreau and McCullum, 1985; Volboth *et al*., 1985; Mathez *et al*., 1985).

In the study by Ballhaus and Stumpfl (1986), a complex suite of H_2O-NaCl-($CaCl_2$)-CO_2-CH_4 fluid inclusions, hosted in postcumulus quartz, of the Merensky Reef, which hosts the world's largest workable concentrations of PGEs. They also identified at least two generations of fluid inclusions, with different compositions, with the earliest generation of comprising of three types of fluid inclusion types: 1) NaCl-(H_2O), which had <10% of water; 2) followed by an assemblage of CO_2 coexisting with brine and halite daughter crystals; 3) and polyphase inclusions with high contents of divalent cations, and with up to six daughter and accidental

phases. This generation of fluid inclusions was trapped at pressures of 4-5 kbar and at temperatures not greater than 730°C. The later generation of fluid inclusions are CO_2-H_2O, H_2O-NaCl, and pure CH_4 and CO_2 (Ballhaus and Stumpfl, 1986).

Schiffries (1990) first described a new class of aqueous (liquid-absent aqueous fluid inclusions and phase equilibria in the system $CaC1_2$-NaCl-H_2O) fluid inclusions that hold special significance as they violate several common assumptions regarding phase equilibria in inclusions, in secondary quartz, from the core of a zoned mafic pegmatiod, in the Upper Zone of the Eastern limb of the Bushveld Igneous Complex. The interpretation was drawn from the microthermometric and Raman spectra data. He observed multiple generations of fluid inclusions in the quartz crystals. Most of these inclusions occur along fractures Schiffries (1990).

This new class of aqueous fluid inclusions, which is referred to as type-3a, are spatially associated with a second type of inclusions (type-1h) comprised of liquid, vapour, antarcticite and halite at ambient temperature (20 ˚C), whereas for the former the liquid-phase is absent at the same temperature (Schiffries, 1990). The bulk compositions of these two types of fluid inclusions were found to be similar, but differ fundamentally in terms of melting behaviour as their compositions lie on opposite sides of two closely spaced sub-solidus joins. This study found that analysis of the liquidus diagram for the $CaC1_2$-NaCl-H_2O system shows that fluid inclusions rich in $CaC1_2$ may display a rich variety of unusual phase equilibria (Schiffries, 1990).

Zhitova *et al*. (2007; 2009) investigated fluid inclusions in symplectitic quartz from the Merensky Reef of the BIC in order to improve our understanding of the evolution trend of magmatogene fluids of intercumulus crystallization stage, as magmatogene fluids play significant role in the formation of PGE-sulfide mineralization of different types in

differentiated ultramafic-mafic intrusive complexes (Naldrett, 2003). The fluid inclusions were identified in two generations of quartz corresponding to successive stages of crystallization of intercumulus liquid, of pyroxene-pegmatites– (1) Early generation from symplectitic intergrowth with plagioclase, and also in the (2) later generation from miarolitic cavities (Zhitova *et al*., 2009). The earliest generation of the fluid inclusions comprised of homogeneous highly dense CH_4 and nitrogen gas mixture, followed by a generation of fluid inclusions, composed of heterogeneous composition, which comprises brines with a free less-dense gas phase (mostly of CO_2) from the miarolitic quartz crystals. The latest generation of fluid inclusions were also found to be heterogeneous in composition, which comprised free-low-dense gas phase (syngenetic gas) and low salinity water-solution (primary water-salt) (Zhitova *et al*., 2007). For the first time in the Bushveld Igneous Complex, they reported primary combined and gaseous inclusions that are said to characterise the initial stage of fluid separation from boiling residual alumosilicate intercumulus liquid (Zhitova *et al*., 2009).

The minimum possible estimates of pressure and temperatures of entrapment of these fluid inclusions were found to be between 400 and 900ºC for the temperature and 3.50–1.00 kbar for pressures (Zhitova *et al*., 2009). They proposed that their findings can be used for estimation of the ore-bearing capacity of various zones of differentiated ultramafic-mafic intrusions.

Zhitova *et al*. (2016) recently investigated fluid inclusions in the Merensky Reef quartz and later pegmatite veins crosscutting the Platreef rocks of the Bushveld Complex in order to improve our understanding on the role of magmatic fluids of metal-bearing reefs and post magmatic fluids of the Bushveld Igneous Complex. This study identified a few types of fluids, some having been separated during the crystallization of volatile matter-rich residual melt of original mafic magma, while others are derivatives of later felsic (granite) melts that formed crosscutting veins in fully devitrified ultramafic and mafic rocks. The earliest of these fluids occurs as a homogenous dense dry reduced gas ($CH_4 – N_2 \pm CO_2$) mixture separated from the

alumina-silicate melt at 800–900°C and 3050 bar in the quartz quartz in symplectitic intergrowths with intercumulus plagioclase from the Merensky Reef pyroxenite. Followed by the later, heterophase highly concentrated fluids (60–80 wt % NaCl eq.) that separated over 550°C and below 3050 bar from granite (quartz–feldspar) melts. Zhitova *et al*. (2016) shows that metal-bearing magmatogene fluids successively separated from the aluminosilicate melt, were heterophase salt melt–brines or solutions with isolated mainly carbon dioxide gas phase. Results obtained by Zhitova *et al*. (2016) clearly show that the oxidation of reduced heterophase fluids is one of the most important geochemical barrier caused by the crystallization of solid mineral phases from heterophase fluids.

Table 1: Summary of published fluid inclusion data for the Bushveld Igneous Complex

Principal Reference	Zhitova et al. (2016)	Zhitova *et al*. (2009)	Schiffries (1988; 1990)	Ballhaus and Stumpfl (1986)
P_T and T_T Summary of results of fluid inclusion studies	1. Trapping conditions: Tt= 800–900°C; and; Pt= 3 kbar for the earliest fluid, which occurs as a homogenous dense dry reduced gas mixture 2. Trapping conditions: Tt=550°C; Pt= 3 kbar for the heterophase highly concentrated fluids	Trapping conditions: Tt= 400-900ºC; Pt= 1.00–3.50 kbar	Trapping conditions: Tt= <750ºC; Pt= 4–5 kbar	Trapping conditions: Tt= 730ºC; Pt= 4–5 kbar
Types of fluid inclusions (FLINC)	1. Observed primary inclusions (L + H + V, L + V & L + S + V); Secondary inclusions (V+ L_1+L_2), L + H+4S+ V); composition: (CH_4 – N_2 ± CO_2). 2. Observed in miarolitic pegmatite from later crosscutting veins of the Platreef include multiphase water-salt inclusion (L + V + H + 1-4S); (three-phase water-salt inclusions (L + V + H); inclusion with Liquid carbon dioxide (L + LCO2 + V); composition: 60–80 wt % NaCl eq.).	Observed primary combined (intergrowth of plagioclase or quartz crystals with bubbles of gaseous phase e.g. CH_4-N_2) & gaseous fluid inclusions (CH_4-CO_2-N_2).	Secondary inclusions in postcumulus quartz, composition: Composite suite of $CaC1_2$-NaCl-H_2O	Secondary inclusions in postcumulus quartz, composition: Complex suite of H_2O-NaCl-($CaCl_2$)-CO_2-CH_4; with the following compositions: immiscible NaCl-H_2O-CO_2 (15–60 wt % $NaCl_{equiv}$); NaCl-H_2O (70 to 480 wt % NaClequiv); hydrated $CaCl_2$
Interpretation of FLINC results	This shows that oxidation of reduced heterophase fluids may be the most important geochemical barrier invoking the crystallization of solid mineral phases from heterophase fluids.	These fluid inclusions characterize the initial stages fluid separation from boiling intercumulus aluminosilicate liquids.	The study found that analysis of the Liquidus diagram for the $CaC1_2$-NaCl-H_2O system shows that fluid inclusions rich in $CaC1_2$ may display a rich variety of unusual phase equilibria.	They concluded that the fluid inclusion of H_20-NaC1-CO_2 characterizes the physico-chemical state of the intercumulus fluid at the time of quartz growth. These fluids played a significant role in the mineralization of platinum and sulphide.
Stratigraphic position of FLINC used	Merensky Reef and Platreef	Merensky Reef	Upper Critical Zone	Merensky Reef

1.12 Aims of this study

The aim of this study is to look at the poorly-documented record of fluid inclusions in the Upper Zone of the Bushveld Igneous Complex. Emphasis was placed on the following areas:

1) To determine the nature (type(s)) of fluid present, type of phase relations at room temperature, petrogenesis of the fluid inclusion, shapes and distribution patterns.

2) To constrain the entrapment temperatures and pressures of primary magmatic fluid inclusions

3) If possible, try to constrain the timing of the fluid inclusions with respect to the host mineral,

4) Determine the origin of the fluid inclusions found in the rocks of the Upper Zone, Bushveld Igneous Complex,

5) To show the significance of primary magmatic fluid inclusions.

1.13 Hypotheses

The methane in the fluid inclusions is abiogenic in origin. The methane-rich fluid inclusions found in the quartz of the Upper Zone of the Bushveld Igneous Complex were formed by respeciation (formation of a new species as result of the change in environmental conditions) of a C-O-H-rich fluid during the late stages of magmatic crystallization. Carbonic (CO_2- and CH_4-rich) fluid inclusions resulted from in situ phase separation. The fluids represented by fluid inclusions played a significant role during the evolution of the Bushveld Igneous Complex.

CHAPTER 2

METHODOLOGY

2.1 Introduction

Various techniques were used to achieve the aims and objectives set out for this research project, using material collected from the Stoffberg area and the Bellevue core (BV-1) which is in good condition— and these include: microthermometry, petrographic studies (i.e., fluid inclusion petrography and mineral assemblages), Raman microprobe analysis, and titanium-quartz-thermometry. Results obtained from both areas would serve as a useful test of Cawthorn's (2013) ideas about the area of Stoffberg, particularly the latter phases of evolution of the BIC. These ideas include: (1) relating to the top contact between the evolving mafic rocks of the Bushveld Complex and their overlying roof rocks; (2) he also proposed that the rocks from the Stoffberg area be designated as the Residual or Roof Zone of the Bushveld Complex.

2.2 The Bellevue (BV-1) drillcore, stratigraphy and lithologies

Knoper and von Gruenewaldt (1996) presented a detailed core log of the BV-1, which is available online: http://www/geocities.com/mwk.geo/bic.htm, Ashwal *et al*. (2005) produced detailed measurements of petrological, mineralogical and geophysical properties, which were made in stratigraphic context for ~3 Km of the BIC cumulate rocks. The BV-1 core is considered as an ideal borehole to study the significance of the fluid inclusions within the Upper Zone, of the Bushveld Igneous Complex as it provides a complete section through the Upper Zone. Results obtained in this study may be relevant in establishing an improved

understanding of methane generation and other carbon-bearing species in the Earth and their role in various geological processes related to the Bushveld Igneous Complex.

A selection of samples was made from the Upper Zone units of the BV-1 drillcore, including olivine ferrodiorites, leucogabbronorites, anorthosites and quartz anorthosites. Sampling of these quartz-bearing igneous rocks was done at the following depths: 83.69, 83.81, 105.23, 106.90, 306.10, 352.60, 417.90, 893.90, 910.10, 1046.50, 1413.80 and 1454.35. Detailed petrographic examinations were carried out on these samples, with emphasis on quartz and its textures, to determine its origin, relative to the other minerals present in the samples.

2.3 Stoffberg Area

Mafic rocks of the Stoffberg area used in this study are from the vertical section through the so-called fayalite diorites identified by Groeneveld (1970). These rocks were collected over a vertical height of about 60 m. Contact between the Rooiberg Group felsite and the layered rocks can be identified to within 10 m on the ground as there is sufficient outcrop to do so (Cawthorn, 2013). These rocks have been highly metamorphosed and possibly remelted, and are presently recrystallized microgranites, granophyres and hornfels, as described by Wager and Brown (1968) and Von Gruenewaldt (1972). In most of the literature these rocks were alluded to as leptites, a term signifying a fine grained felsic rock of questionable or complex origin. In a few places close to the contact, these rocks occur as xenoliths within the coarser grained rocks and the mafic rocks of the intrusion.

The limited outcrop in this study area necessitated substantial sampling and detailed examination of the uppermost rocks of the Bushveld Igneous Complex. The mafic samples collected in this represent ~230 m stratigraphically, when taking into account a conservative dip of 16°. These samples were collected by Professor Grant Cawthorn, from the University of the Witwatersrand, Johannesburg. For this study, I have assigned the uppermost sample collected as being at – 10 m underneath the contact, and refer to every other sample by reference

to estimated depths from this contact. However, a previous study by Cawthorn (2013) places the uppermost sample at – 5 m below the contact, and refere to all other samples by reference to depth below this contact. Meaing that every sample is placed reletaive to the contact as their stratigraphic position.

Table 2.1: Information on the mafic rocks from the Stoffberg section

Sample	Rock name based on Cawthorn's Geochem data	Rock Name based on Modal abundance	Depth	Latitude (25° +´S)	Longitude (29°+´E)
RGC20	Quartz Monzonite	Recrystallized microgranite	-10	26.743	49.104
RGC19	Quartz Monzodiorite	Recrystallized microgranite	-32	26.759	49.155
RGC24	Granodiorite	Recrystallized microgranite	-57	26.622	49.162
RGC22	Granodiorite	Recrystallized microgranite	-85	26.397	49.166
RGC16	Quartz Monzodiorte	Recrystallized microgranite	-89	26.346	49.149
RGC12	Monzodiorite	Recrystallized microgranite	-220	26.343	49.243

2.4 Raman microprobe analysis

For this study, micro-laser Raman spectrometry was used to study the fluid inclusions hosted in magmatic quartz of the Upper Zone, using the Horiba Jobin-Yvon LabRAM HR Raman spectrometer at university of the Witwatersrand, Microscopy and Micro-analysis Unit. This analytical technique was used for qualitative detection of components (i.e., solids, liquids, and gases) that make up the phases in the fluid inclusions, as earlier studies on fluid inclusions have shown that methane, carbon dioxide, and nitrogen gas can be recognized by this technique (e.g. Dubessy *et al*., 1989; Touret, 2001; Frezzotti *et al*., 2012). What makes this technique important for

this study is the fact that it can be used in the study of molar proportions of gaseous mixtures, and the chemistry of aqueous fluids present as inclusions.

Raman spectroscopy is a versatile non-destructive technique that permits chemical and structural characterization of components that make up the phases in the fluid inclusions of samples that are at least one micron in diameter. Since the 1970s Raman spectroscopy has become a conventional method in the research of fluid inclusions (e.g., Burke and Lustenhouwer, 1987; Dubessy *et al*., 1982, 1989; Seitz *et al*., 1987; Frezzotti *et al*., 2012). The importance of this analytical technique is shownby the number of publications and reviews in this field of research (e.g., Burke, 1994; McMillan *et al*., 1996; Nasdala *et al*., 2004; Frezzotti *et al*., 2012).

2.5 Fundamentals of Raman spectroscopy

This technique is based on inelastic (Raman) scattering of light by matter in its liquid, gas, or solid state. Raman spectroscopy is primarily based on the Raman Effect, which is the scattering of radiations with change in frequency (or wavenumber) (Long, 1977), where monochromatic light scattered by matter comprises radiations of different frequencies from the exciting light (Figure 2.1) (Frezzotti *et al*., 2012). The Raman Effect was first predicted by Smekal (1923), and subsequently demonstrated by Raman (1928). This effect can be explained by the quantum mechanical model, as it considers the interaction of molecules with photons in terms of energy-transfer mechanisms (e.g., Karr, 1975; Frezzotti *et al.*, 2012). Measurements obtained from spectroscopic analysis are usually presented in a graphical form known as a Raman spectrum, which is plotted as light intensity (i.e., arbitrary units/counts) against energy expressed as frequency of scattered light in frequency units (Frezzotti *et al*., 2012). Raman spectra that are resolved spatially can be used to recognize the distribution of mineral species or fluids within single fluid inclusions (Frezzotti *et al*., 2011; Korsakov *et al*., 2011; Frezzotti *et al*., 2012).

Characteristically, only the Stokes Raman scattered frequencies are represented as they are ten times more frequent than their counterparts the anti-Stokes even though they have the same energy (Figure 2.2). The Raman frequencies are presented as Raman shifts, or relative wavenumbers (wavenumbers (in cm^{-1} units)$\sim_{\nu} = \frac{\nu}{c} = \frac{1}{\lambda}$, where the velocity of light is represented by the symbol c (Frezzotti *et al*., 2012). On this scale, frequencies do not dependent on the wavelength of the light source, but do correspond to the energy levels of different molecular vibrations. A Raman spectrum comprises at least one band which reflect the vibrational energies of the molecules within the sample of interest; these thus are related to the nature of the bonding. Main molecular vibrations include bending and stretching modes, bending frequencies being generally lower than stretching frequencies (Frezzotti *et al*., 2012). According to Frezzotti *et al*., (2012) for a normal mode of vibration to be Raman active, it should produce change in the polarizability of the molecule. Hence, Raman-poor scatters are observed from molecules that are not easily polarized.

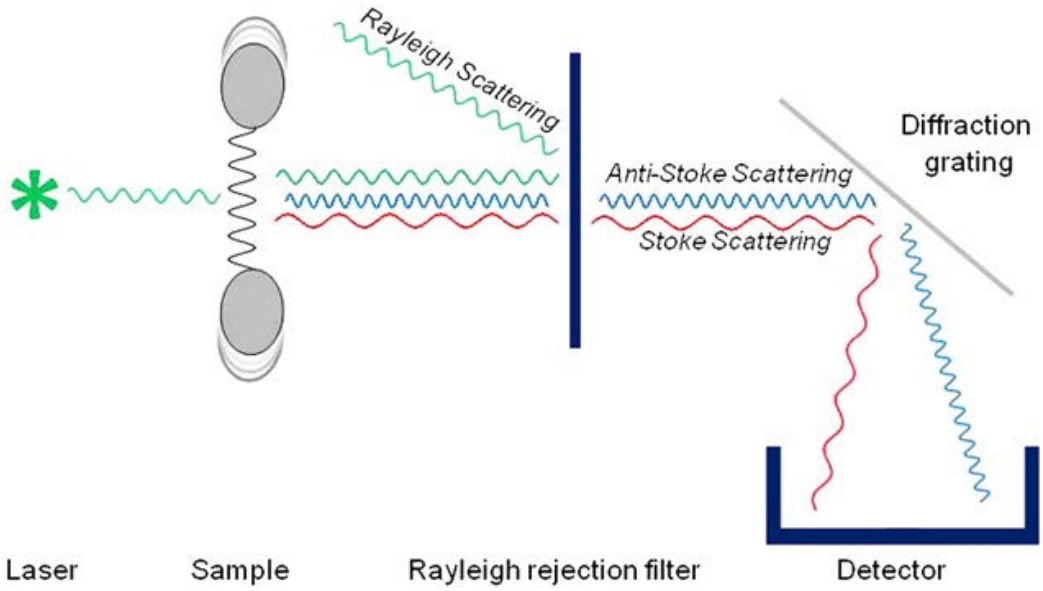

Figure 2.1: Schematic diagram of a Raman spectrometer (Frezzotti *et al*., 2012).

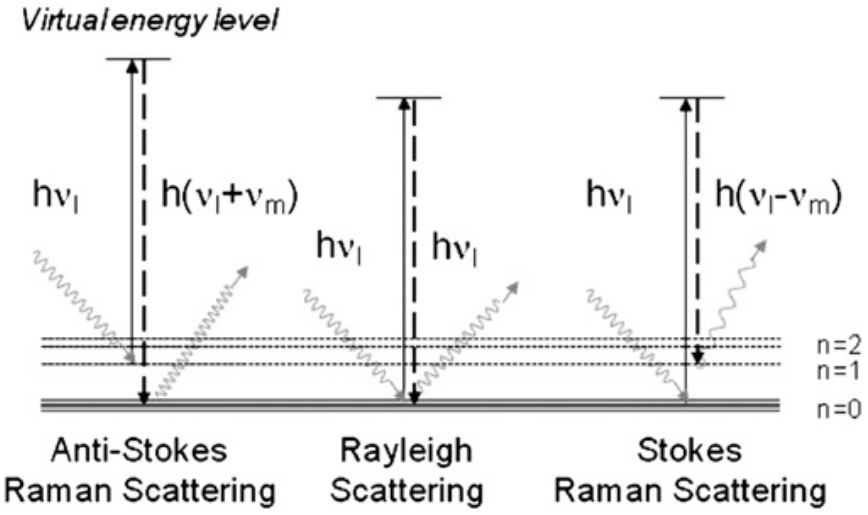

Figure 2.2: Energy scheme for Raman (inelastic) scattering at the frequency of the light source. After Frezzotti *et al.*, (2012).

2.6 Method of analysis

The basic instrumental set up for the Raman spectrometer requires a monochromatic light source, commonly a laser, focused on the sample; the light is scattered, collected at an angle of about 180º or 90º, and analysed by detector (e.g., multi-channel charge-coupled devices (CCD)) (Figure 2.2) (Frezzotti *et al*., 2012). The first dispersive Raman spectrometer used monochromatized sunlight as the exiting source, and a detector made up of photographic film (Kahlrausch, 1943; Colthup *et al*., 1975; Frezzotti *et al*., 2012). Raman spectrometers have evolved markedly since the beginning of 1986, with the introduction of charge-coupled devices, near-infrared lasers, Fourier transform—Raman, and small computers (McCreery, 2000). In modern Raman spectrometers, polarized laser light sources in ultraviolet, infrared, and visible wavelengths are used as exiting sources, as they emit a narrow bandwidth of wavelength and high intensity, multi-channel CCD are commonly used as detectors, and notch holographic filters are used to remove the Rayleigh lines. Introduction of these components has improved the intensity of the Raman scatter, with considerably low detection limits, and with significantly less measuring time to obtain high signal to noise spectra (Frezzotti *et al*., 2012).

Studies of fluid inclusions using Raman spectrometers are founded on the same fundamental principles: scattering is generated by the laser that excites the molecules. Raman micro-spectrometer is the common type of Raman spectrometer used in fluid inclusion studies, where the scattered light generated by the excitation of the sample is collected at an angle of about 180º. This is accomplished by means of using a conventional optical microscope focused on a single fluid inclusion by means of objective lenses of high-magnification (i.e., 50 × or 100×) (Frezzotti *et al*., 2012). This instrument offers a clear visualization of the laser spot and subsurface of samples, which allows one to choose the appropriate inclusions for analysis. The spot size of the sample depends typically on the magnification of the objective lens, and on the excitation wavelength (Frezzotti *et al*., 2012). Raman analysis was conducted on thick double-polished sections (200 μm) that require minimal preparation.

Potential problems associated with Raman spectroscopy analyses of fluid inclusions are well documented by Burke (2001) and Frezzotti *et al*., (2012). Specifically, the signals of inclusion of interest can be affected by the instrument calibration, the existence of the overlapping bands and the fluorescence from the host mineral, surface of the thick section, and sometimes the fluid inclusion itself if it contains fluorescent daughter minerals. The former can be corrected for when the spectral efficiency of the instrument is determined and when the relative Raman scattering cross-sections for the different fluid species are accurately known (Burke, 2001). The last two effects have a huge effect on the weak Raman shifts from the inclusion of interest. Fluorescence can be eliminated by cleaning the samples and/or by using non-fluorescent epoxies. This effect can also be mitigated by increasing the wavelength of the light source and/or by repeating spectral acquisitions for several times (Frezzotti *et al*., 2012). Raman spectroscopy of fluid inclusions has some limitations on a number of a species that can be quantitatively analayzed, namely a few polynuclear species in solution and the polyatomic gases (Burke, 2001).

2.7 Thermometry of quartz

Titanium-in-quartz geothermometry using the programme "TitaniQ" was used to constrain the quartz crystallization temperatures, the host mineral in quartz-bearing rocks of the uppermost units of the Bushveld Igneous Complex. Wark and Watson (2004) first introduced this technique, which they dubbed "TitaniQ". This technique has proven to be an accurate recorder of plutonic temperatures (Wiebe *et al*., 2007), as previously applied by Buthelezi et *al.* (2017) in the Bushveld Igneous Complex. Crystallization temperatures obtained from this technique are to be used to constrain the relative timing of the fluid inclusions with respect to the host mineral quartz, which crystallized from trapped interstitial melts Buthelezi *et al*. (2017).

2.7.1 Fundamentals of titanium-in-quartz geothermometry

Titanium-in-quartz geothermometry is based on the substitution system of titanium for silicon in the mineral quartz as it is temperature dependent (Wark and Watson, 2006). The thermodynamic principles of this technique are straight-forward like those for Zircon-in-rutile and Titanium-in-zircon (Watson *et al*., 2006; Wark and Watson, 2006), where the presence of nearby pure TiO_2 phases (typically rutile) makes the titanium activity fixed in many systems. Hence, the extent of substitution of silicon by titanium in the mineral quartz ought to vary systematically with temperature (Wark and Watson, 2006).

2.7.2 Method of Analysis

For the purpose of this study the CAMECA SXFive electron microprobe at the Microscopy and Micro-Analysis Unit, University of the Witwatersrand, was used to quantify the titanium content in quartz of quartz-bearing rocks, by simultaneously counting the titanium K-α X-rays using PET crystals on 4 spectrometers and averaging the results. Analyses were carried out at high current 20 nA at 15 kV. A minimum of ten spot analyses was carried out for each quartz

grain, with at least 2 spot analyses on a quartz grain, in each of the doubly polished thick sections.

For the purpose of this study temperatures reported by Buthelezi *et al.* (2017) were used as an independent geothermometer for the Bellevue samples, whereas for the Stoffberg samples the technique is carried out as previously applied by Buthelezi *et al.* (2017). Principals of this technique are fully described in Buthelezi (2015). The temperatures were obtained by converting the measured titanium content in quartz grains using either one of the two equations Huang and Aude´tat (2012) and Wark and Watson (2006), respectively.

The equation derived by Huang and Audétat (2012) is as follows:

$$T(^{\circ}\mathrm{C}) = \left(\frac{-0.2794.10^{4} - 660.53.P^{0.35}}{\mathrm{Log(Ti)} - 5.6459}\right) - 273, \quad (1)$$

The equation derived by Wark and Watson (2006) is as follows:

$$T(^{\circ}\mathrm{C}) = \left(\frac{-3765}{Log(X_{Ti}^{Qtz}) - 5.69}\right) - 273, \quad (2)$$

Temperatures obtained from both equations (Eq. 1 and 2) are representative of the quartz crystallization temperatures, where the temperature is reported in degrees Celsius (°C) and the titanium (Ti) concentrations within quartz (X_{Ti}^{Qtz}) are in parts per million (ppm) by weight (Wark and Watson, 2006).

2.8 Fluid Inclusion Microthermometry.

Fluid inclusions were observed in various forms of quartz that form part of the trapped interstitial melts of the Bushveld cumulate mafic rocks. Hence, the fluid inclusions hosted in these quartz grains represent fluids of solidus and/or sub-solidus conditions that were present during the cooling of the Bushveld Igneous Complex. The data acquired from these fluid

inclusions, using freezing and heating methods include: observation of temperatures at which phase changes occur, documentation of phases present at various temperatures, and estimates of relative volumes of phases present in the fluid inclusions. Data acquired from this technique were used to identify the compositions of the fluids in the inclusions and to estimate the densities of the inclusions to establish the significance of primary magmatic CH_4—CO_2—H_2O fluid inclusions with respect to the Bushveld Igneous Complex.

2.8.1 Theoretical aspects of fluid inclusion microthermometry

Fluid trapped in small cavities within minerals that are sparingly soluble, such as quartz, are representative of systems that are of constant volume and composition, in which phase transition can be observed (Shepherd *et al*., 1985). The investigation of phase transitions over an extensive range of temperatures (between +375º C and -105ºC during heating and freezing runs) on a dual purpose heating and freezing stage is a useful non-destructive technique, with reference to suitable pressure-volume-temperature-composition (P-V-T-X) phase diagrams. This type of analytical method is usually referred to as microthermometry. This technique is the most common and extensively used non-destructive analytical technique in fluid inclusion studies (Shepherd *et al*., 1985). It is relatively inexpensive and provides an opportunity to constrain the physico-chemical parameters such as temperature and pressure (T-P), and the bulk density of the fluids, as well as the composition of the fluids during trapping with reference to simple systems (e.g. ternary and binary) (Table 3). However, most of the natural chemical systems are rarely simple, but are multicomponent. Hence, the estimates of the P-V-T-X states derived from natural systems are semi-quantitative (Shepherd *et al*., 1985).

Microthermometry relies on the careful recognition and observation of phase changes that occur within any fluid inclusion during freezing or heating. By accurately determining the temperature at which phase changes takes place, it is possible to derive semi-quantitative

estimate of P-T-V-X state for fluids at the time of trapping (Shepherd *et al*., 1985). For meaningful interpretations to be derived from micothermometric data, it is important that the moment of entrapment of inclusions be representative of a homogenous system (i.e. 1 phase). However, in some cases inclusions are present that represent heterogeneous systems, such as those that host a vapour bubble, which results from differential contraction between the host mineral and the fluid, during cooling after trapping. During this period, the fluid may unmix resulting into two immiscible liquids. However, if fluid boiling takes place, then two types of inclusions form, representing the trapping of either the vapour phase or the liquid phase, with the liquid phase being saturated with respect to one or more solute components result in the formation of daughter minerals (Shepherd *et al.,* 1985).

2.8.2 Method of Microthermometry Analysis

Melting refers to the procedure whereby fluid inclusions cooled below room temperature are heated to observe the solid (S) to liquid (L) phase transformation. Data obtained during this procedure yields results that can be interpreted primarily of fluid composition and its density. In theory, vapour + liquid inclusions containing pure non-aqueous fluid (e.g. CO_2) or pure water ought to freeze at - 56.6 and + 0.015 °C, respectively. However, in natural samples it is rare to find fluids that comprise a single chemical component. The addition of another chemical component in an inclusion greatly affects the temperature interval over which melting takes place, lowering it by several degrees celsius (see Figure 2.3; Shepherd *et al*., 1979). The range over which melting takes place is a direct function of composition, and can therefore be used to estimate the composition of the fluids (Shepherd *et al.,* 1985).

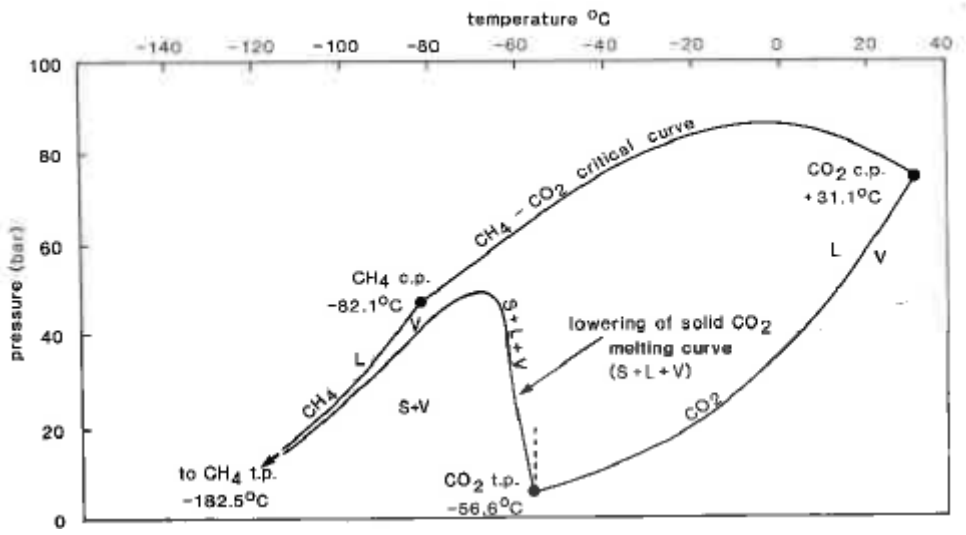

Figure 2.3: Phase diagram illustrating the effect of adding another chemical component in an inclusion (i.e. the phase relation in the system CO_2-CH_4 at sub-ambient temperatures; the final melting temperature of the solid CO_2 in equilibrium with liquid and vapour is depressed) (Shepherd *et al*., 1979).

During the melting cycle, it is possible to have more than one melting event. The first melting event is referred to as the temperature of first melting ($T_{m\ ice}$) (Table 2.2). This temperature corresponds to the eutectic temperature, which is the temperature determined by the composition of the end-member components (Table 2.3; Brass, 1980). With a continuous raise in temperature, the ice hosted in the fluid inclusion melts, until the last ice melts in the inclusion. The temperature at which this last ice melts is referred to as the final temperature (T_m H_2O) (Table 2.2). This temperature is determined by the nature of the salts present in the inclusion.

During the cooling of CO_2-bearing inclusions, a second measurable event is observed, when the gas hydrates or clathrates freezes out prior to the freezing of the remaining aqueous solution to ice. Clathrates ($CO_2.5\frac{3}{4}H_2O$) lock up large amounts of water in their structure, and normally melt over the interval of -6˚to + 12℃ (T_mCLATH). The clathration effect results in the increase in the salt concentration (salinity) of the residual aqueous. This then results in the overestimation of the true salinity. An alternative method for estimating salinity using depression of the temperature of decomposition during heating, of the CO_2-hydrate, in the

presence of CO_2 gas and liquid, is used to measure the salinity of these inclusions (Figure 2.4; Collins, 1979).

The heating data are collected for identifying the final homogenization temperature (T_h), which is generally the temperature of total vapour-liquid homogenization (Table 2.2). However, for fluid inclusions with daughter crystals, such a temperature could be the temperature of total dissolution (Td) (Table 2.2), which is interpreted to represent the minimum estimate of the temperature of entrapment of the fluid. Data acquired from early studies (e.g. Sorby, 1858) have shown that there is a numerical relationship between the temperature of homogenization (T_h) and the relative size of the vapour bubble in an inclusion of fixed composition.

Three modes of homogenization have been identified: (1) homogenization into vapour state (L+V → V), (2) critical homogenization by fading of the vapour-liquid meniscus (L + V → supercritical fluid), and (3) homogenization into the liquid state (L+V → L). For fluid inclusions of pure water, the exact mode of homogenization is determined by the overall density of the fluid or the degree of fill (Figure 2.5). When another component (e.g. NaCl) is added into the solution the critical point rises, resulting in an extended liquid-vapour field to higher temperatures (Shepherd *et al*., 1985).

Table 2.2: Abbreviations of thermometric parameters

Abbreviation	Explaination
$T_{m\ ice}$	Temperature of first melting (eutectic temperature)
$T_m\ H_2O$	Final temperature of melting
T_mCLATH	Clathrate melting temperatures
Td	Temperature of total dissolution
T_h	Temperature of homogenization

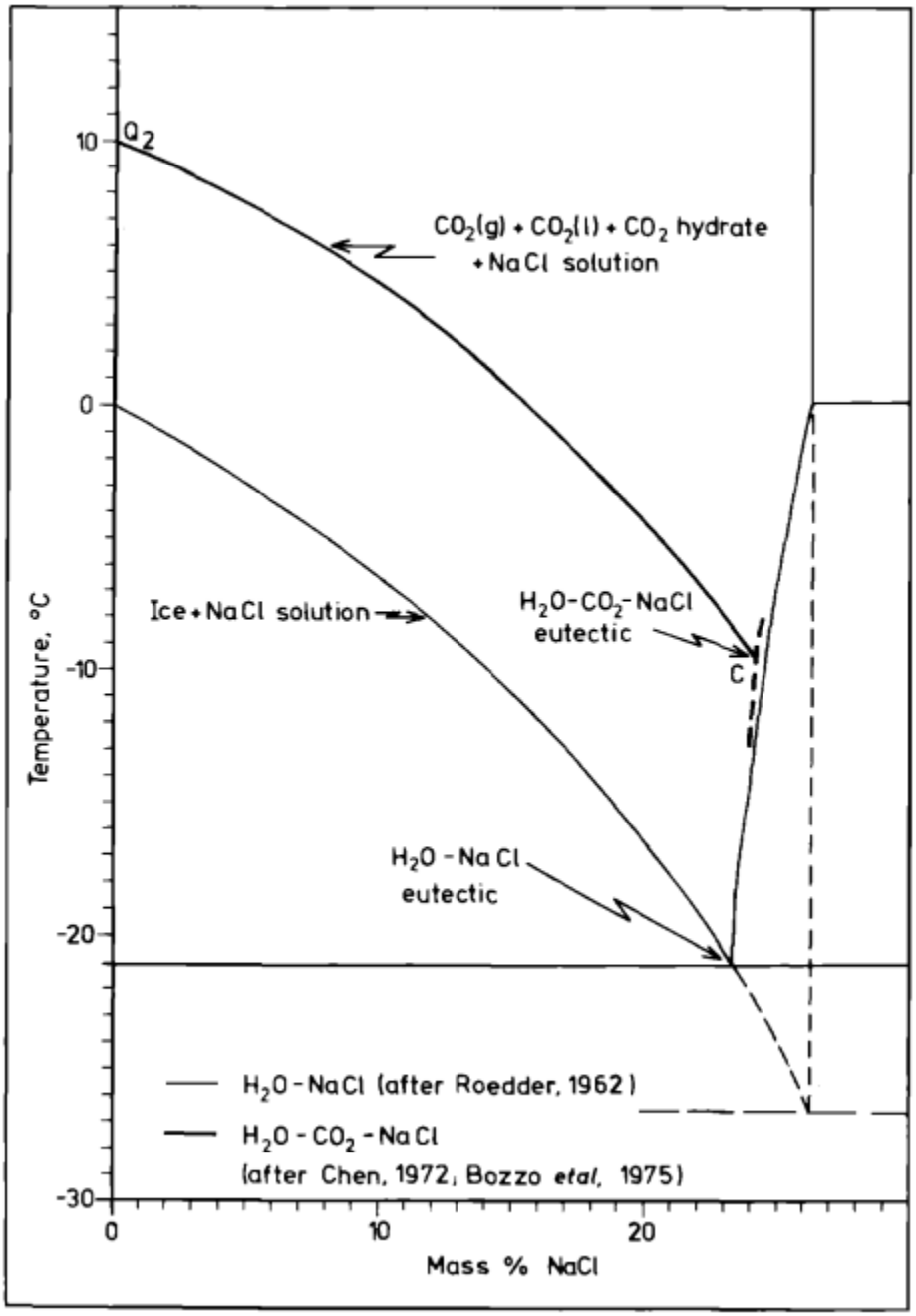

Figure 2.4: Depression of the decomposition temperature of CO_2 hydrate by NaCl in the presence of CO_2 gas and liquid. The melting temperature depression of ice NaCl is included for comparison (Chen, 1972; Bozzo *et al.*, 1975; Collins, 1979).

Table 2.3: Invariant points in systems containing brine at 1 atmospheric pressure

Binary			
	Temperature	Brine compostion	Brine compostion
1. Ice + $NaCl.2H_2O$	-21.2℃	23.3 % NaCl	
2. Ice + KCl	-10.8℃	19.9 % NaCl	
3. Ice + $CaCl_2.6H_2O$	-49.8℃	30.2 % $CaCl_2$	
4. Ice + $MgCl_2.12H_2O$	-33.6℃	21.0 % $MgCl_2$	
Other binary invariant points			
5. $NaCl.2H_2O$ + NaCl	+0.1℃	26.3 % NaCl	
6. $MgCl_2.12H_2O$ + $MgCl_2.8H_2O$	-16.8℃	31.6 % $MgCl_2$	
Tenary eutectic			
7. Ice + $NaCl.2H_2O$ + KCl	-22.9℃	20.2 % NaCl	5.8 % KCl
8. Ice + $CaCl_2.6H_2O$ + $MgCl_2.12H_2O$	-55.0℃	26.0 % $CaCl_2$	5.0 % $MgCl_2$
9. Ice + $CaCl_2.6H_2O$ + $NaCl.2H_2O$	-55.0℃	29.0 % $CaCl_2$	1.5 % NaCl
10. Ice + $MgCl_2.12H_2O$ + $NaCl.2H_2O$	-35.0℃	22.7 % $MgCl_2$	1.6 % NaCl
11. Ice + $CaCl_2.6H_2O$ + KCl	(-52)℃	(29.3) % $CaCl_2$	(1.0) % KCl
12. Ice + $MgCl_2.12H_2O$ + KCl	(-35?)℃	(22?) % $MgCl_2$	(2?) % KCl
Other ternary invariant points			
13. NaCl+ $NaCl.2H_2O$ + KCl	-2.3℃	20.3 % NaCl	5.8 % KCl
14. $CaCl_2.6H_2O$ + $MgCl_2.12H_2O$ + $MgCl_2.8H_2O$	-20.7℃	10.6 % $CaCl_2$	23.2 % $MgCl_2$
15. $CaCl_2.6H_2O$ + $NaCl.2H_2O$ + NaCl	(-22)℃	(33.3) % $CaCl_2$	(1.4) % NaCl
16. $NaCl.2H_2O$ + NaCl + $MgCl_2.12H_2O$	-26.0℃	1.8 % NaCl	23.4 % $MgCl_2$

Values in parentheses are extrapolated from nearby low-temperature (below℃) measurements. Values with a question mark are extrapolated from the appropriate binary phase diagrams and from data on ternary systems at 0℃. All data from Linke (1958). The KCl phase present at low temperature is hydrate with an unknown number of water molecules but represented in the table as KCl. Brine compositions are given in weight percent (Brass, 1980).

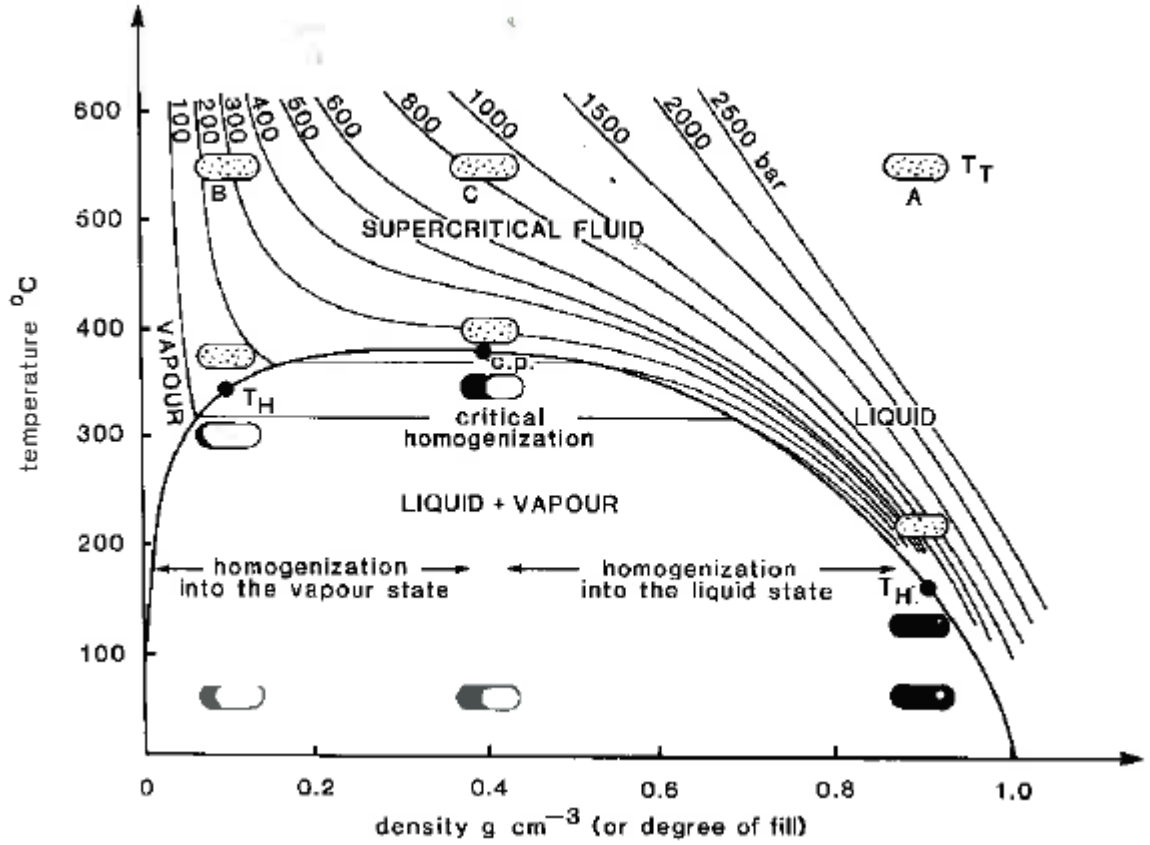

Figure 2.5: Temperature-density plot for pure water showing the principal modes of homogenization for inclusions with (a) low, (b) medium and (c) high bulk densities at the same temperature but different pressures; C.P = critical pressure, T_H= homogenization temperature, T_T=temperature of trapping (after Shepherd *et al*., 1985).

When multiphase fluid inclusions containing daughter minerals are heated, the more soluble ones start to dissolve, and the rate at which they dissolve is related to the solubility in the liquid phase. Different daughter minerals have different dissolution temperatures (Td), which can be used to determine the wt % equivalence of these various salts present in the inclusions (Figure 2.6, Roedder, 1984; Shepherd *et al*., 1985). In inclusions where more than one type of daughter mineral is present, reference should then be made to the appropriate mixed salt system, recording the dissolution temperature for each salt (Shepherd *et al*., 1985).

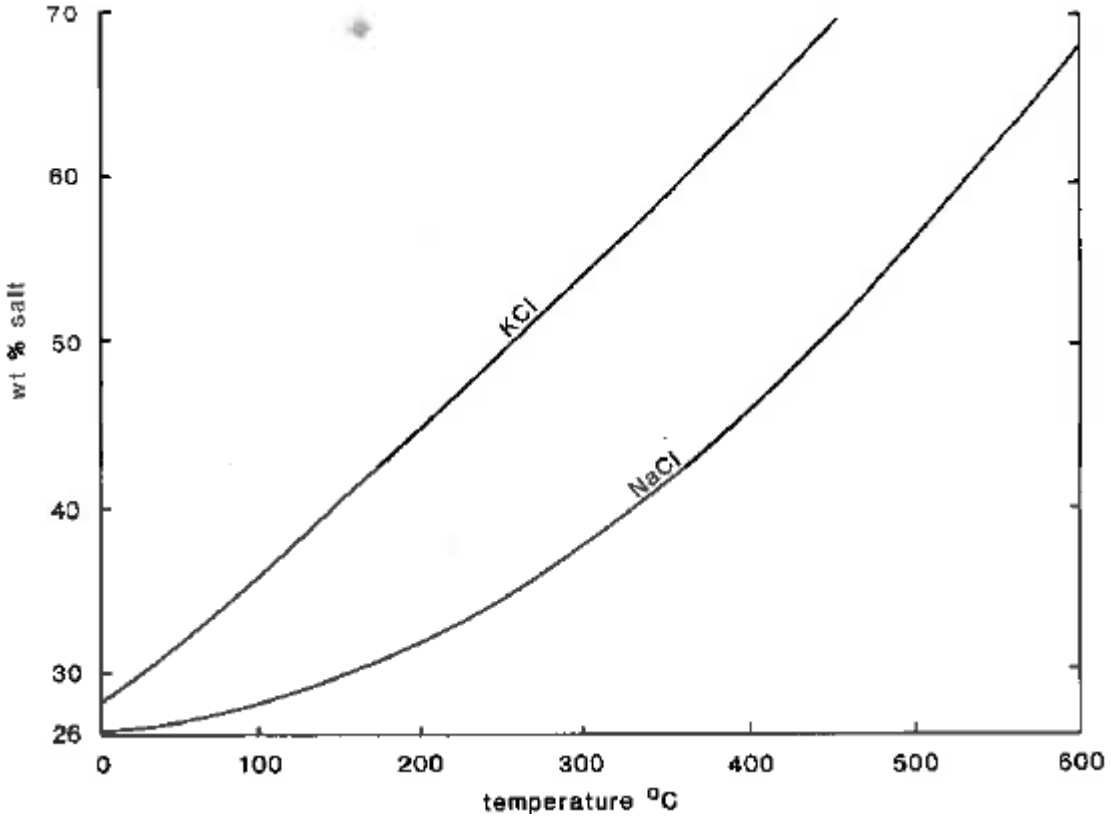

Figure 2.6: Solubility curves for KCl and NaCl in aqueous solutions. To obtain the weight percent of these salts in fluid inclusions, the measured dissolution temperatures (Ts KCl, Ts NaCl) should be plotted along the temperature axis (After Roedder, 1984).

Fluid inclusions formed by trapping of a heterogeneous H_2O-CO_2 mixture usually show two immiscible liquids at room temperature a H_2O-rich phase and a CO_2-rich phase. This is due to the restricted mutual solubility of H_2O and CO_2 at low temperatures. Also, it is possible to find CO_2-rich vapour bubbles within the liquid CO_2. Hence, on heating, a temperature is reached where these two-phase become completely miscible. This temperature is interpreted as the homogenization temperature, and is represented by a point on the H_2O-CO_2 solvus (Figure 2.7, Shepherd *et al.*, 1985,). The position of the H_2O-CO_2 solvus is determined by the pressure at the time of trapping and the salinity of the H_2O phase; increasing the salinity results in a raise of the solvus, whilst increasing pressure has an opposite effect (Shepherd *et al.*, 1985). Inclusions having low CO_2/H_2O ratios typically homogenize by disappearance of the CO_2-rich phase, whereas those with high CO_2/H_2O ratio homogenize by the disappearance of the H_2O-

rich phase. Fluid inclusions whose composition is close to the critical value tend to homogenize by gradual fading of the meniscus. Homogenization by miscibility only gives minimum estimates of the temperature of entrapment (See Figure 2.7, Shepherd *et al*., 1985).

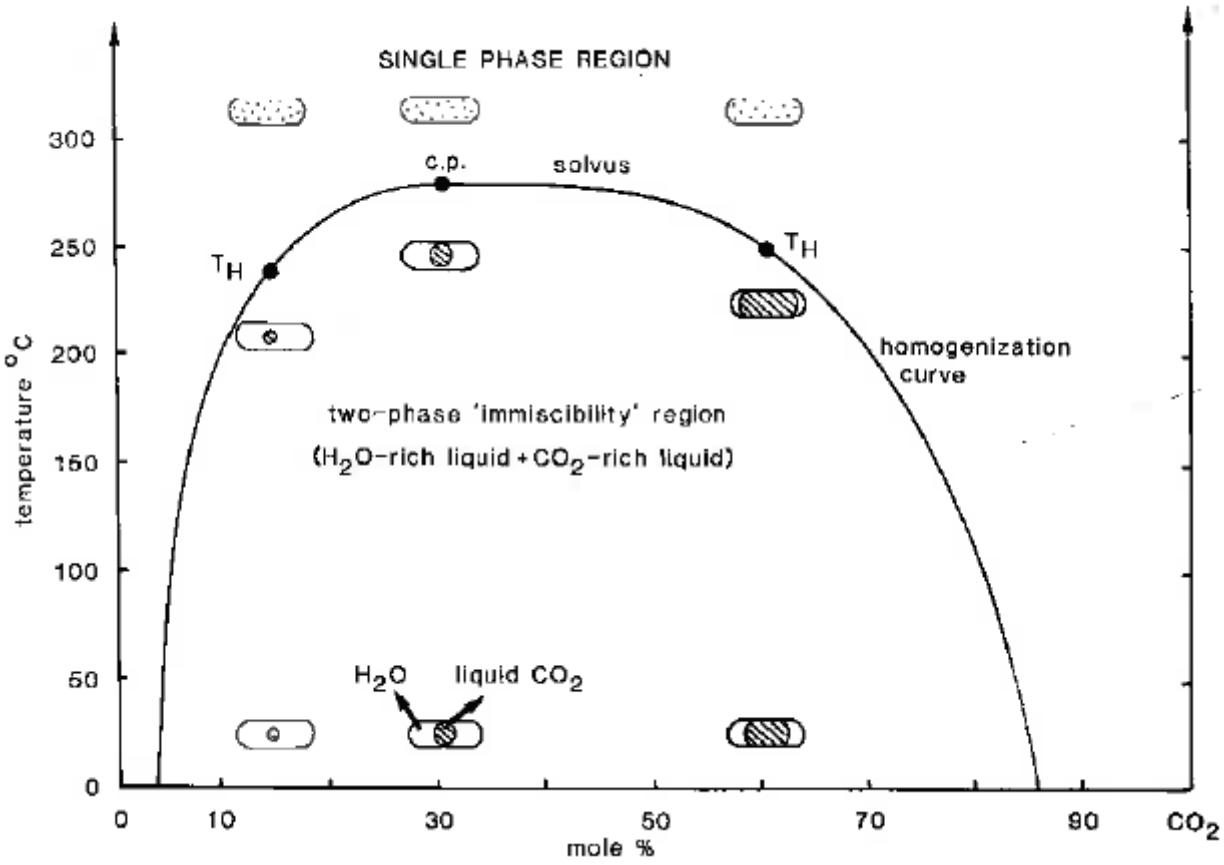

Figure 2.7: Temperature-CO_2 diagram showing the effect of content on the mode and temperature of homogenization of various inclusions; T_H= homogenization temperature, C. P= critical pressure; pressure = 1kb (Shepherd *et al*., 1985).

CHAPTER 3

3.0 Theories on the origin of hydrocarbons in igneous rocks

3.1 Introduction

Hydrocarbons found in igneous rocks have received comparative little attention as compared to those found in sedimentary and metamorphic rocks, as there are relatively small amounts of hydrocarbons in igneous rocks. In 1902 Mendelyev first noted the presence of hydrocarbons in mafic-ultramafic rocks (see review by Porfir'ev 1974; Potter and Konnerup-Madsen, 2003). Although they are an unusual feature in igneous rocks, they have been documented in evolved gases and in fluid inclusions derived from a number of magmatic sequences of plutonic (e.g., Larsen *et al*., 1992; Krot *et al*., 1994; Potter *et al*., 1998), and hypabyssal and volcanic rocks (e.g., Gerlach, 1980; Gize and McDonald, 1993; Kelly, 1996). They are well-documented in plutonic rocks from alkaline intrusions, as they are common in such types of rocks (e.g., Petersilie and Sørensen, 1970; Konnerup-Madsen, 1988; Salvi and Williams-Jones; 1992; Ting *et al.,* 1994), where these alkaline rocks are a product of differentiated primary, mantle-derived melt (Potter *et al*., 1998).

The origin of hydrocarbons in igneous rocks remains a controversial topic, as to whether they are (1) abiogenic or (2) biogenic in origin and also the mechanism by which they are generated (Potter and Konnerup-Madsen, 2003), whereas the mechanism by which are generated in sedimentary and metamorphic rocks is well documented. Hydrocarbons in sedimentary rocks, where they are most abundant they are derived from organic material during burial and diagenesis (e.g. Schidlowski, 1982; Belokon *et al.*, 1995; Potter and Konnerup-Madsen, 2003).

In metamorphic rocks, hydrocarbons occur in fluid inclusions and are generated abiogenetically through reaction between bitumen or graphite and an H_2O-rich fluid during metamorphism (e.g. Samson and William-Jones, 1991; Andersen and Burke, 1996; Potter and Konnerup-Madsen, 2003). The aim of this study is to investigate the occurrence of methane in the Upper Zone of the Bushveld Igneous Complex.

3.2 The origin of hydrocarbons (methane) in igneous rocks

A variety of models have been proposed for the origin of hydrocarbons in igneous rocks some have stood the test of time, but some have fallen short due to the advances in the analytical tools used to study them. However, it is universally accepted that reduction of carbon dioxide-rich fluids during post-magmatic serpentinization results in the production of hydrocarbons in ultramafic-mafic rocks (e.g. Neal and Stranger, 1983; Sherwood-Lollar *et al*., 1993; Potter and Konnerup-Madsen, 2003). Hydrocarbons in igneous rocks can be derived from two possible sources: (1) abiogenic source or a biogenic (orogenic) source. These sources are distinguished by the $\delta\ ^{13}C$ (Potter and Konnerup-Madsen, 2003) and $\delta\ ^{2}H$ (Etoipe and Sherwood-Lollar, 2013) values of the hydrocarbons. This study largely focuses on methane only as it is the most widespread and the simplest form of hydrocarbons, whose possible origin is not questioned unlike the heavy hydrocarbons.

3.2.1 Biotic hydrocarbon occurrences in igneous rocks

The term biotic CH_4 refers to organically (e.g. bacteria) derived hydrocarbons that are generated from either one of the three processes: (1) by thermogenic processes (thermal alteration) or (2) CO_2 reduction or by (3) fermentation. In most of the igneous rock, organically derived hydrocarbons are generally produced thermogenically. Thermogenically derived hydrocarbons, are thought to be produced from biotic material that has experienced thermal alteration from an igneous body (Figure 3). During this process, the organic matter in the

country rocks may be leached out by the hydrothermal late magmatic fluids that are accompanied with the igneous body (e.g. Simoneit, 1988; Gize and McDonald, 1993; Potter and Konnerup-Madsen, 2003) or be completely incorporated into and then be recycled magmatic-hydrothermal system (e.g. Des Marias *et al*., 1981; Darling *et al*., 1995; Darling, 1998; Potter and Konnerup-Madsen, 2003).

3.2.2 Abiogenic hydrocarbon occurrences in igneous rocks

Since the beginning of the 20thcentury Russian scientists have been interested in the origin of abiogenic hydrocarbons in igneous rocks. However, there is still little knowledge about this phenomenon outside Russia. Hence, the presence of hydrocarbons of abiogenic origin in crystalline rocks have generally been noted only by eastern scientists (Potter and Konnerup-Madsen, 2003), but in the last three decades there has been an increase in the number of reports published on the occurrence of abiogenically formed hydrocarbons. These types of hydrocarbons are usually produced in a small amount on a global scale. Thus, they are seen to be economically insignificant for exploitation, with some controversial and rare exceptions (e.g. Dia *et al*., 2005; Ni *et al*., 2009; Jin *et al*., 2009; Etiope and Sherwood-Lollar, 2013). It is universally accepted that abiogenic CH_4 is produced by inorganic reactions.

The mechanism for abiogenically formed hydrocarbons remains controversial, as to whether they are: or (a) magmatic in origin ÷ (1) primordial origin, where methane is delivered by meteorites during Earth's accretion (e.g. Gold, 1979; Sugisaki and Mimura, 1994), (2) during high temperature reactions in the mantle (e.g. Petersilie, 1962; Petersilie and Søresen, 1970;Welhan and Craig, 1983; Matveev *et al*., 1997; Zhang and Duan, 2009), or (b) late magmatic origin ÷ (1) generated from the respeciation of primary Carbon-Oxygen-Hydrogen fluids during late stage of crystallization below 600 ºC (e.g.Gerlach, 1980; Konnerup-Madsen *et al*., 1985; Kogarko *et al*., 1987; Andersen and Burke, 1996; Kelley and Früh-Green, 1999;

Potter and Konnerup-Madsen, 2003), or (C) gas-water-rock reactions ÷ (1) post-magmatic origin- where hydrocarbons are generated from post-magmatic alteration processes involving Fischer-Tropsch reaction (i.e. serpentinization) (e.g. Abrajano *et al*.,1990; Sherwood Lollar eta l., 1993; Kelley, 1996; Charlou *et al*., 1998; Potter *et al*., 1998; Potter *et al*., 2004; Etiope *et al*., 2011) or (2) post-magmatic high temperature reactions (400-500˚C) (e.g. Kiyosu *et al*., 1992; Giggenbach, 1997). These classes are mainly based on the theoretical ideas and experimental evidence.

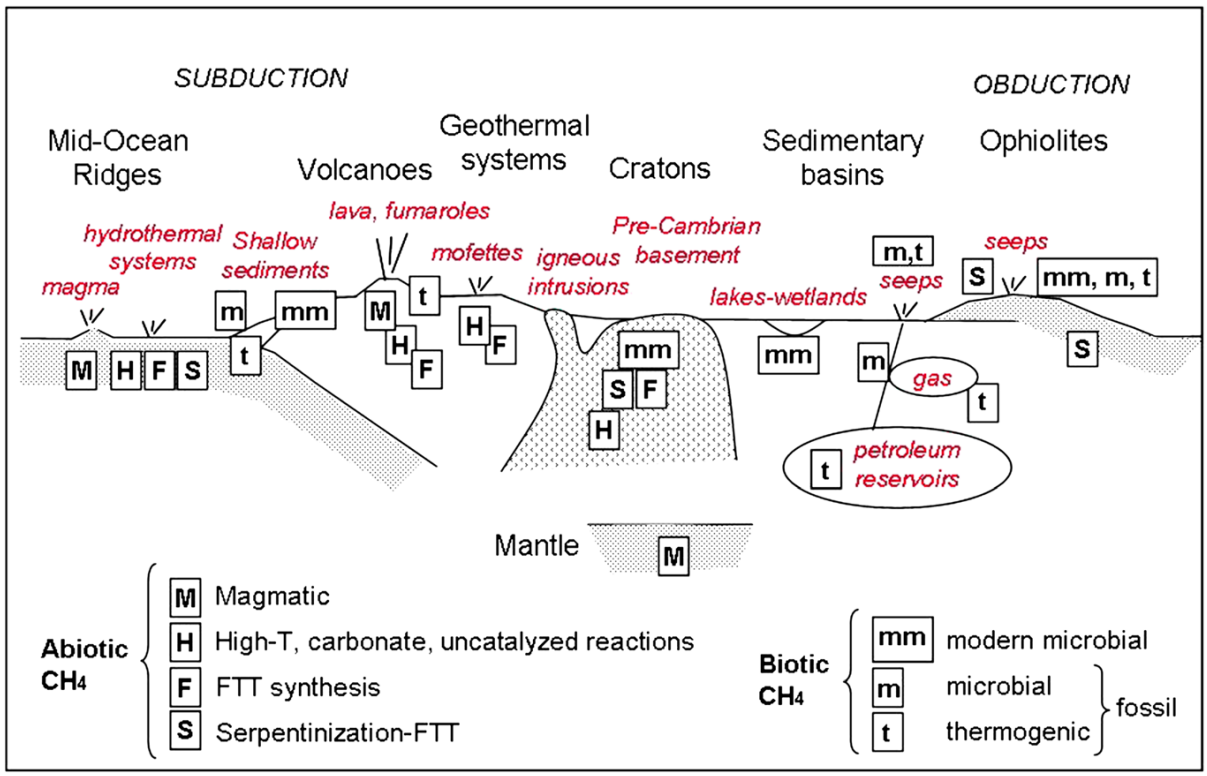

Figure 3.1: Schematic diagram showing the general geological setting of the occurrence of abiotic methane on Earth. Fischer-Tropsch Type synthesis (F) associated with serpentinization of ultramafic rocks and also one independent of serpentinization of ultramafic rocks (S); Magmatic (M)-High temperature reactions in the mantle and/or respeciation of C-O-H fluids; Post-magmatic high temperature reactions (H). Typical organic methane occurrences are also shown. Adopted from Etiope and Sherwood-Lollar (2013).

3.3 Magmatic origin

3.3.1 Primordial origin of methane "extraterrestrial methane sysnthesis"

Gold (1979) postulated the idea of primeval CH_4 being delivered by extra-terrestrial bodies such as meteorites during the accretion of the Earth which eventually get preserved in the Earth's mantle to a rather similar manner as juvenile helium (Craig and Lupton, 1976). This idea is derived from Hoyle's (1995) hypothesis—which has been verified by numerous studies (e.g. Yuen *et al*., 1984)— which suggest the presences of hydrocarbons in chondritic material that contributed in the formation of the Earth. However, to date evidence presented in support of this idea is not compelling enough to suggest the existence of such a primeval CH_4 in significant amounts in the interior of the Earth. Thus, the isotopic signatures of methane (δ^2 H and δ^{13}C) used to define the primordial methane end-member is yet to be confirmed. Hence, this type of origin is theoretically sound, but abstract from an observational and experimental viewpoint (Etiope and Sherwood-Lollar, 2013).

3.3.2 High temperature reactions in the mantle

This type of hydrocarbon origin is based on one of the major theories proposed by Mendeleev (1877) on the synthesis of hydrocarbon inorganically in the Earth's mantle, based on the hydrolysis of metal carbides —binary compounds composed of carbon and more electropositive elements— naturally occurring in meteorites, ophiolitic chromitites and in inclusions derived from the mantle (Eitope and Sherwood-Lollar, 2013). This idea of hydrolysis of metal carbides is appreciated in industrial chemistry, where water is reacted with metal carbides, such as beryllium and aluminium carbides to produce methane via the following reaction:

$$Al_4C_3 + 12H_2O = 3C_4 + 4Al(OH)_3$$

Methane may also be produced by the hydrolysis of iron carbides. Even though metal carbides have been discovered in both terrestrial mantle minerals and extraterrestrial material (e.g. meteorites) (e.g. Kaminsky and Wirth, 2011), there are no modern experimental, systematic studies on these reactions, and there no evidence on how abundant they are in the Earth's mantle (Etiope and Sherwood, 2013).

However, CH_4 derived from the mantle is said to be synthesized from carbon monoxide and/or carbon dioxide at very high temperatures (~1000°C). Especially CH_4 formed by carbonate reduction in the Earth's upper mantle from calcium carbonate, water, and iron oxide at high pressures (5-11Gpa) and temperatures (500 - 1500°C) as suggested by Scott *et al*., (2004). Petersilie *et al*. (1961) and Beeskow *et al.* (2006) both invoked a similar process to explain for the presence of CH_4 documented in fluid inclusions from the Khibiny Complex.

3.3.3 Late magmatic origin

Respeciation of carbon-oxygen-hydrogen (C-O-H) fluids

During the late crystallization stages of magma cooling, at temperatures <500-600°C, C, O and H atoms may reorganize to form CH_4. This reorganization of atoms is referred to as respeciation (Etiope and Sherwood-Lollar, 2013). Potter and Konnerup-Madsen (2003) provided a comprehensive discussion on the phase relations for the C-O-H system and the possibility of generating CH_4 from H_2-rich or CO_2-rich fluids (Fig. 2). They showed that CH_4-rich fluids can evolve from the re-equilibration of CO_2- H_2O fluids at temperatures described above via the following reaction equilibria:

$$C + O_2 \leftrightarrow CO_2 \quad (1),$$

$$CO_2 + \frac{1}{2} O \leftrightarrow CO_2 \quad (2),$$

$$H_2 + \frac{1}{2} O_2 \leftrightarrow H_2O \quad (3),$$

$$2H_2O + CO_2 \leftrightarrow CH_4 + 2O_2 \quad (4)$$

These four independent reaction equilibria are conducted in the presence of graphite (activity =1) and they also control the relative proportions of the main volatile species— CH_4, H_2O and CO_2 — of the C-O-H system (Figure 3.2). Further studies were done to investigate the effects of varying physio-chemical parameters of the C-O-H system— these include temperature, pressure and activity of graphite — on the speciation of a variety of fluids in the C-O-H system and the actual concentration of CH_4 produced (e.g. Holloway, 1984; Huizenga, 1995; Cesare, 1995). Some of these effects are clearly demonstrated in Potter and Konnerup-Madsen (2003). Such type of model was invoked for methane sampled in fluid inclusions from Ilmaussaq alkaline intrusion, Greenland (Konnerup-Madsen, 2001); in the samples from Niragongo volcano, (Gerlach, 1980); in Southwest Indian Ridge (Kelley and Früh-Green, 1999); and in the fluid inclusions from south Norway (Andersen and Burke, 1996).

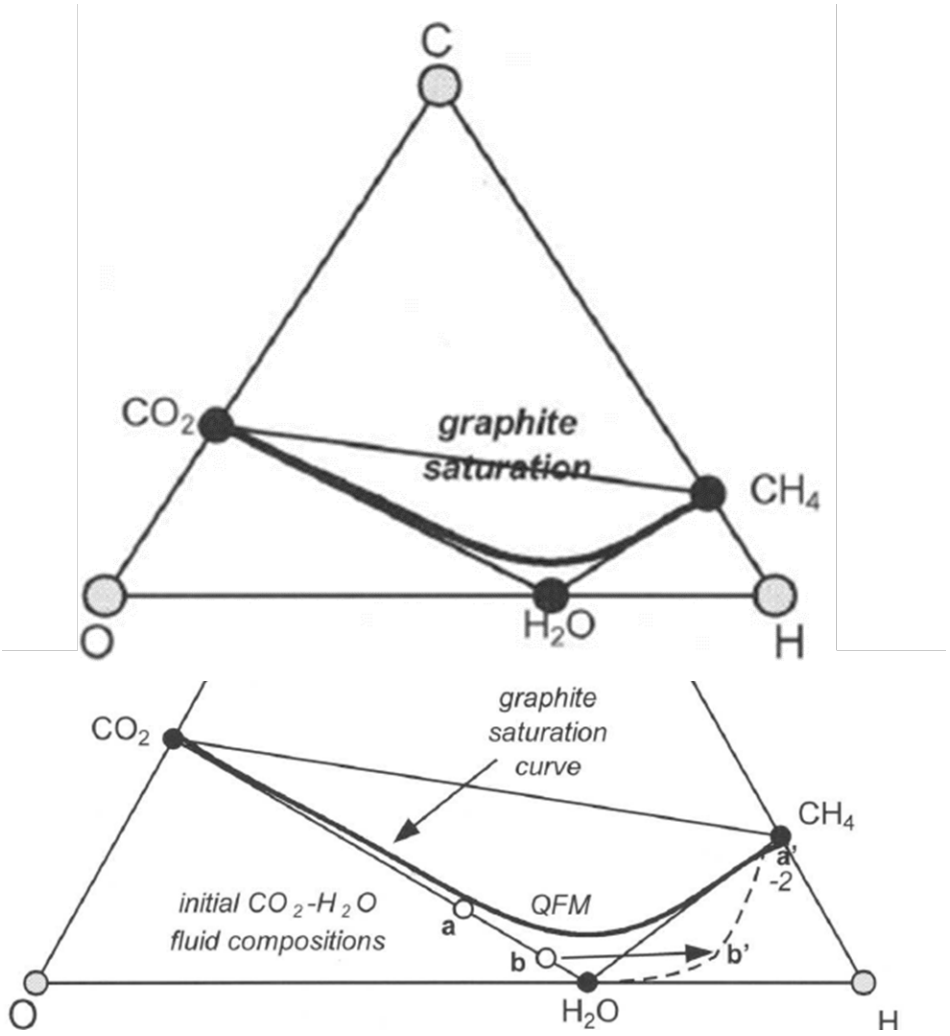

Figure 3.2: Phase diagram illustrating the phase relations in the C-O-H system at specified temperatures (500 ˚C) and pressures (2Kbar) and demonstrating how CH_4-rich fluids can evolve from the re-equilibration of CO_2- H_2O fluids by varying oxygen fugacity A schematic diagram showing phase relations in the C-O-H system at fixed temperatures and pressures (500 ~ 2 kbar) demonstrating the evolution of two fluid compositions (a and b) towards CH_4-rich compositions (a r and b') with decreasing fO2 conditions (QFM to QFM-2) (Potter and Konnerup-Madsen (2003).

This model can be readily applied to CH_4 generation in metamorphic terranes (Hollway, 1984), but for magmatic systems unusually low solidus temperatures are required (Potter and Konnerup-Madsen, 2003). Studies by Gerlatch (1980), Konnerup-Madsen (2001), and Salvia and Williams-Jones (1992) all argue in support of this model for the generation of methane in alkaline intrusions, such as Lovozero, Strange Lake, Khibina and Ilimaussaq. Compelling evidence for this model is derived from the Ilimaussaq intrusion, which during its final solidification stages evolved into a hyper-agpatic melt. These kinds of melts have the necessary

low temperatures (<450) required to evolve CH- rich gas due to the high concentrations of volatiles (i.e. F, Cl) (Konnerup-Madsen, 1988; Potter and Konnerup-Madsen, 2003).

3.4 Gas-water-rock reactions

3.4.1 Post-magmatic high temperature reactions

This type of model was first presented by Giggenbach (1997), who derived it from reactions identified in geothermal systems. In his fundamental work he described in detail the isotopic and chemical equilibria that exists between CH_4 and CO_2 under post-magmatic conditions. This idea was demonstrated using geothermal systems, which are characterized by high heat flow (> 80Mw/m^2), which permit CO_2 and CH_4 to tend towards both carbon isotopic and chemical equilibrium (e.g. Kiyosu *et al.*, 1992; Giggenbach, 1997). However, as the temperature decreases the equilibria eventually ceases to exist.

Methane formed by postmagmatic high temperature (200 and 500˚C) reactions only takes place once the magma has completely solidified and igneous rocks are formed, via a series of reaction equilibria involving CO_2, H_2O and metal oxides such as FeO (Etiope and Sherwood-Lollar, 2013). Via reactions such as

$$CO_2 + 2H_2O \leftrightarrow CH_4 + 2O_2 \quad (5)$$

$$8FeO + 2H_2O + CO_2 \leftrightarrow 4Fe_2O_3 + CH_4 \quad (6)$$

3.4.2 Fischer-Tropsch type (FTT) reactions

Most of the studies done on abiotic methane in natural settings invoke the FTT reactions as a mechanism for the generation of such methane, particularly those in serpentinized ultramafic rocks (e.g. Szatmari, 1989; Abrajano *et al*., 1988, 1990; Sherwood Lollar *et al*., 1993, 2002; Kelley, 1996; Salvi and Williams-Jones, 1997; Charlou *et al*., 1998, 2002; Potter *et al*., 1998, 1999, 2004; McCollom and Seewald, 2006; Proskurowski *et al*., 2008; Etiope *et a*l., 2011). Serpentinization is a postmagmatic hydrothermal alteration of mafic minerals by hydration of primary mineral assemblages including olivine ($5Mg_2SiO_4$ - $FeSiO_4$) and/or pyroxene, in silica under-saturated mafic and ultramafic rocks, to produce serpentine, brucite, and magnetite, to produce H_2 due to the dissociation of H_2O molecules and the conversion of Fe^{2+} to Fe^{3+}in magnetite, through reactions such as (eq.7a-b):

$$5Mg_2SiO_4 + FeSiO_4 + 9H_2 \rightarrow 3Mg_3Si_2O_5(OH)_4 + Mg(OH)_2 + 2Fe(OH)_2, \quad (7a)$$

$$3Fe(OH)_2 \rightarrow Fe_2{}^{2+}Fe^{3+}\,O_4 + H_2 + 2H_2O, \quad (7b)$$

This H_2 then reacts with carbonic (CO_2 or CO) to form CH_4 (reduced carbon species) (Sherwood-Lollar, 1993, 2002; Sugisaki and Mimura, 1994; Potter et al., 1998, 1999). Such a model was invoked for CH_4 generation in ultramafic and silica under-saturated rocks, such as ophiolite sequences in the Philippines and Oman, in altered and serpentinized ultramafic rocks from Juuka, and several sites in both Finland and Canada. However, there is still a long-standing debate on the quantity of CH_4 generated during serpentinization. One school of thought believes that it is widespread (e.g. Sherwood-Lollar *et al.,* 1993; Berndt *et al*., 1996; Horita and Berndt, 1999), whereas the other school of thought argues otherwise, suggesting that abiogenic processes of CH_4 production may be more limited than previously anticipated, citing the fact that previous studies that argue for widespread abiogenic processes of CH4

production misinterpreted their results, suggesting that they are bogus as they noted that hydrocarbons reported in these studies were already present in the olivine at the beginning of their experiments (e.g. McCollom an Seewald, 2003).

The Fischer-Tropsch-Type reaction can also be independent serpentinization of ultramafic rocks, meaning that H_2 can be generated by other processes, such as radiolysis, catalysis of silicates in fault zones, or magmatic degassing (Smith *et al*., 2005; Onsotto *et al*., 2006). This type of synthesis of hydrocarbons was first discovered by two German scientists Franz Fischer and Han Tropsch in the 1920s (Etiope and Sherwood-Lollar, 2013).

The FTT expression incorporates the Fischer-Tropsch reaction *in sensu stricto*, which alludes to the reactant hydrogenation of carbon monoxide to create an extensive variety of straight, long-chain hydrocarbons (Anderson, 1984; Schulz, 1999)

$$nCO + 2nH_2 \leftrightarrow C_nH_{2n+2} + nH_2O \quad (8),$$

and for carbon dioxide-dominant initial fluid compositions, the catalytic hydrogenation of CO_2 proceeds in either the two step (reverse water-gas shift) reaction or the one step (Sabatier or methanation) reaction, to produce CH_4 (e.g., Anderson, 1984; Wang *et al*., 2011):

$$nCO_2 + (3n + 1)\, H_2 \leftrightarrow C_nH_{2n+2} + 2nH_2O \quad (9),$$

Two-steps reverse water-gas shift reaction (RWGS):

$$CO_2 + H_2 \leftrightarrow CO + H_2O \qquad (Cn = 1) \qquad (10),$$

$$CO + 3H_2 \leftrightarrow CH_4 + H_2O \qquad (Cn = 1) \qquad (11),$$

One-step (Sabatier or Methanation):

$$CO_2 + 4H_2 \leftrightarrow CH_4 + H_2O \qquad (Cn = 1) \qquad (12),$$

The FTT reactions are catalyzed in the presence of transitions metals (Fe, Ni, Cr, Ru, Co), Fe-oxides and Fe-silicates (e.g., Lancet and Anders, 1970; Szatmari, 1989; Etiope and Sherwood-Lollar, 2013), so that the transformation of these gas molecules takes place on the metal surface. The one-step methanation— the simplest form of the FTT is an exothermic (enthalpy of reaction (H) is – 167Kj/mol), reversible system and proceeds catalytically and spontaneously at relative low temperatures, whereas the two-step RWGS reaction is a moderately endothermic reversible reaction ($\Delta H = + 40.6$ KJ/mol) and it is also an equilibrium-limited reaction that is favoured at high temperatures (Daza *et al*., 2014).

Numerous experiments have been reported for this type of abiogenic process under hydrothermal conditions, at pressures (0.35 -0.40 Kbar) and at temperatures above 200 ˚C, using various types of metallic catalyst, which are common in ultramafic rocks such as Ni, Fe-Cr (e.g., Foustoukos and Seyfried, 2004; McCollom and Seewald, 2006). Production of CH_4 in in any of these experiments is usually observed over a time scale ranging from hours to days, whereas for those taking place at lower temperatures are theoretically much slower, with few exceptions (e.g. methanation catalysed by ruthenium and rhodium at room temperature and atmospheric pressure) (Thampi *et al*., 1987; Jacquemiun *et al*., 2010). However, these PGEs occur in trace amounts in ultramafic rocks, so their role as catalysts needs to be verified in future studies. Even though this idea may be theoretically feasible it is yet to be tested experimentally in laboratory work (Etiope and Sherwood-Lollar, 2013).

CHAPTER 4

4.0 Mineral and fluid inclusion petrography

4.1 Mineral petrography

Doubly polished thick sections (~180-220 μm) were prepared from olivine ferrodiorites, quartz anorthosites, anorthosites, leucogabbronorites and two-feldspar granites, from the Bellevue (BV-1) borehole and Stoffberg area, respectively. Detailed petrographic examinations of these were undertaken in order to determine the origin of the mineral that hosts the fluid inclusions, based on textural relations and association with the surrounding minerals. Petrography of fluid inclusions was also carried out on the same samples to characterize their nature and origin of the fluid trapped in these fluid inclusions.

Seventeen samples from two different locations within the Bushveld Igneous Complex (BIC) were studied (Figure 4.1.1-4.1.3, Appendix 1.1). Six samples from the Stoffberg area, Eastern limb, were collected from presently recrystallized microgranite, granophyres and hornfels that form the upper most part of the BIC (Cawthorn, 2013). The other eleven samples were collected from the Bellevue drillcore, from the Northern limb, of the BIC (Ashwal et al., 2005).

All samples (including olivine ferrodiorite, quartz anorthosite, anorthosite and leucogabbronorite) from the Bellevue drill core are characterized by euhedral plagioclase laths as the main cumulus phase, ranging from 45 to 90 % of the rock volume. The cumulus plagioclase is generally euhedral with a grain size that ranges from 0.2-1.9 mm. These cumulus plagioclase laths are closely packed together such that there is small interstitial space (180 – 650 μm across) between them (Figure 4.1.1a). Plagioclase is variably altered to sericite (Figure 4.1.1b). However, the plagioclase laths are generally relatively fresh (Figure 4.1.1a & c). These samples are also characterized by intercumulus, triangular, patchy quartz grains, representing

crystallization products of trapped interstitial melts (Figure 4.1.1c), and finely disseminated rutile crystals (Figure 4.1.1d). In some of the samples, poikilitic biotite encloses euhedral plagioclase laths (Figure 4.1.2a), and poikilitic amphibole encloses plagioclase, quartz and apatite grains (Figure 4.1.2b), and poikilitic clinopyroxenes (inverted pigeonite) encloses plagioclase (Figure 4.1.2c). In some samples clinopyroxene occurs interstitially between euhedral plagioclase laths (Figure 4.1.2d).

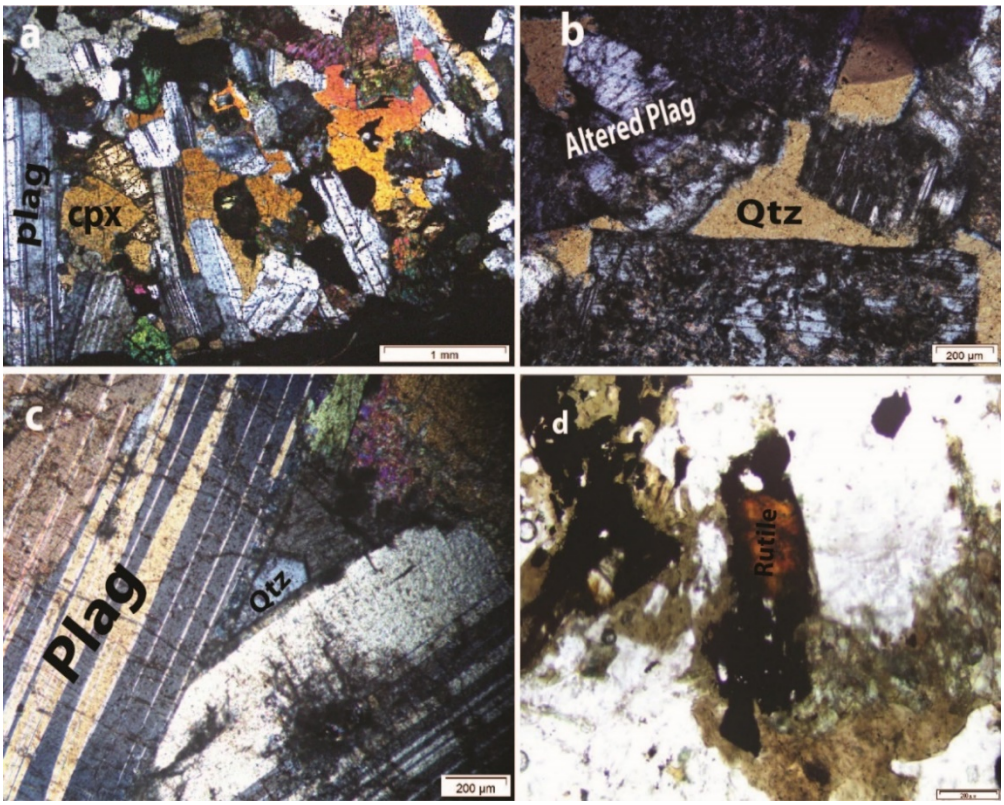

Figure 4.1.1: Microphotographs of thin section from the Bellevue drillcore. a. Photomicrographs of olivine ferrodiorite from a depth of 105.23 m under cross-polarized light. Relatively fresh euhedral plagioclase laths are surrounded by anhedral clinopyroxenes. b. Photomicrograph of quartz anorthosite (sample BV-352.60) under cross-polarized light, showing highly altered plagioclase, associated with interstitial quartz. C. Triangular, patchy interstitial quartz surrounded by euhedral plagioclase laths from sample BV-1413.80. D. Rutile with small inclusions of quartz under plane polarized light from sample BV-83.69.

All samples (recrystallized microgranites) from the Stoffberg area are characterized by two-feldspars (plagioclase and alkaline feldspar) as the main cumulus phases making up 55-71% of the rock volume, with the alkaline feldspars being the dominant phase. Fresh plagioclase is observed only in sample RG-22 and RGC- 12 (Figure 4.1.3a-b). However, most of these samples shown considerable evidence of alteration of feldspars and a number of other minerals

(Figure 4.1.3c). In some samples plagioclase is overgrown is by alkali feldspars, and surrounded by amphibole and quartz (Figure 4.1.3c). Quartz exists in two forms: (1) grains that show an intergrowth texture with alkali feldspars (Figure 4.1.3c), (2) and those that show a triangular, patchy intercumulus texture (Figure 4.1.3d). In some samples, clinopyroxenes have altered to chlorite and amphibole (Figure 4.1.3e). Large rutile crystals with radiating tremolite grains and oxides were observed (Figure 4.1.3f). There is abundant apatite in amphibole and oxide (Figure 4.1.3f)

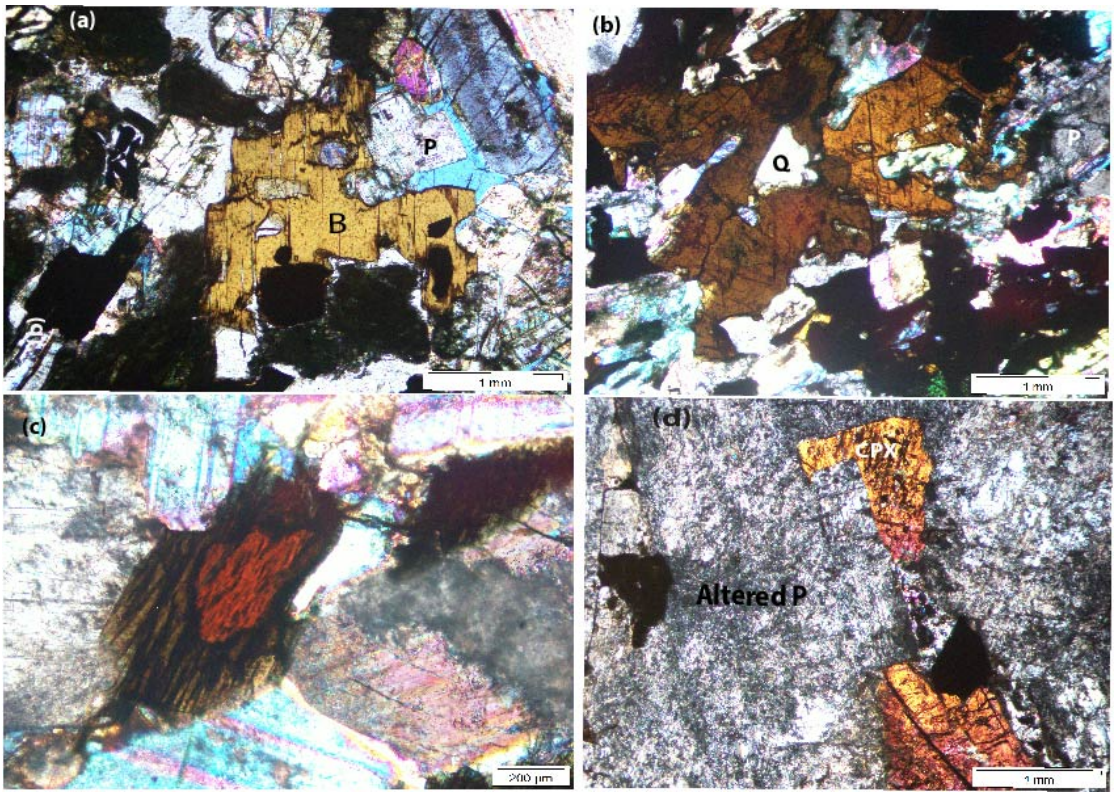

Figure 4.1.2: Microphotographs of thin section from the Bellevue drillcore. (a) Photomicrograph of an olivine ferrodiorite from a depth of 106.20 m under cross-polarized light, showing poikilitic biotite enclosing euhedral plagioclase laths. (B) Poikilitic amphibole enclosing plagioclase laths, apatite and quartz grains from sample BV-83.81. (C). Photomicrograph of olivine ferrodiorite from a depth of 106.20 m under cross-polarized light showing a poikilitic clinopyroxenes enclosing plagioclase laths. (D) Interstitial clinopyroxene between euhedral plagioclase laths from sample BV-893.90.

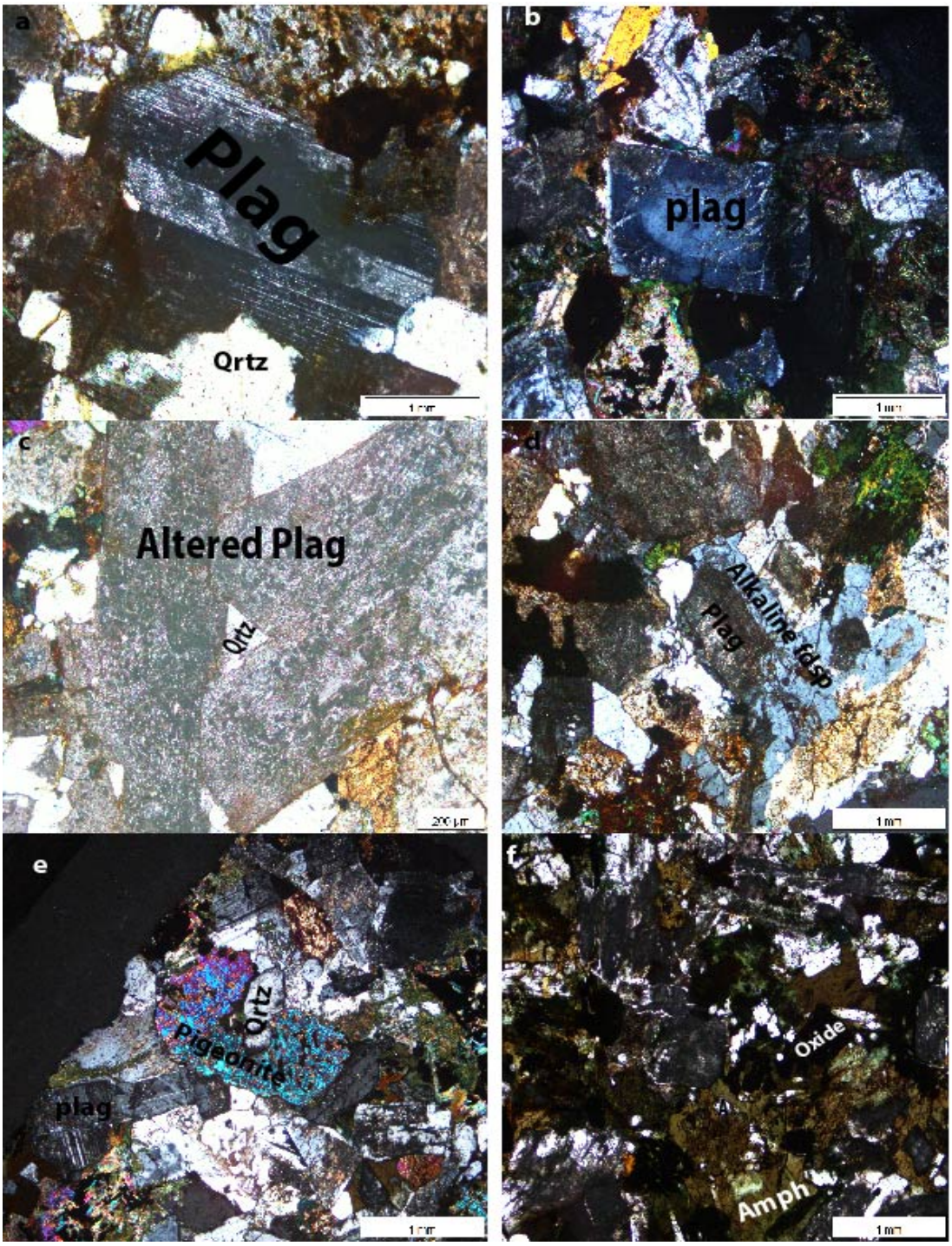

Figure 4.1.3: Microphotographs of thin section from the Stoffberg area. (a) Photomicrograph of granodiorite shows relatively fresh euhedral plagioclase lath with interstitial quartz (RGC-22). (B) Microphotograph of monzonite showing fresh euhedral plagioclase showing zoning patterns, with interstitial quartz and amphibole (RGC-12). (c) Photomicrograph of quartz monzonite showing highly altered plagioclase, with interstitial quartz (RGC-19). Photomicrograph of quartz monzonite showing plagioclase overgrown by alkali feldspars, surrounded by interstitial quartz (RGC-20). (E) Microphograph of pigeonite surrounded by euhedral plagioclase laths and interstitial quartz (RGC-12). (f) Abundant apatite in amphibole and oxide, with cumulate plagioclase at the edges (RGC-12). Amph-amphibole, plag-plagioclase, qrtz-quartz.

4.2 Fluid inclusion petrography

Fluid inclusions are classified in many ways (Roedder, 1984; Goldstein, 2003; Bodnar, 2003), but their relative timing with respect to the growth of the host mineral is, widely accepted as a standard classification scheme (Bodnar, 2003). During growth of the host crystal from any kind of fluid-bearing medium, growth irregularities result in primary fluid inclusions (Roedder, 1984). If fractures are formed during crystal growth, pseudosecondary fluid inclusions may be entrapped in the course of continued growth of the crystal. Secondary fluid inclusions form as result of healing of crystal fractures, as fluids enter fractures after crystal growth is complete (Bodnar, 2003). Petrographically, the appearance of secondary and pseudosecondary fluid inclusions is similar, but the occurrence of secondary fluid inclusions is followed by additional crystal growth (Bodnar, 2003).

In a given sample, fluid inclusions commonly comprise inclusions of multiple generations, representing multiple fluid trapping events, but the host crystals rarely contain inclusions of only one generation. Hence, information obtained from fluid inclusion studies may be useful in understanding various geological processes, particularly in ore settings such as the Bushveld Igneous Complex, where they can be used to provide understanding about the temperature, pressure and depth of emplacement of the BIC magma chamber.

Three types of fluid inclusion assemblages (FIA) were identified in primary magmatic quartz during the petrographic examination of the samples from the Bellevue drillcore (Figure 4.2.1). These include: (1) primary fluid inclusions that are trapped within the crystal growth zones; this FIA lacks any consistent orientation (Figure 4.2.1), (2) secondary fluid inclusions that occur in planar and liner arrays, (3) these assemblages have a well-defined orientation with respect to crystal form (Figure 4.2.1). Psuedosecondary fluid inclusions were observed in most samples occurring along healed fractures in the interior of crystals (Figure 4.2.1).

Types of fluid inclusions identified at room temperature include two-phase liquid-vapour (L-V) inclusions (Figure 4.2.2a), single-phase vapour-rich inclusions (Figure 4.2.2b), three-phase inclusions containing 2 liquids and a vapour (L_1-L_2-V) (Figure 4.2.2c) and/or liquid and vapour phases with a solid daughter crystal (L-V-S) (Figure 4.2.2d). Two-phase liquid-vapour (L-V) inclusion were the most abundant in all samples analysed Single-phase V-rich and the three-phase (L_1-L_2-V and/or L-V-S) inclusions are present locally, but are both volumetrically minor in comparison to the two-phase inclusions. Also identified were rare fluid inclusions comprising large daughter crystals of calcite (14 μm in size) and comparatively minor proportions of a liquid phase, and these have a close spatial relationship with the other inclusions of variable composition (Figure 4.2.3).

Primary fluid inclusions in the primary magmatic quartz grains are predominantly two-phase LV-type inclusions that are commonly large (4 -14 μm), well developed in shape, and have the longest dimensions of <20 μm. Inclusions of this type are typically cubic or spherical in terms of shape (Figure 4.2.4). Additionally, isolated clusters of angular to sub-rounded, mature LV-type of inclusions were recognized (Figure 4.2.2a), as well as three-phase inclusions, that comprise L_1-L_2-V (Figure 4.2.2c) and occur as primary fluid inclusions. These types of three-phase inclusions commonly have negative crystal shapes.

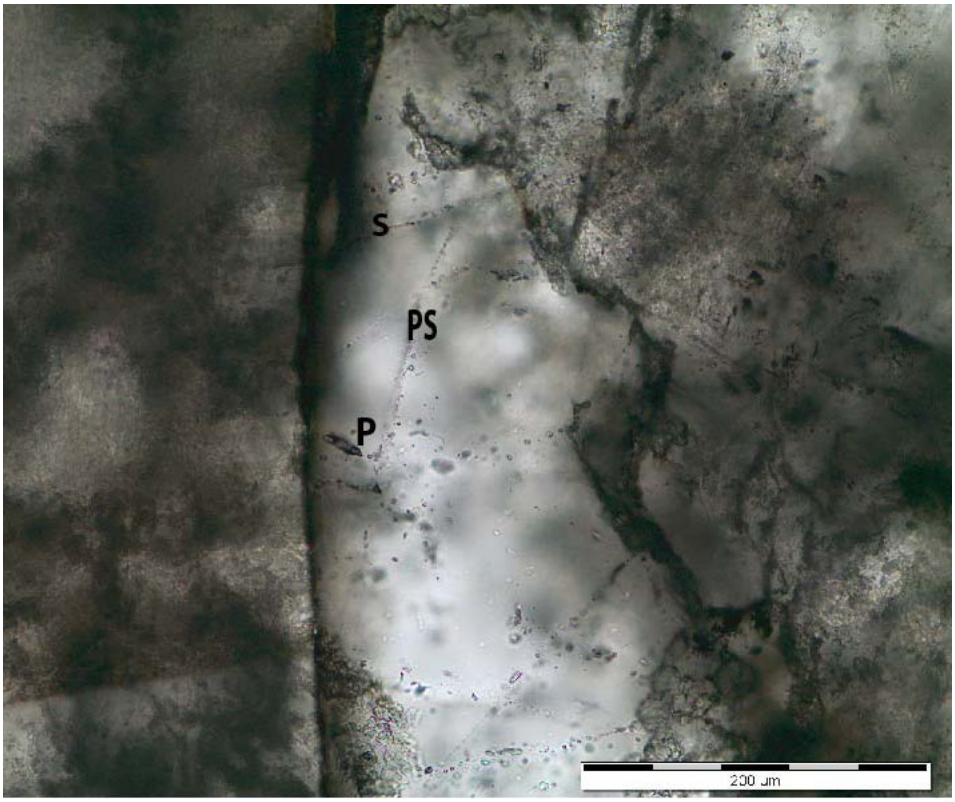

Figure 4.2.1: Microphotographs of various types of fluid inclusions from the Bellevue core samples at room temperature. Microphotograph of BV-417.90, P2 showing three fluid inclusion assemblages and these include primary (P), psuedosecondary (PS) and secondary fluid inclusion assemblages (S). P= primary, S= secondary and PS= psuedosecondary.

Secondary fluid inclusions in magmatic quartz grains are predominantly of the two-phase inclusion L-V-type, which exhibit relatively irregular forms and have the second largest dimensions after the primary inclusions; the longest dimension is no greater than 11 μm (Figure 4.2.5). These types of inclusions occur in healed microfractures with variable vapour: liquid ratios. Additionally, three-phase inclusions (L-V-S) and single-phase V-rich assemblages were recognized as secondary fluid inclusions. Vapour-rich inclusions coexist with L-V-S inclusions in some host minerals (Figure 4.2.2b).

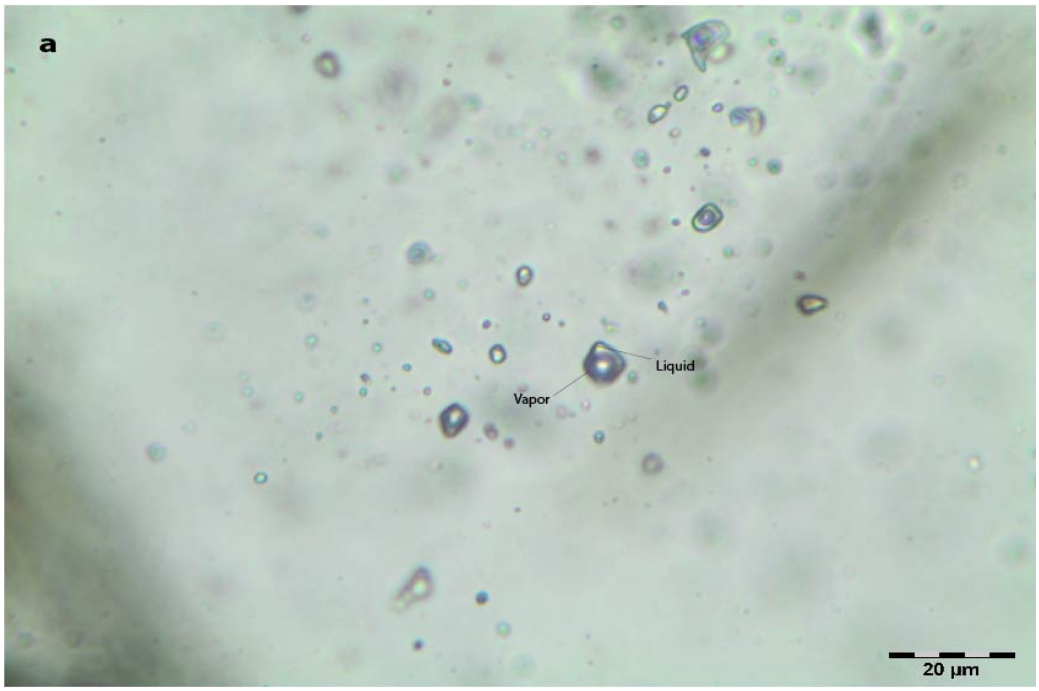

Figure 4.2.2 (a): Photomicrograph of two-phase ─L and V─ fluid inclusions from sample BV-1454.35, P2.

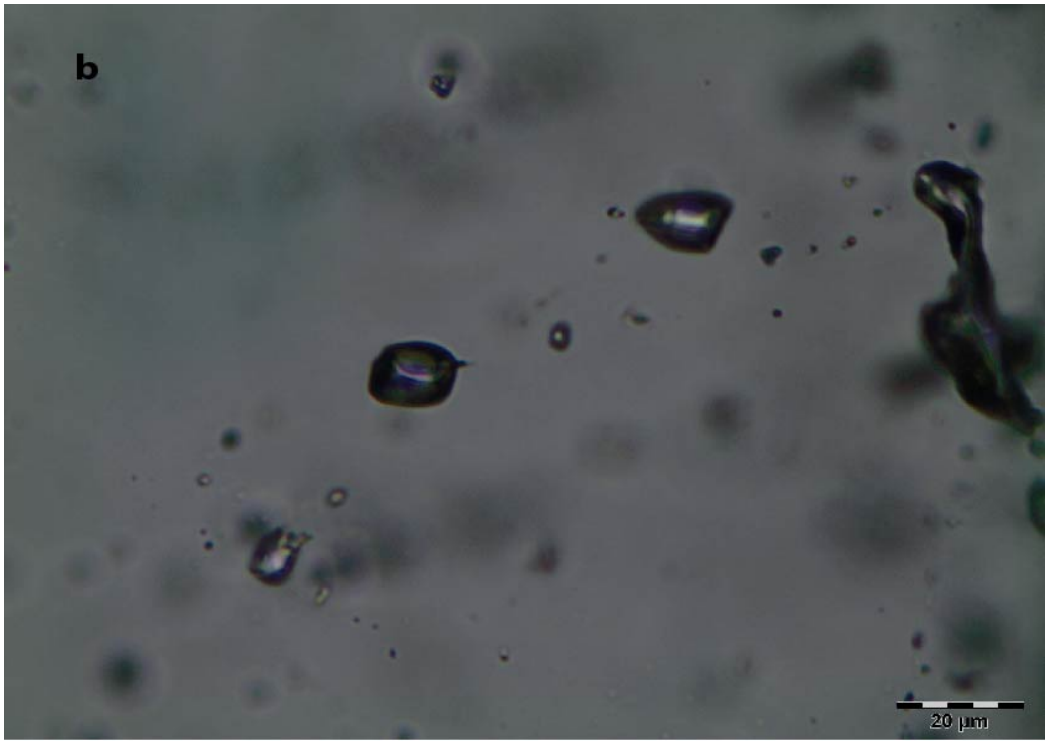

Figure 4.2.2 (b): Dark one phase fluid inclusion from sample BV-417.90, in P1, comprise vapour only.

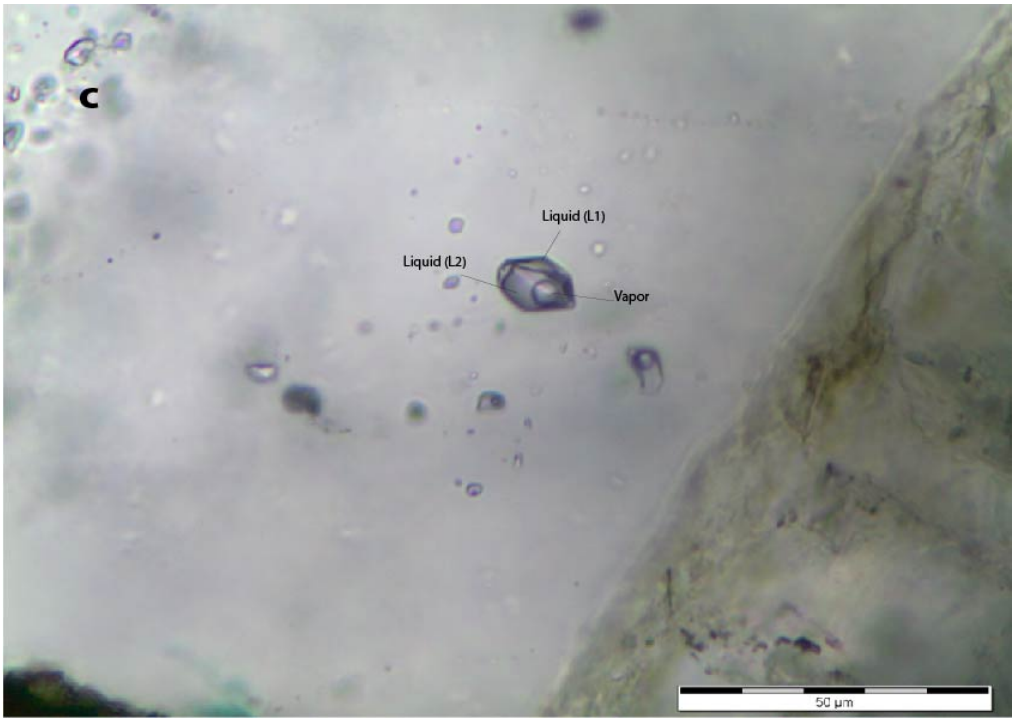

Figure 4.2.2 (c): Photomicrograph showing three phase fluid inclusion comprising two liquid (L_1 and L_2) phases and one vapour phase, from sample BV-417.90, P1.

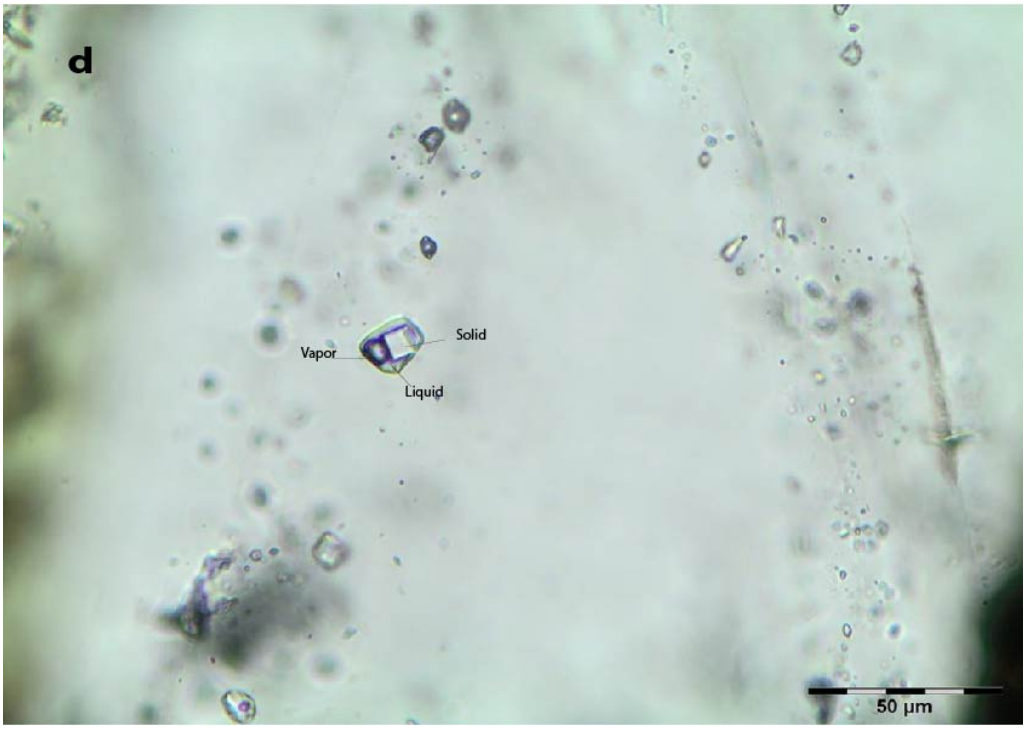

Figure 4.2.2 (d): Microphotograph showing a three-phase ─L, V and S phase─ fluid inclusion from sample BV-417.90, P.

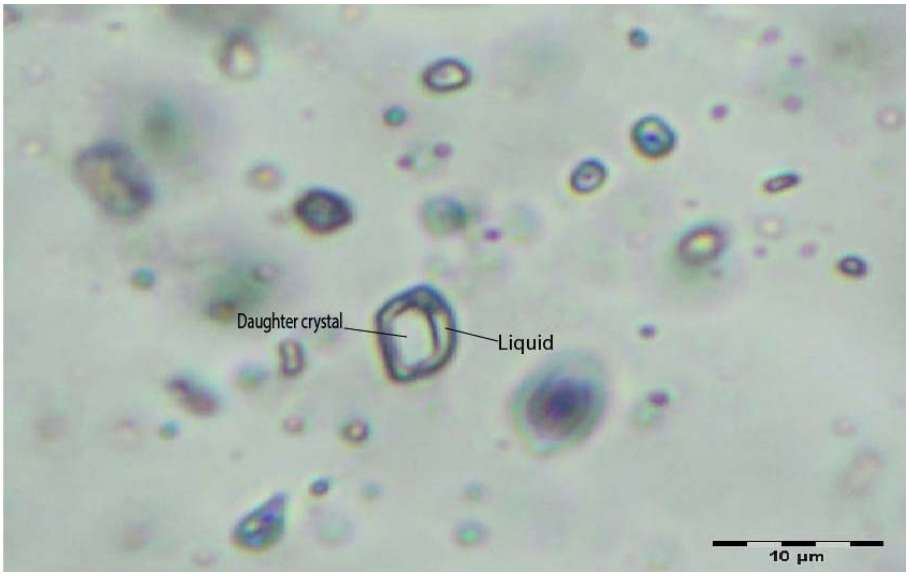

Figure 4.2.3: Photomicrograph from sample BV-1454.35, P2, comprising a large solid crystal and comparatively minor proportions of liquid phase. 4

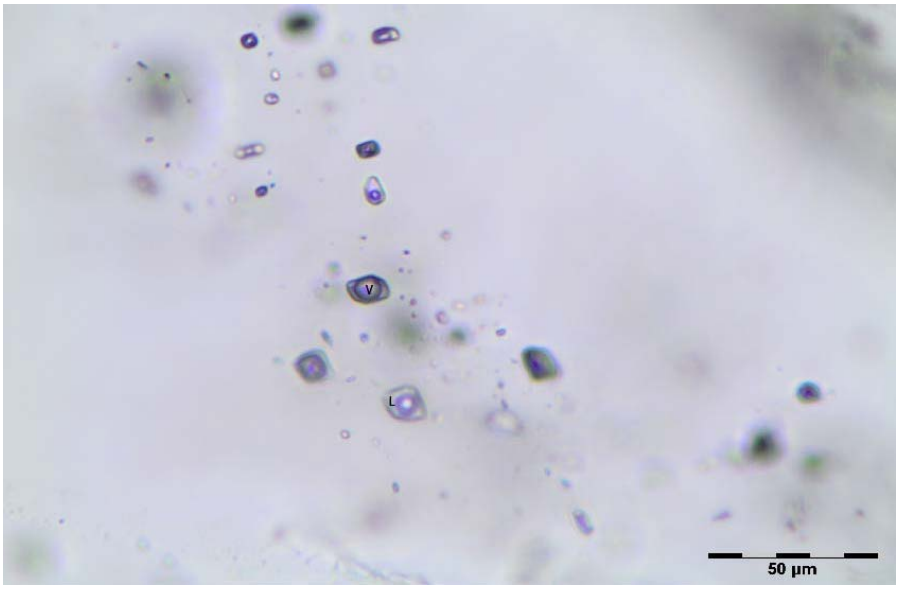

Figure 4.2.4: Photomicrograph showing cubic to spherical two-phase fluid inclusion comprising L and V phases, with varying proportions of liquid and vapour, from sample BV-417.90, P2, whereas photomicrograph

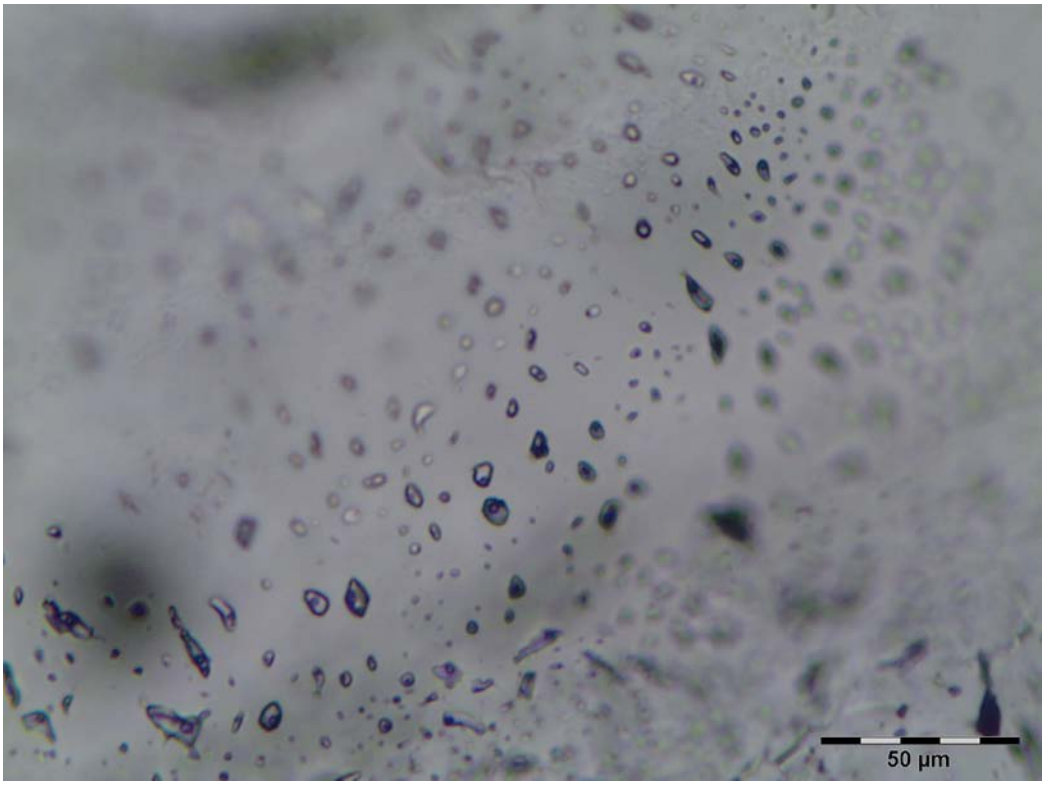

Figure 4.2.5: Microphotograph of secondary two-phase fluid inclusions exhibit relatively irregular forms from BV-417.90, P2 sample at room temperature.

4.3 Types of Fluid inclusions identified in the Stoffberg samples

Abundant fluid inclusions were observed in the Stoffberg samples which are relatively small in size compared to those from the Bellevue core. Several types of fluid inclusion assemblages were identified in the Stoffberg samples. However, by far the most common type are the secondary fluid inclusions recognized in interstitial quartz grains (Figure 4.3.1a), whereas in samples where quartz is intergrown with alkali feldspars, primary fluid inclusions are dominant, and they exist within the growth zones of the host mineral (Figure 4.3.1b).

Additionally, psuedosecondary fluid inclusions are present locally in both the interstitial quartz and in the samples in which quartz is intergrown with alkali feldspars, but these are volumetrically minor in comparison to the other types of fluid inclusion assemblages (Figure 4.3.1c-d).

Several different types of fluid inclusions were identified in both the interstitial quartz and in the quartz intergrown with alkali feldspars. The most common type of fluid inclusions are two-phase inclusions that comprise liquid (L) and vapour (V) phase at room temperature (Figure 4.3.2a). Additionally, monophase vapour-rich (V) inclusions (Figure 4.3.2b), as well as three-phase inclusions comprising a vapour, a liquid and a solid phase (L-V-S) are present (Figure 4.3.2c), but volumetrically, both are minor in comparison to LV-inclusions. Rare inclusions comprising large daughter crystals of halite (~ 5 μm) and comparatively minor proportions of liquid phase have close spatial relationships with the other types of variable composition (Figure 4.3.2d).

Primary fluid inclusions in interstitial quartz are predominantly two-phase inclusions LV-type commonly have the longest dimension of <10 μm. They are either cubic or spherical in shape (Figure 4.3.3), whereas in the samples where quartz is intergrown with alkali feldspar, the primary inclusions are relatively small, irregular in shape even though they are also predominantly LV-type (Figure 4.3.2a). Additionally, three-phase inclusions that comprise L-V-S (Figure 4.3.2c), as well as single-phase vapour-rich (V) (Figure 4.3.2b) were recognized as primary fluid inclusions only in the interstitial quartz of the Stoffberg samples. Both the three-phase and single-phase vapour-rich (V) assemblages occur locally.

Secondary fluid inclusions in both the interstitial quartz the granophyric quartz is also predominantly of the two-phase inclusion LV-type. However, they are relatively irregular forms and small in size; with the longest dimension being <8 μm (Figure 4.3.4.). These types of inclusions occur in healed microfractures with variable vapour: liquid ratios.

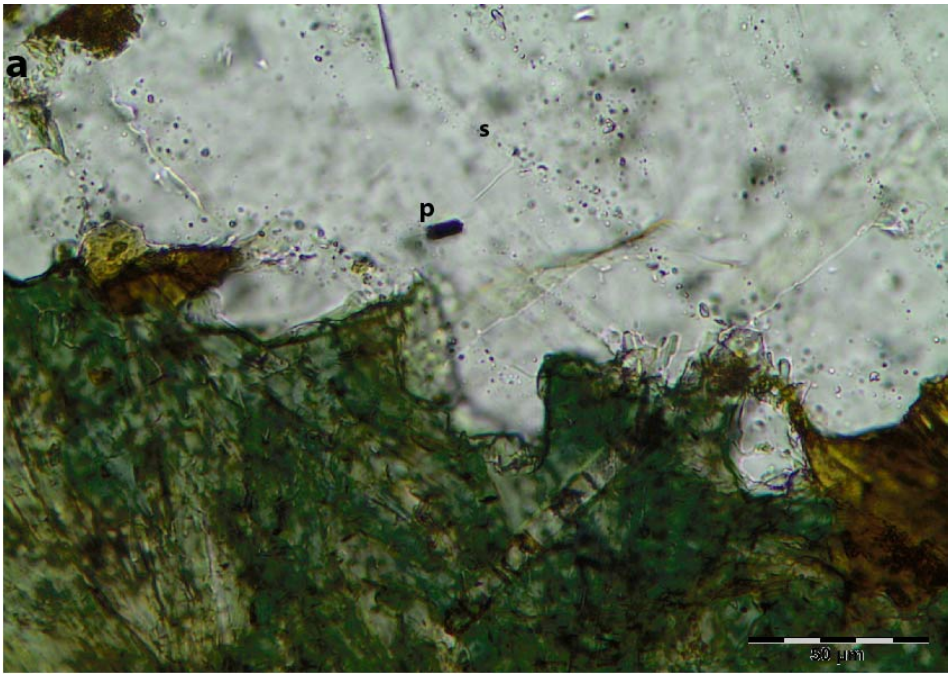

Figure 4.3.1 (a) Microphotograph of RGC-19, P4 showing two fluid inclusion assemblages (FIA's) and these include primary (P) and secondary fluid inclusion assemblages (S), from interstitial quartz.

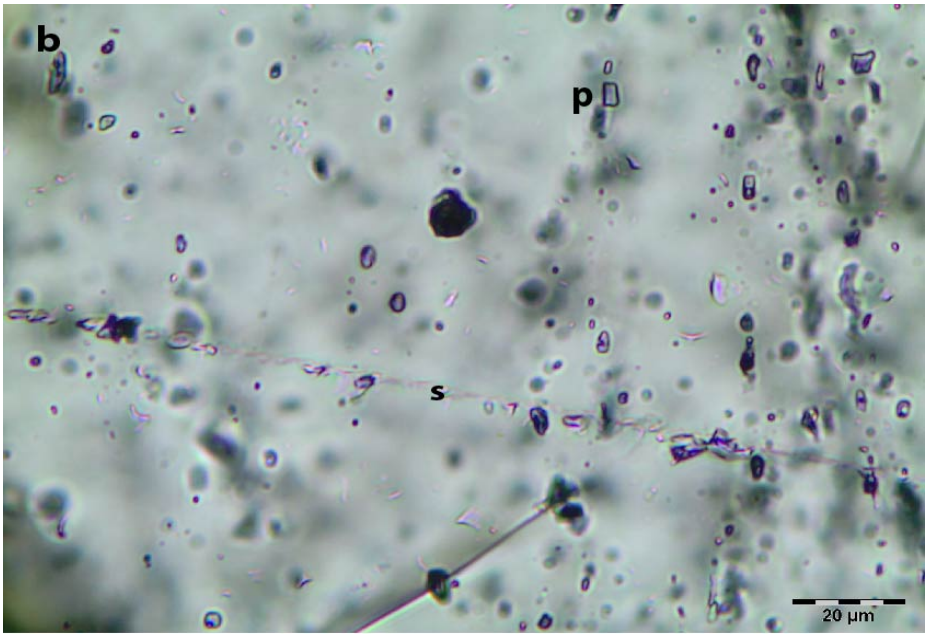

Figure 4.3.1 (b) Microphotograph shows similar types of FIA's, however, in a sample where there is an intergrowth of quartz and alkaline feldspars such as sample RGC-12, P6.

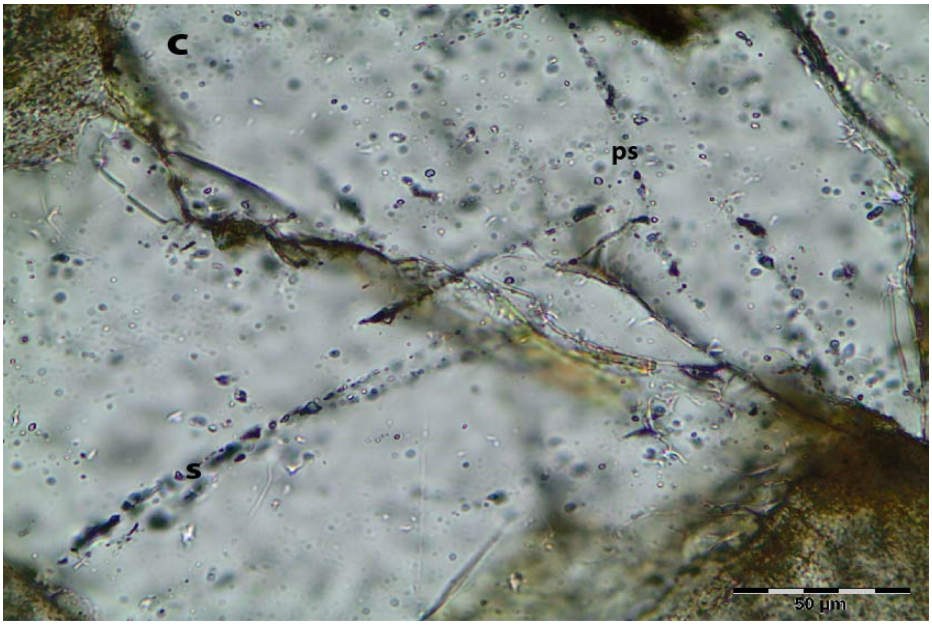

Figure 4.3.1 (c) Microphotograph of RGC-16, P7 shows two fluid inclusion assemblages (FIA's) and these include psuedosecondary (Ps) and secondary fluid inclusion assemblages (S), from interstitial quartz.

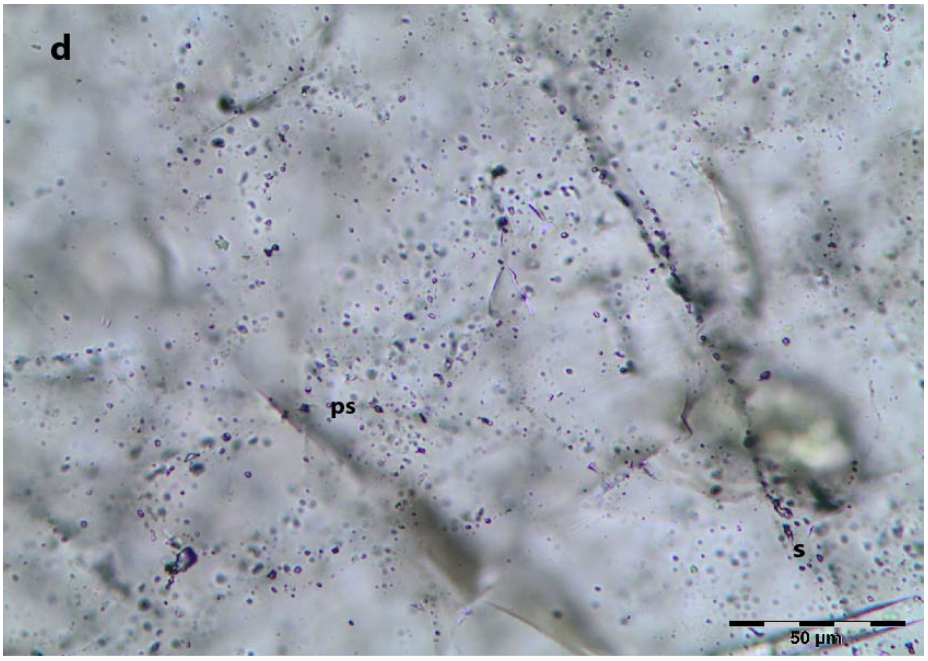

Figure 4.3.1 (d) Microphotograph shows similar types of FIA's, however, in a sample where there is an intergrowth of quartz and alkaline feldspars such as sample RGC-19, P2.

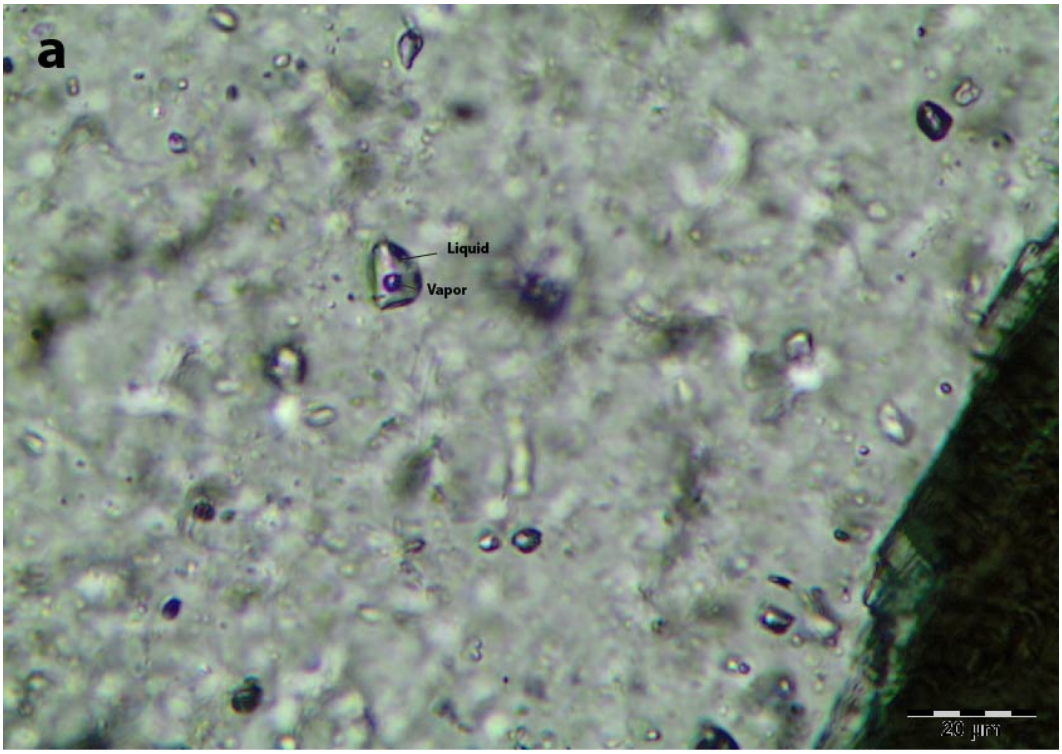
a
Liquid
Vapor
20 µm

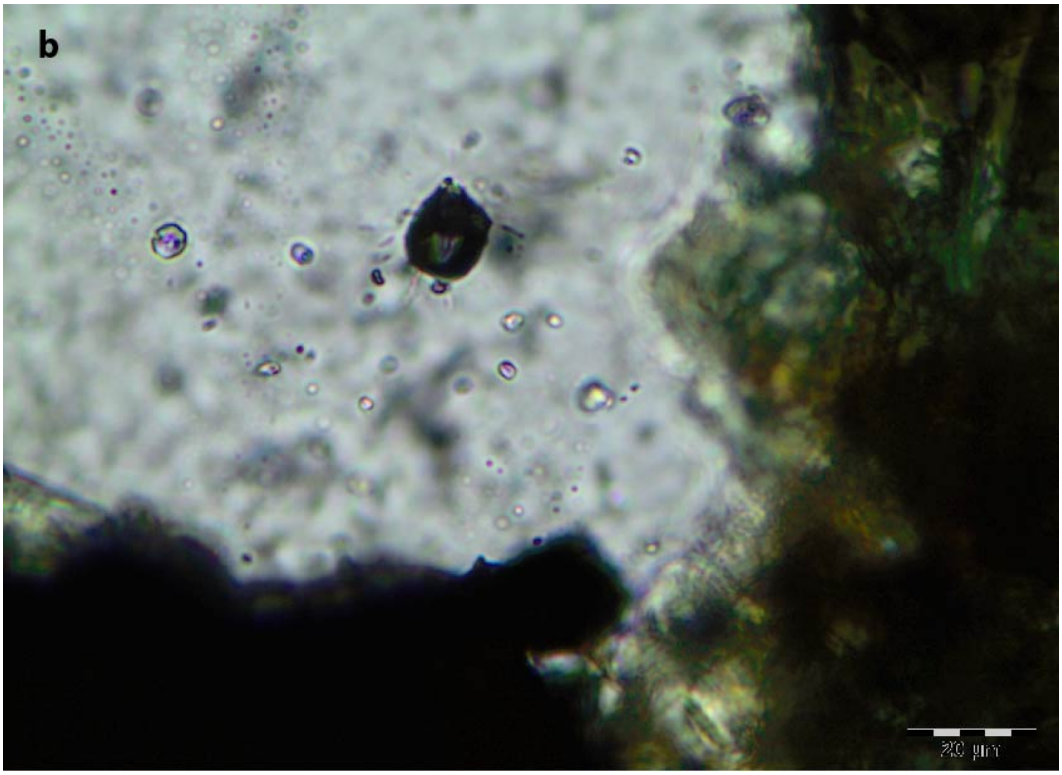
b
20 µm

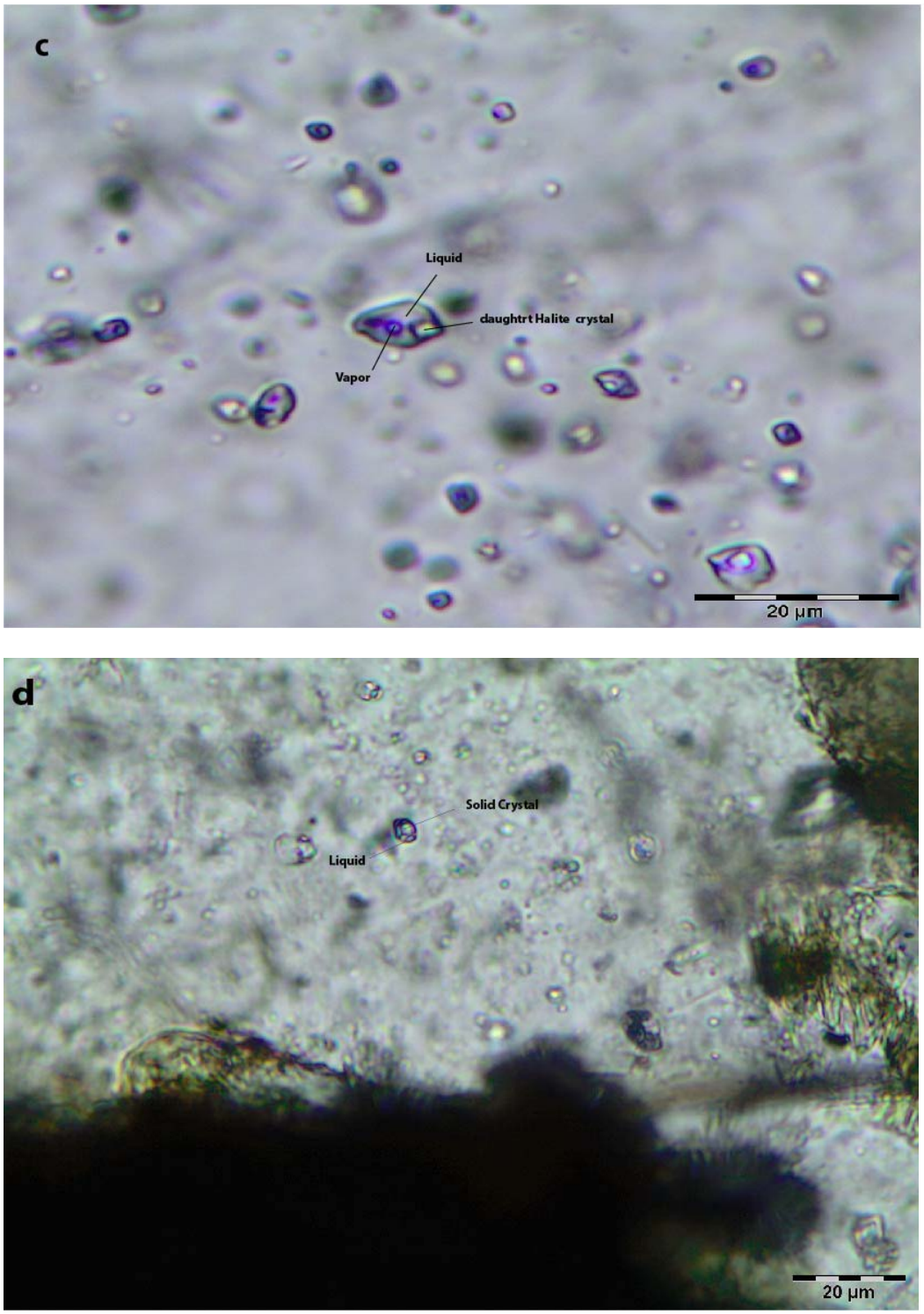

Figure 4.3.2: Microphotographs of various types of fluid inclusions from Bellevue core samples at room temperature. (a) Photomicrograph of two-phase ─liquid and vapour─ fluid inclusions from sample RGC-22, P3. (b) Dark one phase fluid inclusion from sample RGC-16, P3, comprising vapour-rich phase only. (c) Photomicrograph showing three phase fluid inclusion comprising two liquid phases and one vapour phase, from sample RGC-24, P1. (d) Photomicrograph from sample RGC-16, P1, comprising a large solid crystal and comparatively minor proportions of liquid phase.

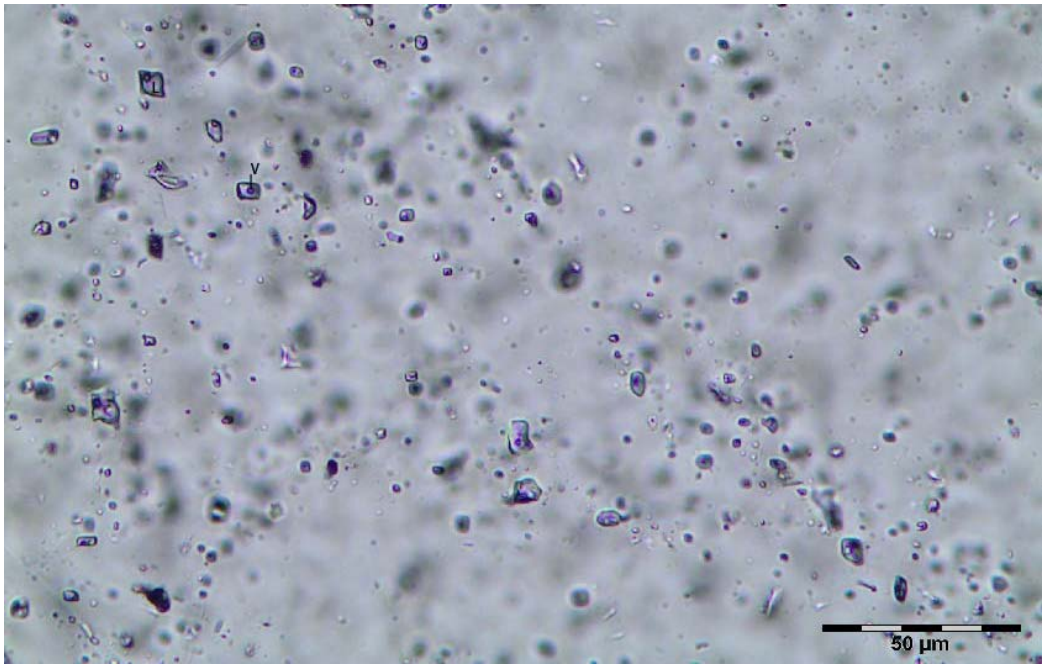

Figure 4.3.3: Microphotograph of cubic to spherical, two-phase inclusions LV-type of the primary FIA, from sample RGC-24, P1 in interstitial quartz.

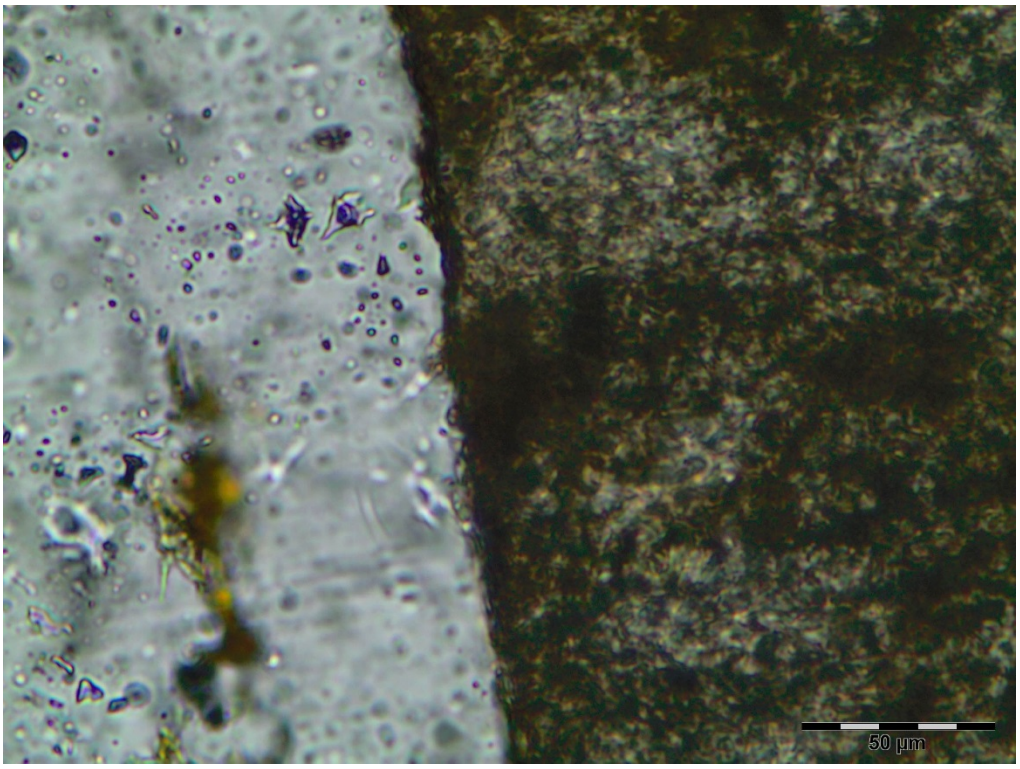

Figure 4.3.4: Microphotograph of secondary two-phase fluid inclusions exhibit features of necking forms from RGC-19, P3 sample at room temperature.

4.4 Classification of fluid inclusion types

A minimum of six distinct fluid inclusion types have been identified in the Bellevue drillcore and the Stoffberg area, based on phase relations observed at room temperature (Table 4.1). They include:

Type 1: Rare single-phase fluid inclusions that occur both as part of the primary and secondary fluid inclusion assemblage. Can either be L- or V-rich inclusion.

Type 2A: Liquid-rich two-phase fluid inclusions that homogenise by vapour bubble disappearance (Figure 4.4 c). Type 2A fluid inclusions are abundant from both sites investigated in this study.

Type 2B: Rare vapour-rich two-phase fluid inclusions that exhibit homogenization behaviour by fading of the meniscus without a change in vapour size of the inclusion or by vapour bubble expansion.

Type 2C: Rare solid-rich two-phase fluid inclusions that exhibit homogenization behaviour by solid dissolution. The least abundant type in the fluid inclusions investigated in this study.

Type 3A: Three-phase liquid-rich hypersaline fluid inclusions (halite + vapour + liquid) that homogenize by vapour bubble disappearance. It is mostly observed in secondary fluid inclusion assemblage. The eventually result in the dissolution of the halite at higher temperatures.

Type 3B: Three-phase liquid-rich fluid inclusions (Carbonate daughter (calite) + vapour + liquid) that homogenize by vapour bubble disappearance. It is mostly observed in secondary fluid inclusion assemblage.

Type 4: CO_2 -rich fluid inclusions that contain CO_2 liquid and gas plus H_2O-liquid phases. Most of them homogenize by vapour disappearance. They are found both in the primary and secondary fluid inclusion assemblage of the Bellevue drillcore.

The number of each type of inclusion, analysed from both sites investigated in this study is presented in Table 5.1. Each fluid inclusion type is further divided into both secondary and primary fluid inclusions.

Table 4.1 Summary of fluid inclusion types, homogenization behaviour at high temperatures, and the phase (s) present at room temperature (25ºC) from the Bellevue drillcore and the Stoffberg area.

Inclusion Type	**Phases at 25 ºC**	**Homogenization behaviour**	**Example**
Type 1	Single phase	N.A.	
Type 2A	Liquid-rich two-phase (Liquid + Vapor)	Vapor bubble disappearance	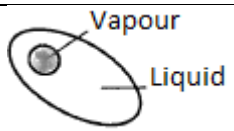
Type 2B	Vapor-rich two-phase (Liquid + Vapor)	Critical Behaviour	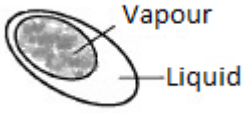
Type 2C	Liquid + Solid	Solid dissolution	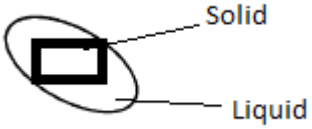
Type 3A	Liquid + Vapor + Halite	Vapor bubble disappearance and eventually the dissolution of the halite.	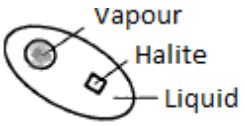
Type 3B	Liquid + Vapor + daughter	Vapor bubble disappearance	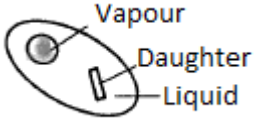

Type 4	CO_2-liquid + CO_2-vapor + H_2O- liquid	CO_2 disappears	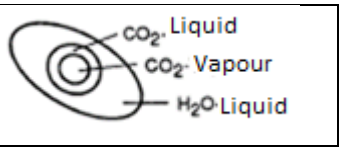

Figure 4.4

A: Type 1 fluid inclusions. Interstitial quartz containing secondary trails of 5-10 µm fluid inclusions with either only vapor (A) or liquid (B) contents. Sample BV-910.10 (2) Circle 2.

B: Type 2A liquid-rich two-phase (Liquid + Vapor) fluid inclusions. Bellevue drillcore contains a large amount of this type inclusions in the interstitial quartz, whereas in the Stoffberg area they exist in both interstitial and intergrown quartz. These inclusions homogenise by vapor bubble disappearance. In the Bellevue samples these types of inclusions have sizes that range from 3 to 8µm. Sample BV-1413.80 (2) P2.

C: Type 2B vapor-rich two-phase (Liquid + Vapor) fluid inclusions from the Bellevue drillcore occur in interstitial quartz, whereas in the Stoffberg samples they mostly occur in the intergrown quartz. These types of inclusions homogenize by critical behaviour. Sample BV-893.90 (2) P1.

: Type 2C solid-rich two-phase fluid inclusions that exhibit homogenization behaviour by solid dissolution e.g. BV-1454.35 P2 (plate 3.2.3a).

D: Type 3A fluid inclusion. The Bellevue samples interstitial quartz contains few of these type in the secondary fluid inclusion assemblage. Similarly, in the Stoffberg samples these types of inclusions exist in the secondary fluid inclusion assemblage. BV-352.60.

E: Type 3B fluid inclusion. Three-phase liquid-rich fluid inclusions (Carbonate daughter (calcite) + vapour + liquid) that homogenize by vapor bubble disappearance. It is mostly observed in secondary fluid inclusion assemblage. BV-417.90 (2).

F: Type 4 fluid inclusion. Bellevue samples contain both primary and secondary fluid inclusion assemblage of this type of fluid inclusion, with size of approximately 12 µm. They comprise CO -liquid + CO -vapour + H O-liquid. Sample BV-352.60.

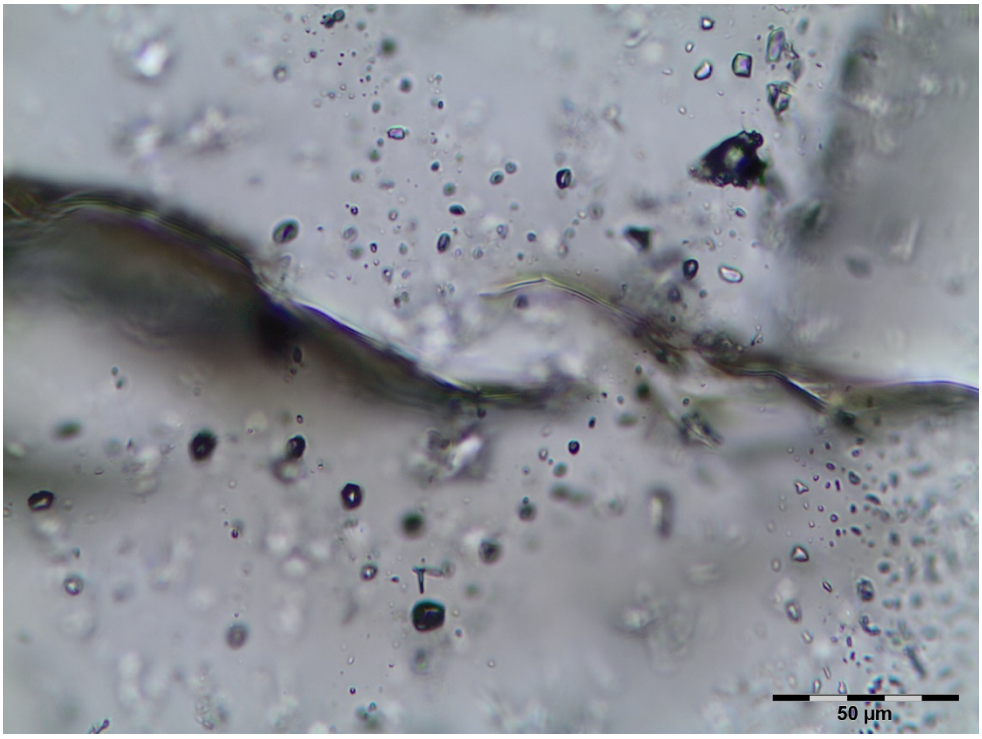

Figure 4.4 (a) Microphotograph of type 1 fluid inclusions from sample BV-910.10 (2)

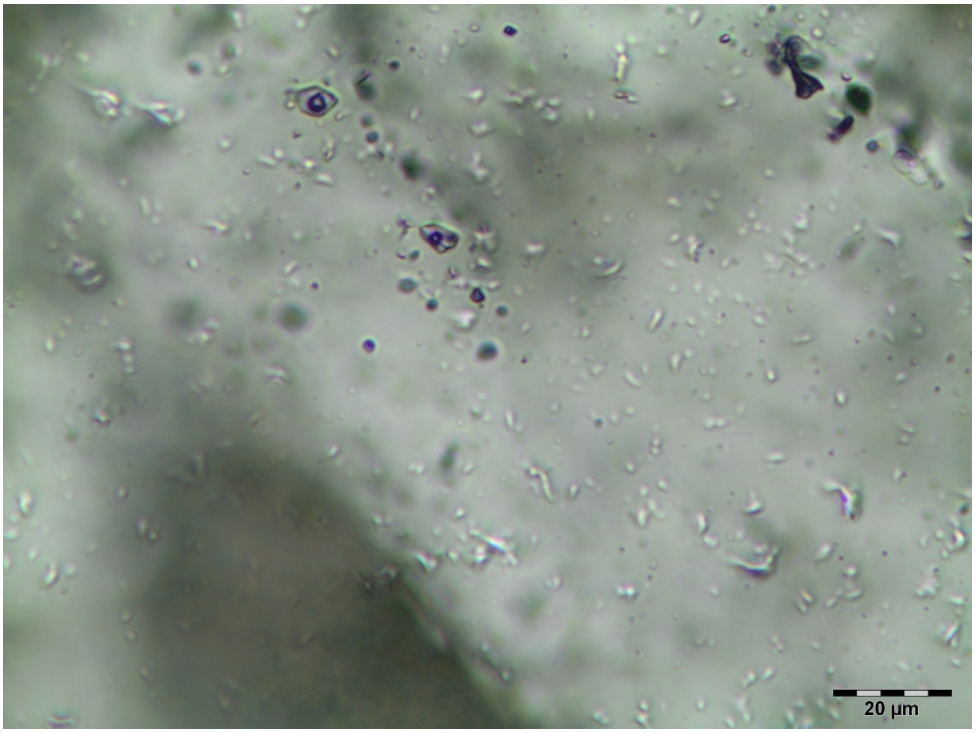

Figure 4.4 (b) Microphotograph of type 2A fluid inclusions from sample BV-1413.80 (2)

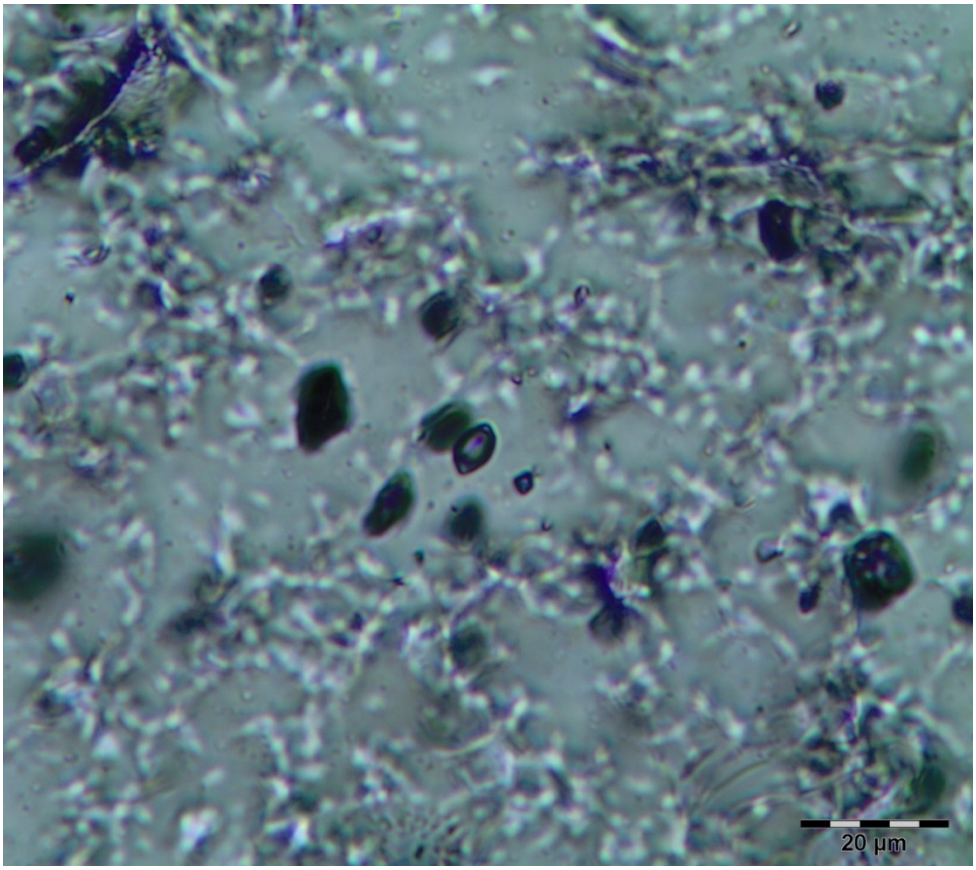

Figure 4.4 (c) Microphotograph of type 2B fluid inclusions from sample BV-893.90 (2)

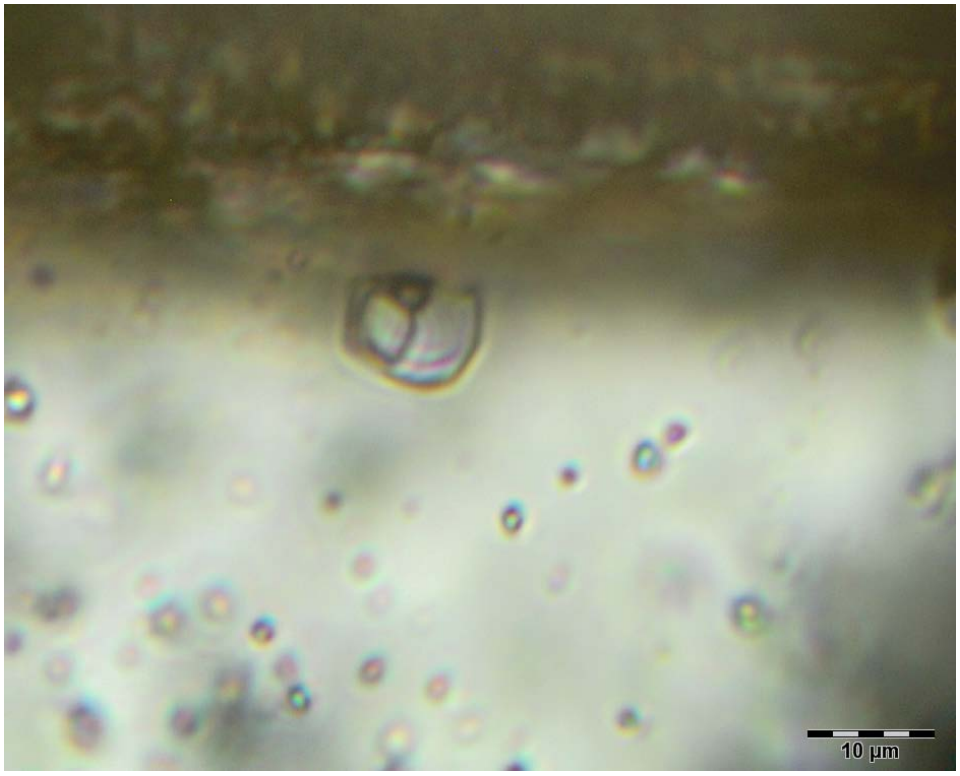

Figure 4.4 (d) Microphotograph of type 3A fluid inclusions from sample BV-352.60 (2)

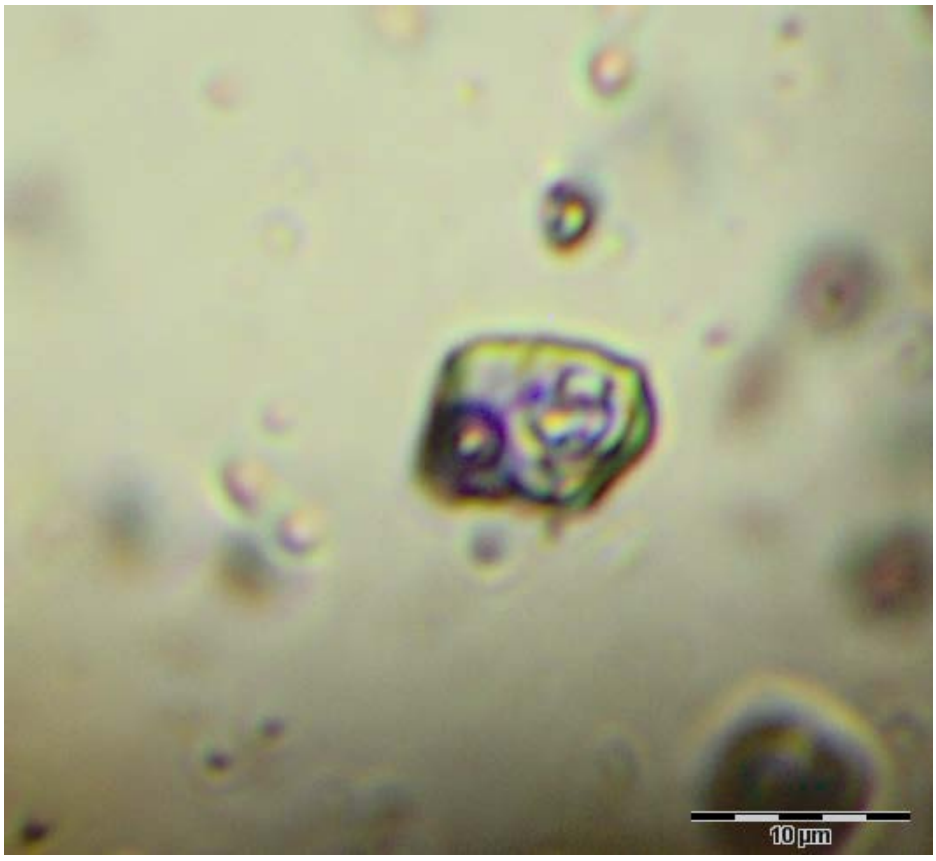

Figure 4.4 (e) Microphotograph of type 3B fluid inclusions from sample BV- 417.90 (2)

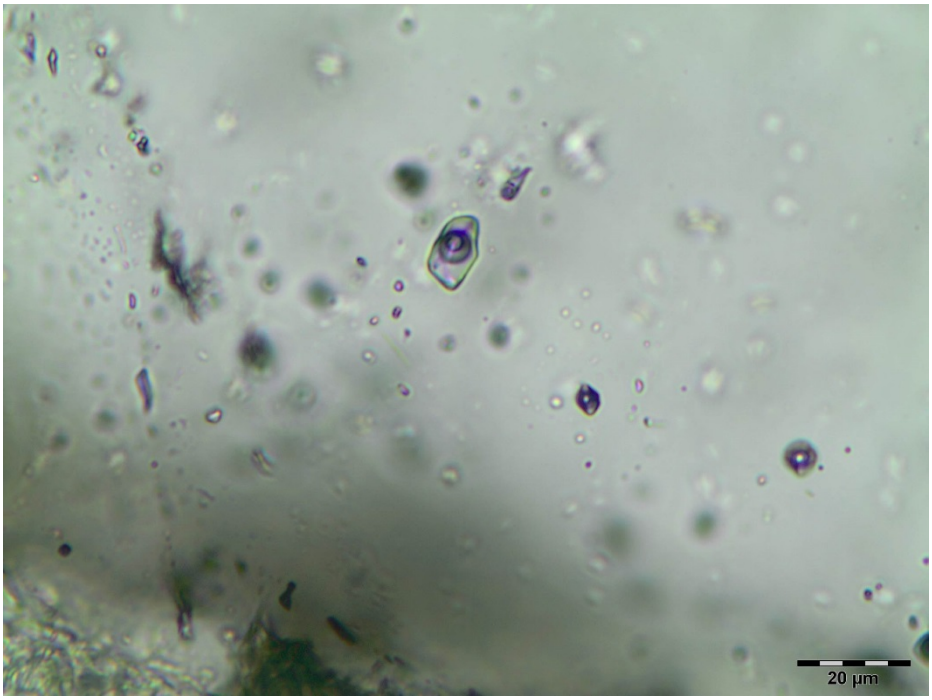

Figure 4.4 (f) Microphotograph of type 4 fluid inclusions from sample BV-352.60 (2)

Table 4.2: Summary of fluid inclusion data collected from the Bellevue drillcore and the Stoffberg area showing the fluid inclusion types with their secondary (S) and primary (P) classification and the number of fluid inclusions where data was acquired.

Site	**Type 1**		**Type 2A**		**Type 2B**		**Type 2C**		**Type 3A**		**Type 3B**		**Type 4**	
	P	S	P	S	P	S	P	S	P	S	P	S	P	S
Bellevue Core	23	14	58	24	10	3	2	0	7	3	3	1	20	4
Stoffberg	5	2	29	10	15	4	1	0	4	2	0	0	-	-

CHAPTER 5

Results

5.1 Raman microprobe analysis

For this study at least four Raman shift bands of interest can be observed and these include Raman peaks for CH_4, CO_2, Quartz and H_2O (see Table 5.1).

Table 5.1: Summary of the Main Raman vibrations (cm−1) of selected native elements, gases and tectosilicates.

Gasses; native element, and tectosilicate	**Main vibrations**
CO_2 Fermi doublet	s 1285; vs 1388
CO_2 in solution	vs 1384; m 1276
CH_4	vs 2917; w 3020
H_2O vapor	vs 3657–3756; w 1595
H_2O liquid	vs 2750–3900*; w 1630
Graphite	1355; 1580
Quartz (SiO_2)	206; 356; 402; 520; 608; 807; 1066; 1161

vs = very strong; m = medium; w = weak; sh = shoulder; * Broad bands of several hundreds of cm−1 (Frezzotti *et al*., 2012)

5.1.1 Bellevue (BV-1)

A total number of 224 Raman analysis points were acquired from 126 fluid inclusions representative of the different inclusions identified. 177 Raman analysis points were from 26 fluid inclusions in samples of the Bellevue core. Analyses from the Bellevue drillcore included spectra for: (1) V-rich inclusions; (2) L-V/S inclusions; (3) L-V-S and (4) L_1-L_2-V.

All of the Raman results from the Bellevue core samples confirm the presence of quartz as the host mineral (Figure 5.1 and Appendix2.1). The analyses also confirm the presence of methane (CH_4), H_2O and carbon dioxide (CO_2) in the gaseous phases of the fluid inclusions (Table 5.2; Figure 5.2-5.4). Strong primary CH_4 peaks occur at 2913-2918 cm^{-1} (Figure 5.2), with some of the samples exhibiting variations in absorbance, as demonstrated in Appendix2.1. Strong CO_2 bands of various intensities are observed at between 1285 and 1385 cm^{-1} (Figure 5.3), mostly associated with two smaller bands at 1235 cm^{-1} and 1411 cm^{-1}. Strong H_2O bands occur within the ranges of 3000-3600 cm^{-1}(Figure 5.4) H_2O was the most abundant gas in these samples, followed by CO_2, and CH_4 with is the least abundant. No carbonic (CH_4 and CO_2) peaks were observed in sample BV-1454.35 and only one carbonic (CO_2) peaks was detected in sample BV-1413.80 out of 18 fluid inclusions investigated. Remnants of graphite peaks can be positively identified (Figure 5.5) in sample BV-417.90 circle 3, BV-910.10 circle 1 (Appendix 2.1).

Calcite was positively identified in samples BV-417.90 P3, BV-1046.50 P1, BV-83.69 P1, BV-893.90(2) P2, BV-106.90 P1, BV-352.60 P4 and BV-893.90 P1 (Figure 5.6 and Appendix 2.1). They have Raman spectra that are characterised by the following primary bands: 156 cm^{-1}, 284cm^{-1}, 711cm^{-1}, 1085 cm^{-1} and 1435 cm^{-1} (http://www.dst.unisi.it/geofluids/raman/spectrum_frame.htm; Frezzotti *et al*., 2012). Calcite was identified within some of the solids of the fluid inclusion.

The various types of gases detected in the samples from the Bellevue drillcore occur as either pure phases or exist in combinations. Raman microanalysis confirms the presence of CO_2 as a pure gas (e.g. BV106.90 and BV-1413.80), coexisting with either CH_4 or H_2O in varying proportions (e.g. BV-893.90, BV-417.90 and BV-83.81) (see Table 5.2). Similarly, CH_4 can exist as a pure gas in the gaseous phase or coexist with other gases such as CO_2 and H_2O. H_2O also exist as both a pure gas (BV-1454.35) and in combination with other gases (BV-83.69), with varying proportions (Appendix 2.1).

A large number of the carbonic (CO_2 and CH_4) fluid inclusions are part of the primary fluid inclusion assemblage (n=33), with a few from the secondary fluid inclusion assemblage (N =15) (see Appendix 2.1). No carbonic inclusions were identified in the psuedosecondary fluid inclusion assemblage. H_2O bands were observed in all three fluid inclusion assemblages (e.g. primary, pseuosecondary and secondary).

The proportion of X CH_4 ($\frac{X\ CH_4}{X\ CH_4 + X\ CO_2}$)gas in the carbonic-rich fluid inclusions ranges from 0.00 to 1.00 ±. There are two population groups of the proportions of X CH_4 gas for the carbonic-rich fluid inclusions. The first population group comprises carbonic-rich fluid inclusions with X CH_4 ranging from 0.00 to 0.05 ± (Figure 5.7). The second population group comprises aqueous fluid inclusions that have X CH_4 ranging from 0.95 to 1.00 ± (Figure 5.7). The first grouping has the largest number of aqueous fluid inclusions (N= 12). The values of X CH_4 gas in the vapour phase of primary fluid inclusion assemblage, with more than one-phase at room temperature, ranges from 0.00 to 1.00, whereas in the secondary fluid inclusion assemblage it ranges from 0.583 to 0.975 (see Appendix 2.1). The X CO_2 gas in the vapour phase, of primary fluid inclusion assemblage, with more than one-phase at room temperature, ranges from 0.00 to 1.00, whereas in the secondary fluid inclusion assemblage it ranges from 0.0254 to 0.2642 (see Appendix 2.1).

Table 5.2: Raman absorbance for gaseous phases of selected fluid inclusions from the late magmatic quartz, Bellevue drillcore from the Northern limb, Bushveld Igneous Complex.

Raman Absorbance- Gaseous phase

			1286 cm-1	**1385 cm-1**	**2913 cm-1**	**3200-3600 cm-1**
Sample	**Inclusion number/ Characteristics**	**FIA**	**CO_2**	**CO_2**	**CH_4**	**H_2O**
BV-417.90(2) Circle 4Grain 4	FI1_fi Dark-vapour-phase (1phase)	Isolated vap inclusions	2023,41	2955,53	-	-
BV-1046.50 Circle 1	Irregular Dark one-phase FLINC	Trail of Fluid inclusions	712434	784736	-	-
BV-1046.50 Circle 4	Dark-one phase FLINC_A3	Trail of Fluid inclusions	-	-	1783,1	-
BV-1046.50 Circle	Dark-one phase FLINC_A1	Trail of Fluid inclusions	1798,99	2028,1	52105,7	-
BV-417.90(2) Circle 3Grain 4	FI1fi vapour (bubble)-phase (3phase, dark)	Cluster of fluid inclusions	1995,76	3700,81	278,274	-
BV-1413.80 (1) Circle 1	Three-phase flinc (1) _vapor-phase	Cluster of FLINCS	-	-	-	Strong
BV-352.60 Circle 4	Fl1 large Vapour-phase (2-phase)	Trail of Fluid inclusions	273,125	457,955	19410,3	-
BV.83.81Circle 1 Trail Edge	Dark FLINC (Vapour-phase) _2-phase	Cluster of fluid inclusions	179428	145189	90729,5	-
BV-83.81 Circle 3	Multiple-phase FLINC (Bubble-phase)	Cluster of fluid inclusions	1738,95	658165	-	-
BV-106.90 Circle 2	Vapor-rich_2-phase FLINC (Vapor-phase) (2-phase)	Trail of Fluid inclusions	-	-	2301,59	-
BV-83.69 Circle 2	Light, two-phase FLINC (1) Vapor-phase	Cluster of FLINCS	308,49	323,976	-	Strong
BV-83.69 Circle 2 Light	CUBIC, two-phase FLINC (5) _Vapor-phase	Trail of FLINCS	-	-	-	Strong

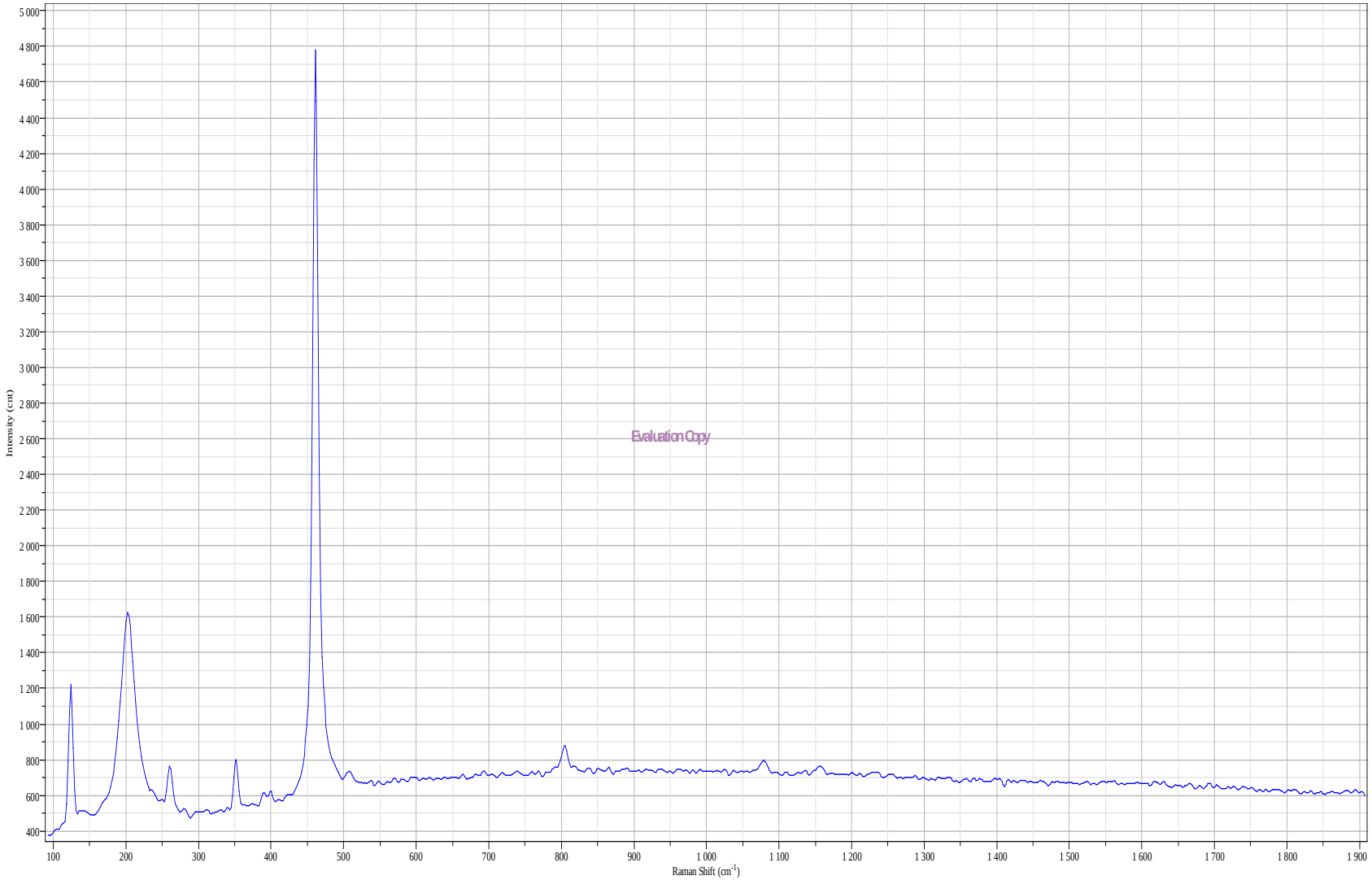

Figure 5.1 : Raman Spectrum for a fluid inclusion exhibiting the composition of quartz, which is the host mineral from BV-893.90(2) Circle 1.

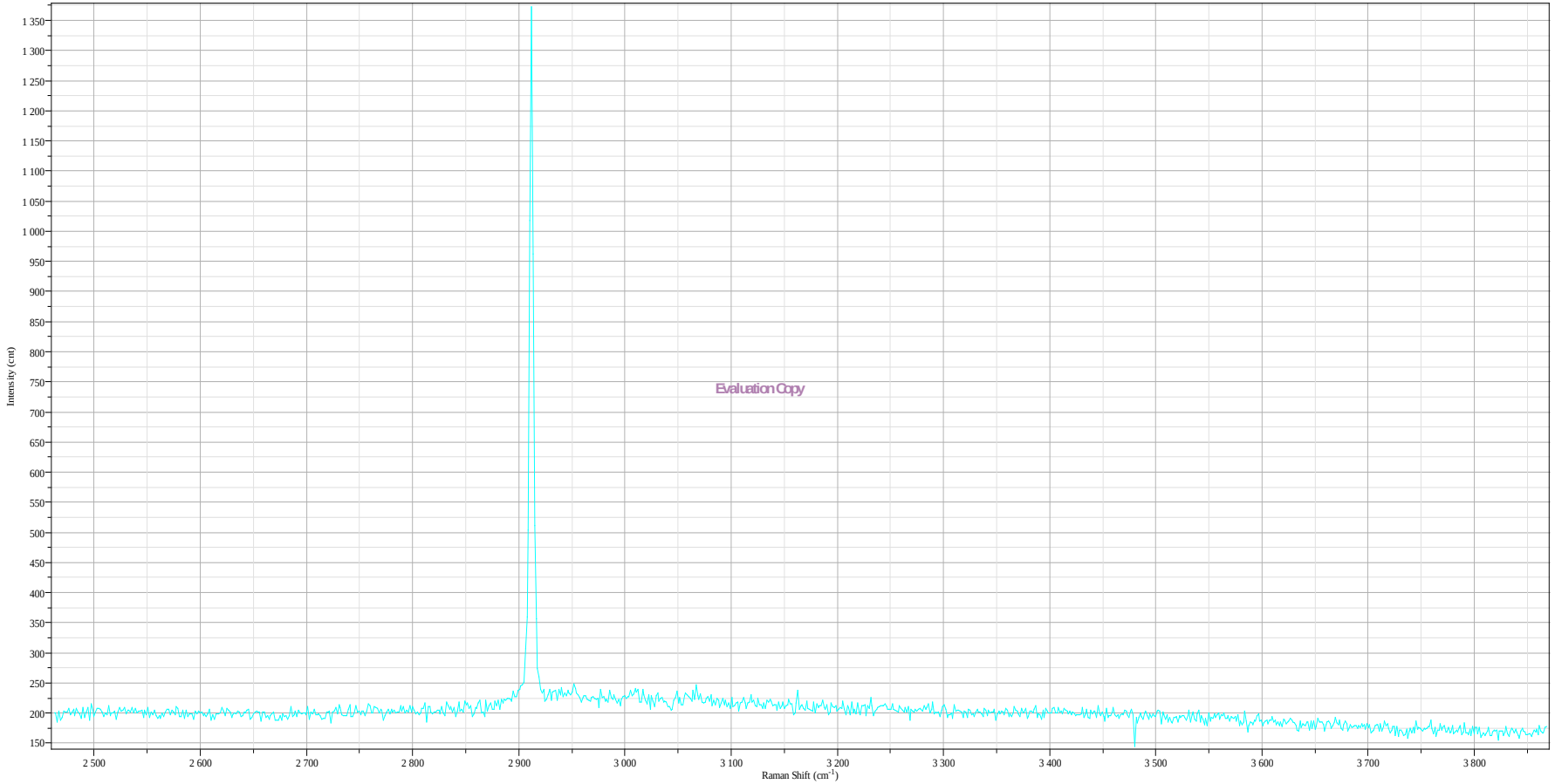

Figure 5.2 : Raman Spectrum for fluid inclusion exhibiting the composition of CH_4 from sample BV-352.60.

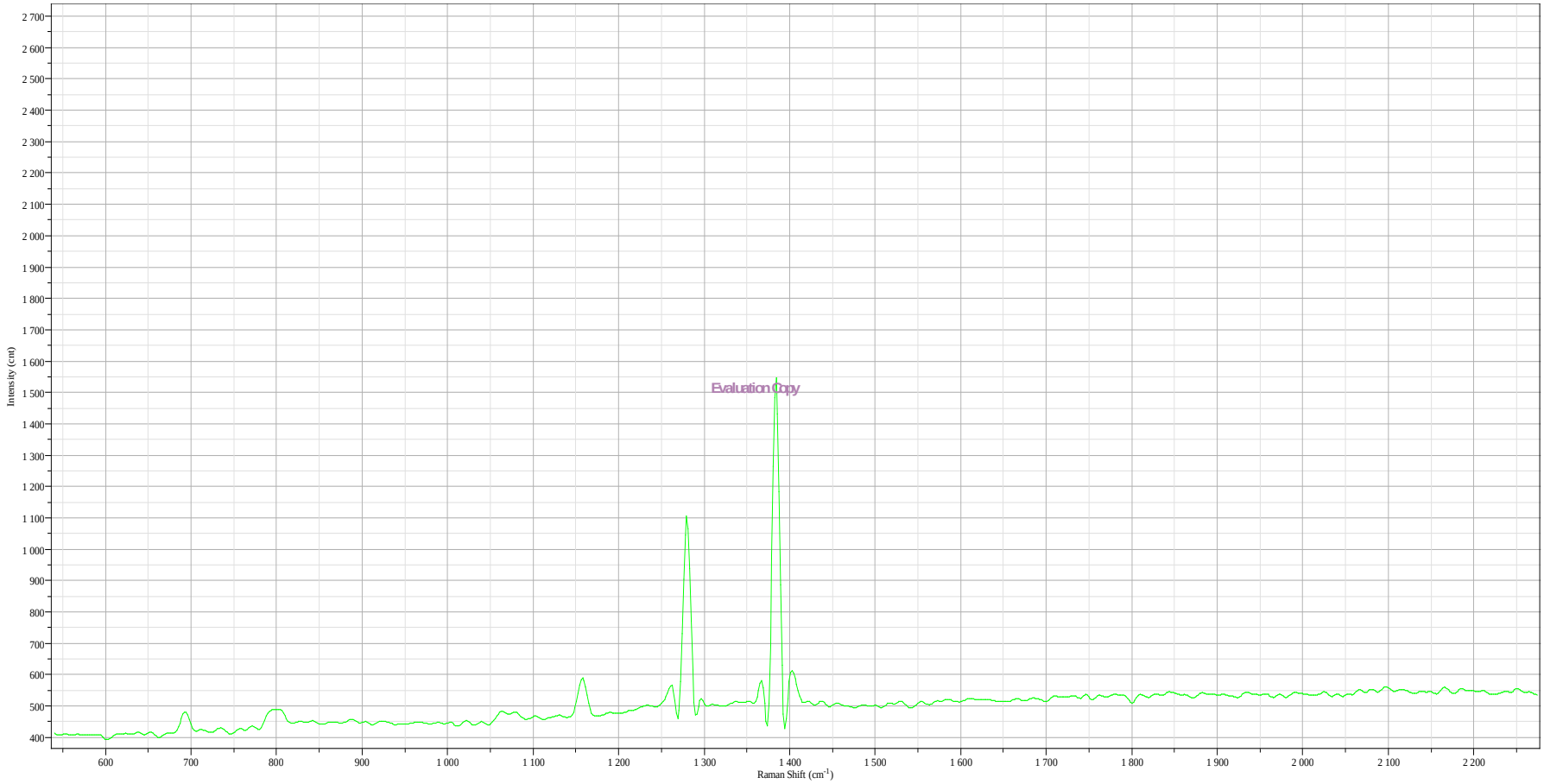

Figure 5.3 : Raman Spectrum for a fluid inclusion exhibiting the composition of CO_2 from sample BV-1046.50.

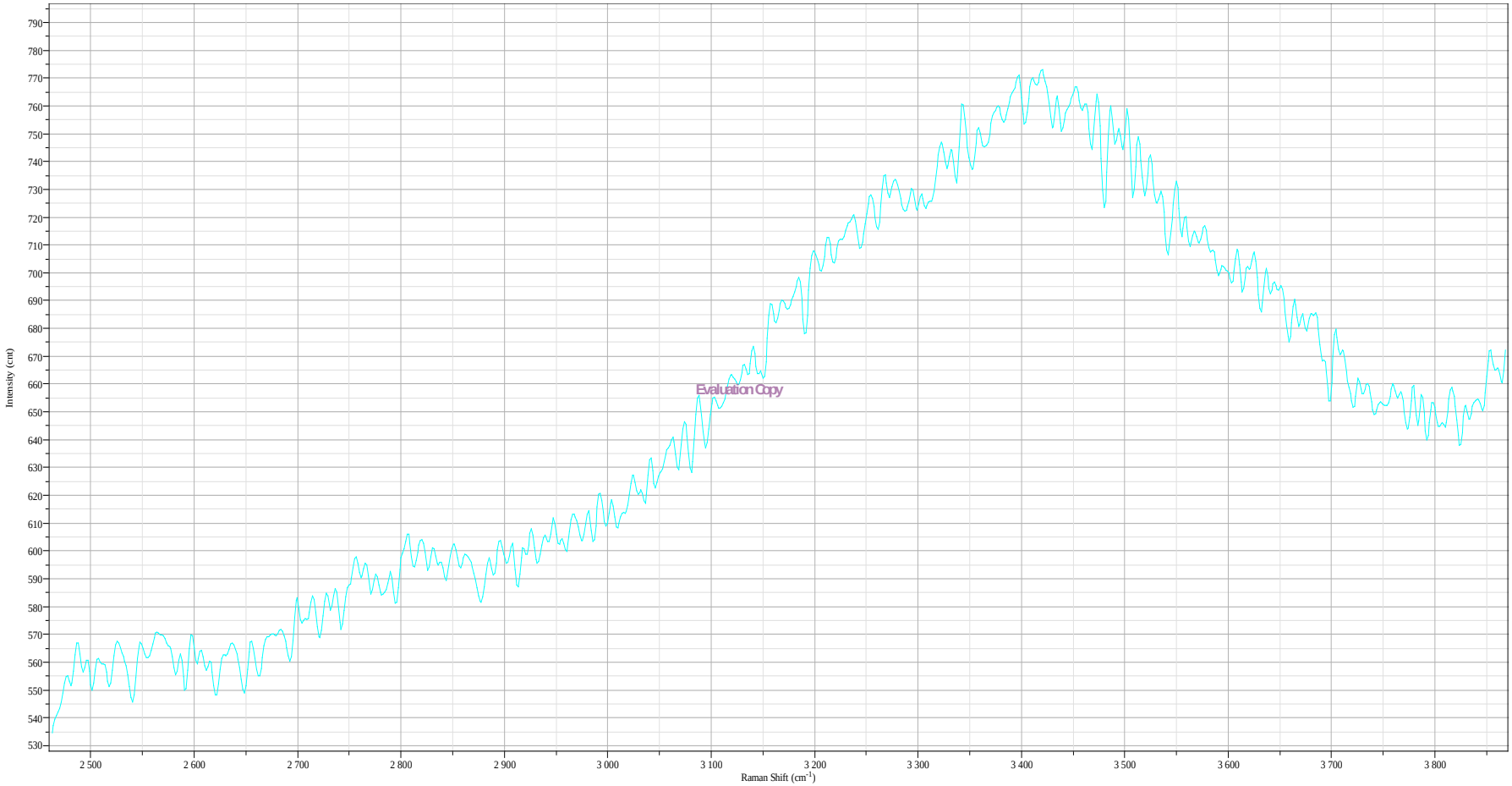

Figure 5.4 : Raman Spectrum for a fluid inclusion exhibiting the composition of H_2O from sample BV-1046.50.

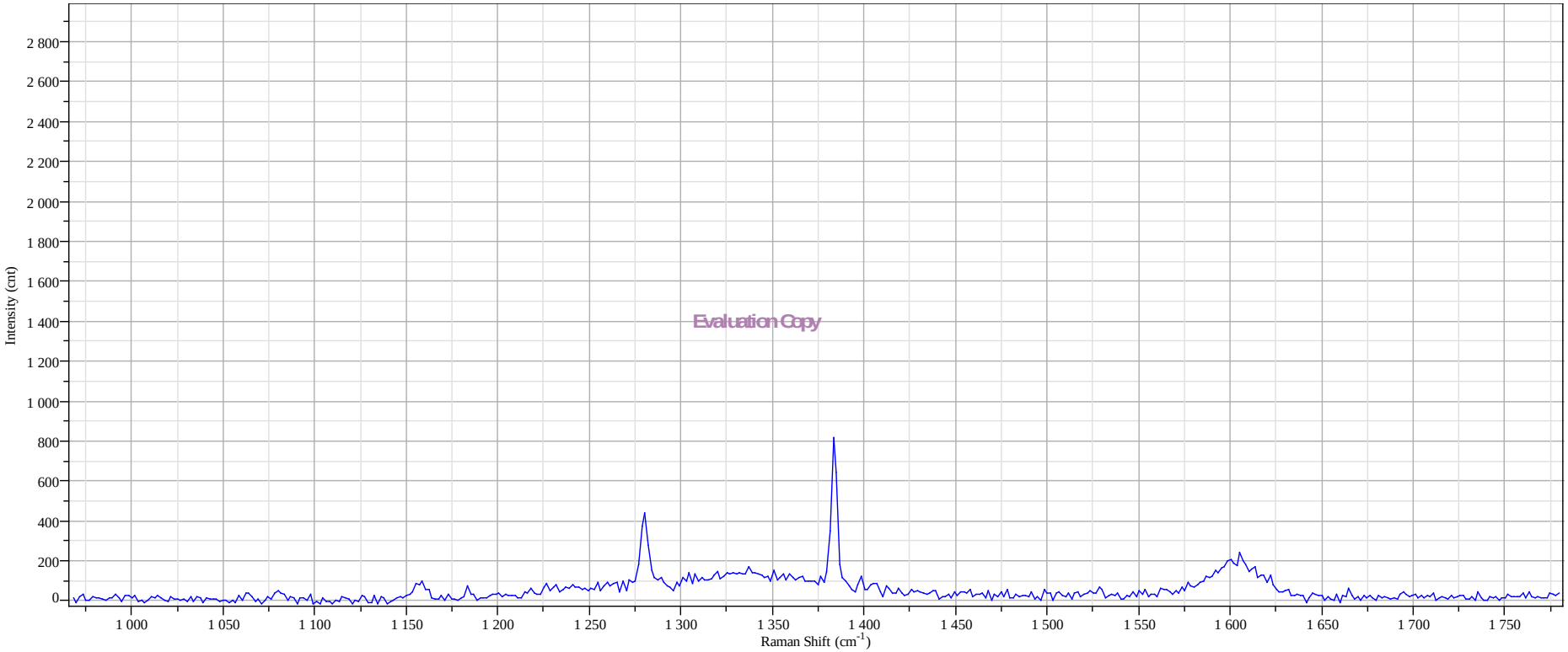

Figure 5.5 : Raman Spectrum for a fluid inclusion exhibiting the composition of graphite from sample BV-417.90 circle 1.

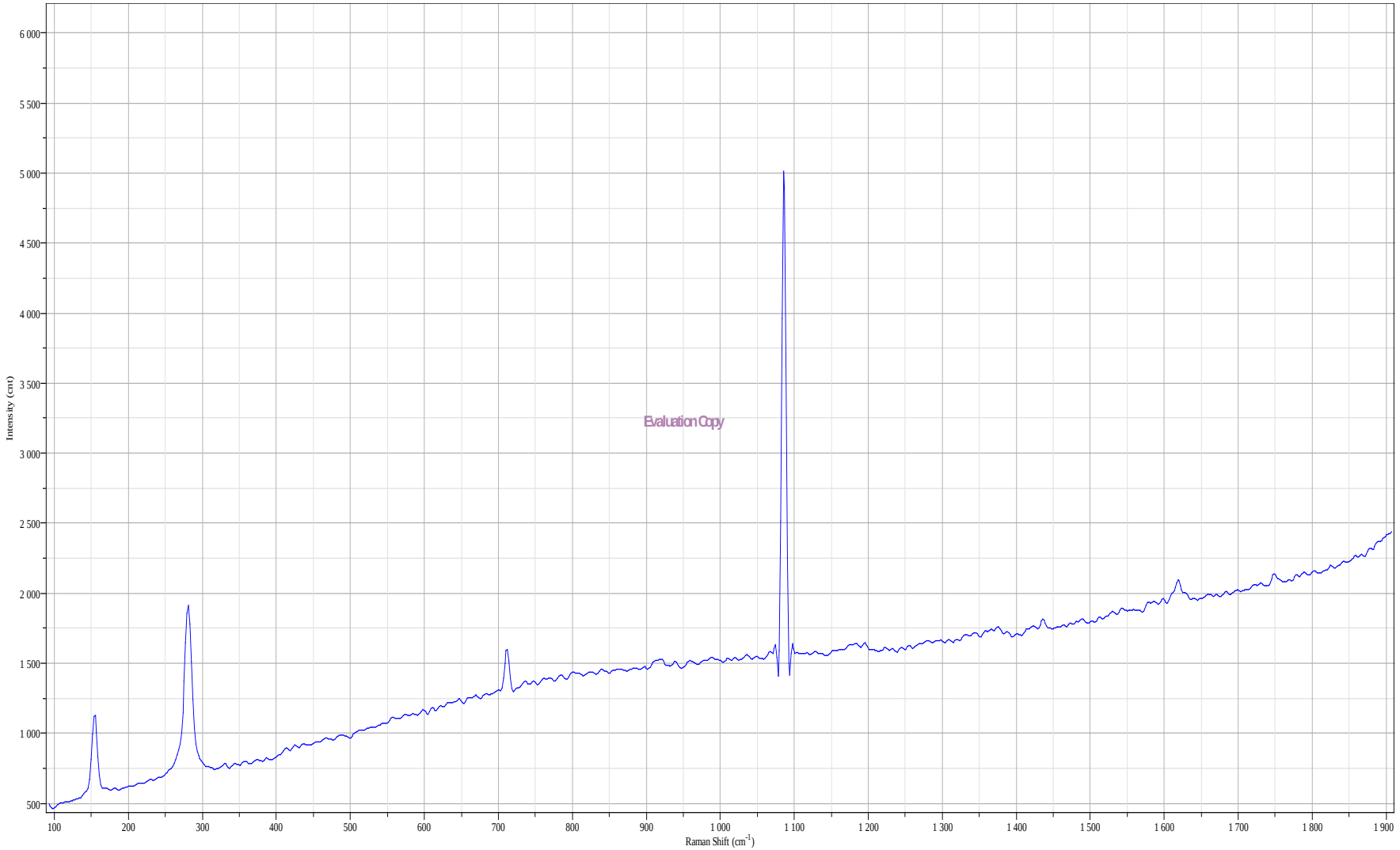

Figure 5.6 : Raman Spectrum for a fluid inclusion exhibiting the composition of calcite daughter crystals from sample BV-893.90 Circle A.

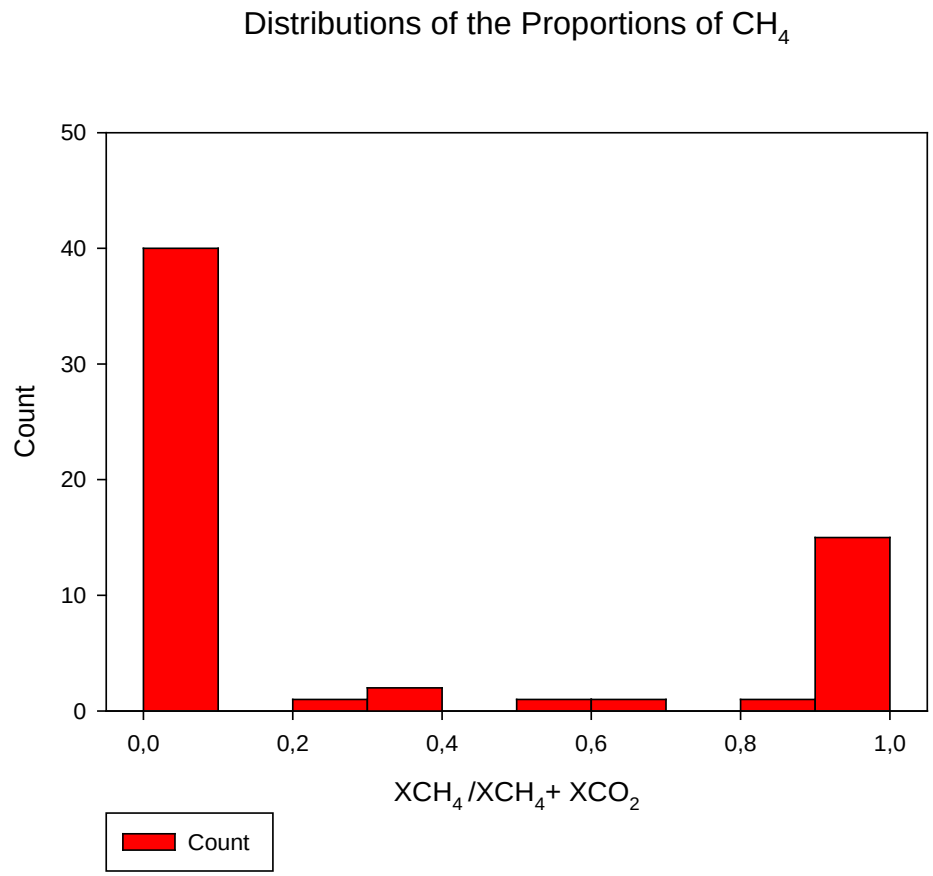

Figure 5.7: Distribution of the proportions (X) of CH_4 ($\frac{X\,CH_4}{X\,CH_4 + X\,CO_2}$) in mafic rocks of the Bellevue drillcore.

5.1.2 Stoffberg Area

A total number of 28 Raman analysis points was acquired on 28 fluid inclusions representative of the various types of inclusions in the samples from the Stoffberg area. These include: one-phase fluid inclusions; (2) two-phase– liquid phase plus either vapour phase or solid phase –fluid inclusions; (3) three phase – liquid phase, vapour phase and solid phase– fluid inclusions.

All of the Raman microanalysis results from the Stoffberg samples confirm the presence of quartz as the host mineral (Figure 5.8 and Appendix2.2). The analyses also confirmed the presence of H_2O that exists in gaseous phases in the analysed fluid inclusions as suggested by strong bands of water in Figure 5.9 and Table 5.3. Except for two primary fluid inclusions in sample RGC-12 P2 FL1 and sample RGC-12 P3 FL1 with a strong primary CH_4 peak that

occurs at 2913-2918 cm^{-1}, respectively (see Table 5.2 and Figure 5.10), most of the fluid inclusions are characterized by strong H_2O bands that occur within the ranges of 3200-3600 cm^{-1} (Figure 5.9). The CH_4 peak of sample RGC-12 P3 FL1, which is a one-phase inclusion at room temperature, has a strong intensity (24083,5 peak area) as compared to that of sample RGC-12 P2 FL1, which is two-phase inclusion at room temperature (1222,26 peak area). The H_2O bands can be identified in all the various types of fluid inclusion assemblages. The CH_4 peak in sample RGC-12 P3 FL1 occurs as pure gas, whereas in sample RGC-12 P2 FL1 the CH_4 coexists with H_2O.

Table 5.3: Laser Raman absorbance for gaseous phases of selected fluid inclusions from both the triangular, patches of quartz and from the quartz intergrown with feldspars, from the Stoffberg area, from the Eastern limb, Bushveld Igneous Complex.

Raman Absorbance- Gaseous phase

			1286 cm-1	**1385 cm-1**	**2913 cm-1**	**3200-3600 cm-1**
Sample	**Inclusion number/ Characteristics**	**FIA**	**CO_2**	**CO_2**	**CH_4**	**H_2O**
RGC-24 P1 Fl2	Dark, one-phase - vapour-phase (1phase), with signal of Alkaline feldspars	Isolated vap inclusions	-	-	-	Medium
RGC-22 P3 Fl2	Dark, one-phase - vapour-phase (1phase	Isolated vap inclusions	-	-	-	Strong
RGC-12 P3 FL1	Dark-one phase, CH4	Cluster of FLINCS	-	-	24083,5	-
RGC-12 P2 FL1	2phase (Liquid + Vapor), H2O, CH4	Cluster of FLINCS	-	-	1222,26	Strong
RGC-20 P3 Fl2	Two-phase Flinc (Liquid +Vapor)	Cluster of FLINCS	-	-	-	Strong
RGC-16 P1 Fl2	Two-phase Flinc (Liquid + Vapor)	Trail of FLINCS	-	-	-	Strong
RGC-22 P1 FI1	3phase (Liquid + Vapour + Halite),	Cluster of FLINCS	-	-	-	Strong
RGC-12 P2 FL2	3phase (Liquid + Vapor + Calcite)	Cluster of FLINCS	-	-	-	Strong
RGC-24 P1 FI4	3phase (Liquid + Vapour + Halite),	Trail of FLINCS	-	-	-	Strong

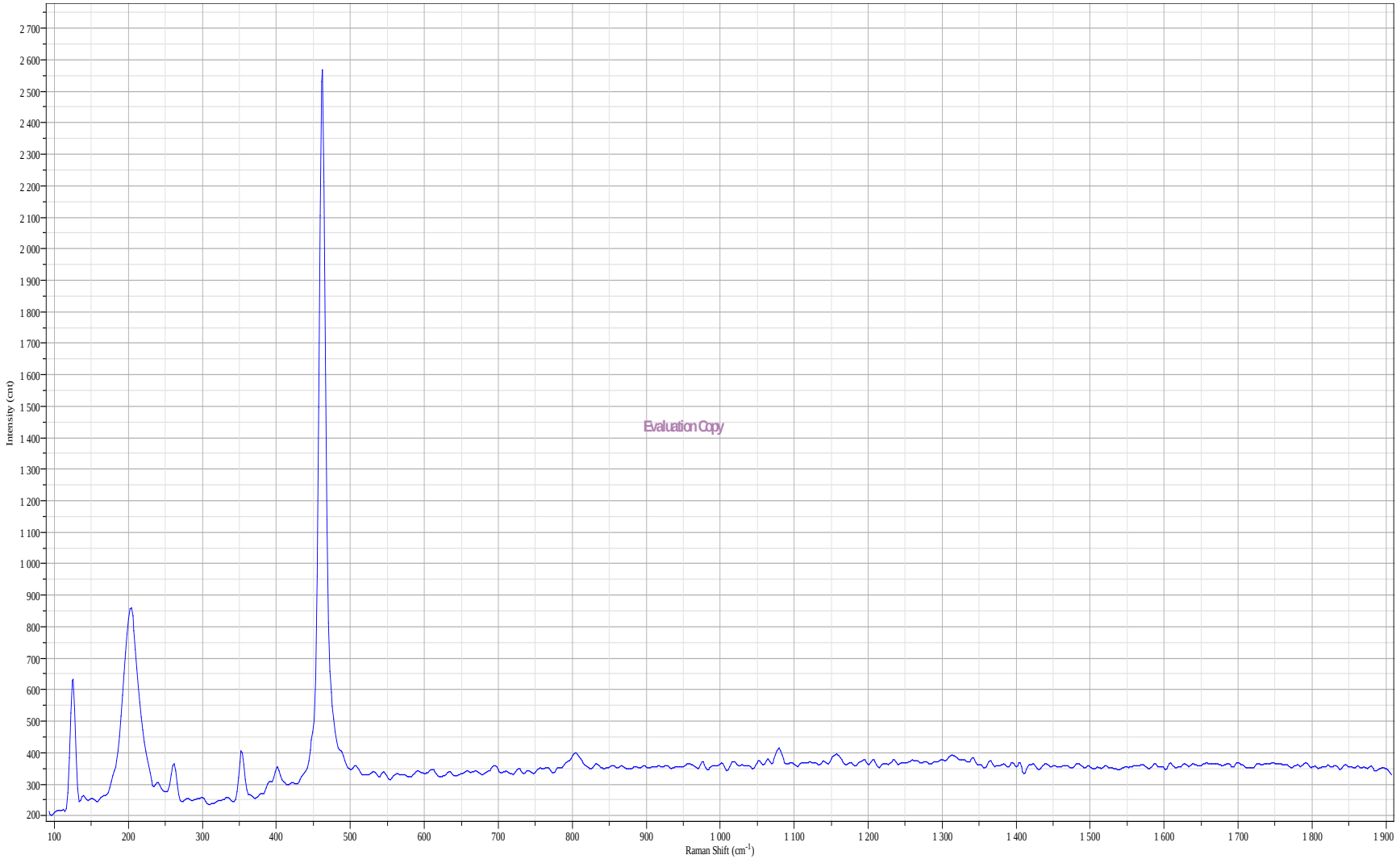

Figure 5.8: Raman Spectrum for fluid inclusion exhibiting the composition of the host mineral quartz from sample RGC-24 P1.

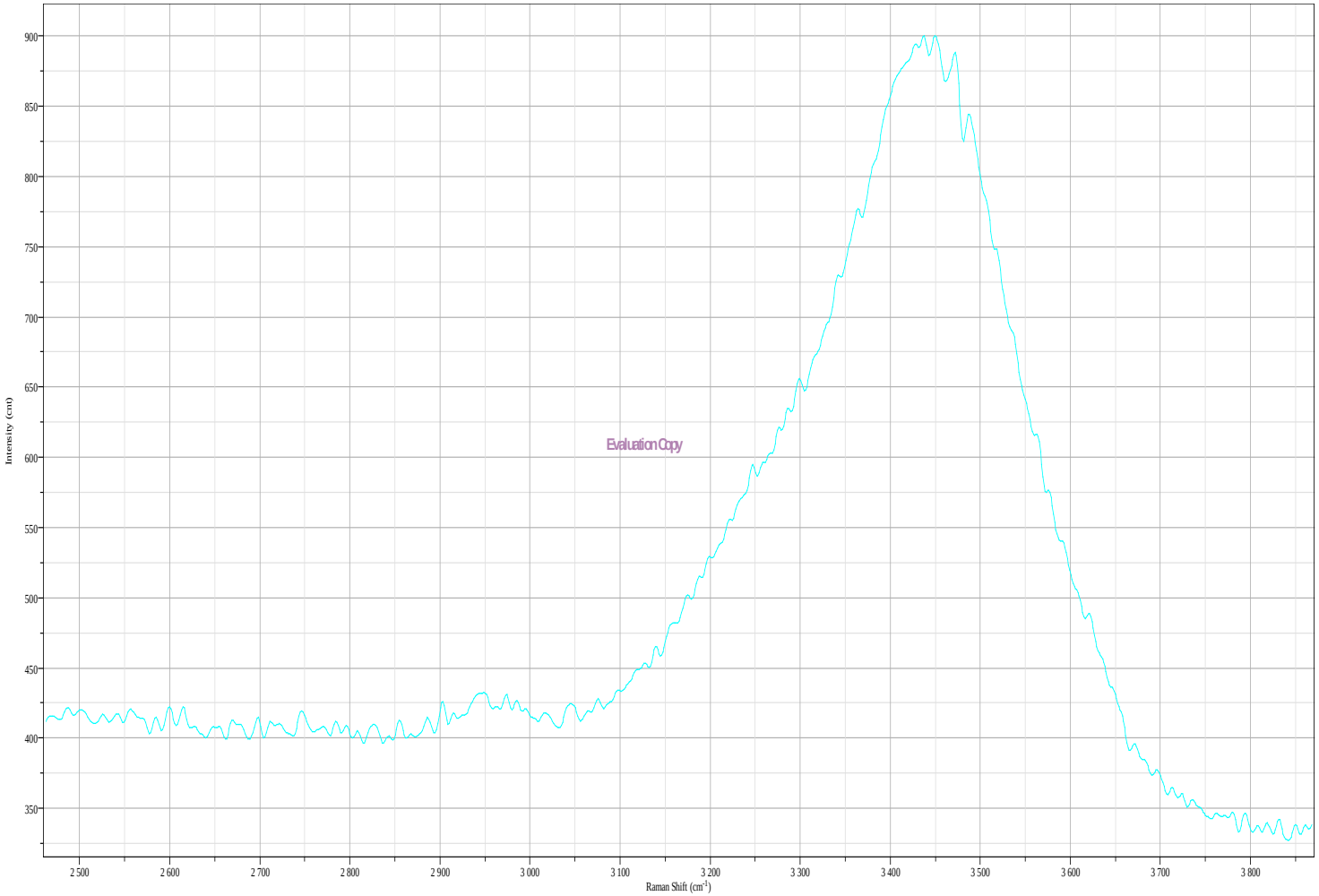

Figure 5.9: Raman Spectrum for fluid inclusion exhibiting the composition of H_2O from sample RGC-12 P4.

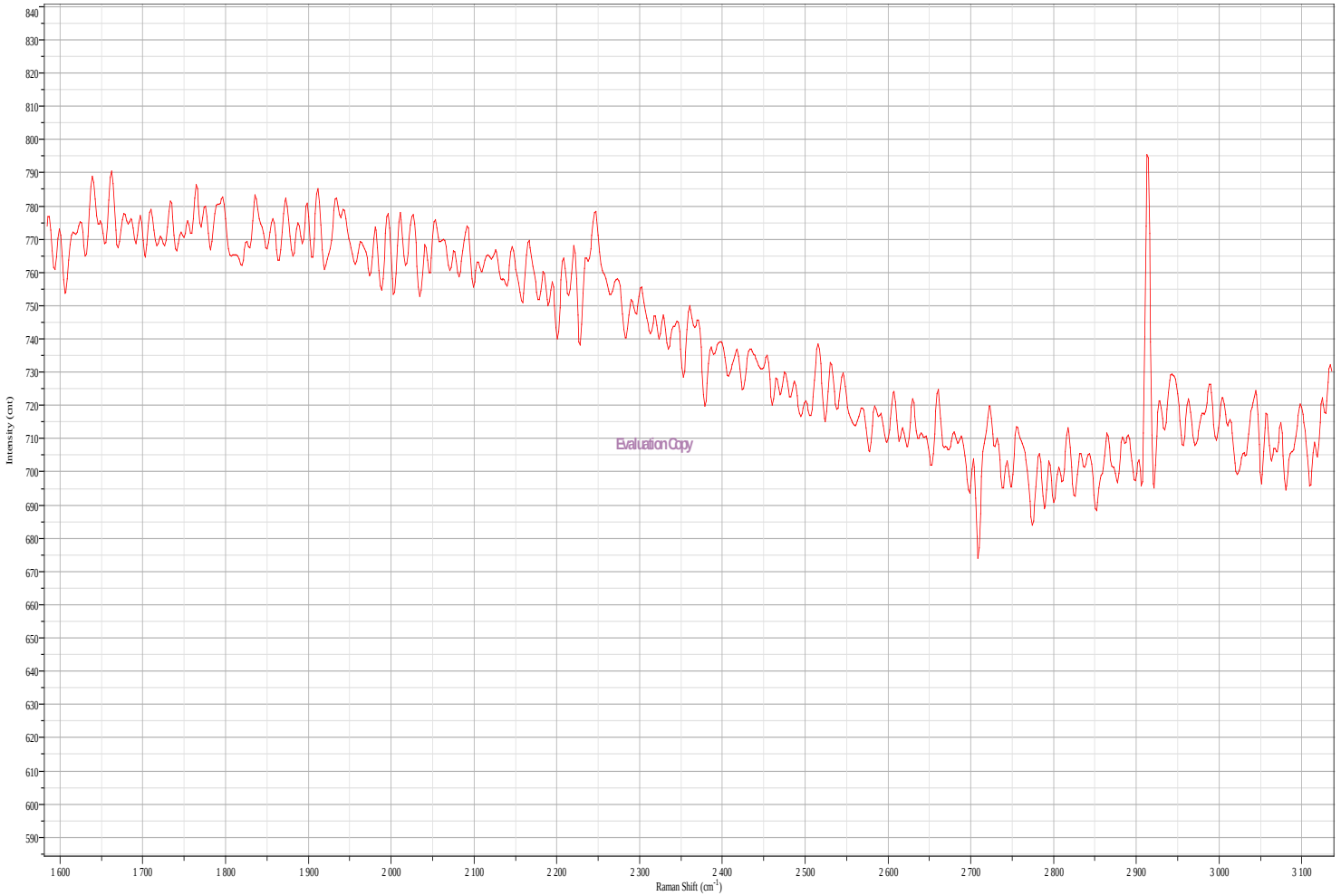

Figure 5.10: Raman Spectrum for fluid inclusion exhibiting the composition of CH_4 from sample RGC-12 P2.

5.2 Summary of the Raman Microprobe Results

Raman microanalysis from the Bellevue core samples confirms the presence of CH_4, H_2O and CO_2 that exist in gaseous phases in the analysed fluid inclusions (Figure 5.2-5.4; Table 4.1; Appendix2.1), and they exist in various forms from simple (pure gases) to complex systems (coexisting gases). Most of the carbonic fluid inclusions (n=33) were identified as part of the primary fluid inclusion assemblage, with a few being part of the secondary fluid inclusion assemblage (n=15). No pure CH_4 gas was observed in the secondary fluid inclusion assemblage of the Bellevue core samples. However, in secondary inclusions, CH_4 coexists with either CO_2 or H_2O, whereas in the primary fluid inclusion assemblage CH_4 can exist as both a pure gas and in combination with other gases such as CO_2 and H_2O in varying proportions. Most of the H_2O bands from the Bellevue drillcore are broader (3000-3600 cm^{-1}) and flat as compared to those of the Stoffberg samples which are more sharp and higher in intensity (3200-3600 cm^{-1}).

Except for sample RGC-12 P2 FL1 and RGC-12 P3 FL1, which detected a trace amount of CH_4, most of the fluid inclusions from the samples are characterized by the presence of H_2O as the existing gaseous phase. No CH_4 inclusions were identified from the secondary fluid inclusion assemblage in the Stoffberg samples. Only one pure CH_4 gas phase was identified in the primary fluid inclusion assemblage. The other CH_4 gas exists in combination with H_2O in the primary fluid inclusion assemblage.

CHAPTER 6

6.1 Fluid inclusion microthermometry

This chapter presents the results of a detailed fluid inclusion study of the late stages of the Bushveld Igneous Complex. Schiffries (1984, 1985) undertook the first microthermometric measurements on quartz from the Upper Critical zone to establish a wide variety of CO_2-rich, CH_4-rich, and aqueous fluid inclusions. Ballhaus and Stumpfl (1986) supplemented these findings with estimates for the maximum trapping temperatures and pressures during the crystallization of the Merensky Reef, and to establish their relevance to platinum and sulphide mineralization in the BIC. Schiffries (1990) used microthermometric data to identify a new class of aqueous fluid inclusions rich in $CaC1_2$, displaying a rich variety of unusual phase equilibria. Zhitova *et al*. (2007; 2009; 2016) recently used fluid inclusion data from a number quartz samples from the Merensky Reef to constrain the evolution trend of magmatogene fluids of the intercumulus crystallization stage.

The aim of this investigation is to describe fluid inclusions associated with late stage magmatic quartz and possibly post-magmatic quartz in the Upper Zone, Bushveld Igneous Complex. These data will be used to evaluate the evolution of magmatic and possibly hydrothermal fluids involved in the crystallization of the BIC.

Freezing-melting and heating runs were performed on the calibrated Linkam 6500 stage. All measurements were duplicated within acceptable limits, differences of less than 1˚C for carbon dioxide homogenization (T_HCO_2), less than 5˚C for water homogenization (T_HH_2O), and less than 0.3˚C for the melting temperatures (T_mH_2O). In the case of multiple-phase inclusions (H_2O-NaCl-CO_2), the temperatures of first ($T_{mice}H_2O$) and final (T_mH_2O) melting of the aqueous phase, final melting of the solid CO_2 (T_mCO_2), dissolution of clathrate (T_mCLATH)

and homogenization temperatures of the CO_2 and aqueous (T_HCO_2 and T_HH_2O), were recorded (Figure 6.1-6.7). In the case of two-phase aqueous inclusions (L+V), the temperatures of first melting (T_{mice}), final melting (T_m) and homogenization (T_H) were recorded. Where definite clathrate was observed, T_mCLATH could also be recorded (Figure 6.1, 6.3 and 6.5).

These data were applied to the interactive programs of Steele-MacInnis *et al*., (2012) to determine fluid densities and compositions. Salinities for halite-undersaturated and halite-saturated fluid are expressed in equivalent weight percent NaCl (equiv. Wt% NaCl). For the programme to produce credible data, the following input data is required: (1) measured final melting temperature for both saturated and undersaturated-halite fluid inclusions, (2) measured final homogenization temperature into either a liquid or vapour-phase (Appendix 3.1.1 and 3.1.2).

The isochores and densities for H_2O-NaCl inclusions, and inclusions that contain enough CO_2 to form clathrates but with insufficient CO_2 to form a separate phase of CO_2, were determined using HALWAT program. The data required by the program include: the final melting temperature (Tm) and homogenization temperature, wherether a clathrate occurs, the name of the liquidus solids (NaCl or ice). The salinity is estimated from the function of the melting temperature of ice (Potter *et al*., 1978), the dissolution of halite, or the temperature of the clathrate (Chen, 1972; Bozzo *et al*., 1975), depending on which phase was designated on input.

Table 6.1: Summary of preliminary fluid inclusion data from the Bellevue drillcore, Upper Zone rocks of the Bushveld Igneous Complex

Sample inclusion type	Thermometric properties	Fluid inclusion systems	Density	Salinity (wt % NaCl eq.)
Within **Olivine ferrodiorite:** Dominantly H_2O L + V (2A & 2B), some mixed H_2O-CO_2 L+V and minor CO_2 (Type 4) primary and secondary minor H_2O L+V Some minor H_2O L+V+S (Type 2C)	T_{fm} = -24.7 to -19.9˚C; mean =- 23˚C $T_{fm}CO_2$= -59.7 to -56.8˚C; mean= -58˚C T_mCLATH= -0.9 to +12˚C; mean = +6˚C T_{H1}= +123 - 168˚C; peak =168˚C T_{H2}= +282 - 327˚C; peak =304.5 & 327˚C $T_{TH}H_2O$-CO_2= +3 - 30.8˚C; Major decrepitation between 236 and 259˚C	H_2O-CO_2-NaCl-KCl	0.54-0.98 (mean= 0.74)	9.23
Within **Quartz anorthosite**: Dominantly H_2O L + V primary and secondary fluid inclusions (2A & 2B); H_2O-CO_2 L+V also present (Type 4) Some minor H_2O L+V+S (Type 3A and 3B)	T_{fm} = -49.1 to -19.2˚C; mean = -38.1˚C T_m = - 11.4 to -0.4˚C; mean = -3.9˚C; T_mCLATH= -0.7 to +12˚C; mean = +4.7˚C; T_{H1}= +124.5 – 198.2˚C; peak =˚C T_{H2}= +222.7 – 271.2˚C; T_{H3}= +296 - 370˚C;	H_2O-CO_2-NaCl ± other cations (Ca and K)	0.35 - 0.65 (mean= 0.56)	6.01
Within **Anorthosite**: Dominantly H_2O L + V primary and secondary fluid inclusions (2A & 2B); H_2O-CO_2 L+V also present Some minor H_2O L+V+S (Type 3A and 3B)	T_{fm} = -25.3 to -16.6˚C; mean = -20.8˚C T_m = -11.2 to -2.1˚C; mean = - 6˚C; T_mCLATH= - 0.9 to +13˚C; mean = +3.5˚C; T_H= +89.5 – 286˚C; mean =182 ± 55˚C	H_2O-NaCl-CO_2	0.31─1.06 (mean= 0.84)	9.12
Within **Luecogabbronorite**: Dominantly H_2O L + V primary and secondary fluid inclusions; and minor CO_2 L+V also present	T_{fm} = -43.8 to -31.7˚C; mean = - 37.1 $T_{fm}CO_2$= -59.2 to -58.4˚C; mean= -58.8˚C T_mCLATH= -0.9 + 0.6˚C; mean = +0.15˚C T_{H1}= +280 – 305.9˚C; T_{H2}= +331.8 – 340.5˚C T_{H3} = +349.1 - 375˚C; Major decrepitation at 380˚C	H_2O-NaCl-$MgCl_2$±CO_2	0.66 – 0.79 (mean= 0.73)	6.22

6.2 Fluid inclusion microthermometry Bellevue drillcore

Olivine ferrodiorite is characterized by H_2O L + V (2A & 2B), with some mixed H_2O-CO_2 L+V and minor CO_2 (Type 4) primary and secondary minor H_2O L+V and possibly H_2O L+V+S (Type 2C). During the freezing run, the vapour phase appeared to dark and small, and the vapour phase became bigger and darker as the temperature increases. In some of the inclusions produce distinct CO_2-rich phase, which is represented by the dark thick vapour phase. Clathrate melting temperatures range from -0.9 to +12˚C (n=5; mean = + 6˚C), supporting the suggestion that some CO_2 is present in some of the fluid inclusions, yielding salinity with an average of 9.23 wt. % NaCl eq., for the fluid system that exhibits a density of 0.74 $g.cm^{-3}$. Eutectic melting temperatures range from -24.7 to -19.9˚C (n=21; mean =- 23˚C) (Figure 6.1), corresponding to the eutectic temperature of H2O-CO_2-NaCl-KCl (Shephard et al, 1985). The range in eutectic temperatures and the depression thereof suggests that salts other than NaCl i.e. KCl, $MgCl_2$ and $CaCl_2$, may also be present in the fluid system. Major decrepitation were observed between 236 and 259˚C in some of the fluid inclusions. In examining the heating behaviour two homogenization temperature T_{H1}= +123 - 168˚C; peak =168˚C T_{H2}= +282 - 327˚C; peak =304.5 and 327˚C for the H_2O L + V fluid inclusions, and $T_{TH}H_2O$-CO_2= +3 - 30.8˚C for the H_2O-CO_2 fluid inclusions (Table 6.1and Figure 6.2).

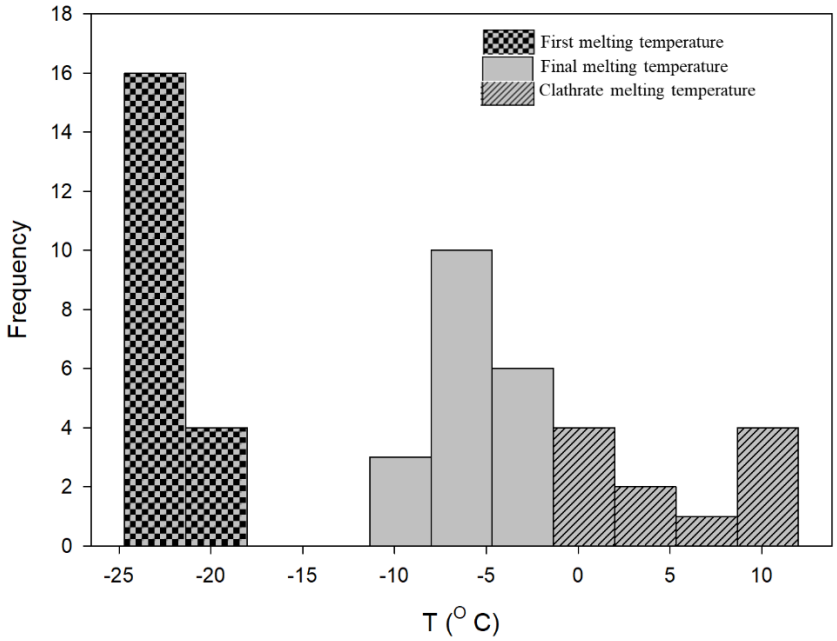

Figure 6.1: Histogram showing melting temperatures for inclusions from olivine ferrodiorite from the BV-01. These temperatures include: Tm ice (temperature of first melting (eutectic temperature)), T_m (H_2O Final temperature of melting), and T_mCLATH (Clathrate melting temperatures).

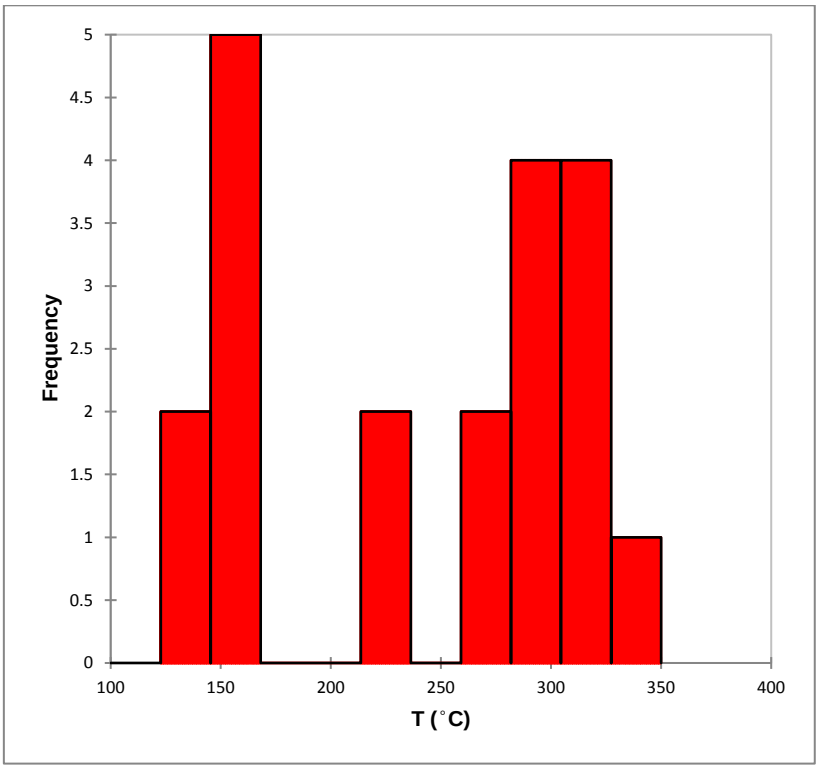

Figure 6.2: Histogram showing the temperature of homogenizations for inclusions from olivine ferrodiorite from the BV-01.

The quartz anorthosite are characterized by H_2O L + V (2A & 2B), H_2O-CO_2 L+V also present (Type 4) and some minor H_2O L+V+S (Type 3A and 3B). These fluid inclusions are typically

primary and secondary. Some of the fluid inclusions are characterized by metastable effects, which manifested during the heating cycles were some of the vapour bubbles reappeared smaller than prior to freezing.

The melting behaviour of the H_2O L + V (2A & 2B) inclusions has eutectic temperatures that range from -49.1 to -19.2˚C (mean = -38.1˚C), which corresponds to the fluid composition of eutectic temperature of H_2O-NaCl and some other cations (Ca and K) (Shephard et al, 1985) (Figure 6.3), with an average salinity of 6.01 wt.% NaCl eq. for all three homogenization temperatures (T_{H1}= +124.5 – 198.2˚C; T_{H2}= +222.7 – 271.2˚C; T_{H3}= +296 - 370˚C) (Figure 6.4). The bulk density for these fluid inclusions ranges from 0.35 to 0.65 g.cm^{-3}. Clathrate melting temperatures range from -0.7 to +12˚C (n=12; mean = + 4.7 C), supporting the suggestion that some CO_2 is present in some of the fluid inclusions. Although some of the fluid inclusions decrepitated between 236 and 259˚C, a minimum trapping temperature of 370˚C is suggested from T_{H3} of the H_2O L+V fluid inclusions (Table 6.1).

The fluid inclusions from the anorthosite ─ Dominantly H_2O L + V primary and secondary fluid inclusions (2A & 2B); H_2O-CO_2 L+V also present Some minor H_2O L+V+S (Type 3A and 3B) ─ samples are characteristic of fluid compositions within the binary H_2O-NaCl system (Tfm = -25.3 to -16.6˚C; mean = -20.8˚C), having salinity of 9.12 wt.% NaCl eq. (Tm = -11.2 to -2.1˚C; mean = - 6˚C) (Figure 6.5), and a density of 0.84 g.cm^{-3}. The homogenization temperature (T_H) of 286˚C provides an estimate of the minimum temperature at which these types of fluid inclusions were trapped (Table 6. and Figure 6.6).

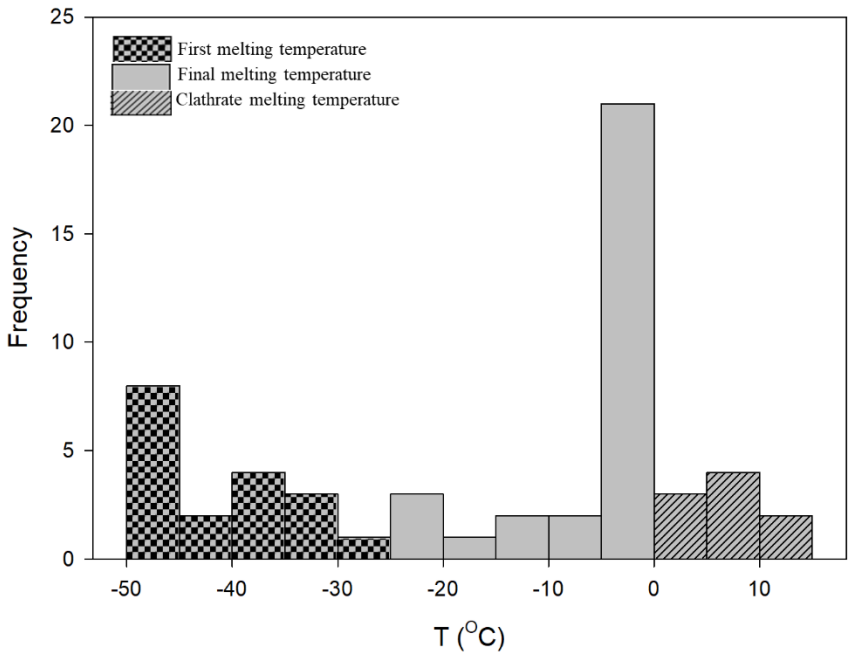

Figure 6.3: Histogram showing the melting temperatures for inclusions from quartz anorthosite from the BV-01. These temperatures include: Tm ice (temperature of first melting (eutectic temperature)), T_m (H_2O Final temperature of melting), and T_mCLATH (Clathrate melting temperatures).

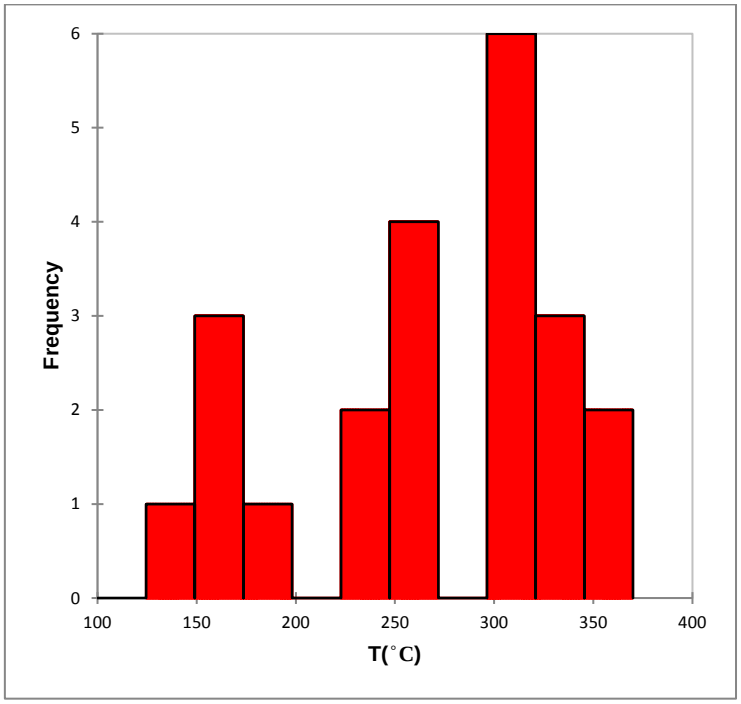

Figure 6.4: Histogram showing the temperature of homogenization for inclusions from quartz anorthosite from the BV-01.

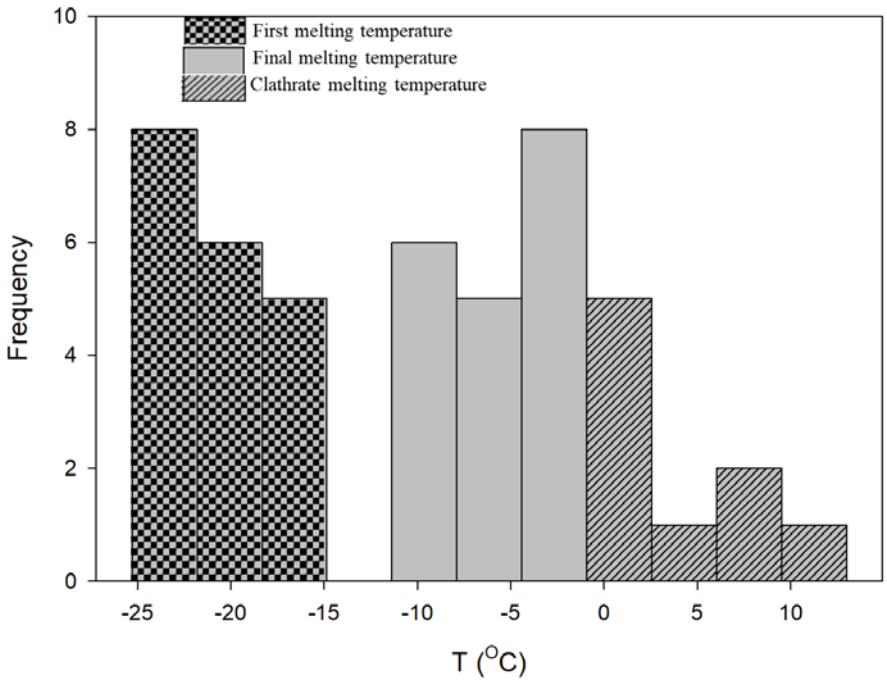

Figure 6.5: Histogram showing the melting temperatures for inclusions from anorthosite from the BV-01. These temperatures include: Tm ice (temperature of first melting (eutectic temperature)), T_m (H_2O Final temperature of melting), and T_mCLATH (Clathrate melting temperatures).

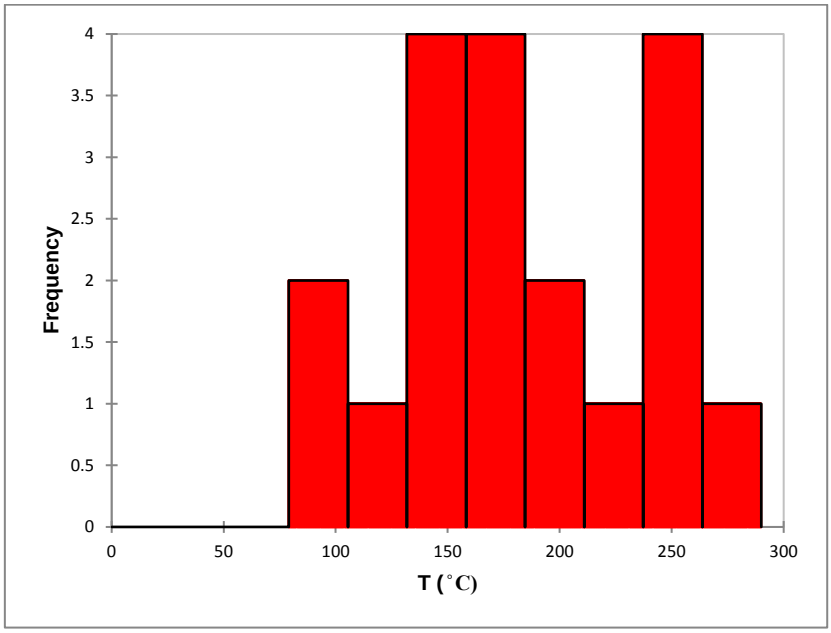

Figure 6.6: Histogram showing the temperature of homogenization for inclusions from anorthosite from the BV-01.

The leucogabbronorite are characterized by H_2O L + V primary and secondary fluid inclusions; and minor CO_2 L+V also present. The melting behaviour of the H_2O L + V (2A & 2B) inclusions has eutectic temperatures that range from -43.8 to -31.7˚C (mean = -37.1˚C), which

corresponds to the fluid composition of eutectic temperature of H_2O-NaCl-$MgCl_2$±CO_2 (Shephard et al, 1985) (Figure 6.7), with an average salinity of 6.2 wt.% NaCl eq. for all three homogenization temperatures T_{H1}= +280 – 305.9˚C; T_{H2}= +331.8 – 340.5˚C; T_{H3} = +349.1 - 375˚C and major decrepitation at 380˚C (Figure 6.8). The bulk density for these fluid inclusions ranges from 0.66 to 0.79 g.cm^{-3}. Clathrate melting temperatures range from -0.9 to +0.6˚C (n=2; mean = -0.15 °C), supporting the suggestion that some CO_2 is present in some of the fluid inclusions (Table 6.1).

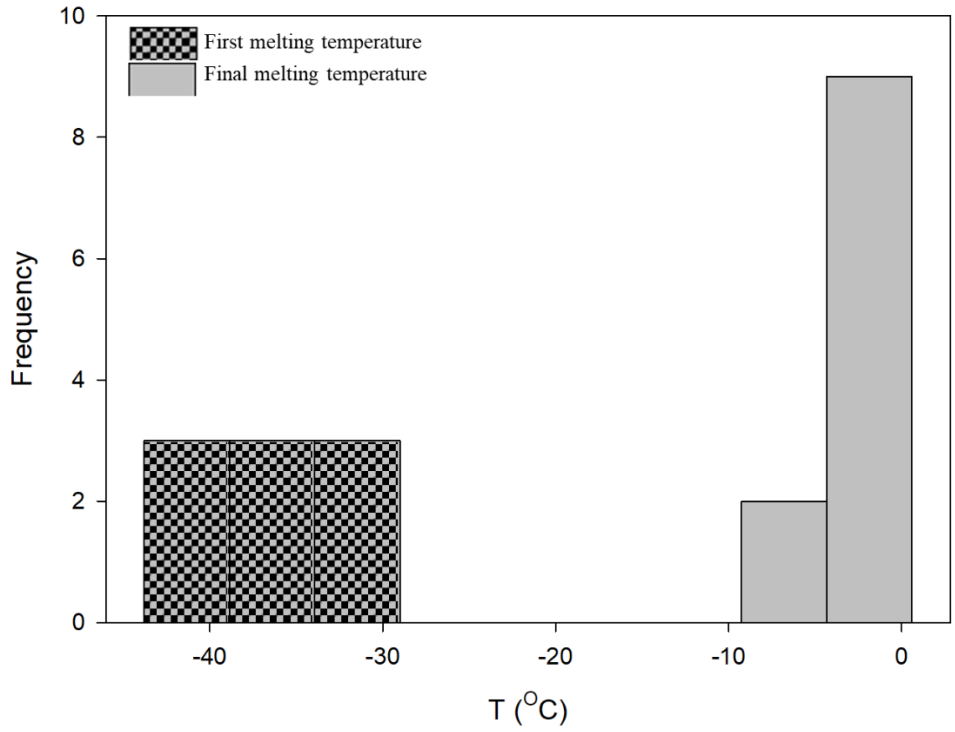

Figure 6.7: Histogram showing the melting temperatures for inclusions from anorthosite from the BV-01. These temperatures include: Tm ice (temperature of first melting (eutectic temperature)) and T_m (H_2O Final temperature of melting).

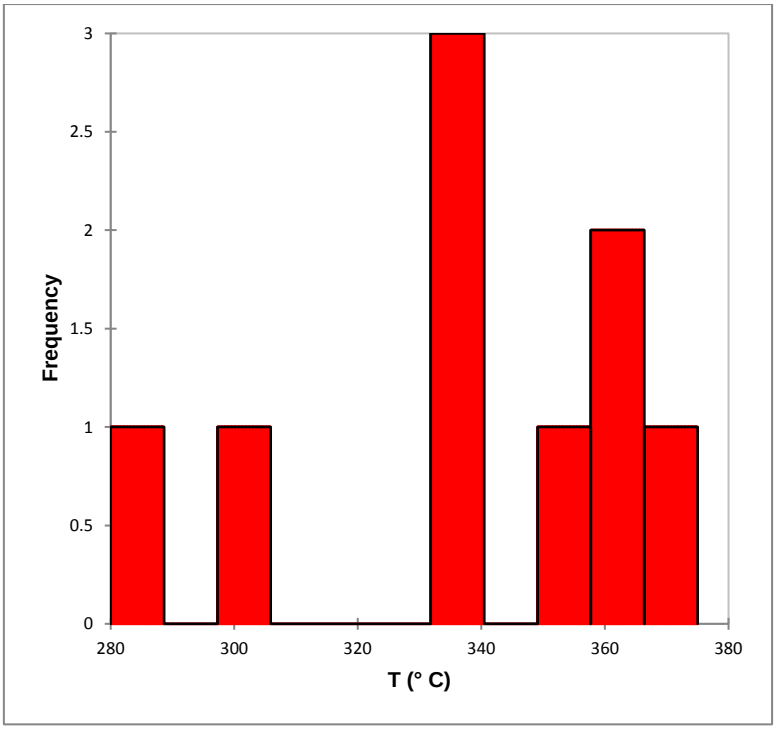

Figure 6.8: Histogram showing temperature of homogenization for inclusions from Leucogabbronorite from the BV-01.

Minimum temperatures of entrapment for the fluid inclusions are estimated from the homogenization temperatures. However, inclusions two fluids can provide better estimates provided the appropriate P-V-T-X data are available, for the two immiscible fluids, each saturated with respect to other, are present at the time of trapping (Roedder, 1984). The homogenization temperatures (T_H) isochores for the aqueous-rich fluid inclusions were generated using the algorithm as approximated (version 01/03) by the H_2O-NaCl-KCl-$CaCl_2$ system to indicate the variations in the fluid pressures (Figure 6.9-6.10 and Appendix3.3.1). The isochores for the $CO_2 \pm CH_4$ phase intersect each of the aqueous phase, yielding possible pressure-temperature estimates. The H_2O-rich primary fluid inclusions exhibit temperatures between 400 and 451˚C and pressures between 1099 and 2368 (Figure 6.1). The temperatures and pressures estimated for H_2O-rich primary fluid inclusions are geologically reasonable and do apply to the conditions of entrapment of the fluids in the Bushveld Igneous Complex.

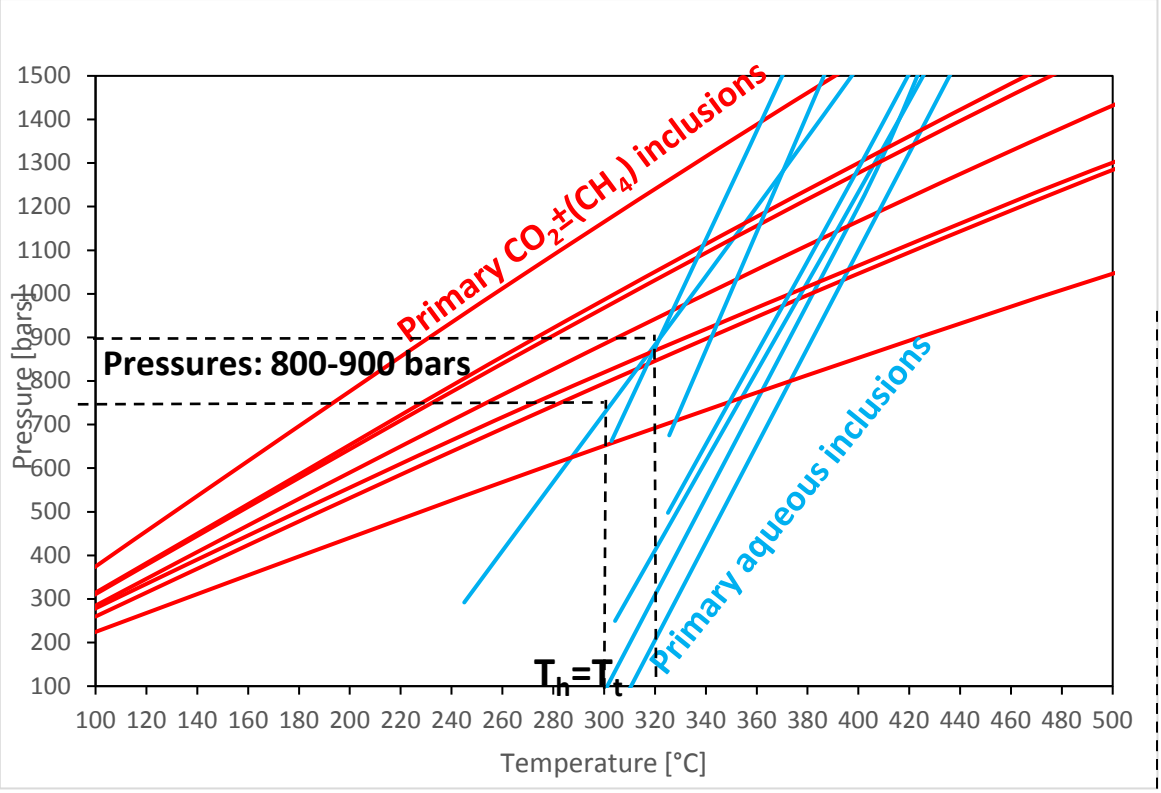

Figure 6.9: Diagram showing isochores of primary fluid inclusions from the Bellevue drillcore. Red lines represent isochores of carbonic fluid inclusion of the primary fluid assemblage and blue lines represents the isochores of the aqueous fluid inclusions of the primary fluid inclusion assemblage.

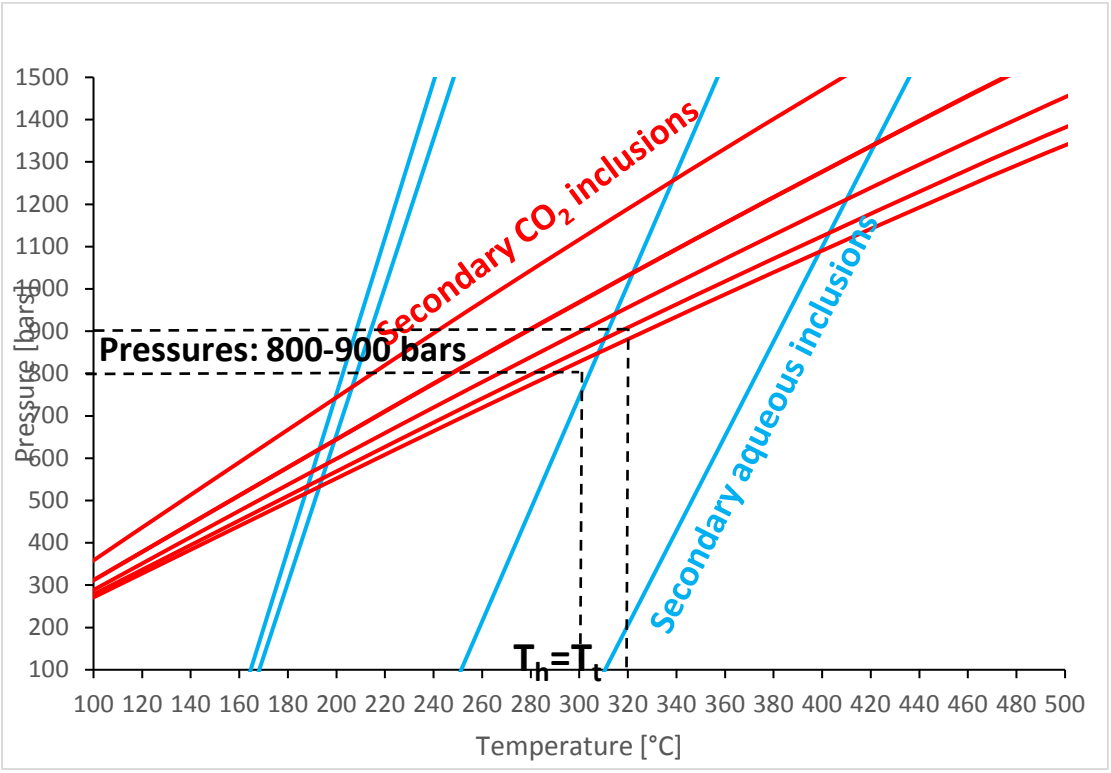

Figure 6.10: Diagram showing isochores of secondary fluid inclusions from the Bellevue drillcore. Red lines represent isochores of carbonic fluid inclusion of the secondary fluid assemblage and blue lines represents the isochores of the aqueous fluid inclusions of the secondary fluid inclusion assemblage.

6.3 Fluid inclusion microthermometry, Stoffberg area

A total of 69 fluid inclusions from Stoffberg samples, are aqueous-rich fluid inclusions, with 42 of these fluid inclusions being primary and the remaining 27 being part of the secondary fluid inclusion assemblage. The aqueous-rich fluid inclusions are dominated by Type 2A and Type 2B fluid inclusion, with rare Type 3A fluid inclusions.

First melting (T_{fm}) temperatures for fluid inclusions within the quartz monzodiorite ranges from - 43.7 – 31.8˚C (mean = - 38.3˚C), suggesting a fluid composition within the ternary H_2O-NaCl-$MgCl_2$ system. The final melting temperatures (T_m= -14.3 to - 0.9˚C; mean= -6.2˚C) (Figure 6.11), yielding salinities of 9.12 wt. % NaCl eq., with densities that range from 0.6 to 0.99 (mean = 0.89 g.cm^{-3}). Two homogenization temperatures were measured (T_{H1} and T_{H2}) were measured during the heating runs (T_{H1}= + 201.8˚C; T_{H2}= + 303.6 – 329.1˚C). The second population inclusions exhibit a minimum trapping temperature of 329.1˚C (Table 6.2 and Figure 6.12).

Within the quartz of the granodiorite, the characteristic inclusions are H_2O L + V primary and secondary fluid inclusions. These fluid inclusions have a melting behaviour (T_{fm} = - 55.5 – -46.7˚C; mean = - 51.7˚C) suggestive of a fluid composition within the ternary H_2O-NaCl-$CaCl_2$. The final melting of these fluid inclusions ranges from -14.1 to -0.2˚C (mean = -4.8˚C) (Figure 6.13), which corresponds to salinity of 7.24 wt. % NaCl eq. Three homogenization temperatures were measured (T_{H1}, $T_{H2,}$ $T_{H3)}$ were measured during the heating runs (T_{H1}= + 176.4 ─ 201.8˚C; T_{H2}= + 303.6 – 329.1˚C; T_{H3}= + 354.5 – 380˚C) as well as major decrepitation at 390˚C. The third population inclusions exhibit a minimum trapping temperature of 380˚C, which mostly likely represent an estimate for the minimum temperature at which these types of fluid inclusions were trapped (Table 6.2 and Figure 6.14).

The melting behaviour of H_2O L + V primary and secondary fluid inclusions, in monzodiorite (eutectic melting ranges from -23.8 to 18.9˚C, mean= - 21.5˚C) suggesting a fluid composition within the H_2O─ NaCl system. These inclusions exhibit final melting temperatures of -10.3 to -3.8˚C (mean= -5.5˚C) (Figure 6.15), corresponding to salinity of 8.3 wt%. NaCl eq., a density of 0.84 g.cm^{-3}, and three homogenization temperatures T_{H1}= + 187.3 – 209.1˚C; T_{H2}= + 274.5 – 296.4˚C; T_{H3}= + 318.2 – 340˚C. Many of the fluid inclusions decrepitated at approximately 385˚C (Figure 6.16).

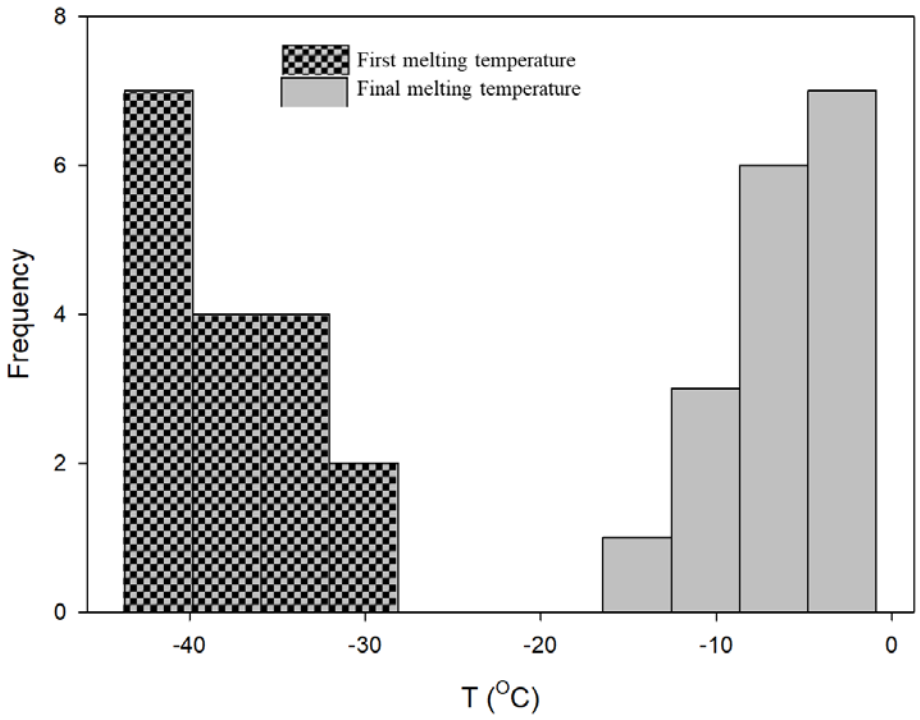

Figure 6.11: Histogram showing melting temperatures for inclusions from quartz monzodiorite from the Stoffberg area. These temperatures include: Tm ice (temperature of first melting (eutectic temperature)) and T_m (H_2O Final temperature of melting).

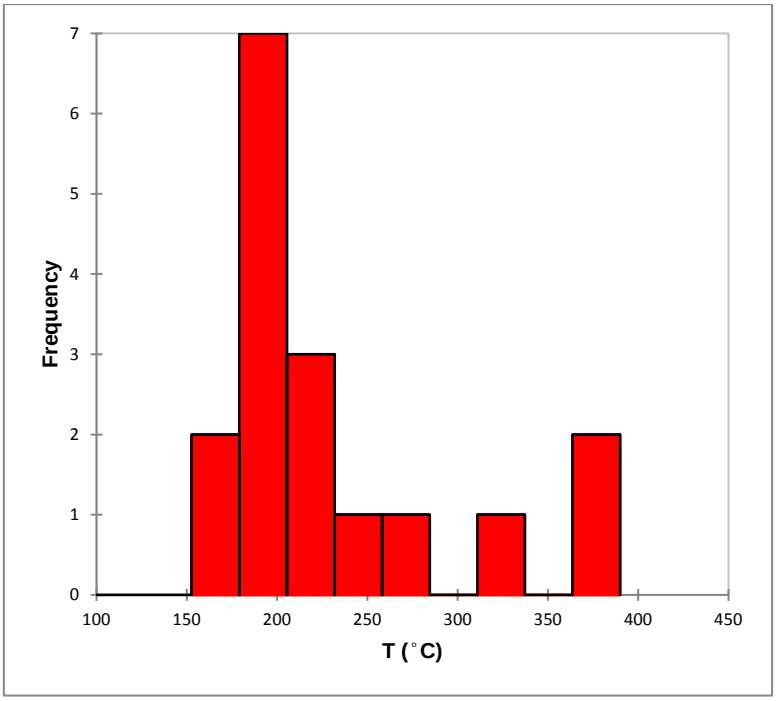

Figure 6.12: Histogram showing homogenization temperatures for inclusions from quartz monzodiorite from the Stoffberg area.

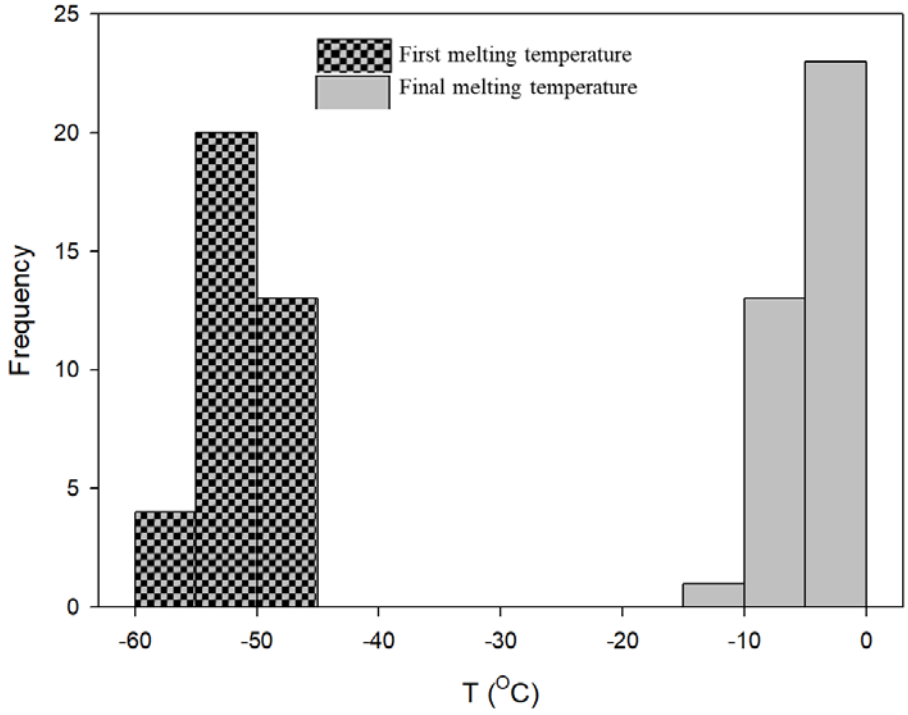

Figure 6.13: Histogram showing melting temperatures for inclusions from granodiorite from the Stoffberg area. These temperatures include: Tm ice (temperature of first melting (eutectic temperature)) and T_m (H_2O Final temperature of melting).

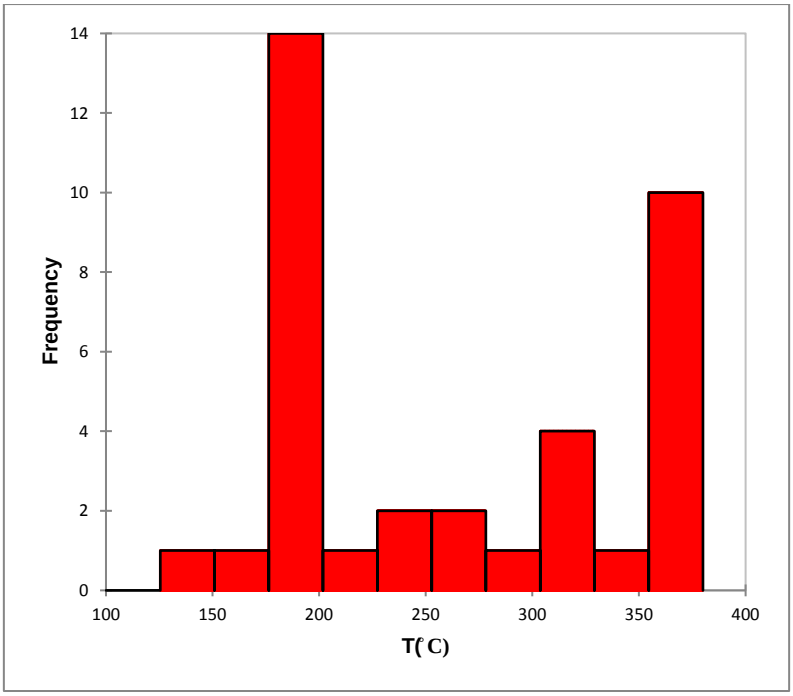

Figure 6.14: Histogram showing homogenization temperatures inclusions from granodiorite from the Stoffberg area.

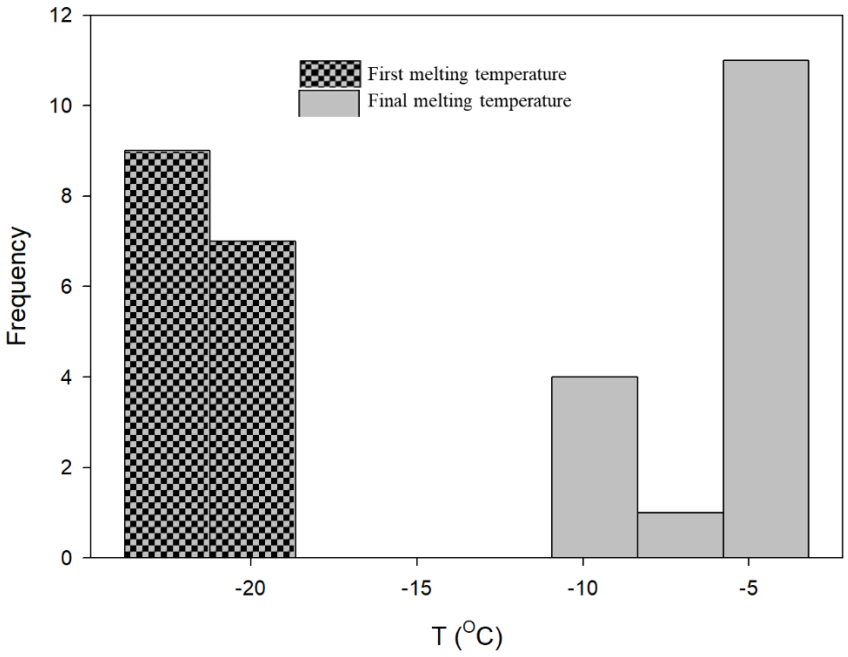

Figure 6.15: Histogram showing melting temperatures for inclusions from granodiorite from the Stoffberg area. These temperatures include: Tm ice (temperature of first melting (eutectic temperature)) and T_m (H_2O Final temperature of melting).

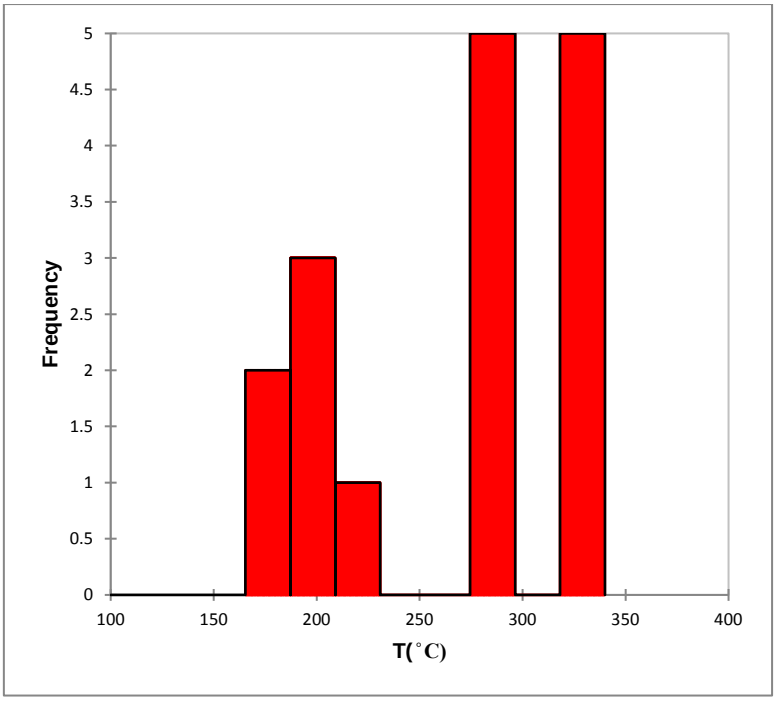

Figure 6.16: Histogram showing homogenization temperatures for inclusions from monzodiorite from the Stoffberg area.

The isochores for the aqueous-rich fluid inclusions were generated using the algorithm as approximated (version 01/03) by the H_2O-NaCl-KCl-$CaCl_2$ system to indicate the variations in the fluid pressures (appendix3.1.2). The isochores for these aqueous fluid inclusions are widely distributed from 356 to 700 °C. Isochores of secondary fluid inclusions cluster around 4- 1704 bar (103- 289 °C), whereas the isochores for the primary fluid inclusions cluster around 296-2997 bar (361-745°C) (Figure 6.17). The primary temperature and pressure estimates for the Stoffberg samples are geologically feasible, and suggest high temperature and pressure conditions, at the time of entrapment of these fluids in the granitoids of the Stoffberg area.

Table 6.2: Summary of preliminary fluid inclusion data from samples of the Stoffberg area

Sample inclusion type	Thermometric properties	Fluid inclusion systems	Density	Salinity (wt % NaCl eq.)
Granodiorite: Dominantly H_2O L + V primary and secondary fluid inclusions	T_{fm} = - 55.5 – 46.7˚C; mean = - 51.7˚C; T_m = -14.1 – - 0.2˚C; mean= -4.8 ˚C T_{H1}= + 176.4 – 201.8˚ C; T_{H2}= + 303.6 – 329.1˚C; T_{H3}= + 354.5 – 380˚C; Major decrepitation at 390˚C	H_2O-NaCl-CaCl2	0.6 – 1.1 (mean = 0.8)	0.35 – 17.9 (mean = 7.24)
Monzodiorite: Dominantly H_2O L + V primary and secondary fluid inclusions	T_{fm} = - 23.8 to -18.9˚ C; mean = - 21.6˚C; T_m = - 10.3 to - 3.2 ˚ C; mean= -5.5 ˚C T_{H1}= + 187.3 – 209.1˚ C; T_{H2}= + 274.5 – 296.4˚C; T_{H3}= + 318.2 – 340˚C; Major decrepitation at 385˚C	H_2O-NaCl	0.70 – 0.98 (mean = 0.84)	5.3 – 14.3 (mean = 8.3)
Quartz Monzodiorite: Dominantly H_2O L + V primary and secondary fluid inclusions	T_{fm} = - 43.7 – 31.8˚C; mean = - 38.3˚C T_m = -14.3 – - 0.9 ˚ C; mean= -6.2 ˚C T_{H1}= + – 201.8˚C; T_{H2}= + 303.6 – 329.1˚ C;	H_2O-NaCl-$MgCl_2$	0.6 - 0.99 (mean = 0.89)	1.6 - 18.0 (mean= 9.12)

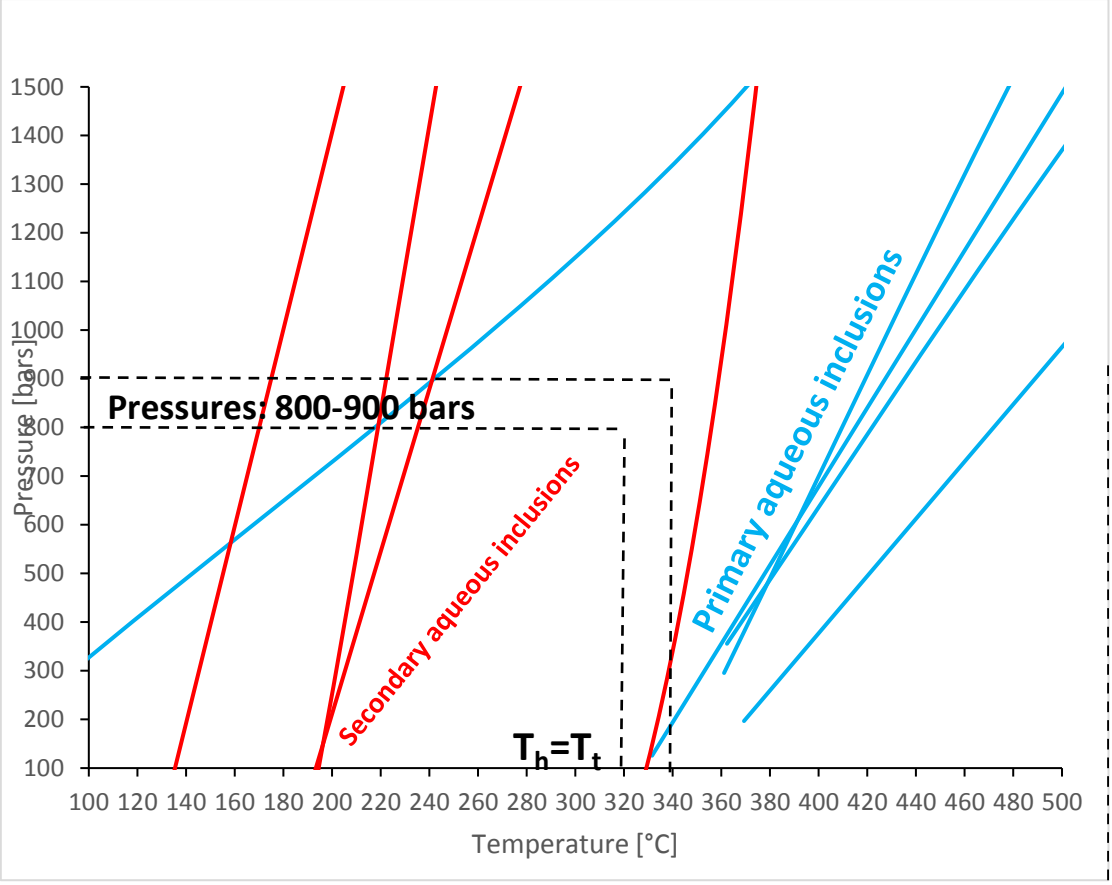

Figure 6.17: Plot showing isochores of aqueous fluid inclusions in quartz, from the Stoffberg area. Red lines represent isochores of aqueous fluid inclusion of the primary fluid assemblage and blue lines represents the isochores of the aqueous fluid inclusions of the secondary fluid inclusion assemblage.

The microthermometric data thus far obtained, pertaining to the fluids that might have played a significant role in the late stage during the magmatic evolution of the Bushveld Igneous Complex, suggest that variations in the fluids existed between these two suites of samples, although fluid inclusion data cannot unequivocally define the fluid source.

The presence of CO_2, CH_4 and various salts in the fluid inclusions of the Bellevue drillcore, suggests that the fluids were capable of transporting and depositing such as the PGEs even though there isn't circumstantial evidence presented in this study.

6.4 Thermometry

6.4.1 Titanium-in-quartz thermometry

The Ti-in-quartz geothermometer was used as an indicator of the trapping pressures and temperatures. Ti-in-quartz results for the Upper Zone reported in Buthelezi *et al.* 2017 were also used in this study. The acquired data were processed with the rutile activity equal to 1 for all samples used in this study, and temperatures were calculated using the calibrations for both 10 and 3 kbar, using the equations of Wark and Watson (2006), and Huang and Audétat (2012), respectively (Figure 6.18 and Table 6.3).

The Ti-in-quartz results from both sites suggest that temperatures calculated using the formulation of Huang and Audétat (2012) at 3 kbar is comparable to the temperatures calculated using the Wark and Watson (2006) at 10 kbar. However, the results from the 10 kbar calibration of Huang and Audétat (2012) are significantly higher than those predicted by the Wark and Watson (2006) calibration at the same pressure. We consider the temperatures obtained using the Huang and Audétat (2012) calibration at 3 kbar as most reliable, as the pressure of the Bushveld Igneous Complex is constrained ~3.0 $\pm$ 0.5 kbar, based on thermobarometry of these rocks in the contact aureole of the BIC (Waters and Lovegrove, 2002).

All Stoffberg samples used in this study are rutile-bearing (RGC-24, -20, -22, -16, -12, and 19). The average within-sample Ti concentrations range from 89 ± 33 to 138 ± 24 ppm, and T estimates ranges between 738 ± 35 and 799 ± 22 °C (Table 6.3 and Figure 6.18). The average within-sample uncertainty in Ti concentration is 22 ppm, corresponding to 35°C. Four samples (RGC-16, -19, -20, -24) yielded at least one spot analysis that was below the detection limit for Ti (22 ppm), with RGC-19 having the largest number (N= 4) of spot analyses below the detection limit.

Quartz grains from sample RGC 12 yielded the lowest average temperature within sample, ranging from 642 ± 22 to 796 ± 71 °C, corresponding to Ti concentrations of 34 ± 22 and 133 ± 22 ppm (Table 6.3 and Appendix 4.2.5), whereas quartz grains from sample RGC 22 yielded the highest average temperature that ranges between 761 ± 18 and 832 ± 27 °C, corresponding to 101 ± 22 and 174 ± 22 ppm (Table 6.3 and Appendix 4.2.3).

Four samples —RGC- 12, -16, -19 and -22—generally have the highest crystallization temperatures at the cores (756-994 ± °C; 624– 829 ± °C) and gradually decrease towards their rims (808-965 ± °C, 756- 797 ± °C) (Appendix 4.2.3-4.2.6), whereas the other two samples—RGC- 20 and -24 —have their highest quartz crystallization temperatures at the rims and gradually decrease towards their cores (Appendix 4.2.1-4.2.2).

Table 6.3 Average within-sample Ti concentrations and corresponding temperatures calculated for Stoffberg samples, using the Ti-in-quartz calibrations of Huang and Audétat (2012) and Wark and Watson (2006).

Sample number	**Average Ti in quartz (ppm)**	**TºC Wark and Watson (2006) at 10 kbar**	**TºC Huang and Audétat (2012) at 3 kbar**	**TºC Huang and Audétat (2012) at 10 kbar**	**Number of spot analyses**
RGC 24	116 ± 36	761 ± 26	773 ± 27	915 ± 31	29
RGC 20	132 ± 33	779 ± 23	792 ± 23	936 ± 26	9
RGC 22	138 ± 24	786 ± 21	799 ± 22	944 ± 25	15
RGC 16	105 ± 31	750 ± 27	798 ± 22	942 ± 25	14
RGC 12	89 ± 33	726 ± 34	738 ± 35	875 ± 39	20
RGC 19	98 ± 36	738 ± 31	750 ± 32	889 ± 36	26

6.4.2 Ti-in-quartz temperatures of the Bushveld Complex

Excluding results from spot analyses with Ti concentrations below the detection limit, which gave spuriously low temperatures, the data for the recrystallized microgranites yielded quartz temperatures ranging from 738 ± 35 to 799 ± 22°C (average = 775 ± 27°C, n = 6) (Table 6.3).

These temperatures are significantly higher than those reported for the Upper Zone samples (including olivine ferrodiorite, anorthosite and leucogabbronorite) in the Bellevue drillcore by Buthelezi *et al*. (2017) calculated at 3 kbar using the same formulation 677 to 767 ºC, but are less than those reported by (Zeh *et al*., 2015) who reported temperatures in the range of T= 670 to 940ºC using the Ti-in-zircon thermometry. Hence, we interpret both the temperatures of Buthelezi *et al*. (2017) and (Zeh *et al*., 2015) as representing solidus temperatures, as the measured quartz grains crystalized from late stage, intercumulus melts, presumably of granitic composition (Figure 6.19), whereas those from the Stoffberg samples record an entirely different event, which possibly post-dates the crystallization of the Bushveld Igneous Complex. When comparing these results with other published geothermometry determinations and geothermal modeling temperatures for the Bushveld Igneous Complex. It is evident that these results reflect conditions that postdate the crystallization of the Complex as these results are significantly higher than those reported by Buthelezi *et al*., 2017 for the mafic cumulate rocks. Even though both the results for Stoffberg and the are Bellevue core (BV-1) samples are nearly isothermal, whereas the temperature modelling of Cawthorn and Walraven (1998) showed an upward decline from the ~ 1200ºC for the Lower Zone rocks, to ~ 900ºC for the top of the Upper Zone, which suggests that their results constrain the liquidus temperatures of magma for the entire sequence of mafic rocks; this is corroborated by the temperature-depth profile shown in Figure 6.19.

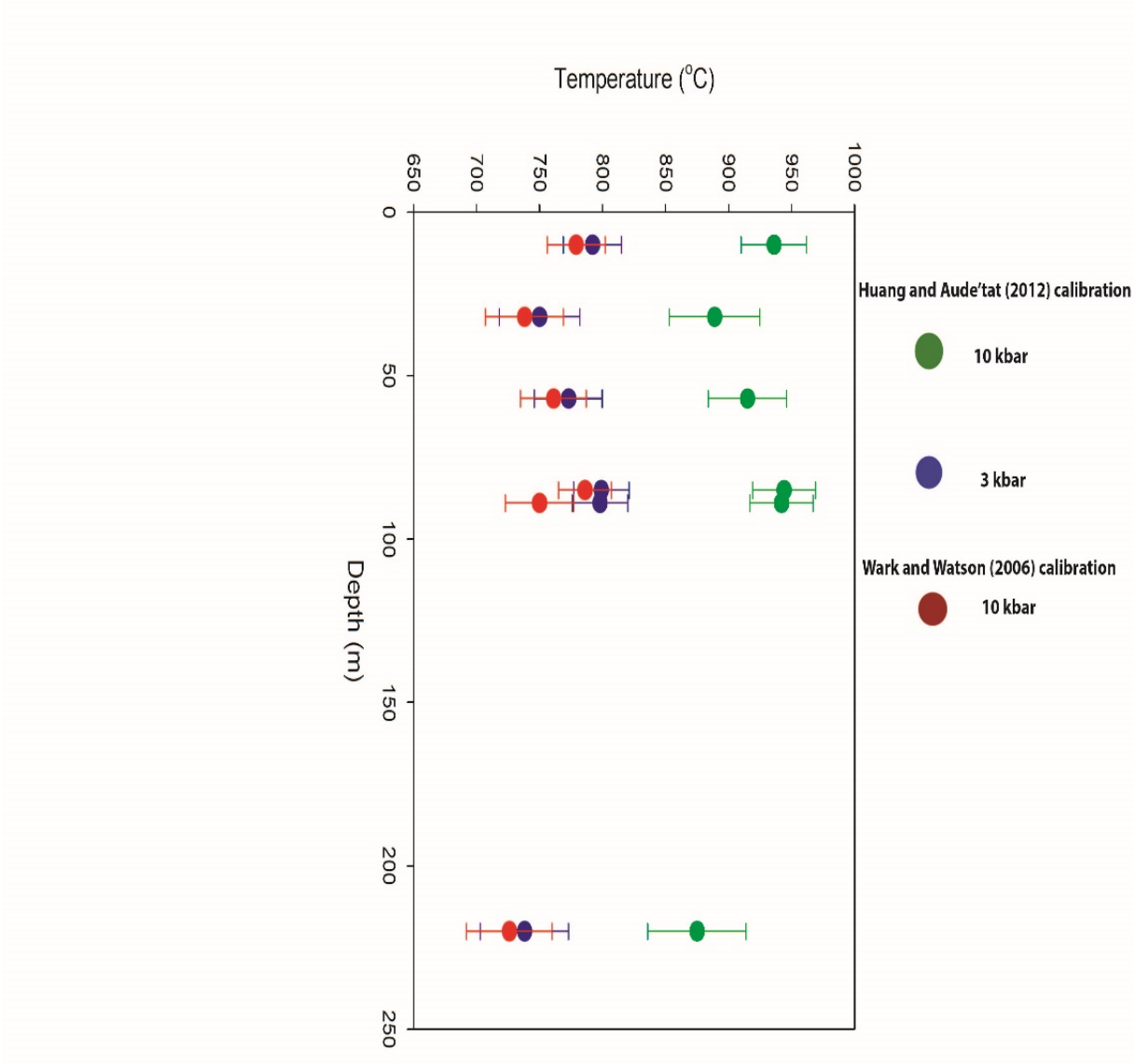

Figure 6.18. Average within-sample temperatures calculated from Ti-in-quartz concentration measurements of interstitial quartz grains in Bushveld samples, using three different TitaniQ calibrations. We consider the results from the 3 kbar calibration of Huang and Audétat (2012) (blue symbols) to be most appropriate for the Bushveld Complex samples. From samples RGC-12, -16, -19, -20, -22, and 24.

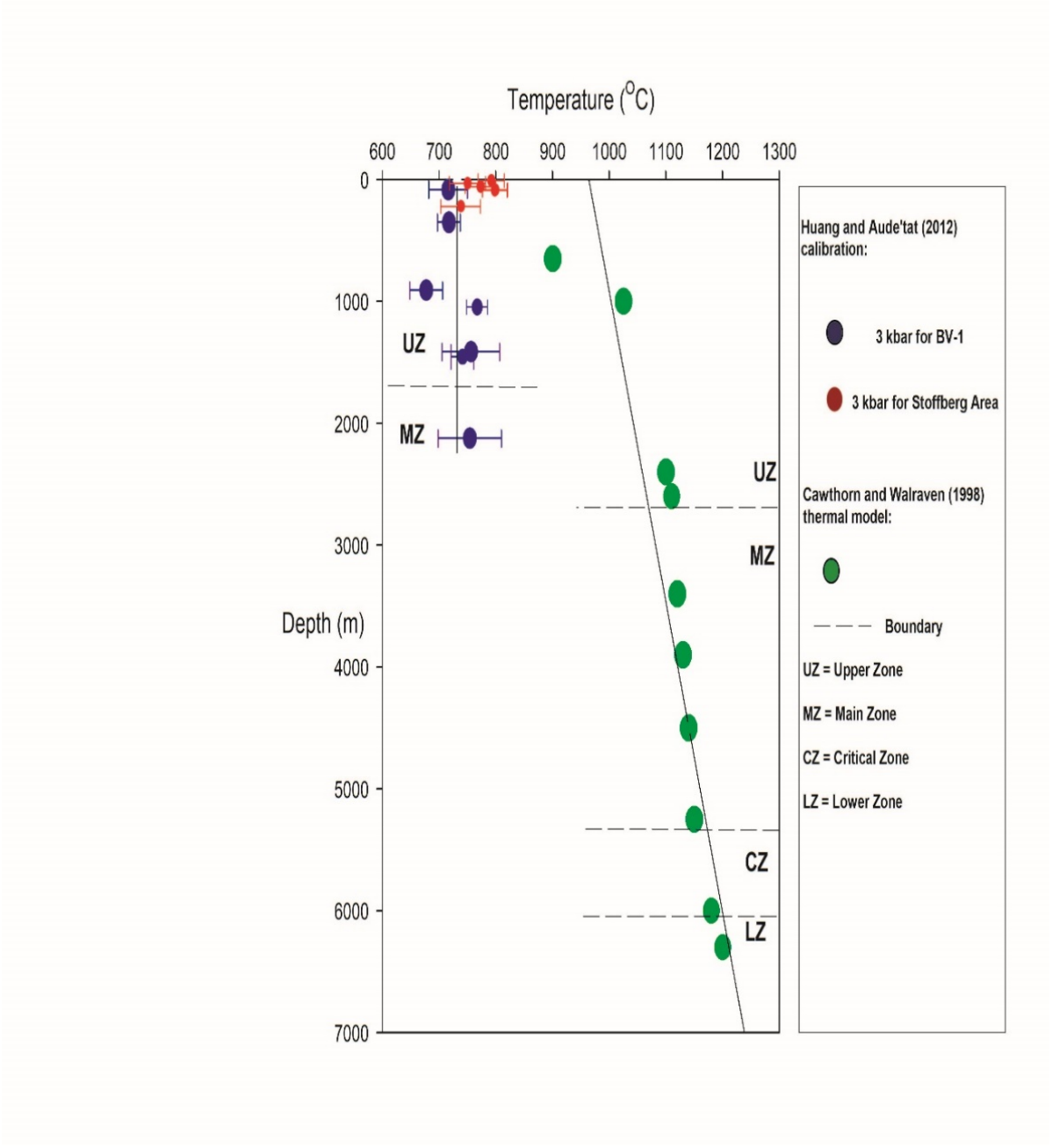

Figure 6.19. Temperature determinations for the Northern and South-Eastern limbs, of the Bushveld Igneous Complex, including solidus temperatures from the Ti-in-quartz of Buthelezi et al., (2017) (blue symbols) and from the Stoffberg area (red symbols, this study), and liquidus temperatures from the thermal modelling of Cawthorn and Walraven (1998) (green symbols). Results from Ti concentrations below the detection limit yield spuriously low temperatures, and are not plotted here. Thermal modelling by Cawthorn and Walraven (1998) for ~ 7.5 km of Bushveld mafic cumulate rocks (Lower to Upper Zones) yielded liquidus temperatures that decrease stratigraphically upward from the Lower Zone to the Upper Zone, whereas solidus temperatures reported in this study and that of Buthelezi *et al.* (2017) appear to be nearly constant with depth.

CHAPTER 7

7.1 DISCUSSION

In the Bellevue drillcore the quartz crystals occur as intercumulus, triangular, patchy grains, representing crystallization products of trapped interstitial melts, whereas in the Stoffberg area the quartz crystals occur either as crystals intergrown with alkali feldspars or as intercumulus, triangular, patchy grains. The quartz crystals from both sites host numerous two-phase inclusions; rarely, single phase liquid-rich and gas-rich are present. The presence of coexisting liquid and gas-rich fluid inclusions suggests that the true trapping temperatures represent homogenization temperatures (Goldstein and Reynolds, 1994).

Except for sample RGC-12 P2 FL1 and RGC-12 P3 FL1 which detected a trace amount of CH_4, most of the fluid inclusions from the Stoffberg samples are characterized by the presence of H_2O as the existing gaseous phase. No CH_4 inclusions were identified from the secondary fluid inclusion assemblage of the Stoffberg samples. Only one pure CH_4 gas was identified in the primary fluid inclusion assemblages. The other CH_4 gas exists in combination with H_2O in the primary fluid inclusion assemblage. There is no microthermometric evidence for carbonic inclusions in the Stoffberg samples. The fluid inclusions in primary magmatic quartz of BV-01 (Figure 4.2.1) represent the fluid composition present during the crystallization of the Upper Zone, whereas secondary fluid inclusions in the primary magmatic quartz represent fluids in the late stages crystallization or possibly post-date the crystallization (Figure 4.2.1).

The rare fluid inclusions containing large (14 μm) daughter crystals of calcite in the primary magmatic quartz of the BV-O1 core can be interpreted as being products of post-entrapment modification of the inclusions. En-Naciri (1995) documented the same type of fluid inclusions, which he interpreted as representing NaCl-saturated brines that resulted in the formation of the trapped solids. However, the petrographic evidence presented in this study argues against the interpretation of En-Naciri (1995) insofar as the inclusions are well developed and are found in proximity to other inclusions of variable composition as illustrated by microphotographs (Figure 4.2.2).

The microthermometric results suggest that NaC1─KCl─$MgCl_2$─$CaCl_2$ are the main electrolyte present, and that the daughter crystal is halite (e.g BV-83.69, -83.81, -106.90, -417.90, -893.90, -910.10, -1046.50 and BV-1413.80). The concentration of the fluids from both the Bellevue drillcore (6.01─9.23 wt % NaCl eq.) and Stoffberg suite (7.24─9.12 wt % NaCl eq.) are less concentrated than the heterophase fluids (60–80 wt % NaCl eq.) that separated at over 550°C and below 3050 bars, which were capable of transporting large number of metals (Zhitova *et al*., 2016). The lack of metals in both the Bellevue drillcore and Stoffberg samples can may be because of the low salinity of the fluids (low wt % NaCl eq). It is also possible that most of the metal were taken up by most of PGE minerals that crystalized at the magmatic stage before the separation of fluids (Zhitova *et al*. 2016). However, it is possible that these fluids might have been involved in the transport and deposition of finely dispersed phases of ore minerals, couple of areas that are minerals in and around both sites studied in this project.

Similar idea was previously invoked for the low-temperature fluids (<120─75°C) that are non-metal bearing (Zhitova *et al.*, 2016).

Based on the microthermometric data acquired from the fluid inclusions of the Bellevue drillcore, four types of fluids were identified, all of which separated during the crystallization of volatile-rich residual melt of original mafic-ultramafic magma. The earliest fluid (H_2O-NaCl-$MgCl_2$±CO_2) is captured by quartz in luecogabbronorite, occurs as H_2O L + V primary and secondary fluid inclusions; and minor CO_2 L+V also present at 925 ± 12°C, followed by (H_2O- CO_2-NaCl ± other cations such as Ca and K) captured by quartz anorthosite at 789 ± 21°C, subsequently followed by the H_2O- NaCl -CO_2 fluids captured in the anorthosite 778 ± 22°C and ends with H_2O- CO_2-NaCl-KCl fluids at 695± 39°C (Figure 6.16). For the Stoffberg samples only three types of fluids were identified. The earliest fluid being (H_2O-NaCl-$CaCl_2$) captured at 799 ± 22°C, followed by H_2O-NaCl-$MgCl_2$ captured at 798 ± 22°C. Finally, the last generation of fluids (H_2O-NaCl) in the Stoffberg samples were captured at 738 ± 35°C (Figure 6.16).

The final lower melting temperature of aqueous-rich fluid inclusions suggest a later entrapment along cracks in quartz, which is consistent with what was proposed by Ballhaus and Stumpfl (1986). The suite of solids in poly- phase inclusions suggests, in part, trapping during quartz growth, and partly secondary entrapment along healed cracks, as suggested by Ballhaus and Stumpfl (1986). To further support this claim, for the identification of various salt hydrates, it would have been wise to conduct a cryogenic Raman spectroscopy on these fluids, as cryogenic

Raman spectroscopy allows for the identification of a variety of salt hydrates that are formed in inclusions from an aqueous liquid solution upon cooling (Baumgartner and Bakker, 2010). Single-phase carbonic (CH_4 and CO_2) fluid inclusions are dark to transparent at room temperature. Aqueous fluid inclusions are more abundant than carbonic fluid inclusions in samples from both the Bellevue drillcore and Stoffberg area. Carbonic fluid inclusions identified in this study are mainly dominated by CO_2 with variable amounts of other gases such as H_2O and CH_4.

A total of 50 of fluid inclusions examined from various lithologies (e.g. olivine ferrodiorite, quartz anorthosite, anorthosite and leucogabbronorite) contained visible CO_2, with 35 of these fluid inclusions being pure gases and the remaining 15 (being CO_2-bearing fluid inclusions coexisting with either H_2O or CH_4. On cooling of CO_2-bearing inclusions where CO_2 coexists with H_2O, CO_2 hydrates form, and cause H_2O and CO_2 to be extracted from solution (Collins, 1979) (Figure 2.7). Therefore, in two-phase fluid inclusions (L-V) that exhibit CO_2 clathration (formation of $C0_2$-hydrates) as illustrated by the decomposition temperature of the hydrates and the presence of mixed CO_2-CH_4 inclusions having variable proportions of CO_2, from CH_4-rich to CO_2-rich inclusions, indicates that CO_2 and CH_4 fluids were not physically isolated from each other (Figure 2.7). The final homogenization temperatures of both the pure CO_2 and impure CO_2 were used to determine the density of the inclusions.

The significant number of carbonic (CO_2 and CH_4) fluid inclusions in the Bellevue drillcore suggests that the carbonic (CO_2 and CH_4) fluids play a significant role in shallow magmatic

systems, which is contrary to the usually accepted idea that carbonic fluids are generally not a major component in shallow magmatic systems, as these fluids tend to escape from magmas at relatively deep environments (Lowenstein, 2001). This idea might apply to the Stoffberg samples, as there was no carbonic (CO_2 and CH_4) fluid inclusions detected. It is suggested that the carbonic fluid inclusions from the Bellevue drillcore resulted from the in-situ phase separation (immiscibility of the fluids in the H_2O-CO_2-CH_4 system) and probably fluid-rock interaction.

The homogenization temperatures for the carbonic (CO_2 and CH_4) fluid inclusions range (e.g. BV-83.81, -106.90, -352.60, -417.90, -893.90, -910.10 and BV-1046.50) from 18.1 º to 30.8 ºC, whereas the melting temperature for the carbonic inclusions ranges from - 59.7 º to -56.8 ºC (mean = -57.7 ± 0.9 ºC; n=50), indicating that these inclusions are dominated by CO_2. Most of the carbonic fluid inclusions have a melting temperature in the range of -57.5 to -56.8°C. These results are consistent with those reported for pyroxenitic pegmatites by Ballhaus and Stumpfl (1986), who they reported homogenization temperatures for CO_2 between 18 and 31 ºC. Similarly, Zhitova *et al*. (2016) found that the solid CO_2 starts to melt between -59 and -60 °C and homogenize into liquid phase at 20°C. In some of the carbonic-rich inclusions with small amount of H_2O the total T_H some was difficult to observe which is like what is reported in Ballhaus and Stumpfl (1986), who noted that the total T_H for carbonic inclusions with some traces of NaCl-undersaturated brines could not be obtained, as it is difficult to observe. The

density of these carbonic fluid inclusions ranges from 0.31 to 0.79 g/cm^3 (average = 0.6 ± 0.1; n= 50).

This study indicates that pure CO_2 can be in chemical equilibrium with H_2O and/or CH_4 at the formation temperatures, which is contrary to what was suggested by Ballhaus and Stumpfl (1986), as traces of water and CH_4 are present on the inclusion walls. This study also shows that CH_4-rich inclusions show recognizable link with other gases (e.g. H_2O and CO_2). Therefore, the CH_4, inclusions in the olivine ferrodiorites, quartz anorthosites, anothosites and leucogabbronorites might be related directly to the late stages of the Upper Zone, which is consistent with what was suggested by Zhitova et al. (2016) for the Merensky Reef quartz and later pegmatite veins crosscutting the Platreef rocks of the Bushveld Igneous Complex.

The Ti-in-quartz results suggest that quartz crystallization temperatures from the Stoffberg area crystallized from post-magmatic fluids with the upper temperature of entrapment for the earliest fluid inclusions having taken place between 738 ± 35 and 799 ± 22°C for the granitic rocks, whereas for the mafic cumulate rocks from the Bellevue core quartz that crystallized from late-stage, silica-saturated, trapped intercumulus melt of the Bushveld Igneous Complex the upper temperature of entrapment for the earliest fluid inclusions took place between 677 ± 29 and 767 ± 18ºC (Buthelezi *et al.*, 2017). Thus, results from Bellevue drillcore constrained the solidus temperature of the Upper Zone and Main Zone cumulate rocks, respectively (Buthelezi *et al.*, 2017), whereas results from Stoffberg constrain recrystallized temperatures of Lebowa Granite Suite or crustal melts into which the Bushveld Igneous Complex intruded

into. This implies that Stoffberg rocks are not fractionation products of the late-stage Upper Zone magmas as suggested by Cawthorn (2013). However, these temperatures are lower than those reported for earliest fluids that occur as homogeneous dry dense gas ($CH_4 – N_2 \pm CO_2$) that separated from the aluminosilicate melt at 800─900 ºC and 3050 bars (Zhitova et al., 2016).

Despite the lack of isotope studies ($\delta^{13}C$ and $\delta^{2}H$ isotopes) it is evident that the CH_4 found in Bellevue drillcore samples was generated inorganically during the late-stages of crystallization of the BIC. However, it is possible that the source of carbon the organic graphite is from the Platreef calcsilicate rocks contain graphite with δ^{13} C of ~ -27 (Buchanan & Rouse 1984, Harris and Chaumba, 2001). So, the biogenic mechanism cannot be totally ignored. It also well known that in the footwall of the Bushveld Complex in the northern limb the Duitschland Formation is graphite-bearing (Buchanan & Rouse 1984, Harris & Chumba 2001). There are some studies that have shown graphite to be organic in origin (Hoering, 1962; Hayes *et al*., 1983; Chacko *et al*., 1991, 2001). However, due to the lack of evidence for any biogenic processes (organic material such as bacteria) generation of CH_4 via biogenic mechanisms were not considered for this study.

At least five mechanisms for generating CH_4 abiogenetically were considered for this study. These include: (1) primordial origin of methane “extraterrestrial methane synthesis”; (2) high temperature reactions in the mantle; (3) post-magmatic high temperature reactions; (4) Fischer-Tropsch type reactions (5) respeciation of carbon-oxygen-hydrogen fluids.

Primordial origin of methane “extraterrestrial methane synthesis” is unlikely to be the mechanism for the generation of methane in the Bellevue drillcore samples as this idea of primordial origin of methane there is no compelling evidence to suggest for the such a primeval in significant amounts in the interior of the Earth, hence it is rejected. The high temperature reactions in the mantle model is rejected on the biases of the lack of compelling evidence for the existence of such reactions and on how abundant they are in the Earth’s interior.

Based on the evidence presented in this study it is evident that the post-magmatic high temperature reaction model cannot be a plausible model for the generation of CH_4 as this model requires magma to be completed solidified, which is contrary to the both the petrographic evidence and microthermometric data, as most of the methane-rich fluid inclusions are primary. Indicating that the inclusions were trapped during the crystallization of the host mineral, quartz.

Due to the lack of evidence for any serpentinization of the ultramafic and mafic rocks of the Bellevue drillcore rocks it fair to reject the Fischer-Tropsch type reaction as this type of reaction requires serpentinization for CH_4 generation to take place. However, this idea is mostly likely applicable to the seperntinised ol-bearing calcsilicate rocks in the Platreef. Even though CH_4 generation via the Fischer-Tropsch type reaction can be independent of serpentinization it is still not a plausible model for the Bellevue drillcore samples as this model requires hydrothermal conditions for the generation of CH_4, which is contrary to the petrographic evidence of the Bellevue core samples.

Respeciation of C-O-H fluids during the late-stages of crystallization of magma is the most plausible model for the generation of CH_4 in the Bellevue drillcore samples during the late-stages of crystallization of the cooling magma, at tempertures <500-600, even though it requires unusually low solidus temperatures (Potter and Konnerup-Madsen, 2003). Due to the presence of graphite, CO_2 and H_2O in the primary fluid inclusion assemblage it is evident that CH_4 was generated from the respeciation of H_2- and CO_2-rich fluids in the presence of graphite which buffers the system to be in equilibrium (Figure 3). The carbon was generated from the breakdown of graphite from the Duitschland Formation, which is graphite-bearing (Buchanan & Rouse 1984, Harris & Chumba 2001).

7.2 CONCLUSIONS

It is suggested that the carbonic fluids of the Upper Zone Bushveld Igneous Complex resulted from the respeciation (in-situ phase separation - immiscibility of the fluids in the H_2O-CO_2-CH_4 system) and probably fluid-rock interaction during the last-stages of crystallization. The presence of graphite in the Bellevue drillcore samples ensures the generation of CH_4 in the Bellevue samples as it buffers the system to ensure equilibrium. The maximum trapping temperature for the Bellevue fluid inclusions is between 677 ± 29 to 767 ± 18ºC at 3 kbar pressure, whereas for the Stoffberg inclusions the maximum trapping temperature is between 738 ± 35 and 799 ± 22°C at 3 kbar pressure. Hence, this confirms that the CH_4 gas observed in these sample is of an abiogenetic origin. However, comprehensive data on isotopes ($\delta\ ^{13}C$ and $\delta\ ^{2}H$) within the Upper Zone will be required to adequately determine the mechanism by which the CH_4 formed.

Most of the carbonic (CO_2 and CH_4) inclusions from the Bellevue core samples, of the C-O-H (e.g. H_2O-CO_2-CH_4) system occur in clusters and trails with variable degrees of filling, only a few occur in isolation. This study shows that carbonic (CO_2 and CH_4) fluids play a significant role in shallow magmatic systems such as the Bushveld Igneous Complex, which is contrary to the usually accepted idea that carbonic fluids are generally not a major component in shallow magmatic systems, as these fluids tend to escape from magmas at relatively deep environments (Lowenstein, 2001). This idea might apply to the Stoffberg samples, as is no carbonic (CO_2

and CH_4) fluid inclusions were detected. The presence of vapor-phase composition inversion (from an oxidized largely CO_2 phase to a reduced CH_4 phase), further emphasizes that the oxidation of reduced heterophase fluids could be the most important geochemical barrier caused the crystallization of solid mineral phases from heterophase fluids, as previously suggested by Zhitova *et al*. (2016).

This study clearly shows that late-magmatic volatile phases dominated, by compounds of the C-O-H system, play a significant role in the evolution of the late-stage crystallization of the Bushveld Igneous Complex. These volatile phases are likely to buffer the magma with respect to oxygen fugacity at a certain temperature when they reach certain concentration levels. This may cause the cooling magma to deviate from its cooling path (trend). Such phenomenon has been invoked for the crystallization of the Merensky Reef and might account for sulphide and PGM precipitation (Ballhaus and Stumpfl 1986).

The evidence presented in this study suggest that the Stoffberg material is unlikely to represent the most evolved part of the Rustenburg Layered Suite as previously suggested by Cawthorn (2013), but represents relic products of the Lebowa Granite Suite or crustal melts during the intrusion of the Bushveld Igneous Complex Hence, there are differences in the compositions of the fluids involved during their crystallization and/or recrystallization.

8. REFERENCES

Abrajano, T.A.,N.C.Sturchio, J. K. Bohlke,G.L.Lyon, R. J.Poreda, and C. M. Stevens (1988). Methane-hydrogen gas seeps, Zambales Ophiolite, Philippines: deep or shallow origin? *Chemical Geolology*, 71, 211–222.

Andersen, T. and Burke, E. A. J. (1996). Methane inclusions in shocked quartz from the Gardnos breccia, South Norway. *European Journal of Mineralogy*, 8, 927 936.

Andersen, T. Rankin, A.H. & Hansteen, T.H. (1990). Meltmineral-fluid interaction in peralkaline silicic intrusions in the Oslo rift, SE Norway. Ill: Alkali geothermometry based on bulk fluid inclusion content. *Norwegian. Journal of geology. Unders. Bulletin.* 417, 33-40.

Ashwal, L.D., Webb, S.J., and Knoper, M.W., (2005). Magmatic stratigraphy in the Bushveld Northern Lobe: continuous geophysical and mineralogical data from the 2950 m Bellevue drillcore, *South African Journal of Geology*, 108,199-232.

Ballhaus, C.G. and Stumpfl, E.F. (1986). Sulphide and platinum mineralization in the Merensky Reef: Evidence from hydrous silicates and fluid inclusions, *Contributions to Mineralogy and Petrology*, 94:193-204.

Barnes, S-J, Savard D., Bédard, L.P. and Maier, W.D., (2009). Selenium and sulphur concentrations in the Bushveld Complex of South Africa and implications for formation of the platinum-group element deposits, *Mineralium Deposita*, 44:647–663.

Barnes, S-J. and Maier, W.D., (2002). Platinum-group element distributions in the Rustenberg Layered Suite of the Bushveld Complex, South Africa. In: *The Geology, Geochemistry, Mineralogy and Mineral Beneficiation of Platinum-Group*

Elements. Edited by L.J. Cabri, Canadian Institute of Mining, Metallurgy and Petroleum, 54:431-458.

Barnes, S-J., Maier, W.D. and Ashwal, L.D., (2004). Platinum-group element distribution in the Main Zone and Upper Zone of the Bushveld Complex, South Africa. *Chemical Geology* 208, 293 –317.

Baumgartner, M. and Bakker, J., (2010). Raman spectra of ice and salt hydrates in synthetic fluid inclusions, *Chemical Geology*, 275, 58–66

Beeskow, B., P. J. Treloar, A. H. Rankin, T. W. Vennemann, and J. Spangenberg (2006), A reassessment of models for hydrocarbon generation in the Khibiny nepheline syenite complex, Kola Peninsula, Russia, *Lithos*, 91, 1–18.

Belokon, T. V., Frik, M. G., Koblova, A. Z., and Kuchina, Y. E. L., (1995). Biomarker distributions in oil and rock organic matter in Russian petroliferous regions. *Geochemistry International*, 32(9), 126-141.

Berndt, M. E., D. E. Allen, and W. E. Seyfried (1996). Reduction of CO_2 during serpentinization of olivine at 300 ◦C and 500 bar, *Geology* 24, 351–354.

Bodnar, R.J., (2003). Introduction to fluid inclusions. In: Samson, I., Anderson, A. and Marshall, D., eds. Fluid Inclusions: Analysis and Interpretation. *Mineralogical Association of Canada, Short Course* 32: 1-8.

Boudreau, A.E. and McCallum, I.S., (1985). Features of the Picket Pin Pt-Pd deposit. In: Czamanske GK and Zientek ML (eds) *The Stillwater Complex, Montana: Geology and Guide. USGS Spec Publ*, 92:346-358

Brass, G.W., (1980). Stability of brines on Mars, *Icarcus*, 42, 20-28

Burke, E.A.J., (1994). Ramanmicrospectrometry of fluid inclusions. In: De Vivo, B., Frezzotti, M.L. (Eds.), Fluid Inclusions in Minerals: Method and Applications. *Short Course of Working Group (IMA) "Inclusions in Minerals", Virginia Polytechnic Institute and State University*, pp. 25–44.

Burke, E.A.J., (2001). Raman microspectrometry of fluid inclusions. *Lithos* 55, 139–158.

Burke, E.A.J., Lustenhouwer, W.J., (1987). The application of a multichannel laser Raman microprobe (Microdril-28) to the analysis of fluid inclusions. *Chemical Geology* 61, 11–17.

Buthelezi, M., (2015): Ti-thermometry of quartz in the rocks from the Bellevue borehole of the Bushveld complex, South Africa, *Honours Thesis, University of the Witwatersrand, Johannesburg, South Africa*,pp.2 & 19.

Buthelezi, M., Ashwal, L.D. and Horváth, P. (2017). Application of titanium-in- quartz geothermometry to magmatic quartz in evolved rocks from the Bushveld Complex, South Africa. *South African Journal of Geology*. 120, 41-250.

Cameron, E. N. (1978). The Lower Zone of the eastern Bushveld Complex in the Olifants River trough. *Journal of Petrology* 19, 437- 462.

Cameron, E. N. (1980). Evolution of the lower Critical Zone, central sector, eastern Bushveld Complex, and its chromite deposits. *Economic Geology*. 75, 845-871.

Cameron, E. N. (1982). The upper Critical Zone of the eastern Bushveld Complex - precursor of the Merensky Reef. *Economic Geology*, 77, 1307-1327.

Cawthorn, R. G., Meyer, P. S. and Kruger, F. J. (1991). Major addition of magma at the Pyroxenite Marker western Bushveld Complex, South Africa. *Journal of Petrology*, 32, 739-763.

Cawthorn, R.G. and Walraven, F., (1998). Emplacement and crystallization time for the Bushveld complex, *Journal of Petrology*, 39:1669-1687.

Cawthorn, R.G. and Webb, S.J., (2001). Connectivity between 302 the western and eastern limbs of the Bushveld Complex, *Tectonophysics*, 330,195–209.

Cawthorn, R.G., (2013). The Residual or Roof Zone of the Bushveld Complex x, South Africa. *Journal of Petrology*, 54:1875–1900.

Cesare, B. (1995). Graphite precipitation in C-O-H fluid inclusions: Closed system compositional and density changes and thermobarometric implications, *Contribution to Mineralogy Petrology*, 122, 25–33.

Charlou, J. L., J. P. Donval, Y. Fouquet, P. Jean-Baptiste, and N. Holm (2002), Geochemistry of high H_2 and CH_4 vent fluidsissuing from ultramafic rocks at the Rainbow hydrothermal field (36˚4'N, MAR), *Chemical Geology*, 191, 345–359,

Cole, J., Webb, S.J. and Finn, C.A., (2013). Overview of the magnetic signatures of the Palaeoproterozoic Rustenburg Layered Suite, Bushveld Complex, South Africa, *Precambrian Research*, 236:193-213.

Collins, P. L. F. (1979) Gas hydrates in CO_2-bearing fluid inclusions and the use of freezing data for estimation of salinity. *Economic. Geology*. 14, 1435-1444.

Cousins, C. A., (1959). The structure of the mafic portion of the Bushveld Igneous Complex: *Transactions of the Geology Society of South Africa*, vol. 62, 179-189.

Craig, H., and J. E. Lupton (1976). Primordial neon, helium, and hydrogen in oceanic basalts, *Earth and Planetary Science Letters*, 31, 369–385.

Dai, J., S. Yang, H. Chen, and X. Shen (2005), Geochemistry and occurrence of inorganic gas accumulations in Chinese sedimentary basins, *Organic Geochemistry*, 36, 1664–1688.

Darling, W. G. (1998). Hydrothermal hydrocarbon gases: 2, Application in the East African Rift system. *Applied Geochemistry*, 13(7), 825-840.

Darling, W. G., Greisshaber, E., Andrews, J. N., Armannson, H. and O'nions, R. K. (1995). The origin of hydrothermal and other gases in the Kenyan Rift Valley. *Geochimica et Cosmochimica Acta*, 59(12), 2501-2512.

Des Marais, D. J., Donchin, J. H., Nehring, N. L. and Truesdell, L, A. H. (1981). Molecular carbon isotopic evidence for the origin of geothermal hydrocarbons. Nature, 292, 826-828.

Diamond, L.W., (2003). Glossary: Terms and Symbols used in fluid inclusion studies. In: Samson, I., Anderson, A. and Marshall, D., eds. Fluid Inclusions: Analysis and Interpretation. *Mineralogical Association of Canada*, Short Course 32: 1-10

Dubessy, J., Audeoud, D., Wilkins, R., Kosztolanyi, C., (1982). The use of the Raman Microprobe Mole in the determination of the electrolytes dissolved in the aqueous phase of fluid inclusions. *Chemical Geology*, 37, 137–150.

Dubessy, J., Poty, B., Ramboz, C., (1989). Advances in C–O–H–N–S fluid geochemistry based on micro-Raman spectrometric analysis of fluid inclusions. *European Journal of Mineralogy* 1, 517–534.

Eales, H.V. and Cawthorn R.G., (1996). The Bushveld Complex. In: Cawthorn, R.G., (Ed) *Layered intrusions*.Elsevier, Amsterdam, The Netherlands, 181–229.

En-Naciri, A. (1995): Contibution á Í etude du district á Co, As, (Ni, Au, Ag) de Bou Azzer, Anti-Atlas (Maroc), Donnés mineralogiques et geochemiques, etude des inclusions fluids. *Ph.D thesis, université d' Orleans, Orléans, France*, 238 pp.

Etiope, G., M. Schoell, and H. Hosgormez (2011). Abiotic methane flux from the Chimaera seep and Tekirova ophiolites (Turkey): understanding gas exhalation from low temperature serpentinization and implications for Mars, *Earth and Planetary Science Letters*, 310, 96–104.

Etoipe, G. and Sherwood-Lollar, B., (2013). Abiotic methane on Earth, *Reviews of Geophysics*, 51, 276–299.

Fall, A., Bodnar, R.J., Szabó, c. and Pál-Molnár, E., (2007). Fluid evolution in the nepheline syenites of the Ditrău Alkaline Massif, Transylvania, Romania. *Lithos*, 95, 331–345

Ferré, E.C., Maes, S.M., Butak, K.C., (2009). The magnetic stratification of layered mafic intrusions: natural examples and numerical models. *Lithos* 111, 83–94.

Foustoukos, D. I., and W. E. J. Seyfried (2004). Hydrocarbons in hydrothermal vent fluids: the role of chromium-bearing catalysts, *Science*, 304, 1002–1005.

Freeman, L. A. (1998). The nature of hydrothermal fluids associated with granite-hosted, polymetallic mineralization in the eastern lobe of the Bushveld Complex. *PhD thesis, University of the Witwatersrand, Johannesburg, South Africa*, 335pp.

Freeman, L. A. and Robb, L. J. (1995). The nature of hydrothermal fluids associated with the granite-hosted Spoedwel Copper Mine, Bushveld Complex, South Africa. *Abstract of the Centennial Geocongress, Geological Society of South Africa*, 717pp.

Freeman, L. A., Robb, L. J., Kesler, S. E. and O'Neil, J. R. (1997). Fluid mixing and the formation of polymetallic mineralization in the Bushveld granites. *Abstract of the International Symposium on Plumes, Plates and Mineralisation (PPM '97), University of Pretoria, South Africa*, 32-33.

Frezzotti, M.L. and Peccerillo, A., (2004). Fluid inclusion and petrological studies elucidate reconstruction of magma conduits. EOS *Transactions of the American Geophysical Union*, 85, 157-163.

Frezzotti, M.L.; Tecce, F. and Casagli, A., (2012): Raman spectroscopy for fluid inclusion analysis, *Journal of Geochemical Exploration*, 112:1-20.

Frost, B.R. and Touret, J.L.R., (189). Magmatic CO_2 and saline melts from Sybille monzosyenite, Laramie anorthosite complex, Wyoming. – *Contribution to Mineralogy. Petrology,* 103, 178-186.

Gerlach, T. M. (1980). Chemical characteristics of the volcanic gases from Nyiragongo Lava Lake and the generation of CH4-rich fluid inclusions. *Journal of Volcanic and Geothermermal Research,* 8, 177-189.

Giggenbach, W. F. (1997). Relative importance of thermodynamic and kinetic processes in governing the chemical and isotopic composition of carbon gases in high-heat flow sedimentary basins, *Geochimica et Cosmochimica Acta,* 61, 3763–3785.

Gize, A. and Macdonald, R. (1993). Generation of compositionally atypical hydrocarbons in CO_2-rich geologic environments. *Geology,* 21, 129-132.

Gleason J. D., Gutzmer J., Kesler S. E., Zwingmann H., (2011). 2.05-Ga Isotopic Ages for Transvaal Mississippi Valley–Type Deposits: Evidence for Large-Scale Hydrothermal Circulation around the Bushveld Igneous Complex, South Africa, *Journal of Geology*, Vol.119, No. 1,69-80

Glebovitsky, V.A., Semenov,V. S., Belyatsky,B.V.,Koptev-Dvornikov,E. V., Pchelintseva, N. F., Kireev, B. S. & Koltsov, A. B. (2001). The structure of the Lukkulaisvaara Intrusion, Oulanka Group, Northern Karelia: Petrological Implications. *Canadian Mineralogist* 39,607-637.

Gold, T. (1979), Terrestrial sources of carbon and earthquake outgassing, *Journal.of Petrology. Geology,* 1.

Goldstein R.H. and Reynolds, T.J. (1994): Systematics of fluid inclusions in diagenetic minerals: *Society for Sedimentary Geology Short Course,* 31, 199 pp.

Goldstein, R.H., (2001). Fluid inclusions in sedimentary and diagenetic systems. *Lithos,* 55, 159–192.

Groeneveld, D. (1970). The structural features and the petrography of the Bushveld Complex in the vicinity of Stoffberg, eastern Transvaal. In: Visser, D. L. and von Gruenewaldt, G. (eds) Symposium on the Bushveld Igneous Complex and Other Layered Intrusions. Johannesburg: *Geological Society of South Africa*, pp. 36—45.

Hanley, J.J., Mungall, J.E., Pettke, T., Spooner, E.T.C. and Bray, C.J. (2008). Fluid and Halide Melt Inclusions of Magmatic Origin in the Ultramafic and Lower Banded Series, Stillwater Complex, Montana, USA. *Journal of Petrology*, 49, 6:1133-1160.

Harris, C., and Chaumba, J.B., (2001). Crustal contamination and fluid-rock interaction during the formation of the Platreef, northern lobe of the Bushveld intrusion, South Africa. *Journal of Petrology*, 42, 1321-1347.

Holloway, J. R. (1984). Graphite-CH_4-H_2O-CO_2 equilibria at low grade metamorphic conditions, *Geology*, 12, 455–458.

Horita, J., and M. E. Berndt (1999). Abiogenic methane formation and isotopic fractionation under hydrothermal conditions, *Science*, 285, 1055–1057.

Huang, R. and Audétat, A, (2012). The titanium-in-quartz (TitaniQ) thermobarometer: A critical examination and re-calibration, *Geochimica et Cosmochimica. Acta*, 84, 75-89.

Jacquemin, M., A. Beuls, and P. Ruiz (2010). Catalytic production of methane from CO_2 and H_2 at low temperature: insight on the reaction mechanism, *Catalysis. Today*, 157, 462–466,

Jin, Z., L. Zhang, Y. Wang, Y. Cui, and K. Milla (2009). Using carbon, hydrogen and helium isotopes to unravel the origin of hydrocarbons in the Wujiaweizi area of the Songliao Basin, China, *Episodes*, 32, 167–176.

Jones, M.Q.W., (2015). Thermophysical properties of rocks from the Bushveld Complex. *Journal of the Southern African Institute of Mining and Metallurgy*, 115:153-160.

Kanitpanyacharoen, W. and Boudreau, A.E., (2013). Sulfide-associated mineral assemblages in the Bushveld Complex, South Africa: platinum-group element enrichment by vapor refining by chloride–carbonate fluids, *Mineralium Deposita*, 48:193–210

Karr, C., (1975). Infrared and Raman Spectroscopy of Lunar and Terrestrial Minerals. *Academic Press, New York*. 375 pp.

Kelley, D. S. (1996). Methane rich fluids in the oceanic crust. *Journal of Geophysical Research*, 101(B2), 2943 2962.

Kelley, D. S., and G. L. Früh-Green (1999). Abiogenic methane in deep-seated mid-ocean ridge environments; insights from stable isotope analyses, *Journal Geophysics Research*, B, 104, 10, 439–10, 460.

Klemd, R., (2004). Fluid Inclusions in Epidote Minerals and Fluid Development in Epidote -Bearing Rocks, *Reviews in Mineralogy & Geochemistry*, Vol. 56, pp. 197-234.

Kinnaird, J.A (2005). *The Bushveld large igneous province*, available on: http://www.argeigneousprovinces.org/LOM.html [accessed 07March 2016]

Kinnaird, J.A., Hutchinson, D., Schurmann, L., Nex, P.A.M. and de Lange, R., (2005). Petrology and mineralization of the southern Platreef: northern limb of the Bushveld Complex, South Africa, *Mineralium Deposita*, 40:576-597.

Kiyosu, Y., N. Asada, and Y. Yoshida (1992). Origin of light hydrocarbon gases from the Matsukawa geothermal area in Japan, *Chemical Geology*, 94, 321–329.

Knoper, M. W. and von Gruenewaldt, G., (1996). The Bellevue (BV-1) borehole core log: 2.9km of Bushveld Complex stratigraphy (northern lobe), Potgietersrus, South Africa. Available online at: http://www/geocities.com/mwk.geo/bic.htm.

Kogarko, L. N., Kosztolanyi, C.H. and Ryabchikov, I. D. (1987). Geochemistry of the reduced fluid in alkali magmas. *Geochemistry International*, 24(7), 20-27.

Konnerup-Madsen, J. (1988). Abiogenic hydrocarbon gases, In: SANTOSH, M. (ed.) FIuid Inclusions. *Special Memoirs of Geological Society of India*, 13-24.

Krot, A. N., Posukhova, T. V., Guseva, YE. V., Galimov, E. M., Botkunov, A. I., Ramenskaya, M. YE. and Oglobina, i. I. (1994). Origin of garnets containing hydrocarbon inclusions in the Mir kimberlite pipe. *Geochemistry International*, 31(1), 122-128.

Kruger, F. J., (2005). Filling the Bushveld Complex magma chamber: lateral expansion, roof and floor interaction, magmatic unconformities, and the formation of giant chromitite, PGE and Ti-V-magnetitite deposits, *Mineralium Deposita*, 40:451-472.

Kruger, F. J., Cawthorn, R. G. and Walsh, K. L. (1987). Strontium isotope evidence against magma addition in the Upper Zone of the Bushveld Complex. *EarthPlanetary Science Letters*, 84, 51-58.

Kruger, F.J., (1990). The stratigraphy of the Bushveld Complex; a reappraisal and the relocation of the Main Zone boundaries**.** *South African Journal of Geology*, 93, 2, 376-381.

Larsen, R. B., Brooks, C. K. & Bird, D. K. (1992). Methane-bearing, aqueous, saline solutions in the Skaergaard intrusion, east Greenland. *Contributions to Mineralogy and Petrology* 112, 428-437.

Lee, C.A., (1996). A review of mineralization in the Bushveld Complex and some other layered intrusions. *In:* R.G. Cawthorn (Editor), *Layered Intrusions. Developments in Petrology*, 15:103-145.

Linke, W.F., (1958). Solubilities: Inorganic and metal-organic compounds, vol. I. *American Chemical Society*, Washington

Lomberg, K., (2012). Exploration Results of the Waterberg Platinum Project, South Africa, *Coffey Mining (SA) Pty Ltd*.

Long, A. D., (1977): Raman spectroscopy, McGraw-Hill, *New York*, *Chapter* 1, 1-4.

Lowenstein, J.B. (2001): Carbon dioxide in magmas and implications for hydrothermal systems. *Mineralium Deposita*, 36:490–502

Lum, J.E., (2011). Plagioclase compositions in the Upper Zone of the Bushveld Complex. Available online: http://hdl.handle.net/10539/10270.

Mathez, E.A., Boudreau, A.E., McCallum, I.S., (1985) Aptatite and biotite from the Stillwater and Bushveld Complexes and the nature of hydrothermal activity. *Canadian Mineralogy* 23:308

Matveev, S., C. Ballhaus, K., Fricke, J. Truckenbrodt, and D. Ziegenbein (1997), Volatiles in the Earth's mantle; I, Synthesis of CHO fluids at 1273K and 2.4 GPa, *Geochimica et Cosmochimica. Acta*, 61, 3081–3088 (97) 00142-7.

McCollom, T. M., and J. S. Seewald (2006). Carbon isotope composition of organic compounds produced by abiotic synthesis under hydrothermal conditions, *Earth Planetary Science Letters*, 243, 74–84.

McCreery, R.L., (2000): Raman Spectroscopy for Chemical Analysis, John Wiley & Sons, Chichester. In: Winefordner, J.D., A series of Monographs on Analytical Chemistry and Its Applications, *Chemical Analysis*, Vol. 157, 1.

McMillan, P.F., Dubessy, J., Hemley, R., (1996). Applications in Earth, planetary and environmental sciences. In: Turrell, G., Corset, G. (Eds.), Raman Microscopy. *Academic Press*, pp. 289–351.

Meyer, R., and de Beer, J. H. (1987). Structure of the Bushveld Complex from resistivity measurements. *Nature*, 325, 610-612.

Mungall, J.E., Kamo, S.L. and McQuade, S., (2016). U–Pb geochronology documents out-of-sequence emplacement of ultramafic layers in the Bushveld Igneous Complex of South Africa, *Nature Communications* 7, 13385.

Molyneux, T. G. (1974). A Geological investigation of the Bushveld Complex in Sekhukhuneland and part of the Steelport Valley. *Transactions of the Geological Society of South Africa, 77* 329-338

Naldrett, A.J. (2003). Magmatic Sulfide Deposits of Nickel─Copper and Platinum─Metal Ores (St. Petersburg Univ., St. Petersburg, 2003), pp. 1–487.

Nasdala, L., Smith, D.C., Kaindl, R., Zieman, M.A., (2004). Raman spectroscopy: analytical perspectives in mineralogical research. In: Beran, A., Libowitzky, E. (Eds.), *Spectroscopic methods in mineralogy: EMU Notes in Mineralogy*, 6, pp.281–343.

Neal, C. and Stanger, G. (1983). Hydrogen generation from mantle source rocks in Oman. *Earth and Planetary Science Letters*, 60, 315-321.

Ni, Y., J. Dai, Q. Zhou, X. Luo, A. Hu, and C. Yang (2009). Geochemical characteristics of abiogenic gas and its percentage in Xujiaweizi Fault Depression, Songliao Basin, NE *China. Petrology. Exploration. Development*, 36, 35–45.

Ollila, J. T. (1981). A fluid inclusion and mineralogical study of tin deposits on rocks associated with the Bushveld Complex at the Zaaiplaats, Union and Rooiberg tin mines in the central Transvaal, South Africa. *Unpublished PhD thesis, Rand Afrikaans University, Johannesburg, South Africa*, 257pp.

Ollila, J.T. (1984). Fluid inclusions and tin deposition at Zaaiplaats, the Central Transvaal, South Africa. *Bulletin Geology Socciety Finland, 56,* Part 1—2, 59—73.

Petersilie, I. A. 1962. Origin of hydrocarbon gases and dispersed bitumens of the Khibina alkalic massif. *Geochemistry International*, 1, 14-29.

Petersilie, I. A., Ikorski, S. V., Smirnova, L. I., Romanikhin, A. M. and Proskuryakova, E. B. (1961). Application of gas logging to the investigation of natural gases and bitumens in the Khibina intrusive massif. *Geochemistry International*, 10, 945-962.

Petersilie, I.A. and Sørensen, H., (1970). Hydrocarbon gases and bituminous substances in rocks from the Ilimaussaq alkaline intrusion, south Greenland. *Lithos*, 3: 59-76.

Pollard, P. J., Andrew, A. S. and Taylor, R. G. (1991). Fluid inclusion and stable isotope evidence for interaction between granites and magmatic hydrothermal fluids during formation of disseminated and pipe-style mineralization at the Zaaiplaats Tin Mine. *Economic Geology*, **86**, 121-141.

Potter, J. and Konnerup-Madsen, J., (2003). A review of the occurrence and origin of abiogenic hydrocarbons in igneous rocks, *Geological Society Special Publications, London* 214:151–173.

Potter, J., Rankin, A. H., Treloar, P. J., Nivin, V. A., Ting, W. and NI, P. (1998). A preliminary study of methane inclusions in alkaline igneous rocks of the Kola igneous province, Russia: implications for the origin of methane in igneous rocks. *European Journal of Mineralogy*, 10, 1167 1180.

Potter, J., Rankin, A.H., Treloar, P.j., (2004). Abiogenic Fischer–Tropsch synthesis of hydrocarbon in alkaline igneous rocks; fluid inclusion, textural and isotopic evidence from the Lovozero complex, N.W. Russia. *Lithos* 75, 311–330.

Proskurowski, G., M. D. Lilley, J. S. Seewald, G. L. Früh-Green, E. J. Olson, J. E. Lupton, S. P. Sylva, and D. S. Kelley (2008). Abiogenic hydrocarbon production at Lost City hydrothermal field, *Science*, 319, 604–607.

Raman, (1928): A new radiation, *Indian Journal of Physics*, 387.

Reynolds, I. M., (1985a). Contrasted mineralogy and textural relationships in the uppermost Ti magnetite layers of the Bushveld Complex in the Bierkraal area north of Rustenburg: *Economic Geology*, v. 80, 1027-1048.

Ripley, E. M. (2005). Re/Os isotopic and fluid inclusion studies of Fluid-rock interaction in the contact aureole of the Duluth Complex, Minnesota. *Geochimica et Cosmochimica Acta 69, 10*, Supplemental 332.

Robb, L. J., Robb, V. M. and Walraven, F. (1994). The Albert Silver Mine revisited: Towards a model for polymetallic mineralization in granites of the Bushveld Complex, South Africa. *Exploration and Mining Geology*, **3**, 247-262.

Roedder, E., (1979). Fluid inclusions as samples of ore fluids. In: Barnes, H.L. (Ed.), *Geochemistry of Hydrothermal Ore Deposits. 2nd edn. Wiley, New York*, pp. 684–737.

Roedder, E., (1984). Fluid inclusions. *Reviews in Mineralogy* 12, 644.

Salvi, S. and William-Jones, A. E. (1992). Reduced orthomagmatic C-O-H-N-NaCI fluids in the Strange Lake rare-metal granitic complex, Quebec/Labrador, Canada. *European Journal of Mineralogy*, 4, 1155-1174.

Samson, I. M. and Williams-Jones, A. E. (1991). C-O-H-N-salt fluids associated with contact metamorphism, McGerrigle mountains, Quebec: A Raman spectroscopic study. *Geochimica et Cosmochimica Acta*, 55, 169-177.

Schidlowsk, M. (1982). Content and isotopic composition of reduced carbon in sediments. In: Holland, H. D. and Schlidowski, M. (eds) *Mineral deposits and the evolution of the biosphere. Springer-Verlag, New York*, 103-122.

Schiffries, C.M. (1984). The Bushveld hydrothermal system: 27th *International Geological. Congress. Abstract.* (Moscow) 2, 385-386.

Schiffries, C.M. (1988). Fluid inclusion phase equilibria in the system $CaCl_2$─NaCl─H_2O: Cotectic relationship between antarcticite and halite. *Eos Transactions of the American Geophysical Union, **69***, 1490

Schiffries, C.M. (1989). Liquid-absent aqueous fluid inclusions. *Eos Transactions of the American Geophysical Union*, 70, 495.

Schiffries, C.M. (1990). Liquid absent aqueous fluid inclusions and phase equilibria in the system $CaCl_2$─NaCl─H_2O, *Geochemica et Cosmomichica Acta*, 54:611-619.

Schouwstra, R. P. and Kinloch, E. D., (2000). A Short Geological Review of the Bushveld Complex, *Platinum metals Review*, 44, 1, 33-39

Schulz, H. (1999). Short history and present trends of Fischer–Tropsch synthesis, *Applied. Catalysis*, 186, 3–12.

Scoon, R.N. and Mitchell, A.A., (2012). The upper zone of the Bushveld complex at Roossenekal, South Africa: geochemical stratigraphy and evidence of multiple episodes of magma replenishment, *South African Journal of Geology*, 115.4:515-534.

Scoon, R.N. and Viljoen, M.J., (2016). The Eastern Limb of the Bushveld Complex. In: Anhaeusser, C.R., Viljoen, M.J. and Viljoen, R.P. (eds) *Africa's Top Geological Sites. Struik Nature, Cape Town*. Pp. 55-60

Seitz, J.C., Pasteris, J.D., Wopenka, B., (1987). Characterization of CO2-CH4-H2O fluid inclusions by microthermometry and laser Raman microprobe spectroscopy: inferences for clathrate and fluid equilibria. *Geochimica et Cosmochimica Acta* 51, 1651–1664.

Sharman-Harris, E.R., Kinnaird, J.A., Harris, C. and Horstmann, U.E., (2005). A new look at sulphide mineralisation of the northern limb, Bushveld Complex: a stable isotope study, *Applied Earth Science IMM Transactions Section B*, 114:252-263.

Sharpe, M. R., (1985). Strontium isotope evidence for preserved density stratification in the Main Zone of the Bushveld Complex, South Africa. *Nature* 316, 119-126.

Shepherd, T.J., Rankin, A.H., Alderton, D.H.M. (1985). A practical guide to fluid inclusion studies. *Blackie & Sons*, Glasgow, pp. 239.

Shepherd, T.J., Rankin, A.H., Alderton, D.H.M., (1985). A Practical Guide to Fluid Inclusion Studies. *Blackie and Son, Glasgow*,239 pp.

Sherwood-Lollar, B., Frape, S. K., Weise, S. M., Fritz, P., Macko, S. A. & Welhan, W. A. (1993). Abiogenic methanogenesis in crystalline rocks. *Geochimica et Cosmochimica Acta*, 57, 5087-5097.

Simoneit, B. R. T. (1988). Organic matter in hydrothermal systems--maturation, migration and biogeochemistry. *Pergamon, Oxford.*

Smekal, (1923). The quantum theory of dispersion, *Naturwissenschaften*, 11, 873-875.

Sobolev, V.S., Bazarova, T.Yu., Kostyuk, V.P., (1974). Inclusions in the minerals of some types of alkaline rocks. In: Sørensen, H. (Ed.). The Alkaline Rocks. J. Wiley and Sons, London, pp. 389–401.Sørensen, H., 1974. *The Alkaline Rocks. J. Wiley and Sons, London*, p. 622.

Sonnenthal, E. L. (1992). Geochemistry of dendritic anorthosites and associated pegmatites in the Skaergaard Intrusion, East Greenland: Evidence for metasomatism by a chlorine-rich fluid. *Journal of Volcanology and Geothermal Research* 52, 209-230.

Sorby, H.C. (1858) On the Microscopic Structure of Crystals, Indicating the Origin of Minerals and Rocks. Quarterly *Journal of the Geological Society of London*, 14, 453-500.

South African Committee for Stratigraphy (SACS), (1980). Stratigraphy of South Africa. Part I (Compiler, L. E. Kent): South Africa Geol. Survey, Handbook 8, 690 p.

Spear F.S. and Selverstone, J., (1983). Water exsolution from quartz: implications for the generation of retrograde metamorphic fluids. *Geology*, 11, 82-85.

Spear, F.S. and Wark, D.A., (2009). Cathodoluminescence imaging and titanium thermometry in metamorphic quartz; *Journal of Metamorphic Geology*, 27, 187-205.

Steele-MacInnis, M., Lecumberri-Sanchez, P., and Bodnar, R.J., (2012). HOKIEFLINCS-H2ONACL: A Microsoft Excel spreadsheet for interpreting microthermometric data from fluid inclusions based on the PVTX properties of H2O–NaCl, *Computational Geosciences*, v. 49, p. 334–337.

Sugisaki, R., and K. Mimura (1994). Mantle hydrocarbons: Abiotic or biotic, *Geochimica Cosmochimica Acta*, 58, 2527–2542.

Szatmari, P. (1989): Petroleum formation by Fischer-Tropsch synthesis in platetectonics, *American. Association.of Petroleum Geologist Bulletin*, 73, 989–998.

Tegner, C., Cawthorn, R. G. and Kruger, F. J. (2006). Cyclicity in the Main and Upper Zones of the Bushveld Complex, South Africa: crystallization from a zoned magma sheet. *Journal of Petrology* 47, 2257—2279.

Thampi,K. R., J. Kiwi, and M. Grätzel (1987). Methanation and photomethanation of carbon dioxide at room temperature and atmospheric pressure, *Nature*, 327, 506–508

Ting, W., Burke, E. A., Rankin, A. H. and Wooeeey, A. R. (1994): Characterisation and petrogenetic significance of CO_2, H_20 and CH_4 fluid inclusions in apatite from the Sukulu Carbonatite, Uganda. *European Journal of Mineralogy*, 6, 787-803.

Touret, J.L.R., (2001). Fluids in metamorphic rocks. *Lithos* 55, 1–25.

Van den Kerkhof, A.M., (1988). The system CO_2—CH_4—N_2in fluid inclusions: Theoretical modelling and geological applications, *PhD. Thesis, Free University Press, Amsterdam*

Van der Merwe, (1978). The geology of the basic and ultramafic rocks of the Potgietersrus Limb of the Bushveld Complex, *Ph.D., University of the Witwatersrand, Johannesburg, South Africa*, 176.

Van Tongeren, J.A., (2011). The 'Ins' and 'Outs' of the Bushveld Complex Upper Zone, Ph.D. Columbia.University.Academic.Commons, http://hdl.handle.net/10022/AC:P:10961

Volborth, A. A., Stumpfl, E. F., Tarkian, M., Housley, R. M., (1985). Examples of Pd-Pt mineralization along the 35-km strike of the Stillwater Reef, Mmatana. *Canadian Mineralogist,* 23:319

Von Gruenewaldt, G., (1973). The Main and Upper Zones of the Bushveld Complex in the Roossenekel area, Eastern Transvaal. *Transactions of the Geological Society of South Africa*, 76, 207-227.

Von Gruenewaldt, G., (1976). Sulfides in the Upper Zone of the eastern Bushveld Complex. *Economic Geology*, vol. 71 no. 7 1324-1336

Wang, W., S. Wang, X. Ma, and J. Gong (2011). Recent advances in catalytic hydrogenation of carbon dioxide, *Chemical Socociety Review*, 40, 3703–3727.

Wark, D.A. and Watson, E.B., (2004). The TITANiQ: A Titanium-in-Quartz thermometer, *Geochimica et Cosmochimica Acta*, Suppl. 68, A543.

Wark, D.A. and Watson, E.B., (2006). TitaniQ: a titanium-in-quartz geothermometer, *Contributions to Mineralogy and Petrology*, 152,743-754.

Waters, D. J. and Lovegrove, D. P. (2002). Assessing the extent of disequilibrium and overstepping of prograde metamorphic reactions in metapelites from the Bushveld Complex aureole, *South Africa Journal of Metamorphic Geology*, 20: 135–149.

Webb, S.J., Cawthorn, R.G., Nguuri, T. and James, D., (2004). Gravity modelling of Bushveld Complex connectivity supported by South African Seismic Experiment results, *South African Journal of Geology*, 107, 207 —218.

Welhan, J. A., and H. Craig, (1983). Methane, hydrogen and helium in hydrothermal fluids of 21" N on the East Pacific Rise, in *Hydrothermal Processes at Seafloor Spreading*

Centers, edited by P. A. Rona, K. Bostriim, L. Laubier, and K. L. Smith, Jr., pp. 391–409, *Plenum, New York, N.Y.*

Wiebe, R.A., Wark, D.A. and Hawkwins, D.P., (2007). Insights from quartz cathodoluminescence zoning into crystallization of the Vinalhaven granite, coastal Maine. *Contributions to Mineralogy and Petrology*, 154,439-453.

Willemse, J. (1969). The geology of the Bushveld Igneous Complex, the largest repository of magmatic ore deposits in the World. *Economic Geology Monograph* 4, 1—22.

Yong, C., Yaoqi, Z., Huanqin, X., Yongjun, R., Ximian, S., Qiang, W. and Shiyong, Y. (2007). Immiscibility of high salinity fluids in volcanic rocks and the mechanism of magma degassing in the Dongying sag, eastern China, *Front. Earth Science China*, 1(2): 206–211.

Yuen, G., N. Blair, D. J. Des Marais, and S. Chang (1984). Carbon isotope composition of low molecular weight hydrocarbons and monocarboxylic acids from Murchison meteorite, *Nature*, 307,252–254.

Zeh, A., Ovtcharova, M., Wilson, A.H. and Schaltegger, U. (2015). The Bushveld Complex was emplaced and cooled in less than one million years - results of zirconology, and geotectonic implications. *Earth and Planetary Science Letters*, 418,103–114.

Zhang, C., and Z. Duan (2009). A model for C-O-H fluid in the Earth's mantle, *Geochimica Cosmochimica Acta*, 73, 2089–2102.

Zhitova, L.M., Borovikov, A.A., Gora, M.P. and Shevko, A.Ya. (2009). Evolution trend of Magmatogene fluids of the intercumulus crystallization stage of the Merensky Reef, Bushveld Complex, Republic of South Africa, Doklady *Earth Sciences*, 429, 8:1299-1304.

Zhitova, L.M.; Borisenko, A.; Morgunov, K. and Zhukova, I. (2007). Immiscibility of Fluid Phases at Magmatic-hydrothermal Transition: Formation of Various PGE-sulfide

Mineralization for Layered Basic *Intrusions. American Geophysical Union, Fall Meeting 2007*, abstract #V43A-1118.

Zhitova, L.M., Kinnard, J.A., Gora, M.P. and Shevko, E.P., (2016). Magmatogene Fluids of Metal-Bearing Reefs in the Bushveld Complex, South Africa: Based on Research Data on Fluid Inclusions in Quartz, *Geology of Ore Deposits*, Vol. 58, No. 1, pp. 58–81. ISSN 1075-7015

Zientek, M.L., (2012). Magmatic ore deposits in layered intrusions—Descriptive model for reef-type PGE and contact-type Cu-Ni-PGE deposits: *U.S. Geological Survey Open-File Report* 2012– 1010, 1-48.

APPENDIX

Appendix 1.1: Samples from Bellevue drillcore polished thick section description

Sample number and Rock name	Major Minerals	Minor Minerals	Modal abundance (%)	Comments (e.g. alteration & degree of alteration; textures, and other features)
BV-83.69 (Olivine ferrodiorite)	Plagioclase; Olivine; Clinopyroxene	Opaque; Amphibole; Quartz; Apatite	Plagioclase = 44; Olivine = 17; Clinopyroxene = 12; Opaque = 10; Amphiboles = 8; Quartz = 7; Apatite = 2	Dominantly comprises relatively fresh plagioclase laths. 2. Poikilitic amphibole enclosing plagioclase laths.
BV-83.81 (Olivine ferrodiorite)	Plagioclase; Olivine; Clinopyroxene	Opaque; Amphibole; Quartz; Apatite	Plagioclase = 46; Olivine = 16; Clinopyroxene = 18; Opaque = 10; Amphiboles = 9; Quartz = 7; Apatite = 2	1. Dominantly comprises relatively fresh plagioclase laths. 2. Poikilitic amphibole enclosing plagioclase laths. 3. Olivine with small inclusions of clinopyroxene.
BV-105.23 Olivine ferrodiorite)	Plagioclase; Olivine; Amphibole	Quartz; Clinopyroxene; Opaque; Alkali feldspars; Apatite; Biotite	Plagioclase= 40; Olivine= 18; Amphibole=14; Quartz= 7; Clinopyroxene= 5; Opaque= 7; Alkali feldspars= 4; Apatite= 3; Biotite= 2	1. Abundant plagioclase laths. Poikilitic amphibole enclosing euhedral plagioclase laths. Also characterized by triangular, patchy intercumulus quartz.

BV-106.20 Olivine ferrodiorite)	Plagioclase; Olivine; Amphibole	Quartz; Opaque; Clinopyroxene; Alkali feldspars; Apatite; Biotite	Plagioclase= 40; Olivine= 20; Amphibole=15; Quartz= 5; Clinopyroxene= 4; Opaque= 4; Alkali feldspars= 5; Apatite= 2; Biotite= 4	Dominated by euhedral plagioclase laths surrounded by anhedral amphibole and intercumulus quartz and clinopyroxene. Poikilitic biotite enclosing plagioclase laths.
BV-352.60 (Quartz Anorthosite: Altered)	Plagioclase; Quartz	Opaque; Biotite	Plagioclase= 87; Quartz=7; Opaque=3; Biotite=3	Dominated by fresh euhedral plagioclase surrounded by anhedral triangular, patchy intercumulus quartz and small amounts of biotite and amphibole grains.
BV-417.90 (Quartz Anorthosite)	Plagioclase; Quartz	Opaque; Amphibole	Plagioclase=84; Quartz=11; Opaque=2; Amphibole=3	Observed replacement texture of amphiboles. There are two types of feldspars: (a) altered feldspar; (b) fresh feldspar
BV-910.10 (Leucogabbronorite)	Plagioclase; Inverted pigeonite; Clinopyroxene	Quartz; Biotite; Amphibole; Opaque	Plagioclase=65; Inverted pigeonite=10; Clinopyroxene=10; Quartz=5; Biotite=4; Amphibole=2; Opaque=4	Characterized by triangular, patchy intercumulus quartz surrounded by euhedral plagioclase laths.
BV-893.90 (Anorthosite)	Plagioclase	Quartz; Clinopyroxene; Biotite; Opaque, Amphibole	Plagioclase=88; Quartz=5; Clinopyroxene=2; Biotite=2; Opaque=2, Amphibole=1	1. Interstitial CPX surrounded by euhedral plagioclase laths. 2. Poikilitic amphibole enclosing opaque, plagioclase and clinopyroxene
BV-1046.50 (Quartz Anorthosite)	Plagioclase; Quartz	Opaque; Biotite	Plagioclase=86; Quartz=11; Opaque=2; Biotite=1	Dominated by fresh euhedral plagioclase surrounded by anhedral triangular, patchy intercumulus quartz

BV-1413.80 (Anorthosite)	Plagioclase	Inverted pigeonite; Amphibole; Quartz; Clinopyroxene; Biotite	Plagioclase=86; Inverted pigeonite=4; Amphibole=4; Quartz=3; Clinopyroxene=2; Biotite=1	The plagioclase laths have prominent Carlsbad and albite twins. The altered plagioclase laths are replaced by or altered to finely concentrated clay minerals. Also characterized by triangular, patchy intercumulus quartz.
BV-1454.35 (Leucogabbronorite)	Plagioclase	Opaque; Clinopyroxene; Inverted pigeonite; Biotite; Amphibole; Quartz	Plagioclase=78; Opaque=6; Clinopyroxene=5; Inverted pigeonite=4; Biotite=3; Amphibole=2; Quartz=2	Slightly altered plagioclase occurs in close distance with the interstitial quartz. Sericite replaces plagioclase.

Appendix 1.2: Samples from Stoffberg area polished thick section description

Sample number	Major Minerals	Minor Minerals	Modal abundance (%) and Rock name	Comments (e.g. alteration & degree of alteration; textures, and other features)
RGC- 22	Plagioclase; Alkali feldspar; Quartz; Amphibole;	Tremolite-Chlorite; Opaque; Clinopyroxene; Rutile	Plagioclase=30; Alkali feldspar=25; Quartz=28; Amphibole=10; Tremolite-Chlorite=3; Opaque=2; Clinopyroxene=1; Rutile=1	Characterized by euhedral plagioclase and Opaques with rather anhedral quartz and amphiboles. Also has a granophyric texture. Find poikilitic amphibole enclosing resorbed CPX and plagioclase surrounded by highly altered alkali-feldspar. Find tremolite-chlorite intergrowth.
RGC-12	Plagioclase; Alkali feldspar; Quartz	Apatite; Opaque; Clinopyroxene; Amphibole	Plagioclase=42; Alkali feldspar=28; Quartz=15; Apatite=2; Opaque=5; Clinopyroxene=1; Amphibole=7	Characterized by moderately altered euhedral plagioclase laths. Abundant apatite in amphiboles, Opaques and the edge of the plagioclase. Find

				poikilitic amphibole enclosing resorbed CPX
RGC-19	Plagioclase; Alkali feldspar; Quartz	Amphiboles; Apatite; Opaque; chlorite	Plagioclase=32 Alkali feldspar=30; Quartz=21; Amphiboles=13; Apatite=1; Opaque=2; chlorite=1	K-feldspar is highly altered compared to plagioclase. Qaurtz occurs as intercumulus material in between the cumulus minerals. Intergrowth of tremolite and chlorite. Apatite exists as small in inclusions in the amphiboles.
RGC-16	Plagioclase; Alkali feldspar; Quartz	Amphibole; Clinopyroxene; Opaque	Plagioclase=38; Alkali feldspar=33; Quartz=14; Amphibole=7; Clinopyroxene=5; Opaque=3	Dominated by feldspars: alkali feldspar and plagioclase. Find Triangular, patchy intercumulus clinopyroxene surrounding plagioclase laths. Also find poikilitic amphibole enclosing resorbed Clinopyroxene and plagioclase laths.
RGC-24	Plagioclase; Alkali feldspar; Quartz; Amphibole;	Agerene; Opaque; Apatite	Plagioclase=32; Alkali feldspar=29; Quartz=20; Agerene=1; Amphibole=15; Opaque=2; Apatite=1	Characterized by strong granophyric texture (alkali feldspar intergrown with quartz). Quartz is also present as triangular, patchy, intercumulus mineral. Agerene is also present interstitially.
RGC-20	Plagioclase; Alkali feldspar; Quartz; Amphibole	Clinopyroxene; Opaque	Plagioclase=29; Alkali feldspar=26; Quartz=21; Amphibole=17 Clinopyroxene=4; Opaque=3	Dominated by highly altered K-feldspar and relatively fresh plagioclase, surrounded by anhedral amphiboles and triangular, patchy intercumulus quartz. In some areas k-feldspar and quartz are intergrown. Also see Poikilitic amphibole with small inclusions of apatite.

Appendix 2.1: Gas Ratios calculations in fluid inclusions, Bellevue drillcore

No	Flinc name	Flinc type	FIA	CH_4 (area peak)	N_2 (area peak)	CO_2 (area 1286 cm-1 peak)	CO_2 (area 1388 cm-1 peak)	CH4-N2-CO_2 sum	X(CH_4)	X(N_2)	X(CO_2)	Comments	Solids
1	BV417_90(2)__Circle 4_Grain 4_FI1_fi Dark-vapour-phase	1phase, CH4 &CO2	Isolated vap inclusions		0	2023.41	2955.53	3993.763333	0.00	0.00	1.00	lack of water band, Its in equilibrium with the host mineral	-
2	BV417_90(2)__Circle 3_Grain 4_FI1_fi vapour(bubble)-phase	3phase, dark	cluster of FLINCS	3317.75	0	568.167	841.397	1571.465	0.28	0.00	0.72	lack of water band,it is equilibrium with the host mineral	-
2	BV417_90(2)__Circle 3_Grain 4_FI1_fi Liquid-phase	3phase, dark	cluster of FLINCS	0	0	0	0	0	#####	####	#DIV/0!	traces of water, it is equilibriu with the Host mineral	-
2	BV417_90(2)__Circle 3_Grain 4_FI1_fi Solid-phase	3phase, dark	cluster of FLINCS	0	0	0	0	0	#####	####	#DIV/0!	lack of water band,it is equilibrium with the host mineral	Quartz
3	BV417_90_P2_FI2_fi vap ph	2phase, carbonic	cluster of carbonic inclusions	0	0	781.354	1186.42	1572.300667	0.00	0.00	1.00	traces of water in the vapor	-
4	BV417_90_P1_FI4_fi liq ph	2phase, carbonic	cluster of carbonic inclusions	278.274	0	1995.76	3700.81	4500.069867	0.01	0.00	0.99	Lack of water band, inclusion with water rim?	-
4	BV417_90_P1_FI4_fi vap ph	2phase, carbonic	cluster of carbonic inclusions	0	0	1204.55	1749.56	2370.923333	0.00	0.00	1.00	Lack of water band, inclusion with water rim?	-
5	BV417_90_P2_FI1_fi vap ph	3phase, aqueous	individual	0	0	0	0	0	0	0	0	traces of water in the vapor	CALCITE
6	BV417_90_P3_FI1_fi liq phase	3phase, carbonic	individual	872.372	0	13179	21053.8	27331.18293	0.004	0.00	0.996	lack of water band	-
6	BV417_90_P3_FI1_fi vap phase	3phase, carbonic	individual	0	0	5270.61	5407.51	8875.616667	0.00	0.00	1.00	lack of water band	GRAPHITE
6	BV417_90_P3_FI1_fi rim phase	3phase, carbonic	individual	0	0	757.647	1404.85	1694.213667	0.00	0.00	1.00	traces of water	-
6	BV417_90_P3_FI1_fi rim-2	3phase, carbonic	individual	0	0	8523.85	13360.5	17430.85	0.00	0.00	1.00	lack of water band	GRAPHITE
7	BV352_60 Circle 4 FL1 large Liquid-phase	2phase,	Trail of Fluid inclusins	0	0	0	0	0	#####	####	#DIV/0!	traces of water in the Liquid, it is in equilibrium with the host mineral	

7	BV352_60 Circle 4 FL1 large Vapour-phase	2phase, CH4 & CO2	Trail of Fluid inclusins	19410.3	0	273.125	457.955	3166.468333	0.82	0.00	0.18	Strong Methane peak,it is equilibrium with the host mineral	
8	BV352_60 Circle 4 Fl2 Medium Liquid-phase	2phase,Methane-rich	cluster of FLINCS	0	0	0	0	0	#####	####	#DIV/0!	strong water band,It is in equilibrium with the host mineral	
8	BV352_60 Circle 4 Fl2 Medium vapour-phase	2phase, methane-rich	cluster of FLINCS	4733.97	0		0	631.196	1.00	0.00	0.00	lack of water band,it is equilibrium with the host mineral	
9	BV352_60 Circle 4 Fl1 medium two-phase	2phase,vapour-rich	cluster of FLINCS	0	0	0	0	0	#####	####	#DIV/0!	lack of water band,it is equilibrium with the host mineral	
10	BV352_60 Circle 4 Small two-phase Vapour-phase	2phase,Dark	cluster of FLINCS	0	0	0	0	0	#####	####	#DIV/0!	lack of water band,it is equilibrium with the host mineral	
10	BV352_60 Circle 4 Small two-phase Liquid-phase	2phase,Dark	cluster of FLINCS	0	0	0	0	0	#####	####	#DIV/0!	traces of water, it is equilibrium with the Host mineral	
11	BV352_60 Circle 4 two-phase containing a Solid (Liquid-phase)	2phase with a Solid	Trail of Fluid inclusins	0	0	0	0	0	#####	####	#DIV/0!	traces of water, it is equilibrium with the Host mineral	
11	BV352_60 Circle 4 two-phase containing a Solid (Solid-phase)	2phase with a Solid	Trail of Fluid inclusins	0	0	0	0	0	#####	####	#DIV/0!	Strong band of water, it is equilibrium with the Host mineral	
12	BV105_23 Circle 4 Dark-one-phase Fl	1phase, water-rich		0	0	0	0	0	#####	####	#DIV/0!	strong flourescence,with a strong band of water, with some similarities with the host mineral	
13	BV83_81_Circle 1 Irregular 3_Phase FLINC (Liquid-phase)	3phase, water-rich	cluster of FLINCS	0	0	0	0	0	#####	####	#DIV/0!	Medium band, trace of water; it's in equilibrium with the host mineral	
13	BV83_81_Circle 1 Irregular 3_Phase FLINC (Solid-phase)	3phase,	cluster of FLINCS	0	0	0	0	0	#####	####	#DIV/0!	Lack of water band, it is equilibrium with the host mineral	
13	BV83_81_Circle 1 Irregular 3_Phase FLINC (Vapour-phase)	3phase, water-rich	cluster of FLINCS	0	0	0	0	0	#####	####	#DIV/0!	Shows a trace of water band, It is equilibrium with the host mineral	

14	BV83_81_ Circle 1 Trail Edge 2-Dark FLINC(Liquid-phase)	2phase, dark	cluster of FLINCS	0	0	0	0	0	#####	####	#DIV/0!	lacks water band, it is in equilibrium with the host mineral	
14	BV83_81_ Circle 1 Trail Edge 2-Dark FLINC(Vapour-phase)	2phase, dark CH4&CO2	cluster of FLINCS	90729.5	0	179428	145189	288317.9333	0.04	0.00	0.96	Lacks water band, it is in equilibrium with the host mineral and has CH4&CO2	
15	BV83_81_Circle 1(G1) 3_Phase FLINC(Liquid-phase)	3phase with a Solid	Isolated vap inclusions	0	0	0	0	0	#####	####	#DIV/0!	Shows a strong peak at 3627.97 cm_1; it's in equilibrium with the host mineral	
15	BV83_81_Circle 1(G1) 3_Phase FLINC(Solid-phase)	3phase with a Solid	Isolated vap inclusions	0	0	0	0	0	#####	####	#DIV/0!	Shows a strong peak at 3627.97 cm_1; it's in equilibrium with the host mineral	
15	BV83_81_Circle 1(G1) 3_Phase FLINC(Vapour-phase)	3phase with a Solid	Isolated vap inclusions	0	0	0	0	0	#####	####	#DIV/0!	Shows a strong peak at 3627.97 cm_1; it's in equilibrium with the host mineral	
16	BV83_81_Circle 3_Dark 2-phase FLINC(Dark area only)_Bubble-phase	2phase, carbonic	cluster of carbonic inclusions	0	0	2256.93	279	2442.93	0.00	0.00	1.00	Shows trace of water; trace of carbon dioxide	
16	BV83_81_Circle 3_Dark 2-phase FLINC(Dark area only)_Liquid-phase	2phase, carbonic	cluster of carbonic inclusions	0	0	2392.91	2131.98	3814.23	0.00	0.00	1.00	lack of water band, trace of carbon dioxide; it's in equilibrium with the host mineral	
17	BV83_81_Circle 2 Two-phase FLINC_A_(Liquid-phase)	2phase, cubic	Isolated inclusion	0	0	0	0	0	#####	####	#DIV/0!	Shows trace of water?	
17	BV83_81_Circle 2 Two-phase FLINC_A_(Vapour-phase)	2phase, cubic	Isolated inclusion	0	0	0	0	0	#####	####	#DIV/0!	Lacks trace of water band; strong fluorescence	
18	BV83_81_Circle 2 Dark 2-phase FLINC_b_(Liquid-phase)	2phase,Dark	cluster of FLINCS	0	0	0	0	0	#####	####	#DIV/0!	Lacks trace of water band; strong fluorescence; it's in equilibrium with the host mineral	
18	BV83_81_Circle 2 Dark 2-phase FLINC_b_(Vapour-phase)	2phase,Dark	cluster of FLINCS	0	0	0	0	0	#####	####	#DIV/0!	Shows a trace of water band, It is equilibrium with the host mineral	
19	BV83_81_Circle 2_Light 2-phase FLINC_(Bubble/Solid-phase)	2phase, water-rich	cluster of FLINCS	0	0	0	0	0	#####	####	#DIV/0!	Shows a trace of water band, It is	

												equilibrium with the host mineral	
19	BV83_81_Circle 2_Light 2-phase FLINC_(Liquid-phase)	2phase, light	cluster of FLINCS	0	0	0	0	0	#####	####	#DIV/0!	Lacks trace of water band	
20	BV83_81_Circle 2 Red two-phase FLINC(Bubble-PHASE)	2phase, red bubble	Isolated inclusions	0	0	0	0	0	#####	####	#DIV/0!	Peak at 2251; 2949	
20	BV83_81_Circle 2 Red two-phase FLINC(Liquid-PHASE)	2phase, red bubble	Isolated inclusions	0	0	0	0	0	#####	####	#DIV/0!	Peak at 2249; 2947	
21	BV83_81 Circle 3 Multiple_phase FLINC(Bubble-phase)	multiple phase(2), carbonic	cluster of FLINCS	0	0	1738.95	658165	440515.6167	0.00	0.00	1.00	Lacks trace of water band	
21	BV83_81 Circle 3 Multiple_phase FLINC(Liquid-phase)	multiple phase(2), dark	cluster of FLINCS	0	0	0	0	0	#####	####	#DIV/0!	lack of water band; no carbonic gases	
22	BV83_81_Circle 2 two Very Dark 2-phase FLINC (Bubble-phase)	2phase, dark CH4&CO2	cluster of FLINCS	1146.86	0	553685	11355.9	561408.5147	0.00	0.00	1.00	Lack of water band	
22	BV83_81_Circle 2 two Very Dark 2-phase FLINC (Dark area only)	2phase, dark	cluster of FLINCS	0	0	0	0	0	#####	####	#DIV/0!	lacks trace of water band; strong fluorescence	
22	BV83_81_Circle 2 two Very Dark 2-phase FLINC (Liquid-phase)	2phase,dark CH4&CO2	cluster of FLINCS	188995	0	8205.33	6971.29	38052.19	0.66	0.00	0.34	Lacls trace of water band	
23	BV-106.90 Circle 1 FL1 Two-phase FLINC(Vapour-phase)	2phase,light	cluster of FLINCS	0	0	0	0	0	#####	####	#DIV/0!	Lack trace of water band	
23	BV-106.90 Circle 1 FL1 Two-phase FLINC(Liquid-phase)	2phase,light	cluster of FLINCS	0	0	0	0	0	#####	####	#DIV/0!	Lack trace of water band	
24	BV-106.90 Circle 1_Dark one-phase FLINC	1PHASE, Methane	Isolated	100910	0	0	0	13454.66667	1.00	0.00	0.00	Weak Methane peak,it is equilibrium with the host mineral	
25	BV-106.90 Circle 2 FL1 Dark-one-phase FLINC	1phase, carbonic	cluster of FLINCS	0	0	1417.92	1700.2	2551.386667	0.00	0.00	1.00	methane and possibly CO2	
26	BV-106.90 Circle 2 FL2 Light-two-phase FLINC(Vapour-phase)	2phase,carbonic	Trail of Fluid inclusins	0	0	1180.12	1357.2	2084.92	0.00	0.00	1.00	strong CO2 peaks, it is in equilibrium with the host mineral	
26	BV-106.90 Circle 2 FL2 Light-two-phase FLINC(Liquid-phase)	2phase,dark	Trail of Fluid inclusins	0	0	0	0	0	#####	####	#DIV/0!	Weak trace of water band, It is in equilibrium with the host mineral,	
27	BV-106.90 Circle 2 FL3 Dark irregular FLINC	1phase,dark	cluster of FLINCS	0	0	0	0	0	#####	####	#DIV/0!	Lacks trace of water band, it is in equilibrium with the host mineral	
28	BV-106.90 Circle 2 FL 4 two-phase FLINC(Vapour-phase)	2phase,vapour-rich,carbonic	Trail of Fluid inclusins	0	0	1188.12	1357.2	2092.92	0.00	0.00	1.00	Medium Methane peak, it is in quilibrium with the host mineral	
28	BV-106.90 Circle 2 FL4 two-phase FLINC(Liquid-phase)	2phase,vapour-rich,H2O	Trail of Fluid inclusins	0	0	0	0	0	#####	####	#DIV/0!	Trace of water band,it is in	

												equilibrium with the host mineral	
29	BV-106.90 Circle 2_FL4 vapour-rich_2-phase FLINC(Liquid-phase)	2phase,CH4-RICH&H2O	Trail of Fluid inclusins	3286.73	0	0	0	438.2306667	1.00	0.00	0.00	Strong Methane peak and medium water band3,it is equilibrium with the host mineral	
30	BV-106.90 Circle 3_FL1 small light 2-phase FLINC(Vapour-phase)	2phase,ligh	Trail of Fluid inclusins	0	0	0	0	0	#####	####	#DIV/0!	Lacks trace of water band, it is in equilibrium with the host mineral	
30	BV-106.90 Circle 3_FL1 small light 2-phase FLINC(Liquid-phase)	2phase,ligh,H2O	Trail of Fluid inclusins	0	0	0	0	0	#####	####	#DIV/0!	Weak trace of water band, It is in equilibrium with the host mineral,	
29	BV-106.90 Circle 2_FL 5vapour-rich_2-phase FLINC(Vapour-phase)	2phase, CH4-RICH ONLY	Trail of Fluid inclusins	2301.59	0	0	0	306.8786667	1.00	0.00	0.00	Weak Methane peak,it is equilibrium with the host mineral, but lacks trace of water band	
31	BV-352.60 Circle 2 FL1 Oval 2-phase FLINC(Vapour-phase)	2phase,	cluster of FLINCS	0	0	0	0	0	#####	####	#DIV/0!	It is in equilibrium with the host mineral	
31	BV-352.60 Circle 2 FL1 Oval 2-phase FLINC(Liquid-phase)	2phase,	cluster of FLINCS	0	0	0	0	0	#####	####	#DIV/0!	weak water band, it is in equilibrium with the host mineral	
32	BV-352.60 Circle 2_FL2 bubble rings_(inner ring phase)	3phase,carbonic	cluster of FLINCS	0	0	1277.95	8332.31	6832.823333	0.00	0.00	1.00	Strong Carbon dioxide peaks,it is equilibrium with the host mineral	
32	BV-352.60 Circle 2_FL2 bubble rings_(outter ring phase)	3phase,carbonic	cluster of FLINCS	0	0	730256	28110.6	748996.4	0.00	0.00	1.00	Strong Carbon dioxide peaks,it is equilibrium with the host mineral	
32	BV-352.60 Circle 2_FL2 bubble rings_(Liquid-phase)	3phase,H2O	cluster of FLINCS	0	0	0	0	0	#####	####	#DIV/0!	strong water band,It is in equilibrium with the host mineral	
33	BV-352.60 Circle 2 FL3 Spherical light 2-phase FLINC(vapour-phase)	2phase,carbonic	cluster of FLINCS	0	0	1446.75	530361	355020.75	0.00	0.00	1.00	Medium Carbon dioxide peaks, it is in equilibrium with the host mineral	
33	BV-352.60 Circle 2 FL3 Spherical light 2-phase FLINC(Liquid-phase)	2phase	cluster of FLINCS	0	0	0	0	0	#####	####	#DIV/0!	It is in equilibrium with the host mineral, lacks trace of water band	

34	BV-352.60 Circle 2 FL4 Cubic 2-phase FLINC(Liquid-phase)	2phase,carbonic&H2O	Trail of Fluid inclusins	0	0	1236.07	1314.04	2112.096667	0.00	0.00	1.00	Weak Carbon dioxide peak, strong water band,it is equilibrium with the host mineral	
34	BV-352.60 Circle 2 FL 4 Cubic 2-phase FLINC(Vapour-phase)	2phase,carboniC	Trail of Fluid inclusins	0	0	1185.9	424345	284082.5667	0.00	0.00	1.00	strong CO2 peaks, with a trace of water band, it is in equilibrium with the host mineral	
35	BV-352.60 Circle 2 FL5 Rectangular 2-phase FLINC(Vapour-phase)	2phase,carbonic	Trail of Fluid inclusins	0	0	624729	34035	647419	0.00	0.00	1.00	strong CO2 peaks, it is in equilibrium with the host mineral	
35	BV-352.60 Circle 2 FL5 Rectangular 2-phase FLINC(Liquid-phase)	2phase,H2O	Trail of Fluid inclusins	0	0	0	0	0	#####	####	#DIV/0!	Medium water band, it is in equilibrium with the host mineral	
36	BV-352.60 Circle 2 FL6 two_bubble-phase FLINC(Vapour-phase)	2phase,two bubbles,carbonic	cluster of FLINCS					0	#####	####	#DIV/0!	strong CO2 peaks, it is in equilibrium with the host mineral	
36	BV-352.60 Circle2 FL6 two_bubble-phase FLINC(Liquid-phase)	2phase,two bubbles	cluster of FLINCS					0	#####	####	#DIV/0!	It is in equilibrium with the host mineral	
37	BV-352.60 Circle 2 FL7 irregular 2-phase FLINC(Vapour-phase)	2phase,CH4	cluster of FLINCS	6409.48	0	0	0	854.5973333	1.00	0.00	0.00	Strong Methane peak,it is equilibrium with the host mineral	
37	BV-352.60 Circle 2 FL7 irregular 2-phase FLINC(Liquid-phase)	2phase,no gas	cluster of FLINCS	0	0	0	0	0	#####	####	#DIV/0!	It is in equilibrium with the host mineral	
38	BV-352.60 Circle 2 FL8 multiple-phase FLINC(Liquid-phase)	2phase,H2O	Isolated	0	0	0	0	0	#####	####	#DIV/0!	strong fluorescence, it is in equilibrium with the host mineral	
38	BV-352.60 Circle 2 FL8 multiple-phase FLINC(Solid-phase)	2phase,	Isolated	0	0	0	0	0	#####	####	#DIV/0!	very strong fluorescence	
38	BV-352.60 Circle 2 FL8 multiple-phase FLINC(Vapour-phase)	2phase,	Isolated	0	0	0	0	0	#####	####	#DIV/0!	weak fluorescence	
39	BV-352.60 Circle 2_FL9 3-phase FLINC(moving bubble)_Liquid-phase	3phase,moving bubble	Trail of Fluid inclusins	0	0	0	0	0	#####	####	#DIV/0!	strong fluorescence, it is in equilibrium with the host mineral	
39	BV-352.60 Circle 2_FL9 3-phase FLINC(moving bubble)_Vapour-phase	3phase,moving bubble, carbonic	Trail of Fluid inclusins	0	0	1.16E+06	1.16E+06	1938700	0.00	0.00	1.00	Strong peaks of carbon dioxide, it is in equilibrium with the host mineral	

40	BV-1046,50 Circle 1 FL1 Irregular Dark one-phase FLINC	Dark 1phase, Carbonic	Trail of Fluid inclusins	0	0	712434	784736	1235591.333	0	0	1	Strong Carbon dioxide peaks, it is in equilibrium with the host mineral, strong fluorescence	
41	BV-1046,50 Circle 1 FL2 Irregular Dark 2-phase FLINC (Liquid-phase)	Dark 2phase	Isolated FLINC	0	0	0	0	0	#####	####	#DIV/0!	strong fluorescence, it is in equilibrium with the host mineral, strong Raman peak at 1088	
41	BV-1046,50 Circle 1 FL2 Irregular Dark 2-phase FLINC (Solid-phase)	Dark 2phase	Isolated FLINC	0	0	0	0	0	#####	####	#DIV/0!	strong fluorescence, it is in equilibrium with the host mineral, strong Raman peak at 1089	
42	BV-1046,50 Circle 1 FL3 Elongated 2-phase FLINC(Liquid-phase)	2phase,carbonic&H2O, with a moving bubble	cluster of FLINCS	0	0	897.36	1198.54	1696.386667	0	0	1	Medium CO2 peaks, with a strong trace of water band, it is in equilibrium with the host mineral	
42	BV-1046,50 Circle 1 FL3 Elongated 2-phase FLINC(Vapour-phase)	2phase,carbonic&H2O, with a moving bubble	cluster of FLINCS	0	0	15630.6	12218.3	23776.13333	0	0	1	Strong Carbon dioxide peaks,it is equilibrium with the host mineral, lacks trace of water	
43	BV-1046,50 Circle 2 FL1 irregular Light 2-phase FLINC(Liquid-phase)	2phase,H2O	cluster of FLINCS	0	0	0	0	0	#####	####	#DIV/0!	Shows a trace of water band, It is equilibrium with the host mineral	
43	BV-1046,50 Circle 2 FL1 irregular Light 2-phase FLINC(Vapour-phase)	2phase, Carbonic	cluster of FLINCS	0	0	1313.04	1377.37	2231.286667	0	0	1	Weak Carbon dioxide peaks,it is equilibrium with the host mineral, lacks trace of water	
44	BV-1046.50 Circle2 FL2 Triangular Dark 2-phase FLINC(Liquid-phase)	2phase,H2O	cluster of FLINCS	0	0	0	0	0	#####	####	#DIV/0!	Shows a weak trace of water, it is in equlibrium with the host mineral	
44	BV-1046.50 Circle 2 FL2 Triangular Dark 2-phase FLINC(Vapour-phase)	2phase, no H2O	cluster of FLINCS	0	0	0	0	0	#####	####	#DIV/0!	Lacks any trace of gaseous peaks, it is in equilibrium with the host mineral	
45	BV-1046.50 Circle2 FL3 Cubic phase FLINC(Vapour-Phase)		cluster of FLINCS	0	0	0	0	0	#####	####	#DIV/0!	Strong fluorescence,	

												Shows a strong band of water	
45	BV-1046.50 Circle2 FL3 Cubic phase FLINC(Liquid-Phase)		cluster of FLINCS	0	0	0	0	0	#####	####	#DIV/0!	Strong fluorescence, Shows a strong band of water	
46	BV-1046.50 Circle 2 FL4 Dark-one phase FLINC	Dark 1phase, H2O	cluster of FLINCS	0	0	0	0	0	#####	####	#DIV/0!	Weak trace of water band, It is in equilibrium with the host mineral,	
47	BV-1046.50 Circle 2 FL5 Elongated irregularly 2-phase FLINC(Liquid-phase)	2PHASE, H2O	cluster of FLINCS	0	0	0	0	0	#####	####	#DIV/0!	strong water band,It is in equilibrium with the host mineral	
47	BV-1046.50 Circle 2 FL5 Elongated irregularly 2-phase FLINC(Vapour-phase)	2PHASE, H2O	cluster of FLINCS	0	0	0	0	0	#####	####	#DIV/0!	strong water band,It is in equilibrium with the host mineral	
48	BV-1046.50 Circle 2 FL6 Rectangular 2-phase FLINC (Liquid-phase)	2PHASE, H2O	cluster of FLINCS	0	0	0	0	0	#####	####	#DIV/0!	medium sized water band, it is equilibrium with the host mineral	
48	BV-1046.50 Circle 2 FL6 Rectangular 2-phase FLINC (Vapour-phase)	2phase, carbonic	cluster of FLINCS	0	0	14100.8	18842.2	26662.26667	0	0	1	Strong Carbon dioxide peaks,it is equilibrium with the host mineral, lacks trace of water	
49	BV-1046.50 Circle 2 FL7 Round 2-phase FLINC (Liquid-phase)	2phase, H2O	cluster of FLINCS	0	0	0	0	0	#####	####	#DIV/0!	Shows a trace of water band, It is equilibrium with the host mineral	
49	BV-1046.50 Circle 2 FL7 Round 2-phase FLINC (Vapour-phase)	2phase, carbonic	cluster of FLINCS	0	0	11730.3	9023.81	17746.17333	0	0	1	Strong Carbon dioxide peaks,it is equilibrium with the host mineral, lacks trace of water	
50	BV-1046.50 Circle 4 FL1 Dark-one phase FLINC_A1	Dark 1phase, Carbonic	Trail of Fluid inclusins	52105.7	1828.07	1798.99	2028.1	11926.55333	0.5825	0.15	0.2642	Strong Methane peak, and medium sized carbon dioxide peaks, trace of N2, lacks water band	
51	BV-1046.50 Circle 4 FL1 Dark-one phase FLINC_A1	Dark 1phase, Carbonic, LARGE	Trail of Fluid inclusins	0	0	2456.17	802873	537704.8367	0	0	1		
52	BV-1046.50 Circle 4 FL2 Dark-one phase FLINC_A2	Dark 1phase, Carbonic	Trail of Fluid inclusins					0	#####	####	#DIV/0!		

53	BV-1046.50 Circle 4 FL3 Dark-one phase FLINC_A3	Dark 1phase, Eye, CH4	Trail of Fluid inclusins	1783.1	0	0	0	237.7466667	1	0	0	Shows two CH4 peaks	
54	BV-1046.50 Circle 4 FL4 Dark-one phase FLINC_A2	Dark irregular one-phase,Carbonic	Trail of Fluid inclusins	653032	0	1303.72	1453.29	89343.51333	0.9746	0	0.0254	Shows a stronfg methane peak, with some resonable carbon dioxide peaks, it is in equilibrium with trhe host mineral, appears to lack trace of water	
55	BV-1046.50 Circle 4 FL5 Light two-phase FLINC_FL4(VAPOUR-phase)	ligth 2phase, H2O	Isolated	0	0	0	0	0	#####	####	#DIV/0!	Shows a weak trace of water, it is in equlibrium with the host mineral	
55	BV-1046.50 Circle 4 FL5 Light two-phase FLINC_FL4(Liquid-phase)	light 2phase	Isolated	0	0	0	0	0	#####	####	#DIV/0!	Lacks trace of water band, it is in equilibrium with the host mineral	
55	BV-1046.50 Circle 4 FL5 Light two-phase FLINC_FL4(Solid-phase)	Multiple phase, H2O-rich	Isolated	0	0	0	0	0	#####	####	#DIV/0!	strong water band,It is in equilibrium with the host mineral	
56	BV-1046.50 Circle 4 FL6 Two-phase FLINC (VAPOUR-PHASE)	2PHASE, H2O	Trail of FLINCS	0	0	0	0	0	#####	####	#DIV/0!	strong water band,It is in equilibrium with the host mineral	
56	BV-1046.50 Circle 4 Two-phase FLINC_ (VAPOUR-PHASE)	No gaseous peaks	Trail of FLINCS	0	0	0	0	0	#####	####	#DIV/0!	Lacks any trace of gaseous peaks, it is in equilibrium with the host mineral	
57	BV-1046.50 Circle 4 Two-phase FLINC_FL6 (VAPOUR-PHASE)	2PHASE, H2O	Trail of FLINCS	0	0	0	0	0	#####	####	#DIV/0!	strong water band,It is in equilibrium with the host mineral	
57	BV-1046.50 Circle 4 Two-phase FLINC_FL6 (Liquid-PHASE)	2PHASE, H2O	Trail of FLINCS	0	0	0	0	0	#####	####	#DIV/0!	weak water band, it is in equilibrium with the host mineral	
58	BV-1045.60 Circle 3 Dark one-phase FLINC_FL1	2PHASE, H2O	Trail of FLINCS	0	0	0	0	0	#####	####	#DIV/0!	strong water band,It is in equilibrium with the host mineral	
59	BV-1045.60 Circle 3 Dark one-phase FLINC_FL2	Dark 1phase, Carbonic	Trail of FLINCS	0	0			0	#####	####	#DIV/0!	strong CO2 peaks, it is in equilibrium with the host mineral	

60	BV-1046.50 Circle 3 Two-phase FLINC _FL3 (Vapour-phase)	2PHASE, H2O	Isolated	0	0	0	0	0	#####	####	#DIV/0!	strong water band,It is in equilibrium with the host mineral	
60	BV-1046.50 Circle 3 Two-phase FLINC _FL3 (Liquid-phase)	2phase, no H2O	Isolated	0	0	0	0	0	#####	####	#DIV/0!	Lacks any trace of gaseous peaks, it is in equilibrium with the host mineral	
61	BV-1045.60 Circle 3 Dark one-phase FLINC_FL4	Dark one-phase, CH4	Isolated	90932.7	0	0	0	12124.36	1	0	0	Strong methane peak, trace of N2, lacks water band	
62	BV-1046.50 Circle 3 Two-phase FLINC _FL5 (Vapour-phase)	2PHASE, H2O	cluster of FLINCS	0	0	0	0	0	#####	####	#DIV/0!	strong water band,It is in equilibrium with the host mineral	
62	BV-1046.50 Circle 3 Two-phase FLINC _FL5 (Liquid-phase)	2PHASE, H2O	cluster of FLINCS	0	0	0	0	0	#####	####	#DIV/0!	Lacks any trace of gaseous peaks, it is in equilibrium with the host mineral	
63	BV-1046.50 Circle 3 Two-phase FLINC _FL6 (Vapour-phase)	2PHASE, H2O	cluster of FLINCS	0	0	0	0	0	#####	####	#DIV/0!	strong water band,It is in equilibrium with the host mineral	
63	BV-1046.50 Circle 3 Two-phase FLINC _FL6 (Liquid-phase)	2phase, no H2O	cluster of FLINCS	0	0	0	0	0	#####	####	#DIV/0!	Lacks any trace of gaseous peaks, it is in equilibrium with the host mineral	
64	BV-910.10 (1) Circle 1 Dark one-phase FLINC_1	1 Phase, H2O	Trail of FLINCS	0	0	0	0	0	#####	####	#DIV/0!	Shows a a trace of water; It is equilibrium with the host mineral	
65	BV-910.10 (1) Circle 1 Cubic two-phase FLINC_1 (Liquid-phase)	2Phase,	Trail of FLINCS	0	0	0	0	0	#####	####	#DIV/0!	Shows a strong fluorescence	
65	BV-910.10 (1) Circle 1 Cubic two-phase FLINC_1 (Vapor-phase)	2 Phase, CH4	Trail of FLINCS	1.23E+06	0	0	0	163501.3333	1	0	0	Shows a strong a methane peak (2912.0 cm_1), it is in equilibrium with the host mineral	GRAPHITE
66	BV-910.10 (1) Circle 1 Dark one-phase FLINC_2	Dark, 1Phase, CH4	Trail of FLINCS					0	#####	####	#DIV/0!	Shows a strong a methane peak (2912.0 cm_1), strong fluorescence, it is in equilibrium with the host mineral	

67	BV-910.10 (1) Circle 1 Oval two-phase FLINC (4)_Liquid-phase	2 Phase, aqueous	Trail of FLINCS	0	0	0	0	0	#####	####	#DIV/0!	lack of water band; Raman peaks for Graphite	GRAPHITE
67	BV-910.10 (1) Circle 1 Oval two-phase FLINC (4)_Vapor-phase	2 Phase, aqueous	Trail of FLINCS	0	0	0	0	0	#####	####	#DIV/0!	lack of water band	
68	BV-910.10 (1) Circle 1 Square two-phase FLINC (2)_Liquid-phase	2 Phase, aqueous	Trail of FLINCS	0	0	0	0	0	#####	####	#DIV/0!	lack of water band	
68	BV-910.10 (1) Circle 1 Square two-phase FLINC (2)_Vapor-phase	2 Phase, aqueous	Trail of FLINCS	0	0	0	0	0	#####	####	#DIV/0!	lack of water band	
69	BV-910.10 (1) Circle 1 Triangle two-phase FLINC (3)_Liquid-phase	2 Phase, aqueous	Trail of FLINCS	0	0	0		0	#####	####	#DIV/0!	lack of water band	
69	BV-910.10 (1) Circle 1 Triangle two-phase FLINC (3)_Vapor-phase	2 Phase, aqueous	Trail of FLINCS	0	0	0	0	0	#####	####	#DIV/0!	lack of water band	
70	BV-910.10 (1) Circle 2_ Rectangle two-phase FLINC (2) Liquid-phase	2 Phase, H2O & CH4	Trail of FLINCS	693.681				92.4908	1	0	0	strong water band, weak CH4 peak, It is in equilibrium with the host mineral	
70	BV-910.10 (1) Circle 2_ Rectangle two-phase FLINC (2) Vapor-phase	2 phase, H2O	Trail of FLINCS	0	0	0	0	0	#####	####	#DIV/0!	weak water band,It is in equilibrium with the host mineral	
71	BV-910.10 (1) Circle 2_ v-rich, cubic, 2-phase FLINC (1)_Vapor-phase	2 phase	Trail of FLINCS	0	0	0	0	0	#####	####	#DIV/0!	lack of water band	GRAPHITE
71	BV-910.10 (1) Circle 2_ v-rich, cubic, 2-phase FLINC (1) Liquid-phase	2 phase, CH4	Trail of FLINCS	789.631	0	0	0	105.2841333	1	0	0	Weak CH4, It is inequilibrium with the host mineral	
72	BV-910.10 (1) Circle 2_ v-rich, cubic, 2-phase FLINC (2) Vpaor-phase	2 phase, CO2	Trail of FLINCS	0	0	1642.35	1787.95	2834.316667	0	0	1	Strong CO peaks, it is in equilibroum with the host mineral	
72	BV-910.10 (1) Circle 2_ v-rich, cubic, 2-phase FLINC (2) Liquid-phase	2 phase, CH4, CO2	Trail of FLINCS	1036.41	0	1556.87	1974.55	3011.424667	0.0459	0	0.9541	Srong CO peaks; Weak CH4 peak, it is equilibrium with the host mineral	
73	BV-83.69 (1) Circle 3 Elongated 2-phase FLINC (1)_Vapor-phase	2 Phase, aqueous	Trail of FLINCS	0	0	0	0	0	#####	####	#DIV/0!	lack of water band	
73	BV-83.69 (1) Circle 3 Elongated 2-phase FLINC (1) Liquid-phase	3 Phase, aqueous	Trail of FLINCS	0	0	0	0	0	#####	####	#DIV/0!	lack of water band	
74	BV_83_69(1)_CIRCLE 3_LIGHT IREGGULAR_one-phase FLINC(1)_	1 Phase, H2O	Trail of FLINCS	0	0	0	0	0	#####	####	#DIV/0!	strong water band,It is in equilibrium with the host mineral	

75	BV_83_69 (1) Circle 1_CUBIC_2_PHASE FLINC(3)_LIQUID-PHASE_	2 phase, H2O	Trail of FLINCS	0	0	0	0	0	#####	####	#DIV/0!	strong water band,It is in equilibrium with the host mineral; weak fluorescence	
75	BV_83_69 (1) Circle 1_CUBIC_2_PHASE FLINC(3)_VAPOR-PHASE_	2 Phase, H2O	Trail of FLINCS	0	0	0	0	0	#####	####	#DIV/0!	Weak water band,It is in equilibrium with the host mineral; weak fluorescence	
76	BV_83_69_Circle 1_Dark FLINC(1)_Area_1	1 Phase, H2O	Trail of FLINCS	0	0	0	0	0	#####	####	#DIV/0!	strong water band,It is in equilibrium with the host mineral; weak fluorescence	
76	BV_83_69_Circle 1_Dark FLINC(1)_Area_2_	1 Phase, H2O	Trail of FLINCS	0	0	0	0	0	#####	####	#DIV/0!	Weak water band,It is in equilibrium with the host mineral; weak fluorescence	
77	BV_83_69_Circle 1_Dark FONE-PHASE FLINC(2)	1 Phase, H2O	Trail of FLINCS	0	0	0	0	0	#####	####	#DIV/0!	Weak water band,It is in equilibrium with the host mineral; strong fluorescence	
78	BV_83_69_Circle 1_light 2-phase FLINC(1)_Liquid-phase	2 Phase, H2O	Trail of FLINCS	0	0	0	0	0	#####	####	#DIV/0!	Weak water band,It is in equilibrium with the host mineral; strong fluorescence	
78	BV_83_69_Circle 1_light 2-phase FLINC(1)_Vapor-phase	2 Phase, H2O	Trail of FLINCS	0	0	0	0	0	#####	####	#DIV/0!	Weak water band,It is in equilibrium with the host mineral; strong fluorescence	
79	BV_83_69 Circle 2 Light, CUBIC, two-phase FLINC (2)_Liquid-phase_	2 Phase, H2O	Trail of FLINCS	0	0	0	0	0	#####	####	#DIV/0!	strong water band,It is in equilibrium with the host mineral; weak fluorescence	
79	BV_83_69 Circle 2 Light, CUBIC, two-phase FLINC (2)_Vapor-phase_	2 Phase, Rutile	Trail of FLINCS	0	0	0	0	0	#####	####	#DIV/0!	lack of water band, strong peak at 609 possible evidence for Rutile	
80	BV_83_69 Circle 2 Light, CUBIC, two-phase FLINC (5)_Liquid-phase_	2 Phase, H2O	Trail of FLINCS	0	0	0	0	0	#####	####	#DIV/0!	strong water band,It is in equilibrium with the host	

												mineral; weak fluorescence	
80	BV_83_69 Circle 2 Light, CUBIC, two-phase FLINC (5)_Vapor-phase	2 Phase, H2O	Trail of FLINCS	0	0	0	0	0	#####	####	#DIV/0!	weak water band,It is in equilibrium with the host mineral	
81	BV_83_69 Circle 2 Light, two-phase FLINC (1)_LIQUID-phase	2 Phase, H2O	cluster of FLINCS	0	0	0	0	0	#####	####	#DIV/0!	strong water band,It is in equilibrium with the host mineral	
81	BV_83_69 Circle 2 Light, two-phase FLINC (1)_Vapor-phase	2 Phase, H2O, CO2	cluster of FLINCS	0	0	308.49	323.976	524.474	0	0	1	Strong water band; weak CO2 peaks, it is in equilibrium with the host mineral	
82	BV_83_69 Circle 2 OVAL two-phase FLINC (3)_Liquid-phase	2 Phase, H2O, CO2	Trail of FLINCS	0	0	85734.3	7380.01	90654.30667	0	0	1	Weak water band; weak CO2 peaks, it is in equilibrium with the host mineral	
82	BV_83_69 Circle 2 OVAL two-phase FLINC (3)_Vapor-phase	2 Phase	Trail of FLINCS	0	0	0	0	0	#####	####	#DIV/0!	lack of water band, no gaseous peak, it is in equilibrium with the host mineral	
83	BV_83_69 Circle 2 OVAL two-phase FLINC (6)_Liquid-phase	2 Phase	Trail of FLINCS	0	0	0	0	0	#####	####	#DIV/0!	lack of water band, no gaseous peak, it is in equilibrium with the host mineral	
83	BV_83_69 Circle 2 OVAL two-phase FLINC (6)_Vapor-phase	2 Phase, H2O, CO2	Trail of FLINCS	0	0	468.338	562.414	843.2806667	0	0	1	Strong water band; weak CO2 peaks, it is in equilibrium with the host mineral	
84	BV_83_69 Circle 2 three-phase FLINC (1)_AREA 2_	three Phase, H2O-liquid, CO2	Isolated FLINC	0	0	66240	11700.6	74040.4	0	0	1	Strong water band; Strong CO2 peaks, it is in equilibrium with the host mineral, Strong fluorescence	
84	BV_83_69 Circle 2 three-phase FLINC (1)_AREA 1	three Phase, H2O-Vapor, CO2, CH4	Isolated FLINC	399.785	0	590.156	684.796	1099.991333	0.0485	0	0.9515	Strong vapor-phase water band, Peaks for CO2 and CH4	
84	BV_83_69 Circle 2 three-phase FLINC (1)_LIQUID-PHASE	three Phase, H2O-LIQUID phase, CO2	Isolated FLINC	0	0	136903	458014	442245.6667	0	0	1	Strong water band; Strong CO2 peaks, it is in equilibrium with the host	

												mineral, Strong fluorescence	
85	BV_83_69 Circle 2_DARK, VAL two-phase FLINC (4)_Liquid-phase	2 Phase, H2O, CO2; CH4	Trail of FLINCS	223.371	0	102618	2252.4	104149.3828	0.0003	0	0.9997	Weak water-liquid band, weak CH4 peak, Strong CO2 peaks, it is in equilibrium with the host mineral	
85	BV_83_69 Circle 2_DARK, VAL two-phase FLINC (4)_Vapor-phase	2 Phase	Trail of FLINCS	0	0	0	0	0	#####	####	#DIV/0!	lack of water band, no gaseous peak, it is in equilibrium with the host mineral	
86	BV_1413_80 (1) Circle 1_ CUBIC, LIGHT ONE-PHASE FLINC (2)	1 phase	Trail of FLINCS	0	0	0	0	0	#####	####	#DIV/0!	Lack of water band	Calcite
87	BV_1413_80 (1) Circle 1_ CUBIC, TWO-PHASE FLINC (1)_LIQUID-PHASE	2 Phase, H2O	cluster of FLINCS	0	0	0	0	0	#####	####	#DIV/0!	strong water band,It is in equilibrium with the host mineral; weak fluorescence	
87	BV_1413_80 (1) Circle 1_ CUBIC, TWO-PHASE FLINC (1)_VAPOR-PHASE	2 Phase, H2O	cluster of FLINCS	0	0	0	0	0	#####	####	#DIV/0!	Weak water band,It is in equilibrium with the host mineral; weak fluorescence	
88	BV_1413_80 (1) Circle 1_ DARK ONE-PHASE FLINC (1)	1 Phase, CO2	cluster of FLINCS	0	0	369532	420862	650106.6667	0	0	1	strong CO2 peaks, it is in equilibrium with the host mineral	
89	BV_1413_80 (1) Circle 1_ THREE-PHASE FLINC (1)_LIQUID-PHASE	3 Phase, aqueous	cluster of FLINCS	0	0	0	0	0	#####	####	#DIV/0!	strong water band,It is in equilibrium with the host mineral; weak fluorescence	
89	BV_1413_80 (1) Circle 1_ THREE-PHASE FLINC (1)_SOLID-PHASE	3 Phase, aqueous, Calcite	cluster of FLINCS	0	0	0	0	0	#####	####	#DIV/0!	strong water band,It is in equilibrium with the host mineral; weak fluorescence	Clcite
89	BV_1413_80 (1) Circle 1_ THREE-PHASE FLINC (1)_VAPOR-PHASE	3 Phase, aqueous	cluster of FLINCS	0	0	0	0	0	#####	####	#DIV/0!	strong water band,It is in equilibrium with the host mineral; weak fluorescence	
90	BV_1413_80(1) CIRCLE 4_DARK CUBIC ONE-PHASE FLINC (3)	Aqueous 1-phase	cluster of FLINCS	0	0	0	0	0	#####	####	#DIV/0!	water band characteristic of OH-	

91	BV_1413_80(1) CIRCLE 4_DARK OVAL ONE-PHASE FLINC (2)	Aqueous 1-phase	cluster of FLINCS	0	0	0	0	0	#####	####	#DIV/0!	Weak water band,It is in equilibrium with the host mineral; weak fluorescence	
92	BV_1413_80(1) CIRCLE 4_IRREGULAR LIGHT 2-PHASE FLINC (1)_Liquid-phase	Aqueous 2-phase	Trail of FLINCS	0	0	0	0	0	#####	####	#DIV/0!	Weak water band,It is in equilibrium with the host mineral; weak fluorescence	
92	BV_1413_80(1) CIRCLE 4_IRREGULAR LIGHT 2-PHASE FLINC (1)_VAPOR-PHASE	Aqueous 2-phase	Trail of FLINCS	0	0	0	0	0	#####	####	#DIV/0!	Lacks trace of water band; strong fluorescence; it's in equilibrium with the host mineral	
93	BV_1413_80(1)_CIRCLE 2_Dark solid one-phase FLINC	1 phase	isolated	0	0	0	0	0	#####	####	#DIV/0!	Lacks trace of water band; strong fluorescence; it's in equilibrium with the host mineral	
94	BV_1413_80(1)_CIRCLE 3_LIGHT one-phase FLINC(6)	Aqueous 1-phase	cluster of FLINCS	0	0	0	0	0	#####	####	#DIV/0!	Weak water band,It is in equilibrium with the host mineral; weak fluorescence	
95	BV_1413_80(1)_CIRCLE_3_CUBIC 2-PHASE FLINC(3)_LIQUID-PHASE_	Aqueous 2-phase	cluster of FLINCS	0	0	0	0	0	#####	####	#DIV/0!	Weak water band,It is in equilibrium with the host mineral; weak fluorescence	
95	BV_1413_80(1)_CIRCLE_3_CUBIC 2-PHASE FLINC(3)_VAPOR-PHASE_	Aqueous 2-phase	cluster of FLINCS	0	0	0	0	0	#####	####	#DIV/0!	Lacks water band,It is in equilibrium with the host mineral; weak fluorescence	
96	BV_1413_80(1)_CIRCLE_3_DARK 2-PHASE FLINC(4)_LIQUID-PHASE	Aqueous 2-phase	isolated	0	0	0	0	0	#####	####	#DIV/0!	Weak water band,It is in equilibrium with the host mineral; weak fluorescence	
96	BV_1413_80(1)_CIRCLE_3_DARK 2-PHASE FLINC(4)_VAPOR-PHASE	Aqueous 2-phase	isolated	0	0	0	0	0	#####	####	#DIV/0!	Lacks water band,It is in equilibrium with the host mineral; weak fluorescence	
97	BV_1413_80(1)_CIRCLE_3_LIGHT CUBIC 2-PHASE FLINC(5)_LIQUID-PHASE	Aqueous 2-phase	Trail of FLINCS	0	0	0	0	0	#####	####	#DIV/0!	Weak water band,It is in equilibrium with the host	

												mineral; weak fluorescence	
97	BV_1413_80(1)_CIRCLE_3_LIGHT CUBIC 2-PHASE FLINC(5)_VAPOR-PHASE	Aqueous 2-phase	Trail of FLINCS	0	0	0	0	0	#####	####	#DIV/0!	strong water band,It is in equilibrium with the host mineral; Strong fluorescence	
98	BV_1413_80(1)_CIRCLE_3_OVAL 2-PHASE FLINC(1)_LIQUID-PHASE	Aqueous 2-phase, H2O	cluster of FLINCS	0	0	0	0	0	#####	####	#DIV/0!	strong water band,It is in equilibrium with the host mineral; weak fluorescence	
98	BV_1413_80(1)_CIRCLE_3_OVAL 2-PHASE FLINC(1)_VAPOR-PHASE	Aqueous 2-phase	cluster of FLINCS	0	0	0	0	0	#####	####	#DIV/0!	Lacks trace of water band; strong fluorescence; it's in equilibrium with the host mineral	
99	BV_1413_80(1)_CIRCLE_3_OVAL 2-PHASE FLINC(2)_LIQUID-PHASE	Aqueous 2-phase, H2O	cluster of FLINCS	0	0	0	0	0	#####	####	#DIV/0!	Weak water band,It is in equilibrium with the host mineral; weak fluorescence	
99	BV_1413_80(1)_CIRCLE_3_OVAL 2-PHASE FLINC(2)_VAPOR-PHASE	Aqueous 2-phase	cluster of FLINCS	0	0	0	0	0	#####	####	#DIV/0!	Lacks trace of water band; weak fluorescence; it's in equilibrium with the host mineral	
100	BV_1413_80(1)_CIRCLE_4_CUBIC 2-PHASE FLINC(4)_LIQUID-PHASE	Aqueous 2-phase, H2O	Trail of FLINCS	0	0	0	0	0	#####	####	#DIV/0!	Weak water band,It is in equilibrium with the host mineral; weak fluorescence	
100	BV_1413_80(1)_CIRCLE_4_CUBIC 2-PHASE FLINC(4)_VAPOR-PHASE	Aqueous 2-phase	Trail of FLINCS	0	0	0	0	0	#####	####	#DIV/0!	Lacks trace of water band; weak fluorescence; it's in equilibrium with the host mineral	
101	BV_1413_80(1)_CIRCLE_4_CUBIC 2-PHASE FLINC(5)_LIQUID-PHASE	Aqueous 2-phase	cluster of FLINCS	0	0	0	0	0	#####	####	#DIV/0!	Lacks trace of water band; weak fluorescence; it's in equilibrium with the host mineral	
101	BV_1413_80(1)_CIRCLE_4_CUBIC 2-PHASE FLINC(5)_VAPOR-PHASE	Aqueous 2-phase, H2O	cluster of FLINCS	0	0	0	0	0	#####	####	#DIV/0!	strong water band,It is in equilibrium with the host mineral; weak fluorescence	

102	BV_1413_80(1)_CIRCLE_4_DARK ONE-PHASE FLINC (6)	Aqueous 2-phase, PEAK AT 3477.39	cluster of FLINCS	0	0	0	0	0	#####	####	#DIV/0!	WEAK PEAK AT 3477.39	
103	BV_893_90_(2)_ (CIRCLE 2)_FL1_One-phase	Aqueous 1-phase, H2O	Isolated	0	0	0	0	0	#####	####	#DIV/0!	Strong water band,It is in equilibrium with the host mineral; weak fluorescence and strong peak @ 1158	
104	BV_893_90 _(2)_(CIRCLE 2)_FL2_One-phase	Aqueous 1-phase, H2O	cluster of FLINCS	0	0	0	0	0	#####	####	#DIV/0!	Weak water band,It is in equilibrium with the host mineral; weak fluorescence and a weak peak @ 1158	
105	BV_893_90 _(2)_(CIRCLE 2)_FL3_One-phase	Aqueous 1-phase	cluster of FLINCS	0	0	0	0	0	#####	####	#DIV/0!	Weak water band,It is in equilibrium with the host mineral; weak fluorescence and a weak peak @ 1159, Small band @ ~2950	
106	BV_893_90_(2)_ (CIRCLE 2)_FL4_Cubic, TWO-phase_Vapour-Phase	2-Phase, C=N & C-H	cluster of FLINCS	0	0	0	0	0	#####	####	#DIV/0!	Strong Peaks at 2247,09 & 2941,47, Lacks water band, it is in equilibrium with the host mineral	
106	BV_893_90_(2)_ (CIRCLE 2)_FL4_Cubic, TWO-phase_Liquid-Phase	2 Phase, H2O	cluster of FLINCS	0	0	0	0	0	#####	####	#DIV/0!	Strong Peaks at 2247,09 & 2941,47, has a weak water band, Strong methane peak, it is in equilibrium with the host mineral	
107	BV_893_90_(2)_ (CIRCLE 2)_FL5_TWO-phase_Vapour-Phase	Weak band @ ~2900	Isolated FLINC	0	0	0	0	0	#####	####	#DIV/0!	Trace of Liquid-H2O, it is in equilibrium with the host mineral	
107	BV_893_90_(2)_ (CIRCLE 2)_FL5_TWO-phase_Liquid-Phase	Weird Peaks around 3400-3650 (H2O-Vapour)	Isolated Flinc	0	0	0	0	0	#####	####	#DIV/0!	Water band characteristic of OH-Vapour	
108	BV_893_90_(2)_ (CIRCLE 2)_FL6_TWO-phase_Vapour-Phase	2-Phase, C3H6(Cyclopropane) & C=N	Trail of FLINCS	0	0	0	0	0	#####	####	#DIV/0!	Strong Cyclopropane peaks, strong C=N bond, lacks water band, it is in	

												equilibrium with the host mineral	
108	BV_893_90_(2)_ (CIRCLE 2)_FL6_TWO-phase_Liquid-Phase	2-Phase, C3H6(Cyclopropane) & C=N	Trail of FLINCS	0	0	0	0	0	#####	####	#DIV/0!	Strong Cyclopropane peaks, strong C=N bond, lacks water band, it is in equilibrium with the host mineral	
109	BV_893_90_(2)_ (CIRCLE 2)_FL7_TWO-phase_Vapour-Phase	Aqueous 2-phase, H2O	cluster of FLINCS	0	0	0	0	0	#####	####	#DIV/0!	strong water band,It is in equilibrium with the host mineral; Strong fluorescence	
109	BV_893_90_(2)_ (CIRCLE 2)_FL7_TWO-phase_Liquid-Phase	Aqueous 2-phase, H2O	cluster of FLINCS	0	0	0	0	0	#####	####	#DIV/0!	strong water band,It is in equilibrium with the host mineral; Moderate fluorescence	
110	BV_893_90_(2)_ (CIRCLE 3)_Dark, One-phase_FL1	Dark, 1Phase, CH4	cluster of FLINCS	176751	0	0	0	23566.8	1	0	0	Strong Methane peak, lacks water band, it is in equilibrium with the host mineral, strong fluorescence	
111	BV_893_90_(2)_ (CIRCLE 3)_FL2_TWO-phase_Vapour-Phase	2Phase, CH4 & H2O, @2247	cluster of FLINCS	2054.29	0	0	0	273.9053333	1	0	0	Strong Methane Peak, around Strong H2O band, It is in equilibrium with the host mineral	
111	BV_893_90_(2)_ (CIRCLE 3)_FL2_TWO-phase_Liquid-Phase	2Phase, CH4 & H2O, @2248	cluster of FLINCS	1472.88	0	0	0	196.384	1	0	0	Medium methane peak,around Strong H2O, it is in quilibrium with the host mineral	
112	BV_893_90_(2)_(CIRCLE 1)_FL3_One-Phase _	Aqueous 1-phase	cluster of FLINCS	0	0	0	0	0	#####	####	#DIV/0!	Weak water band, it is in equilibrium with the host mineral	
113	BV_893_90_(2)_(CIRCLE 1)_FL5_One-Phase	Aqueous 1-phase	cluster of FLINCS	0	0	0	0	0	#####	####	#DIV/0!	Weak water band, it is in equilibrium with the host mineral	
114	BV_893_90_(2)_(CIRCLE 1)_OVAL ONE-PHASE FLINC_FL2	Aqueous 1-phase	cluster of FLINCS	0	0	0	0	0	#####	####	#DIV/0!	Weak water band, it is in equilibrium with the host mineral	

115	BV_893_90_(2)_(CIRCLE 1)_Round, Dark One-phase FLINC_FL4	Dark, 1Phase, CH4	cluster of FLINCS	8327.16	0	0	0	1110.288	1	0	0	Strong Methane Peak, it is in equilibrium with the host mineral	
116	BV_893_90_(2)_(CIRCLE 1)_Vapour-rich 2-phase FLINC_FL1_Liquid-phase	2-Phase, CH4, CO2	cluster of FLINCS	8673.16	0	1050.37	1102.56	2941.831333	0.3931	0	0.6069	Strong CH4 peak, weak CO2 peaks, Lacks water band, it is in equilibrium with the host mineral	
116	BV_893_90_(2)_(CIRCLE 1)_Vapour-rich 2-phase FLINC_FL1_Vapour-phase	2-Phase, CH4, CO2 & H2O	cluster of FLINCS	7109.69	0	1007.66	1051.38	2656.538667	0.3568	0	0.6432	Strong CH4 peak, weak CO2 peaks, Weak water band, it is in equilibrium with the host mineral	
117	BV_893_90_(2)_(Circle 3)_Light One-Phase_FL3	Aqueous 1-phase	Cluster of FLINC	0	0	0	0	0	#####	####	#DIV/0!	Weak water band, it is in equilibrium with the host mineral	
118	BV_1454_35_(B)_CIRCLE 1_3-Phase FLINC_FL4_B1	3-phase	cluster of FLINCS	0	0	0	0	0	#####	####	#DIV/0!	Lacks water band or any other gaseous peaks, It is in equilibrium with the host mineral	
118	BV_1454_35_(B)_CIRCLE 1_3-Phase FLINC_FL4_B2	3-phase	cluster of FLINCS	0	0	0	0	0	#####	####	#DIV/0!	Lacks water band or any other gaseous peaks, It is in equilibrium with the host mineral	
118	BV_1454_35_(B)_CIRCLE 1_3-Phase FLINC_FL4_Liquid-phase	3-phase, H2O	cluster of FLINCS	0	0	0	0	0	#####	####	#DIV/0!	Medium water band, it is in equilibrium with the host mineral	
119	BV_1454_35_(B)_CIRCLE 1_Cubic, 2-Phase FLINC_FL3_Liquid-phase	2-Phase, H2O	cluster of FLINCS	0	0	0	0	0	#####	####	#DIV/0!	Strong water band, it is in equilibrium with the host mineral	
119	BV_1454_35_(B)_CIRCLE 1_Cubic, 2-Phase FLINC_FL3_Vapour-phase	2-phase	cluster of FLINCS	0	0	0	0	0	#####	####	#DIV/0!	Lacks water band or any other gaseous peaks, It is in equilibrium with the host mineral	
120	BV_1454_35_(B)_CIRCLE 1_Dark, One-Phase_FL2	Aqueous 1-phase	Trail of FLINCS	0	0	0	0	0	#####	####	#DIV/0!	Strong water band, it is in equilibrium with the host mineral	

121	BV_1454_35_(B)_CIRCLE 1_L-RICH, 2-Phase_Liquid-Phase_FL1	Aqueous 2-phase	Cluster of FLINC	0	0	0	0	0	#####	####	#DIV/0!	Lacks water band or any other gaseous peaks, It is in equilibrium with the host mineral	
121	BV_1454_35_(B)_CIRCLE 1_L-RICH, 2-Phase_Vapour-Phase_FL1	2-Phase, H2O	Cluster of FLINC	0	0	0	0	0	#####	####	#DIV/0!	Strong water band, it is in equilibrium with the host mineral	
122	BV_1454_35_(B)_CIRCLE 1_CUBIC, 2-Phase_Vapour-Phase_FL2	2-Phase, H2O	Cluster of FLINC	0	0	0	0	0	#####	####	#DIV/0!	Strong water band, it is in equilibrium with the host mineral	
122	BV_1454_35_(B)_CIRCLE 1_CUBIC, 2-Phase_LIQUID-Phase_FL2	Aqueous 2-phase	Cluster of FLINC	0	0	0	0	0	#####	####	#DIV/0!	Lacks water band or any other gaseous peaks, It is in equilibrium with the host mineral	
123	BV_1454_35_(B)_CIRCLE 4_CUBIC, 2-Phase_FL 3_Liquid-Phase	2-Phase, H2O	Cluster of FLINC	0	0	0	0	0	#####	####	#DIV/0!	Strong water band, it is in equilibrium with the host mineral	
123	BV_1454_35_(B)_CIRCLE 4_CUBIC, 2-Phase_FL 3_Vapour-Phase	2-Phase, H2O	Cluster of FLINC	0	0	0	0	0	#####	####	#DIV/0!	Medium water band, it is in equilibrium with the host mineral	
124	BV_1454_35_(B)_CIRCLE 4_Dark, 1-Phase FL1	1-phase, H2O	Isolated	0	0	0	0	0	#####	####	#DIV/0!	Medium water band, it is in equilibrium with the host mineral	
125	BV_1454_35_(B)_CIRCLE 4_Dark, 1-Phase FL4	1-phase, H2O	Isolated	0	0	0	0	0	#####	####	#DIV/0!	Strong water band, it is in equilibrium with the host mineral	
126	BV_1454_35_(B)_CIRCLE 4_V-RICH, 2-Phase_Liquid-Phase_FL5	2-Phase, H2O	Cluster of FLINC	0	0	0	0	0	#####	####	#DIV/0!	Strong water band, it is in equilibrium with the host mineral	
126	BV_1454_35_(B)_CIRCLE 4_V-RICH, 2-Phase_Vapour-Phase_FL5	2-Phase, H2O	Cluster of FLINC	0	0	0	0	0	#####	####	#DIV/0!	Strong water band, it is in equilibrium with the host mineral	

Appendix 2.2: Gas Ratios calculations in fluid inclusions, Stoffberg samples

No	Flinc name	Flinc type	FIA	CH_4 (area peak)	N_2 (area peak)	CO_2 (area 1286 cm-1 peak)	CO_2 (area 1388 cm-1 peak)	Comments	Solids
1	RGC 22__P1_FI1_fi -Liquid-phase	3phase,	cluster of FLINCS	0	0	0	0	Shows a strong water band, it is in equilibrium with the host mineral	-
1	RGC 22__P1_FI1_fi--Solid-phase	3phase,	cluster of FLINCS	0	0	0	0	Shows a strong water band, it is in equilibrium with the host mineral	-
1	RGC 22__P1_FI1_fi -Vapour-phase	3phase,	cluster of FLINCS	0	0	0	0	Shows a strong water band, it is in equilibrium with the host mineral	-
2	RGC 22_P1_Fl2_fi_Dark	1phase, dark	cluster of FLINCS	0	0	0	0	Shows a strong water band, it is in equilibrium with the host mineral	Quartz
3	RGC 22_P1_Fl3_fi_Vapour-phase	2phase,	cluster of inclusions	0	0	0	0	Shows a strong water band, it is in equilibrium with the host mineral	-
3	RGC 22_P1_Fl3_fi_Liquid-phase	2phase,	cluster of inclusions	0	0	0	0	Shows a strong water band, it is in equilibrium with the host mineral	-
4	RGC 22_P3_Fl1_fi_Vapour-phase	2phase,	cluster of inclusions	0	0	0	0	Shows a strong water band, it is in equilibrium with the host mineral	-
4	RGC 22_P3_Fl1_fi_Liquid-phase	2phase,	individual	0	0	0	0	Shows a strong water band, it is in equilibrium with the host mineral	CALCITE
5	RGC 22_P3_Fl2_fi_Dark	1phase, dark	individual	0	0	0	0	Shows a strong water band, it is in equilibrium with the host mineral	-
6	RGC 22_P3_Fl2_fi_Dark	1phase, dark	individual	0	0	0	0	Shows a strong water band, it is in equilibrium with the host mineral	-
7	RGC 24_P1_Fl1_Liquid-phase	2phase,	individual	0	0	0	0	Shows a MEDIUM water band, it is in equilibrium with the host mineral	-
7	RGC 24_P1_Fl1_Vapour-phase	2phase,	individual	0	0	0	0	Lack of water band, it is in equilibrium with the host mineral	-
8	RGC 24_P1_Fl2_Dark, one-phase	1phase, dark	individual	0	0	0	0	Small trace of water band, conatins small solids of Alkaline feldspars, it is in equilibrium with the host mineral	Alkaline fds
9	RGC 24_P1_Fl3_Dark, one-phase	1phase, dark	cluster of inclusions	0	0	0	0	Lack of water band, it is in equilibrium with the host mineral	
10	RGC 24__P1_FI4_fi -Liquid-phase	3phase, H2O	Trail of FLINCS	0	0	0	0	Shows a MEDIUM water band, it is in equilibrium with the host mineral	-
10	RGC 24__P1_FI4_fi--Solid-phase	3phase, H2O	Trail of FLINCS	0	0	0	0	Shows a strong water band, it is in equilibrium with the host mineral	Quartz

10	RGC 24__P1_FI4_fi -Vapour-phase	3phase, H2O	Trail of FLINCS	0	0	0	0	Weak water band, it is in equilibrium with the host mineral	
11	RGC 16_P1_Fl1_Dark, one-phase	1phase, dark	individual	0	0	0	0	Lack of trace of water band, it is in equilibrium with the host mineral	-
12	RGC 16_P1_Fl2_Liquid-phase	2phase,	cluster of FLINCS	0	0	0	0	Lack of trace of water band, it is in equilibrium with the host mineral	
12	RGC 16_P1_Fl2_Vapour_phase	2phase, H2O	cluster of FLINCS	0	0	0	0	Shows a MEDIUM water band, it is in equilibrium with the host mineral	
13	RGC 16_P2_Fl1_TWO-phase Flinc_LIQUID-PHASE	2phase, H2O	Trail of FLINCS	0	0	0	0	Shows a strong water band, it is in equilibrium with the host mineral	
13	RGC 16_P2_Fl1_TWO-phase Flinc_VAPOUR-PHASE	2phase, H2O	Trail of FLINCS	0	0	0	0	Shows a MEDIUM water band, it is in equilibrium with the host mineral	
14	RGC 16_P3_Fl1_Dark, One-phase Flinc	1phase, dark, H2O	cluster of FLINCS	0	0	0	0	Weak water band, it is in equilibrium with the host mineral	
15	RGC 16_P3_Fl2_LTWO-phase Flinc_LIQUID-PHASE	2phase,	cluster of FLINCS	0	0	0	0	Lack of trace of water band, it is in equilibrium with the host mineral	
15	RGC 16_P3_Fl2_TWO-phase Flinc_VAPOUR-PHASE	2phase, H2O	cluster of FLINCS	0	0	0	0	Shows a strong water band, it is in equilibrium with the host mineral	
16	RGC 16_P6_Fl1_Dark, One-phase Flinc	1phase, dark, H2O	individual	0	0	0	0	Small trace of water band, conatins small solids of Alkaline feldspars, it is in equilibrium with the host mineral	Alkaline fds
17	RGC 20_P2_Fl1_Dark, One-phase Flinc	1phase, dark	individual	0	0	0	0	Lack of trace of water band, it is in equilibrium with the host mineral	
18	RGC 20_P2_Fl2_LTWO-phase Flinc_Liquid-phase	2phase,	Trail of FLINCS	0	0	0	0	Lack of trace of water band, it is in equilibrium with the host mineral	
18	RGC 20_P2_Fl2_LTWO-phase Flinc_Liquid-phase	2phase,	Trail of FLINCS	0	0	0	0	Lack of trace of water band, it is not in equilibrium with the host mineral	
19	RGC 20_P3_Fl1_Dark, One-phase Flinc	1phase, dark, H2O	cluster of FLINCS	0	0	0	0	Weak water band, it is in equilibrium with the host mineral	
20	RGC 20_P3_Fl2_LTWO-phase Flinc_LIQUID-PHASE	2phase, H2O	cluster of FLINCS	0	0	0	0	Shows a strong water band, it is in equilibrium with the host mineral	
20	RGC 20_P3_Fl2_LTWO-phase Flinc_VAPOUR-PHASE	2phase, H2O	cluster of FLINCS	0	0	0	0	Shows a MEDIUM water band, it is in equilibrium with the host mineral	
21	RGC_12_P2_FL1_LIQUID-phase	2phase, H2O	cluster of FLINCS	0	0	0	0	Shows a MEDIUM water band, it is in equilibrium with the host mineral	
21	RGC_12_P2_FL1_vapour-phase	2phase, H2O, CH4	cluster of FLINCS	1222.26	0	0	0	Shows a strong water band and medium sized CH4 Peak, it is in equilibrium with the host mineral	
22	RGC_12_P2_FL2_LIQUID-PHASE	3phase, H2O	cluster of FLINCS	0	0	0	0	Shows a strong water band, it is in equilibrium with the host mineral	-
22	RGC_12_P2_FL2_SOLID-PHASE	3phase, H2O & Calcite	cluster of FLINCS	0	0	0	0	Shows a strong water band, it is in equilibrium with the host mineral	Callcite
22	RGC_12_P2_FL2_vapour-PHASE	3phase, H2O	cluster of FLINCS	0	0	0	0	Shows a strong water band, it is in equilibrium with the host mineral	-
23	RGC_12_P3_FL1_Dark_	1phase, dark CH4	cluster of FLINCS	24083.5	0	0	0	Shows a strong CH4 Peka and lacks a water band, it is in equilibrium with the host mineral	-
24	RGC_12_P4_FL1_LIQUID	2phase, H2O	Trail of FLINCS	0	0	0	0	Shows a strong water band, it is in equilibrium with the host mineral	-

24	RGC_12_P4_FL1_VAPOUR	2phase, H2O	Trail of FLINCS	0	0	0	0	Shows a strong water band, it is in equilibrium with the host mineral	-
25	RGC_12_P4_FL2_LIQUID	2phase,	Trail of FLINCS	0	0	0	0	Lack of trace of water band, it is in equilibrium with the host mineral	-
25	RGC_12_P4_FL2_SOLID	2phase, PEAK AT ~3450	Trail of FLINCS	0	0	0	0	Shows a weak peak at ~3495 cm, It is in equilibrium with the host mineral	-
26	RGC_12_P4_FL3_LIQUID	2phase, H2O	cluster of FLINCS	0	0	0	0	Shows a medium water band, it is in equilibrium with the host mineral	-
26	RGC_12_P4_FL3_Vapour	2phase, H2O	cluster of FLINCS	0	0	0	0	Shows a strong water band, it is in equilibrium with the host mineral	-
27	RGC_12_P4_FL4_Dark	1phase, dark, PEAKS AROUND ~3550	individual	0	0	0	0	Shows a strong Peaks at ~3550, it is in equilibrium with the host mineral	-
28	RGC_12_P4_FL5_Dark	1phase, H2O & Calcite		0	0	0	0	Shows a strong water band, it is in equilibrium with the host mineral	Callcite

Appendix 3.1.1: H2O-NaCl spreadsheed for calculations (for the BV-1 Samples)

Inputs:			**Outputs:**					**Inputs:**		**Outputs:**	
			Salinity	**T @ homog.**	**P @ homog.**	**r_{BULK}**	**dP/dT**	**Calculate a P correction?**		**Trapping Conditions**	
Tm	phase	Th_{L-V}	wt% NaCl	(°C)	(bar)	(g/cm_3)	(bar/°C)	Based on:	T or P	T (°C)	P (bar)
-19	ice	347.2	21.68	347.2	134	0.882	11.4	pressure estimate	3000	598	3000
-6.3	ice	217	9.60	217.0	20	0.921	15.8	pressure estimate	3000	405	3000
-1.3	ice	306.1	2.24	306.1	92	0.717	9.6	pressure estimate	3000	609	3000
-3.2	ice	279.6	5.26	279.6	62	0.799	11.7	pressure estimate	3000	532	3000
-6.5	ice	217.6	9.86	217.6	21	0.922	15.8	pressure estimate	3000	406	3000
-3.8	ice	268.2	6.16	268.2	51	0.825	12.4	pressure estimate	3000	506	3000
-1.8	ice	298.2	3.06	298.2	82	0.743	10.3	pressure estimate	3000	583	3000
-2.5	ice	286.7	4.18	286.7	69	0.776	11.1	pressure estimate	3000	551	3000
-2	ice	157.9	3.39	157.9	6	0.937	17.6	pressure estimate	3000	328	3000
-6	ice	152.1	9.21	152.1	5	0.982	19.7	pressure estimate	3000	305	3000
-4.9	ice	155.2	7.73	155.2	5	0.969	18.9	pressure estimate	3000	313	3000
-5.3	ice	153.7	8.28	153.7	5	0.974	19.2	pressure estimate	3000	310	3000
-2.8	ice	332.7	4.65	332.7	130	0.699	8.6	pressure estimate	3000	667	3000
-0.4	ice	245	0.70	245.0	36	0.808	13.3	pressure estimate	3000	468	3000
-2.6	ice	304.3	4.34	304.3	89	0.747	10.1	pressure estimate	3000	592	3000
-20.8	ice	159.7	22.91	159.7	5	1.081	22.2	pressure estimate	3000	295	3000
-2.9	ice	304.2	4.80	304.2	88	0.753	10.2	pressure estimate	3000	589	3000
-1.8	ice	339.8	3.06	339.8	143	0.661	7.6	pressure estimate	3000	714	3000
-2.1	ice	317.8	3.55	317.8	107	0.712	9.2	pressure estimate	3000	633	3000
-2.2	ice	246.6	3.71	246.6	36	0.833	13.3	pressure estimate	3000	470	3000
-4.4	ice	159.6	7.02	159.6	6	0.960	18.5	pressure estimate	3000	322	3000
-5.4	ice	299.5	8.41	299.5	81	0.803	11.1	pressure estimate	3000	562	3000
-7.8	ice	309.8	11.46	309.8	91	0.821	11.2	pressure estimate	3000	570	3000
-2.4	ice	162.9	4.03	162.9	6	0.936	17.5	pressure estimate	3000	334	3000
-10.9	ice	162.4	14.87	162.4	6	1.015	20.8	pressure estimate	3000	306	3000

-1.7	ice	140.1	2.90	140.1	4	0.950	18.2	pressure estimate	3000	305	3000
-4.8	ice	302.8	7.59	302.8	85	0.788	10.8	pressure estimate	3000	572	3000
-5	ice	335.9	7.86	335.9	132	0.738	9.2	pressure estimate	3000	647	3000
-2.9	ice	266.6	4.80	266.6	50	0.814	12.3	pressure estimate	3000	507	3000
-3.5	ice	249.8	5.71	249.8	38	0.847	13.3	pressure estimate	3000	472	3000
-11.4	ice	346.8	15.37	346.8	142	0.814	10.2	pressure estimate	3000	628	3000
-2.9	ice	184.1	4.80	184.1	11	0.920	16.6	pressure estimate	3000	364	3000
-1.8	ice	365.1	3.06	365.1	194	0.605	5.9	pressure estimate	3000	839	3000
-2.3	ice	250.8	3.87	250.8	39	0.829	13.1	pressure estimate	3000	478	3000
-3.5	ice	249.2	5.71	249.2	38	0.848	13.3	pressure estimate	3000	471	3000
-4.9	ice	325.1	7.73	325.1	115	0.754	9.7	pressure estimate	3000	622	3000
-6.5	ice	298	9.86	298.0	78	0.821	11.5	pressure estimate	3000	553	3000
-6.2	ice	313.6	9.47	313.6	98	0.793	10.6	pressure estimate	3000	587	3000
-5.9	ice	302.9	9.08	302.9	84	0.805	11.1	pressure estimate	3000	566	3000
-6.1	ice	309.7	9.34	309.7	93	0.798	10.8	pressure estimate	3000	579	3000
-11.8	ice	148.2	15.76	148.2	4	1.034	22.1	pressure estimate	3000	284	3000
-11.2	ice	139.5	15.17	139.5	3	1.037	22.6	pressure estimate	3000	272	3000
-13.8	ice	129.8	17.61	129.8	2	1.063	23.9	pressure estimate	3000	255	3000
-5.5	ice	339.6	8.55	339.6	138	0.741	9.2	pressure estimate	3000	651	3000
-2	ice	365	3.39	365.0	193	0.611	6.1	pressure estimate	3000	826	3000
-2.9	ice	353.1	4.80	353.1	166	0.661	7.4	pressure estimate	3000	734	3000
-2.6	ice	360.8	4.34	360.8	183	0.637	6.8	pressure estimate	3000	775	3000
-3.6	ice	334.7	5.86	334.7	132	0.713	8.8	pressure estimate	3000	661	3000
-14.9	ice	335.6	18.55	335.6	120	0.863	11.3	pressure estimate	3000	591	3000
-2.3	ice	284	3.87	284.0	66	0.777	11.2	pressure estimate	3000	546	3000
-2.3	ice	301	3.87	301.0	85	0.747	10.2	pressure estimate	3000	586	3000
-1.6	ice	374.1	2.74	374.1	215	0.578	5.1	pressure estimate	3000	922	3000
-11.2	ice	172.7	15.17	172.7	8	1.008	20.1	pressure estimate	3000	321	3000
-10.5	ice	187.5	14.46	187.5	11	0.989	18.9	pressure estimate	3000	346	3000
-3.2	ice	251	5.26	251.0	39	0.841	13.2	pressure estimate	3000	476	3000
-4.9	ice	225.3	7.73	225.3	24	0.896	14.9	pressure estimate	3000	424	3000
-3.3	ice	248.9	5.41	248.9	37	0.846	13.3	pressure estimate	3000	471	3000
-3.7	ice	243.5	6.01	243.5	34	0.858	13.7	pressure estimate	3000	460	3000
-3.5	ice	245.7	5.71	245.7	35	0.853	13.5	pressure estimate	3000	465	3000

-9.7	ice	148.8	13.62	148.8	4	1.017	21.4	pressure estimate	3000	289	3000
-14.6	ice	144.1	18.30	144.1	4	1.057	22.9	pressure estimate	3000	275	3000
-5.8	ice	195.3	8.95	195.3	13	0.939	16.9	pressure estimate	3000	372	3000
-8.8	ice	286	12.62	286.0	64	0.865	12.6	pressure estimate	3000	519	3000
-2.1	ice	159.4	3.55	159.4	6	0.936	17.5	pressure estimate	3000	330	3000
-3.8	ice	131	6.16	131.0	3	0.979	19.7	pressure estimate	3000	283	3000
-3.1	ice	148.3	5.11	148.3	4	0.957	18.5	pressure estimate	3000	311	3000
-8.8	ice	89.5	12.62	89.5	1	1.054	25.6	pressure estimate	3000	207	3000
-2.4	ice	104.2	4.03	104.2	1	0.984	20.1	pressure estimate	3000	254	3000
-6.9	ice	164.4	10.36	164.4	6	0.980	19.3	pressure estimate	3000	320	3000
-5.7	ice	145.2	8.81	145.2	4	0.985	19.9	pressure estimate	3000	295	3000
-6.2	ice	159.1	9.47	159.1	6	0.978	19.3	pressure estimate	3000	314	3000

Appendix 3.1.2: H2O-NaCl spreadsheed for calculations (for the Stoffberg Samples)

Inputs:			**Outputs:**					**Inputs:**		**Outputs:**	
			Salinity	**T @ homog.**	**P @ homog.**	**r_{BULK}**	**dP/dT**	**Trapping Conditions**			
TmH_2O	phase	Th_{L-V}	wt% NaCl	(°C)	(bar)	(g/cm_3)	(bar/°C)	Based on:	T or P	T (°C)	P (bar)
-3.9	ice	247.9	6.30	247.9	37	0.855	13.5	pressure estimate	3000	468	3000
-8.2	ice	185.9	11.93	185.9	11	0.971	18.3	pressure estimate	3000	349	3000
-1.9	ice	362.3	3.23	362.3	187	0.615	6.2	pressure estimate	3000	817	3000
-2.4	ice	256.3	4.03	256.3	43	0.822	12.8	pressure estimate	3000	488	3000
-9.2	ice	184.7	13.07	184.7	10	0.981	18.7	pressure estimate	3000	344	3000
-8.3	ice	183.3	12.05	183.3	10	0.974	18.5	pressure estimate	3000	345	3000
-3.5	ice	249.5	5.71	249.5	38	0.847	13.3	pressure estimate	3000	472	3000
-8	ice	186.9	11.70	186.9	11	0.968	18.2	pressure estimate	3000	351	3000
-7.4	ice	187.9	10.98	187.9	11	0.962	17.9	pressure estimate	3000	355	3000
-14.1	ice	130.7	17.87	130.7	2	1.064	23.9	pressure estimate	3000	256	3000

-6.6	ice	156.6	9.98	156.6	5	0.984	19.6	pressure estimate	3000	309	3000
-7.4	ice	189.7	10.98	189.7	12	0.960	17.8	pressure estimate	3000	357	3000
-7.9	ice	187.2	11.58	187.2	11	0.967	18.1	pressure estimate	3000	352	3000
-8	ice	186.2	11.70	186.2	11	0.969	18.2	pressure estimate	3000	350	3000
-7.1	ice	191.2	10.61	191.2	12	0.956	17.6	pressure estimate	3000	361	3000
-7.4	ice	189.1	10.98	189.1	11	0.961	17.9	pressure estimate	3000	356	3000
-4.2	ice	361.1	6.74	361.1	180	0.676	7.7	pressure estimate	3000	729	3000
-5.6	ice	373.9	8.68	373.9	205	0.682	7.6	pressure estimate	3000	740	3000
-4.6	ice	286.7	7.31	286.7	68	0.810	11.6	pressure estimate	3000	540	3000
-5.7	ice	356.8	8.81	356.8	169	0.715	8.5	pressure estimate	3000	692	3000
-4.3	ice	359.8	6.88	359.8	177	0.681	7.8	pressure estimate	3000	723	3000
-4.1	ice	363.5	6.59	363.5	185	0.669	7.5	pressure estimate	3000	739	3000
-4.2	ice	361.8	6.74	361.8	181	0.674	7.6	pressure estimate	3000	731	3000
-4.3	ice	358.8	6.88	358.8	175	0.682	7.8	pressure estimate	3000	719	3000
-3.6	ice	359.8	5.86	359.8	179	0.664	7.4	pressure estimate	3000	739	3000
-0.2	ice	194.2	0.35	194.2	14	0.877	15.9	pressure estimate	3000	382	3000
-4.1	ice	204.5	6.59	204.5	16	0.911	15.9	pressure estimate	3000	393	3000
-0.9	ice	269.7	1.57	269.7	54	0.776	11.8	pressure estimate	3000	519	3000
-2.3	ice	313.4	3.87	313.4	101	0.725	9.5	pressure estimate	3000	618	3000
-0.8	ice	193.7	1.40	193.7	13	0.885	15.9	pressure estimate	3000	382	3000
-3.1	ice	354.8	5.11	354.8	169	0.662	7.5	pressure estimate	3000	734	3000
-0.3	ice	191	0.53	191.0	13	0.882	16.0	pressure estimate	3000	377	3000
-2.6	ice	321.2	4.34	321.2	112	0.717	9.2	pressure estimate	3000	636	3000
-3.5	ice	332.9	5.71	332.9	129	0.714	8.9	pressure estimate	3000	657	3000
-0.8	ice	195.8	1.40	195.8	14	0.882	15.8	pressure estimate	3000	385	3000
-2.4	ice	308.5	4.03	308.5	94	0.736	9.8	pressure estimate	3000	604	3000
-3.6	ice	328.7	5.86	328.7	122	0.724	9.1	pressure estimate	3000	644	3000
-4.5	ice	189.9	7.17	189.9	12	0.931	16.8	pressure estimate	3000	368	3000
-3.7	ice	195.7	6.01	195.7	14	0.916	16.2	pressure estimate	3000	380	3000
-4.8	ice	236.6	7.59	236.6	30	0.881	14.3	pressure estimate	3000	444	3000
-4.7	ice	208.7	7.45	208.7	18	0.913	15.8	pressure estimate	3000	397	3000

-5.6	ice	182.8	8.68	182.8	10	0.950	17.6	pressure estimate	3000	353	3000
-3.2	ice	216.8	5.26	216.8	21	0.886	15.0	pressure estimate	3000	416	3000
-9.2	ice	171.2	13.07	171.2	7	0.994	19.7	pressure estimate	3000	323	3000
-7.5	ice	179.6	11.10	179.6	9	0.971	18.5	pressure estimate	3000	341	3000
-9.2	ice	173.9	13.07	173.9	8	0.991	19.5	pressure estimate	3000	328	3000
-8.5	ice	188.6	12.28	188.6	11	0.971	18.3	pressure estimate	3000	352	3000
-8.8	ice	182.6	12.62	182.6	10	0.979	18.7	pressure estimate	3000	342	3000
-8.4	ice	196.7	12.16	196.7	13	0.962	17.7	pressure estimate	3000	365	3000
-4.2	ice	214.3	6.74	214.3	20	0.901	15.4	pressure estimate	3000	408	3000
-14.3	ice	389.5	18.04	389.5	221	0.789	9.0	pressure estimate	3000	699	3000
-5.3	ice	280.5	8.28	280.5	61	0.829	12.1	pressure estimate	3000	524	3000
-0.9	ice	369.3	1.57	369.3	206	0.567	4.7	pressure estimate	3000	965	3000
-2.4	ice	331.5	4.03	331.5	128	0.692	8.5	pressure estimate	3000	671	3000
-4.8	ice	169	7.59	169.0	7	0.955	18.1	pressure estimate	3000	334	3000
-3.5	ice	328.9	5.71	328.9	123	0.721	9.1	pressure estimate	3000	646	3000
-4.3	ice	282.2	6.88	282.2	63	0.812	11.8	pressure estimate	3000	532	3000
-3.2	ice	334	5.26	334.0	131	0.705	8.7	pressure estimate	3000	665	3000
-4.5	ice	280.9	7.17	280.9	62	0.817	11.9	pressure estimate	3000	528	3000
-4	ice	288.9	6.45	288.9	70	0.797	11.3	pressure estimate	3000	547	3000
-3.2	ice	336.8	5.26	336.8	136	0.700	8.5	pressure estimate	3000	673	3000
-3.4	ice	325.9	5.56	325.9	118	0.725	9.2	pressure estimate	3000	639	3000
-3.5	ice	329.5	5.71	329.5	124	0.720	9.0	pressure estimate	3000	648	3000
-4.4	ice	285.7	7.02	285.7	67	0.808	11.6	pressure estimate	3000	539	3000
-3.9	ice	278.9	6.30	278.9	61	0.811	11.8	pressure estimate	3000	527	3000
-7.6	ice	174.8	11.22	174.8	8	0.976	18.9	pressure estimate	3000	334	3000
-9.5	ice	208.8	13.40	208.8	17	0.960	17.2	pressure estimate	3000	382	3000
-10.3	ice	194.3	14.25	194.3	12	0.981	18.4	pressure estimate	3000	357	3000
-9.3	ice	195.3	13.18	195.3	13	0.972	18.1	pressure estimate	3000	361	3000
-8.5	ice	209.8	12.28	209.8	17	0.950	16.9	pressure estimate	3000	386	3000

Appendix 3.2.1:

Table a: Microthermometric data for olivine ferrodiorite of the Bellevue drillcore

Sample number	Tmice (H2O)	Tm H2O	Tm CO2	Tm CLATH	ThH2O	ThCO2	Fluid System	Density	Salinity
BV-83.81 Circle 1 FL1			-59.3	-0.5		27.3	H2O-CO2±CH4	0.633	
BV-83.81 Circle 2 two very Dark 2-phase FLINC			-56.8			29.8	CH4-CO2	0.602	
BV-83.81 Circle 3 FL1			-59.7	-0.7		29.9	H2O-CO2±CH4	0.598	
BV-83.81 Circle 2 FL4			-57.8	11		27.1	H2O-CO2±CH4	0.674	
BV-83.81 Circle 2 FL5			-58.1	4		26.8	H2O-CO2±CH4	0.674	
BV-83.81 Circle 2 FL6			-56.9			29.3	CH4-CO2	0.620	
BV-83.81 Circle 3 FL1			-59.7	12		29.9	H2O-CO2±CH4	0.598	
BV-83.81 Circle 2 Dark 2-phase FLINC	-19.9	-2.9			347.2		H2O-CO2-NaCl	0.882	21.68
BV-83.81 Circle 2 2-phase FLINC(A)	-23.2	-6.3			217		H2O-CO2-NaCl	0.921	9.60
BV-83.81 Circle 3 FL2	-20.1	-1.3			306.1		H2O-CO2-NaCl	0.717	2.24
BV-83.81 Circle 3 FL3	-22.8	-3.2			279.6		H2O-CO2-NaCl	0.799	5.26
BV-83.81 Circle 3 FL4	-23.9	-6.5			217.6		H2O-CO2-NaCl	0.922	9.86
BV-83.81 Circle 3 FL5	-23.1	-3.8			268.2		H2O-CO2-NaCl	0.825	6.16
BV-83.81 Circle 3 FL6	-21.2	-1.8			298.2		H2O-CO2-NaCl	0.743	3.06
BV-83.81 Circle 3 FL7	-21.7	-2.5			286.7		H2O-CO2-NaCl	0.776	4.18
BV-106.90 Circle 1 vapour-rich 2-phase FLINC			-56.8			30.8	CH4-CO2	0.538	
BV-106.90 Circle 1 2-phase FLINC(A)			-57.3	6		24.9	H2O-CH4-CO2	0.712	
BV-106.90 Circle 1 2-phase FLINC(B)			-57.6	-0.9		23.2	H2O-CH4-CO2	0.736	
BV-106.90 Circle 1 2-phase FLINC©			-56.9			30.1	CH4-CO2	0.581	
BV-106.90 Circle 1 2-phase FLINC(D)			-57.1			24.9	CH4-CO2	0.712	
BV-106.90 Circle 1 2-phase FLINC €			-56.9			30.5	CH4-CO2	0.566	
BV-106.90 Circle 2 VAPOUR-RICH 2-phase FLINC			-56.8			23.8	CH4-CO2	0.728	
BV-106.90 Circle 2 2-phase FLINC(A)			-57.3	5		24.2	H2O-CH4-CO2	0.722	

BV-106.90 Circle 2 2-phase FLINC(B)			-56.9			30.2	CH4-CO2	0.584	
BV-106.90 Circle 2 2-phase FLINC©			-57.8	12		23.4	H2O-CH4-CO2	0.733	
BV-106.90 Circle 2 2-phase FLINC(D)			-57.4	11		23.9	H2O-CH4-CO2	0.726	
BV-106.90 Circle 3 (Trail) Diamond 2-phase FLINC	-19.9	-2			157.9		H2O-CO2-NaCl	0.937	3.39
BV-106.90 Circle 3 (Trail) FL2 2-phase FLINC	-24.1	-6			152.1		H2O-CO2-NaCl	0.982	9.21
BV-106.90 Circle 3 (Trail) FL3 2-phase FLINC	-23.8	-4.9			155.2		H2O-CO2-NaCl	0.969	7.73
BV-106.90 Circle 3 (Trail) FL4 2-phase FLINC	-23.1	-5.3			153.7		H2O-CO2-NaCl	0.974	8.28
BV-83.69 (1) Circle 5 Oval, V-rich, 2-phase FLINC (1)	-22.9	-4.9			325.1		H2O-CO2-NaCl		7.73
BV-83.69 (1) Circle 5 , 2-phase FLINC (2)	-24.3	-6.5			298		H2O-CO2-NaCl		9.86
BV-83.69 (1) Circle 5 , 2-phase FLINC (3)	-24.1	-6.2			313.6		H2O-CO2-NaCl		9.47
BV-83.69 (1) Circle 5 , 2-phase FLINC (4)	-23.8	-5.9			302.9		H2O-CO2-NaCl		9.08
BV-83.69 (1) Circle 5 , 2-phase FLINC (5)	-23.9	-6.1			309.7		H2O-CO2-NaCl		9.34
BV-83.69 (1) Circle 3 2-phase FLINC (2)	-24.5	-9.8			148.2		H2O-CO2-NaCl		15.76
BV-83.69 (1) Circle 3 2-phase FLINC (3)	-24.1	-9.2			139.5		H2O-CO2-NaCl		15.17
BV-83.69 (1) Circle 3 2-phase FLINC (4)	-24.7	-10.8			129.8		H2O-CO2-NaCl		17.61

Table b: Microthermometric data for quartz anorthosite of the Bellevue drillcore

Sample number	**Tmice (H2O)**	**Tm H2O**	**Tm CO2**	**Tm CLATH**	**ThH2O**	**ThCO2**	**Td**	**Fluid System**	**Density**	**Salinity**
BV-352.60 Circle 2 cluster of FLINCs 2-ring FLINC			-56.8			30.1	-	CH4-CO2	0.589	
BV-352.60 Circle 2 3-phase FLINC (2-BUBBLES)			-57.4	-0.5		28.9	-	H2O-CO2±CH4	0.632	
BV-352.60 Circle 2 Cubic 2-phase FLINC			-57.2	-0.7		30.4	-	H2O-CO2±CH4	0.365	
BV-352.60 Circle 2 Rectangular 2-phase FLINC(Trail)			-57.2	1		28.6	-	H2O-CO2±CH4	0.641	

BV-352.60 Spherical Light 2-phase FLINC			-57.5	6		29.5	-	H2O-CO2±CH4	0.614	
BV-352.60 Triangle-shaped (cluster)			-57.1	9		30.1	-	H2O-CO2±CH4	0.349	
BV-352.60 Circle 4 vapour-rich FLINC			-57.1	12		30.2	-	H2O-CO2±CH4	0.584	
BV-417.90(1) P1 FL5 2-phase FLINC			-57.3	4.5		29.7	-	H2O-CO2±CH4	0.606	
BV-417.90(1) P1 FL6 2-phase FLINC			-57.1	5.3		28.5	-	H2O-CO2±CH4	0.643	
BV-417.90(1) P2 FL1 2-phase FLINC(Moving bubble)			-56.9			28.3	-	CH4-CO2	0.648	
BV-417.90(1) P3 FL1 2-phase FLINC			-56.8			28.8	-	CH4-CO2	0.635	
BV-417.90(2) Circle 5 2-phase cubic FLINC			-57.1			30	-	CH4-CO2	0.594	
BV-1046.50 (1) Circle 1 FL1			-57.1			30.2	-	CH4-CO2	0.584	
BV-1046.50 (1) Circle 1 FL2			-56.9			30.8	-	CH4-CO2	0.538	
BV-1046.50 (1) Circle 1 FL3			-57.5	10		29.4	-	H2O-CH4-CO2	0.617	
BV-1046.50 (1) Circle 3 Light two-phase FLINC (5)			-56.9			29.4	-	CH4-CO2	0.617	
BV-1046.50 (1) Circle 3 Light two-phase FLINC (6)			-57	4		28.6	-	H2O-CH4-CO2	0.641	
BV-1046.50 (1) Circle 3 Light two-phase FLINC (7)			-58.4	6		29.2	-	H2O-CH4-CO2	0.623	
BV-1046.50(1) Circle 3 Dark two-phase FLINC (8)			-57.1	-0.7		28.4	-	H2O-CH4-CO2	0.646	
BV-1046.50 (1) Circle 3 Oval light two-phase FLINC (9)			-56.9			30.2	-	CH4-CO2	0.584	

BV-1046.50 (1) Circle 2 Dark,Cubic two-phase FLINC (1)			-56.9			30.3	-	CH4-CO2	0.578	
BV-352.60 Circle 2 OVAL shaped 2-phase FLINC	-48.5	-2.8			332.7		-			4.65
BV-352.60 Circle 4 Large 2-phase FLINC	-19.2	-0.4			245		480	H2O-CO2-NaCl± other cations (Ca and K)		0.70
BV-352.60 Circle 4Medium sized 2-phase FLINC (A)	-49.1	-2.6			304.3		-	H2O-CO2-NaCl± other cations (Ca and K)		4.34
BV-352.60(1) CIRCLE 1_2-PHASE FLINC_F1	-48.6	-2.9			304.2			H2O-CO2-NaCl± other cations (Ca and K)		4.80
BV-352.60(1) CIRCLE 1_2-PHASE FLINC_F2	-33.9	-1.8			339.8		535	H2O-CO2-NaCl± other cations (Ca and K)		3.06
BV-352.60(1) CIRCLE 1_2-PHASE FLINC_F3	-48.1	-2.1			317.8		-	H2O-CO2-NaCl± other cations (Ca and K)		3.55
BV-417.90(1) P1 FL2 2-phase FLINC	-48.3	-2.2			246.6		-	H2O-CO2-NaCl± other cations (Ca and K)		3.71
BV-417.90(1) P1 FL3 2-phase FLINC	-32.9	-4.4			159.6		-	H2O-CO2-NaCl± other cations (Ca and K)		7.02

BV-417.90(1) P1 FL4 2-phase FLINC	-37.9	-5.4			299.5		-	H2O-CO2-NaCl± other cations (Ca and K)		8.41
BV-417.90(1) P1 FL7 2-phase FLINC	-23.6	-7.8			309.8		-	H2O-CO2-NaCl± other cations (Ca and K)		11.46
BV-417.90(1) P3 FL2 2-phase FLINC	-48.3	-2.4			162.9		-	H2O-CO2-NaCl± other cations (Ca and K)		4.03
BV-417.90(2) Circle 2 2-phase FLINC	-27.8	-10.9			162.4		-	H2O-CO2-NaCl± other cations (Ca and K)		14.87
BV-417.90(2) Circle 2 Oval 2-phase FLINC	-48.2	-1.7			140.1		-	H2O-CO2-NaCl± other cations (Ca and K)		2.90
BV-417.90(2) Circle 2 Large cube 2-phase FLINC	-34.8	-4.8			302.8		-	H2O-CO2-NaCl± other cations (Ca and K)		7.59
BV-417.90(2) Circle 2 Small cube 2-phase FLINC	-24.8	-5			335.9		550	H2O-CO2-NaCl± other cations (Ca and K)		7.86
BV-417.70(2) Circle 3 FL1 (cluster) 2-phase FLINC	-48.5	-2.9			266.6		-	H2O-CO2-NaCl± other cations (Ca and K)		4.80

BV-1046.50 (1) Circle 3 Dark, Cubic two-phase FLINC (10)	-39.8	-3.5			249.8		-	H2O-CO2-NaCl± other cations (Ca and K)		5.71
BV-1046.50 (1) Circle 4 Oval two-phase FLINC (1)	-20.1	-11.4			346.8		-	H2O-CO2-NaCl± other cations (Ca and K)		15.37
BV-1046.50 (1) Circle 4 Cubic two-phase FLINC (2)	-35.8	-2.9			184.1		-	H2O-CO2-NaCl± other cations (Ca and K)		4.80
BV-1046.50 (1) Circle 4 Cubic two-phase FLINC (3)	-40.5	-1.8			365.1		-	H2O-CO2-NaCl± other cations (Ca and K)		3.06
BV-1046.50 (1) Circle 2 Irregular two-phase FLINC (3)	-44.9	-2.3			250.8		-	H2O-CO2-NaCl± other cations (Ca and K)		3.87
BV-1046.50 (1) Circle 2, two-phase FLINC (2)	-39.6	-3.5			249.2		-	H2O-CO2-NaCl± other cations (Ca and K)		5.71

Table c: Microthermometric data for anorthosite of the Bellevue drillcore

Sample number	Tmice (H2O)	TmH2O	Tm CO2	Tm CLATH	ThH2O	ThCO2	Fluid System	Density	Salinity
BV_893.90(2) Circle 1_FL3_L-Rich, 2-Phase FLINC	-25.3	-11.2			172.7		H2O-NaCl	1.008	15.17
BV_893.90(2) Circle 1_FL4, 2-Phase FLINC	-25.2	-10.5			187.5		H2O-NaCl	0.989	14.46
BV_893.90(2) Circle 3_FL3_V-Rich, 2-Phase FLINC	-21.8	-3.2			251		H2O-NaCl	0.841	5.26
BV_893.90(2) Circle 3_FL3, 2-Phase FLINC	-20.7	-4.9			225.3		H2O-NaCl	0.896	7.73
BV_893.90(2) Circle 3_FL4, 2-Phase FLINC	-24.5	-3.3			248.9		H2O-NaCl	0.846	5.41
BV_893.90(2) Circle 3_FL5, 2-Phase FLINC	-19.1	-3.7			243.5		H2O-NaCl	0.858	6.01
BV_893.90(2) Circle 3_FL6, 2-Phase FLINC	-19.6	-3.5			245.7		H2O-NaCl	0.853	5.71
BV-1413.80 (B) CIRCLE 3 FL1, two-Phase FLINC	-16.9	-9.7			148.8		H2O-NaCl	1.017	13.62
BV-1413.80 (B) CIRCLE 3 FL2, two-Phase FLINC	-16.6	-9.9			144.1		H2O-NaCl	1.057	18.30
BV-1413.80 (B) CIRCLE 3 FL3, two-Phase FLINC	-17.3	-5.8			195.3		H2O-NaCl	0.939	8.95
BV-1413.80 (B) CIRCLE 3 FL4, two-Phase FLINC	-21.9	-8.8			286		H2O-NaCl	0.865	12.62
BV-1413.80 (B) CIRCLE 2 FL1, two-Phase FLINC	-22.9	-2.1			159.4		H2O-NaCl	0.936	3.55
BV-1413.80 (B) CIRCLE 2 FL2, two-Phase FLINC	-23.7	-3.8			131		H2O-NaCl	0.979	6.16
BV-1413.80 (B) CIRCLE 2 FL3, two-Phase FLINC	-17.3	-3.1			148.3		H2O-NaCl	0.957	5.11
BV-1413.80 (B) CIRCLE 5 FL1, two-Phase FLINC	-25.1	-8.8			89.5		H2O-NaCl	1.054	12.62
BV-1413.80 (B) CIRCLE 5 FL2, two-Phase FLINC	-18.4	-2.4			104.2		H2O-NaCl	0.984	4.03
BV-1413.80 (B) CIRCLE 5 FL3, two-Phase FLINC	-17.5	-6.9			164.4		H2O-NaCl	0.980	10.36
BV-1413.80 (B) CIRCLE 5 FL4, two-Phase FLINC	-19.2	-5.7			145.2		H2O-NaCl	0.985	8.81
BV-1413.80 (B) CIRCLE 5 FL5, two-Phase FLINC	-21.9	-6.2			159.1		H2O-NaCl	0.978	9.47
BV_893.90(2) Circle 1_FL1_V-Rich, 2-Phase FLINC			-58.9	-0.5		28.9	H2O-CO2±CH4	0.309	
BV_893.90(2) Circle 1_FL2, 2-Phase FLINC			-59.6	4		27.9	H2O-CO2±CH4	0.658	
BV_893.90(2) Circle 1_FL4, 2-Phase FLINC			-58.1	-0.9		29.1	H2O-CO2±CH4	0.627	
BV_893.90(2) Circle 1_FL5, 2-Phase FLINC			-58.5	2		29.4	H2O-CO2±CH4	0.617	
BV_893.90(2) Circle 2_FL1_L-Rich, 2-Phase FLINC			-59.6	7		27.2	H2O-CO2±CH4	0.673	
BV_893.90(2) Circle 2_FL2, 2-Phase FLINC			-57.8	-0.4		25.3	H2O-CO2±CH4	0.706	
BV_893.90(2) Circle 2_FL3, 2-Phase FLINC			-58.9	-0.7		28.9	H2O-CO2±CH4	0.632	

BV_893.90(2) Circle 2_FL4, 2-Phase FLINC			-59.2	13		27.1	H2O-CO2±CH4	0.675	
BV_893.90(2) Circle 2_FL5, 2-Phase FLINC			-58.2	8		28.2	H2O-CO2±CH4	0.651	

Table d: Microthermometric data for leucogabbronorite of the Bellevue drillcore

Sample number	Tmice (H2O)	Tm	TmCO2	ThH2O	Tm CLATH	ThCO2	Fluid System	Density	Salinity
BV_910_(10)_1_ Circle 2_FL4_Oval 2-phase FLINC			-58.4		-0.9	18.1	H2O-CO2±CH4	0.793	
BV_910_(10)_1_ Circle 2_FL9_ 2-phase FLINC			-59.2		0.6	27.5	H2O-CO2±CH4	0.658	
BV_910_(10)_1_ Circle 2_FL1_Irregular 2-phase FLINC	-43.8	-6		339.6			H2O-NaCl-MgCl2		8.55
BV_910_(10)_1_ Circle 2_FL2_ 2-phase FLINC	-33.9	-2		365			H2O-NaCl-MgCl2		3.39
BV_910_(10)_1_ Circle 2_FL5_ 2-phase FLINC	-41.9	-3		353.1			H2O-NaCl-MgCl2		4.80
BV_910_(10)_1_ Circle 2_FL6_ 2-phase FLINC	-40.8	-3		360.8			H2O-NaCl-MgCl2		4.34
BV_910_(10)_1_ Circle 2_FL7_ 2-phase FLINC	-33.8	-4		334.7			H2O-NaCl-MgCl2		5.86
BV_910_(10)_1_ Circle 2_FL8_ 2-phase FLINC	-31.7	-7		335.6			H2O-NaCl-MgCl2		18.55
BV_910_(10)_1_ Circle 2_FL10_ 2-phase FLINC	-35.9	-2		284			H2O-NaCl-MgCl2		3.87
BV_910_(10)_1_ Circle 2_FL11_ 2-phase FLINC	-37.1	-2		301			H2O-NaCl-MgCl2		3.87
BV_910_(10)_1_ Circle 2_FL12_ 2-phase FLINC	-34.9	-2		374.1			H2O-NaCl-MgCl2		2.74

Appendix 3.2.2:

FLUIDS, package of computer programs for fluid inclusion studies

Program 2: ISOC, version 01/03

Product development Ronald J. Bakker

Included components:

1. Fluids: H2O-CO2-CH4-N2-C2H6-H2S-NH3-H2-O2-CO
2. Salts: NaCl-KCl-CaCl2-MgCl2

Isochore calculation in complex fluid systems

Calculation is based on bulk fluid properties (density and composition)

Compressibility and expansion of host mineral are included

Reference:

Bakker RJ (2003) Chemical Geology, vol.194, 3-23.

Selection of fluid system

(1) amount-of-substance fractions of all components

(2) molalities-mass% of salts and amount-of-substance fractions of gases

(3) molalities-mass% (always relative to H2O)

choose number : 1

Composition of fluid, in amount-of-substance fraction (0 to 1),

salts are introduced as dissociated ions (like Na+ and Cl-)

x(H2O) = 0

x(CO2) = 0.86

x(CH4) = 0.14

x(N2) = 0

x(C2H6) = 0

x(H2S) = 0

x(NH3) = 0

x(H2) = 0

x(O2) = 0

x(CO) = 0

x(Na+) = 0

x(K+) = 0

x(Ca++) = 0

x(Mg++) = 0

x(Cl-) = 0 (calculated)

Bulk fluid density:

(1) Value in cc/mol

(2) Value in g/cc

choose number : 2

Density (g/cc) = 0.632

Molar volume = 63.4405 cc/mol

Equation of state for isochore calculation

(1) Redlich & Kwong (1949) : any gas-mixture

(2) Holloway (1977), Flowers (1979) : any gas-mixture

(3) Jacobs & Kerrick (1981), Kerrick & Jacobs (1981) : H2O-CO2-CH4

(4) Bakker (1999) : any gas-mixture + NaCl

(5) Duan et al. (1992a, 1992b) : H2O-CO2-CH4

(6) Duan et al. (1992, 1996) : H2O-CO2-CH4-N2-CO-H2-O2-H2S

choose number : 5

Details Reference:

Duan et al. (1992a), Geochim.Cosmochim.Acta, 56:2605-2617.

Duan et al. (1992b), Geochim.Cosmochim.Acta, 56:2619-2631.

Composition : H2O-CO2-CH4

Limits : pure gas species 273-1273 K and 0-800 MPa

mixtures 323-1273 K and 0-100 MPa (less accurate to 300 MPa)

Describes both vapour- and liquid-like materials

Would you like to CONTINUE with this equation of state? (y/n) : y

---

VOLUMETRIC DATA of HOST MINERAL (Compressibility, Expansion)

Quartz : Hosieni et al. (1985)

other minerals : Berman (1988)

In which mineral group is the fluid trapped:

(0) not specified

(1) Quartz

(2) Carbonate

(3) Olivine

(4) Al2SiO5

(5) Garnet

(6) Feldspar

(7) Pyroxene

(8) Amphibole

(9) Oxides

(10) Cyclo-silicate

(11) Sphene

choose number : 1

Further specification of mineral:

alpha-beta transition is included in calculations

Isochore corrections starting point:

(1) Default (25 °C and 1 bar)

(2) Other temperature/pressure

choose number : 1

TEMPERATURE RANGE

Automatical correction:

1. if lower limit is below homogenisation conditions

2. if calculation results in negative pressures

Lower T (°C) = 600

Upper T (°C) = 1000

Amount of steps (integer) : 25

Write results in file (drive+filename): l

Results of the calculations

T(K)	P(MPa)	V(cc/mol)
873.15	191.638	65.4002
889.15	194.498	65.696
905.15	196.361	66.1486
921.15	200.871	66.1467
937.15	205.367	66.1451
953.15	209.849	66.1437
969.15	214.317	66.1425
985.15	218.774	66.1415
1001.15	223.218	66.1406
1017.15	227.651	66.1397
1033.15	232.074	66.139
1049.15	236.486	66.1383
1065.15	240.889	66.1377
1081.15	245.282	66.1371
1097.15	249.667	66.1366
1113.15	254.043	66.136
1129.15	258.411	66.1355
1145.15	262.771	66.135
1161.15	267.123	66.1345
1177.15	271.469	66.134
1193.15	275.808	66.1335

1209.15 280.139 66.133

1225.15 284.465 66.1325

1241.15 288.784 66.1319

1257.15 293.098 66.1314

1273.15 297.405 66.1309

Appendix 3.3.1:

FLUIDS, package of computer programs for fluid inclusion studies

Program 2: ISOC, version 01/03

Product development Ronald J. Bakker

Included components:

1. Fluids: H2O-CO2-CH4-N2-C2H6-H2S-NH3-H2-O2-CO
2. Salts: NaCl-KCl-CaCl2-MgCl2

Isochore calculation in complex fluid systems

Calculation is based on bulk fluid properties (density and composition)

Compressibility and expansion of host mineral are included

Reference:

Bakker RJ (2003) Chemical Geology, vol.194, 3-23.

Selection of fluid system

(1) amount-of-substance fractions of all components

(2) molalities-mass% of salts and amount-of-substance fractions of gases

(3) molalities-mass% (always relative to H2O)

choose number : 1

Composition of fluid, in amount-of-substance fraction (0 to 1),

salts are introduced as dissociated ions (like Na+ and Cl-)

x(H2O) = 1

x(CO2) = 0

x(CH4) = 0

x(N2) = 0

x(C2H6) = 0

x(H2S) = 0

x(NH3) = 0

x(H2) = 0

x(O2) = 0

x(CO) = 0

x(Na+) = 0

x(K+) = 0

x(Ca++) = 0

x(Mg++) = 0

x(Cl-) = 0 (calculated)

Bulk fluid density:

(1) Value in cc/mol

(2) Value in g/cc

choose number : 2

Density (g/cc) = 1.00

Molar volume = 18.0153 cc/mol

Equation of state for isochore calculation

(1) Redlich & Kwong (1949) : any gas-mixture

(2) Kell (1967), Kell & Whalley (1965) : pure H2O

(3) Holloway (1977), Flowers (1979) : any gas-mixture

(4) Jacobs & Kerrick (1981), Kerrick & Jacobs (1981) : H2O-CO2-CH4

(5) Bakker (1999), Bowers & Helgeson (1983) : any gas-mixture + NaCl

(6) Haar et al. (1984) : pure H2O

(7) Zhang & Frantz (1987) : H2O-NaCl-KCl-CaCl2

(8) Belonoshko & Saxena (1991a) : pure H2O

(9) Sterner & Bodnar (1991) : H2O-CO2

(10) Duan et al. (1992a, 1992b) : H2O-CO2-CH4

(11) Anderko & Pitzer (1993) : H2O-NaCl-KCl

(12) Bodnar & Vityk (1994) Knight & Bodnar (1989) : H2O-NaCl

(13) Duan et al. (1992, 1996) : H2O-CO2-CH4-N2-CO-H2-O2-H2S

choose number : 7

Details Reference:

Zhang & Frantz (1987), Chem.Geol., 64:335-350.

Composition : binary H2O-NaCl, H2O-KCl, H2O-CaCl2

ideal mixture for H2O-NaCl-KCl-CaCl2 fluids.

Limits : 453-973 K and 0.1-300 MPa, liquid-like fluids.

Based on fluid inclusion research.

Isochore construction is based on Th values (liq).

Homogenisation Temperature (°C) = 172.7

Molar Volume at homogenisation = 20.0085 cc/mol

Density at homogenisation = 0.900379 g/cc

Would you like to CONTINUE with this equation of state? (y/n) : y

---

VOLUMETRIC DATA of HOST MINERAL (Compressibility, Expansion)

Quartz : Hosieni et al. (1985)

other minerals : Berman (1988)

In which mineral group is the fluid trapped:

(0) not specified

(1) Quartz

(2) Carbonate

(3) Olivine

(4) Al2SiO5

(5) Garnet

(6) Feldspar

(7) Pyroxene

(8) Amphibole

(9) Oxides

(10) Cyclo-silicate

(11) Sphene

choose number : 1

Further specification of mineral:

alpha-beta transition is included in calculations

Isochore corrections starting point:

(1) Default (25 °C and 1 bar)

(2) Other temperature/pressure

choose number : 1

TEMPERATURE RANGE

Automatical correction:

1. if lower limit is below homogenisation conditions

2. if calculation results in negative pressures

Lower T (°C) = 300

Upper T (°C) = 1000

Amount of steps (integer) : 25

Write results in file (drive+filename): e

Results of the calculations

T(K)	P(MPa)	V(cc/mol)
573.15	225.049	20.1137
601.15	274.396	20.1115
629.15	323.743	20.11
657.15	373.09	20.1093
685.15	422.437	20.1096
713.15	471.784	20.1111

741.15 521.13 20.114

769.15 570.477 20.1181

797.15 619.824 20.1238

825.15 669.171 20.1311

853.15 718.518 20.1402

881.15 767.865 20.1511

909.15 817.211 20.1642

937.15 866.558 20.1797

965.15 915.905 20.1979

993.15 965.252 20.219

1021.15 1014.6 20.2436

1049.15 1063.95 20.2719

1077.15 1113.29 20.35

1105.15 1162.64 20.396

1133.15 1211.99 20.465

1161.15 1261.33 20.6164

1189.15 1310.68 20.6106

1217.15 1360.03 20.6047

1245.15 1409.37 20.5989

1273.15 1458.72 20.593

Appendix 3.3.2:

Table a: Microthermometric data for quartz monzodiorite of the Stoffberg area

Sample Name	T_{mice} (°C)	TmH_2O (°C)	TH (°C)	T_d (°C)	Form of Homogenization	wt% equiv.NaCl	Density of content	Fluid system
RGC_16_P1_FL1	-43.7	-4.5	189.9	-	L+V>L	7.17	0.93	H2O-NaCl-MgCl2
RGC_16_P1_FL2	-40.9	-3.7	195.7	-	L+V>L	6.01	0.92	H2O-NaCl-MgCl2
RGC_16_P1_FL3	-43.6	-4.8	236.6	540 °C	L+S>L	7.59	0.88	H2O-NaCl-MgCl2
RGC_16_P1_FL4	-43.2	-4.7	208.7	-	L+V>L	7.45	0.91	H2O-NaCl-MgCl2
RGC_16_P1_FL5	-39.6	-5.6	182.8	-	L+V>L	8.68	0.95	H2O-NaCl-MgCl2
RGC_16_P1_FL6	-41.7	-3.2	216.8	-	L+V>L	5.26	0.89	H2O-NaCl-MgCl2
RGC_16_P2_FL1	-31.9	-9.2	171.2	-	L+V>L	13.07	0.99	H2O-NaCl-MgCl2
RGC_16_P2_FL2	-33.9	-7.5	179.6	-	L+V>L	11.10	0.97	H2O-NaCl-MgCl2
RGC_16_P2_FL3	-31.8	-9.2	173.9	-	L+V>L	13.07	0.99	H2O-NaCl-MgCl2
RGC_16_P2_FL4	-38.7	-8.5	188.6	-	L+V>L	12.28	0.97	H2O-NaCl-MgCl2
RGC_16_P2_FL5	-33.8	-8.8	182.6	-	L+V>L	12.62	0.98	H2O-NaCl-MgCl2
RGC_16_P7_FL1	-34.1	-8.4	196.7	-	L+V>L	12.16	0.96	H2O-NaCl-MgCl2
RGC_16_P7_FL2	-42.9	-4.2	214.3	-	L+V>L	6.74	0.90	H2O-NaCl-MgCl2
RGC_16_P7_FL3	-32.8	-14.3	389.5	560 °C	L+S>L	18.04	0.79	H2O-NaCl-MgCl2
RGC_16_P7_FL4	-37.9	-5.3	280.5	-	L+V>L	8.28	0.83	H2O-NaCl-MgCl2
RGC_16_P7_FL5	-43.1	-0.9	369.3	-	L+V>L	1.57	0.57	H2O-NaCl-MgCl2
RGC_16_P7_FL6	-36.9	-2.4	331.5	-	L+V>L	4.03	0.69	H2O-NaCl-MgCl2

Table b: Microthermometric data for granodiorite of the Stoffberg area

Sample Name	T_{mice}	TmH_2O	TH	Form of Homogenization	wt% equiv.NaCl	Density of content	Fluid system
RGC_22_P2_FL1	-54.3	-3.9	247.9	L+V>L	6.30	0.86	H2O-NaCl-CaCl2
RGC_22_P2_FL2	-55.2	-8.2	185.9	L+V>L	11.93	0.97	H2O-NaCl-CaCl2
RGC_22_P2_FL3	-49.8	-1.9	362.3	L+V>L	3.23	0.61	H2O-NaCl-CaCl2
RGC_22_P2_FL4	-48.1	-2.4	256.3	L+V>L	4.03	0.82	H2O-NaCl-CaCl2
RGC_22_P2_FL5	-54.9	-9.2	184.7	L+V>L	13.07	0.98	H2O-NaCl-CaCl2
RGC_22_P2_FL6	-50.7	-8.3	183.3	L+V>L	12.05	0.97	H2O-NaCl-CaCl2
RGC_22_P2_FL7	-54.9	-3.5	249.5	L+V>L	5.71	0.85	H2O-NaCl-CaCl2
RGC_22_P2_FL8	-53.9	-8	186.9	L+V>L	11.70	0.97	H2O-NaCl-CaCl2
RGC_22_P2_FL9	-48.9	-7.4	187.9	L+V>L	10.98	0.96	H2O-NaCl-CaCl2
RGC_22_P3_FL1	-55.5	-14.1	130.7	L+V>L	17.87	1.06	H2O-NaCl-CaCl2
RGC_22_P3_FL2	-47.9	-6.6	156.6	L+V>L	9.98	0.98	H2O-NaCl-CaCl2
RGC_22_P3_FL3	-48.5	-7.4	189.7	L+V>L	10.98	0.96	H2O-NaCl-CaCl2
RGC_22_P3_FL4	-49.6	-7.9	187.2	L+V>L	11.58	0.97	H2O-NaCl-CaCl2
RGC_22_P3_FL5	-52.9	-8	186.2	L+V>L	11.70	0.97	H2O-NaCl-CaCl2
RGC_22_P3_FL6	-53.6	-7.1	191.2	L+V>L	10.61	0.96	H2O-NaCl-CaCl2
RGC_22_P3_FL7	-50.6	-7.4	189.1	L+V>L	10.98	0.96	H2O-NaCl-CaCl2
RGC_22_P4_FL1	-52.9	-4.2	361.1	L+V>L	6.74	0.68	H2O-NaCl-CaCl2
RGC_22_P4_FL2	-54.3	-5.6	373.9	L+V>L	8.68	0.68	H2O-NaCl-CaCl2
RGC_22_P4_FL3	-53.9	-4.6	286.7	L+V>L	7.31	0.81	H2O-NaCl-CaCl2
RGC_22_P4_FL4	-53.8	-5.7	356.8	L+V>L	8.81	0.71	H2O-NaCl-CaCl2
RGC_22_P4_FL5	-49.7	-4.3	359.8	L+V>L	6.88	0.68	H2O-NaCl-CaCl2
RGC_22_P4_FL6	-48.4	-4.1	363.5	L+V>L	6.59	0.67	H2O-NaCl-CaCl2
RGC_22_P4_FL7	-47.8	-4.2	361.8	L+V>L	6.74	0.67	H2O-NaCl-CaCl2
RGC_22_P4_FL8	-50.6	-4.3	358.8	L+V>L	6.88	0.68	H2O-NaCl-CaCl2

RGC_22_P4_FL9	-53.9	-3.6	359.8	L+V>L	5.86	0.66	H2O-NaCl-CaCl2
RGC_24_P1_FL1	-46.7	-0.2	194.2	L+V>L	0.35	0.88	H2O-NaCl-CaCl2
RGC_24_P1_FL2	-52.9	-4.1	204.5	L+V>L	6.59	0.91	H2O-NaCl-CaCl2
RGC_24_P1_FL3	-46.9	-0.9	269.7	L+V>L	1.57	0.78	H2O-NaCl-CaCl2
RGC_24_P1_FL4	-47.8	-2.3	313.4	L+V>L	3.87	0.72	H2O-NaCl-CaCl2
RGC_24_P1_FL5	-47.1	-0.8	193.7	L+V>L	1.40	0.88	H2O-NaCl-CaCl2
RGC_24_P1_FL6	-50.7	-3.1	354.8	L+V>L	5.11	0.66	H2O-NaCl-CaCl2
RGC_24_P1_FL7	-51.9	-0.3	191	L+V>L	0.53	0.88	H2O-NaCl-CaCl2
RGC_24_P1_FL8	-54.9	-2.6	321.2	L+V>L	4.34	0.72	H2O-NaCl-CaCl2
RGC_24_P1_FL9	-55.1	-3.5	332.9	L+V>L	5.71	0.71	H2O-NaCl-CaCl2
RGC_24_P1_FL10	-53.9	-0.8	195.8	L+V>L	1.40	0.88	H2O-NaCl-CaCl2
RGC_24_P1_FL11	-54.8	-2.4	308.5	L+V>L	4.03	0.74	H2O-NaCl-CaCl2
RGC_24_P1_FL12	-55.2	-3.6	328.7	L+V>L	5.86	0.72	H2O-NaCl-CaCl2

Table c: Microthermometric data for monzodiorite of the Stoffberg area

Sample Name	**T_{mice}**	**TmH_2O**	**TH**	**T_d**	**Form of Homogenization**	**wt% equiv.NaCl**	**Density of content**	**Fluid system**
RGC_12_P2_FL2	-23.1	-4.8	169.00	450°C	L+V+S>L+S, L+S>L	7.59	0.96	H2O-NaCl
RGC_12_P2_FL3	-22.9	-3.5	328.9	-	L+V>L	5.71	0.72	H2O-NaCl
RGC_12_P2_FL4	-20.4	-4.3	282.2	-	L+V>L	6.88	0.81	H2O-NaCl
RGC_12_P2_FL5	-21.9	-3.2	334	-	L+V>L	5.26	0.71	H2O-NaCl
RGC_12_P2_FL6	-23.1	-4.5	280.9	-	L+V>L	7.17	0.82	H2O-NaCl
RGC_12_P2_FL7	-23.8	-4	288.9	-	L+V>L	6.45	0.80	H2O-NaCl
RGC_12_P2_FL8	-21.9	-3.2	336.8	-	L+V>L	5.26	0.70	H2O-NaCl
RGC_12_P2_FL9	-21.2	-3.4	325.9	-	L+V>L	5.56	0.72	H2O-NaCl
RGC_12_P2_FL10	-20.8	-3.5	329.5	-	L+V>L	5.71	0.72	H2O-NaCl

RGC_12_P2_FL11	-18.9	-4.4	285.7	-	L+V>L	7.02	0.81	H2O-NaCl
RGC_12_P2_FL12	-19.2	-3.9	278.9	-	L+V>L	6.30	0.81	H2O-NaCl
RGC_12_P3_FL1	-19.8	-7.6	174.8	-	L+V>L	11.22	0.98	H2O-NaCl
RGC_12_P3_FL2	-20.8	-9.5	208.8	-	L+V>L	13.40	0.96	H2O-NaCl
RGC_12_P3_FL3	-23.1	-10.3	194.3	-	L+V>L	14.25	0.98	H2O-NaCl
RGC_12_P3_FL4	-22.6	-9.3	195.3	-	L+V>L	13.18	0.97	H2O-NaCl
RGC_12_P3_FL5	-21.8	-8.5	209.8	-	L+V>L	12.28	0.95	H2O-NaCl

Appendix 4.2.1: A: Reporting Ti concentrations and corresponding temperatures for individual spot analyses in sample RGC 24. Calculated temperatures are tabulated for several calibrations of the Ti-in-quartz thermometer, as discussed in the text.

Spot analyses number	Ti in Qtz (ppm)	TºC Wark and Watson (2006) at 10 kbar	TºC Huang and Audétat (2012) at 3 kbar	TºC Huang and Audétat (2012) at 10 kbar	position
1 /2.	188 ± 22	829 ± 16	844 ± 17	994 ± 19	RIM
2 /2.	99 ± 22	746 ± 27	758 ± 28	898 ± 31	CORE
3 /2.	87 ± 22	731 ± 30	743 ± 31	880 ± 35	CORE
4 /2.	147 ± 22	796 ± 20	809 ± 20	955 ± 23	RIM
5 /2.	115 ± 22	764 ± 24	777 ± 25	919 ± 35	RIM
6 /2.	87 ± 22	731 ± 30	743 ± 31	880 ± 28	CORE
7 /2.	112 ± 22	761 ± 24	774 ± 25	915 ± 35	RIM
8 /2.	65 ± 22	698 ± 38	709 ± 39	842 ± 28	CORE
9 /2.	96 ± 22	742 ± 28	755 ± 28	893 ± 44	CORE
10 /2.	81 ± 22	723 ± 32	734 ± 32	870 ± 32	RIM
11 /2.	148 ± 22	797 ± 20	810 ± 20	956 ± 37	RIM
12 /2.	31 ± 22	624 ± 77	633 ± 79	756 ± 23	RIM
13 /2.	161 ± 22	808 ± 18	822 ± 19	969 ± 89	RIM
14 /2.	110 ± 22	759 ± 25	771 ± 21	912 ± 29	RIM
15 /2.	156 ± 22	804 ± 19	817 ± 21	965 ± 22	CORE
16 /2.	141 ± 22	790 ± 20	804 ± 19	949 ±24	CORE
17 /2.	139 ± 22	788 ± 21	802 ± 21	947 ± 24	CORE
18 /2.	133 ± 22	783 ± 21	796 ± 21	940 ± 25	RIM
19 /2.	161 ± 22	808 ± 18	822 ± 22	969 ± 22	RIM
20 /2.	165 ± 22	811 ± 18	825 ± 19	973 ± 21	RIM
22 /2.	96 ± 22	742 ± 28	755 ± 19	893 ± 32	RIM
23 /2.	96 ± 22	742 ± 28	755 ± 28	893 ± 32	RIM
24 /2.	121 ± 22	771 ± 23	784 ± 28	926 ± 27	CORE
25 /2.	139 ± 22	788 ± 21	802 ± 21	947 ± 24	CORE
26 /2.	124 ± 22	774 ± 23	787 ± 23	930 ± 26	CORE
27 /2.	92 ± 22	737 ± 29	749 ± 29	887 ± 33	CORE
28 /2.	60 ± 22	689 ± 41	700 ± 41	832 ± 47	RIM
29 /2.	114 ± 22	763 ± 24	776 ± 25	918 ± 28	RIM
30 /2.	111 ± 22	760 ± 25	773 ± 25	914 ± 29	RIM

Appendix 4.2.2: Ti concentrations and corresponding temperatures for individual spot analyses in sample RGC 20. Calculated temperatures are tabulated for several calibrations of the Ti-in-quartz thermometer, as discussed in the text.

Spot analyses number	Ti in Qtz (ppm)	TºC Wark and Watson (2006) at 10 kbar	TºC Huang and Audétat (2012) at 3 kbar	TºC Huang and Audétat (2012) at 10 kbar	position
31 /2.	101 ± 22	749 ± 27	761 ± 27	900 ± 31	Rim
33 /2.	121 ± 22	771 ± 23	784 ± 24	926 ± 27	Rim
34 /2.	175 ± 22	819 ± 17	833 ± 18	983 ± 20	CORE
35 /2.	158 ± 22	805 ± 19	819 ± 19	967 ± 22	CORE
36 /2.	119 ± 22	769 ± 23	781 ± 24	924 ± 27	CORE
37 /2.	117 ± 22	767 ± 24	779 ± 24	921 ± 27	Rim
38 /2.	142 ± 22	791 ± 20	805 ± 21	950 ± 24	Rim
39 /2.	174 ± 22	818 ± 17	832 ± 18	982 ± 20	Rim
40 /2.	79 ± 22	720 ± 32	731 ± 33	867 ± 37	Rim

Appendix 4.2.3: Ti concentrations and corresponding temperatures for individual spot analyses in sample RGC 22. Calculated temperatures are tabulated for several calibrations of the Ti-in-quartz thermometer, as discussed in the text.

Spot analyses number	Ti in Qtz (ppm)	TºC Wark and Watson (2006) at 10 kbar	TºC Huang and Audétat (2012) at 3 kbar	TºC Huang and Audétat (2012) at 10 kbar	position
1 /1.	174 ± 22	818 ± 17	832 ± 18	982 ± 20	RIM
2 /1.	110 ± 22	759 ± 25	771 ± 25	912 ± 29	RIM
3 /1.	146 ± 22	795 ± 20	808 ± 20	954 ± 23	RIM
4 /1.	133 ± 22	783 ± 21	796 ± 22	940 ± 25	CORE
5 /1.	157 ± 22	805 ± 19	818 ± 19	966 ± 22	CORE
6 /1.	173 ± 22	818 ± 18	832 ± 18	981 ± 20	CORE
7 /1.	140 ± 22	789 ± 21	803 ± 21	948 ± 24	CORE
8/1.	153 ± 22	801 ± 19	815 ± 20	962 ± 22	CORE
9 /1.	157 ± 22	805 ± 19	818 ± 19	966 ± 22	CORE
10 /1.	101 ± 22	749 ± 27	761 ± 27	900 ± 31	CORE
11 /1.	118 ± 22	768 ± 23	780 ± 24	923 ± 27	RIM
12 /1.	119 ± 22	769 ± 23	781 ± 24	924 ± 27	INTERMEDIATE RIM
13 /1.	159 ± 22	806 ± 19	820 ± 19	968 ± 22	CORE
14 /1.	105 ± 22	753 ± 26	766 ± 26	906 ± 30	RIM
15 /1.	120 ± 22	770 ± 23	782± 24	925 ± 27	INTERMEDIATE RIM

Appendix 4.2.4: Ti concentrations and corresponding temperatures for individual spot analyses in sample RGC 16. Calculated temperatures are tabulated for several calibrations of the Ti-in-quartz thermometer, as discussed in the text.

Spot analyses number	Ti in Qtz (ppm)	TºC Wark and Watson (2006) at 10 kbar	TºC Huang and Audétat (2012) at 3 kbar	TºC Huang and Audétat (2012) at 10 kbar	position
16 /1.	75 ± 22	714 ± 34	832 ± 18	982 ± 20	RIM
17 /1.	101 ± 22	749 ± 27	771 ± 25	912 ± 29	RIM
18 /1.	105 ± 22	753 ± 26	808 ± 20	954 ± 23	RIM
19 /1.	93 ± 22	739 ± 28	796 ± 22	940 ± 25	CORE
20 /1.	76 ± 22	715 ± 33	818 ± 19	966 ± 22	CORE
21 /1.	120 ± 22	770 ± 23	832 ± 18	981 ± 20	CORE
22 /1.	87 ± 22	731 ± 30	803 ± 21	948 ± 24	CORE
24 /1.	136 ± 22	786 ± 21	818 ± 19	966 ± 22	CORE
25 /1.	83 ± 22	725 ± 31	761 ± 27	900 ± 31	CORE
26 /1.	177 ± 22	821 ± 17	780 ± 24	923 ± 27	RIM
27 /1.	124 ± 22	774 ± 23	781± 24	924 ± 27	INTERMEDIATE RIM
28 /1.	137 ± 22	787 ± 21	820 ± 19	968 ± 22	CORE
29 /1.	95 ± 22	741 ± 28	766 ± 26	906 ± 30	RIM
30 /1.	62 ± 22	693 ± 39	782 ± 24	925 ± 27	INTERMEDIATE RIM

Appendix 4.2.5: Ti concentrations and corresponding temperatures for individual spot analyses in sample RGC 12. Calculated temperatures are tabulated for several calibrations of the Ti-in-quartz thermometer, as discussed in the text.

Spot analyses number	Ti in Qtz (ppm)	TºC Wark and Watson (2006) at 10 kbar	TºC Huang and Audétat (2012) at 3 kbar	TºC Huang and Audétat (2012) at 10 kbar	position
31 /1.	58 ± 22	686 ± 42	697 ± 43	828 ± 48	Upper RIM
32 /1.	76 ± 22	715 ± 33	727 ± 34	862 ± 39	INTERMIADE RIM
33 /1.	49 ± 22	668 ± 48	679 ± 49	807 ± 56	CORE
34 /1.	35 ± 22	635 ± 67	645 ± 69	769 ± 78	CORE
35 /1.	83 ± 22	725 ± 31	737 ± 32	874 ± 36	CORE
36 /1.	49 ± 22	668 ± 48	679 ± 49	807 ± 56	CORE
37 /1.	133 ± 22	783 ± 21	796 ± 22	940 ± 25	INTERMIADE RIM
38 /1.	91 ± 22	736 ± 29	748 ± 29	886 ± 33	Lower RIM
39 /1.	34 ± 22	632 ± 69	642 ± 71	766 ± 80	RIM
40 /1.	83 ± 22	725 ± 31	737 ± 32	874 ± 36	RIM
41 /1.	84 ± 22	727 ± 31	739 ± 31	875 ± 36	RIM
42 /1.	133 ± 22	783 ± 21	796 ± 22	940 ± 25	RIM

43 /1.	93 ± 22	739 ± 28	751 ± 29	889 ± 33	INTERMIADE RIM
44 /1.	131 ± 22	781 ± 22	794 ± 22	938 ± 25	INTERMIADE RIM
45 /1.	105 ± 22	753 ± 26	766 ± 26	906 ± 30	CORE
46 /1.	101 ± 22	749 ± 27	761 ± 27	900 ± 31	CORE
47 /1.	102 ± 22	750 ± 26	762 ± 27	902 ± 31	INTERMIADE RIM
48 /1.	131 ± 22	781 ± 22	794 ± 22	938 ± 25	INTERMIADE RIM
49 /1.	70 ± 22	706 ± 36	717 ± 36	851 ± 41	RIM
50 /1.	133 ± 22	783 ± 21	796 ± 22	940 ± 25	RIM

Appendix 4.2.6: Ti concentrations and corresponding temperatures for individual spot analyses in sample RGC 19. Calculated temperatures are tabulated for several calibrations of the Ti-in-quartz thermometer, as discussed in the text.

Spot analyses number	**Ti in Qtz (ppm)**	**TºC Wark and Watson (2006) at 10 kbar**	**TºC Huang and Audétat (2012) at 3 kbar**	**TºC Huang and Audétat (2012) at 10 kbar**	**position**
51 /1.	95 ± 22	741 ± 28	753 ± 28	892 ± 32	RIM
52 /1.	58 ± 22	686 ± 42	697 ± 43	828 ± 48	CORE
56 /1.	88 ± 22	732 ± 30	744 ± 30	881 ± 34	RIM
57 /1.	102 ± 22	750 ± 26	762 ± 27	902 ± 31	CORE
58 /1.	91 ± 22	736 ± 29	748 ± 29	886 ± 33	RIM
59 /1.	141 ± 22	790 ± 20	804 ± 21	949 ± 24	RIM
60 /1.	32 ± 22	627 ± 74	636 ± 76	759 ± 86	RIM
61 /1.	41 ± 22	650 ± 57	660 ± 58	786 ± 66	RIM
62 /1.	117 ± 22	767 ± 24	779 ± 24	921 ± 27	Intermediate RIM
63 /1.	98 ± 22	745 ± 27	757 ± 28	896 ± 32	CORE
64 /1.	142 ± 22	791 ± 20	805 ± 21	950 ± 24	CORE
65 /1.	146 ± 22	795 ± 20	808 ± 20	954 ± 24	CORE
66 /1.	138 ± 22	788 ± 21	801 ± 21	946 ± 23	CORE
67 /1.	130 ± 22	780 ± 22	793 ± 22	937 ± 25	Intermediate RIM
68 /1.	81 ± 22	723 ± 32	734 ± 32	870 ± 37	RIM
69 /1.	86 ± 22	730 ± 30	741 ± 31	878 ± 35	RIM
70 /1.	50 ± 22	670 ± 47	681 ± 49	810 ± 55	RIM
71 /1.	78 ± 22	718 ± 33	730 ± 33	865 ± 38	RIM
72 /1.	117 ± 22	767 ± 24	779 ± 24	921 ± 27	RIM
73 /1.	101 ± 22	749 ± 27	761 ± 27	900 ± 31	RIM
74 /1.	167 ± 22	813 ± 18	827 ± 18	975 ± 21	Intermediate RIM
75 /1.	43 ± 22	655 ± 55	665 ± 56	792 ± 63	CORE
76 /1.	148 ± 22	797 ± 20	810 ± 20	956 ± 32	CORE
77 /1.	97 ± 22	744 ± 27	756 ± 28	895 ± 37	CORE
79 /1.	81 ± 22	723 ± 32	734 ± 32	870	RIM
80 /1.	88 ± 22	732 ± 30	744 ± 30	881 ± 34	RIM